**The Dissertation Committee for Kirk Jeremy Ziegler**
**Certifies that this is the approved version of the following dissertation:**

# Chemical Equilibria and Nanocrystal Synthesis in High Temperature Supercritical Solutions

Committee:

Keith Johnston, Supervisor

Brian Korgel, Co-Supervisor

Leon Lasdon

Gary Rochelle

Peter Rossky

# Chemical Equilibria and Nanocrystal Synthesis in High Temperature Supercritical Solutions

by

**Kirk Jeremy Ziegler, B.S.**

**Dissertation**

Presented to the Faculty of the Graduate School of

The University of Texas at Austin

in Partial Fulfillment

of the Requirements

for the Degree of

**Doctor of Philosophy**

The University of Texas at Austin

December, 2001

ProQuest Information and Learning Company
300 North Zeeb Road
PO Box 1346
Ann Arbor, MI 48106-1346

Dedicated to my brother

# Acknowledgements

During the course of my dissertation at the University of Texas at Austin, I benefited from interactions with many people. I would like to take the time to thank them here. A special thanks to Dr. Keith P. Johnston, who was responsible for immeasurable contributions to the completion of this thesis, and to my co-advisor, Dr. Brian A. Korgel, for his guidance in the field of nanomaterials. I would also like to thank Dr. Leon Lasdon, Dr. Peter Rossky, and Dr. Gary Rochelle for their valuable contributions as members of my dissertation committee.

I would like to give a very special thanks to the members of my research group for their help, advice, and friendship especially to Justin Holmes, Parag Shah, Steve Sirard, Jerzy Chlistunoff, Gabriel Luna-Barcenas, Ted Lee, Tim Young, Petros Psathas, Lourdes Calvo, Sandro daRocha, Marazban Sarkari, Won Ryoo, and Shabbir Husain. In addition, I would like to thank members of Dr. Korgel's research group: Chris Doty, Lindsay Pell, Mike Sigman, Inaas Darrat, and especially Cindy Stowell and Tobias Hanrath who were quite helpful in the waning days of my work here at UT. The department staff has also been helpful in the completion of my thesis and I want to thank them, especially Mark Smith, Jim Smitherman, T. Stockman, Eddie Oliver, Eddie Ibarra, Kevin Haynes, Mary Lindholm, and Kay Swift. I would also like to acknowledge support from caffeine, which was quite helpful during the late nights and early mornings.

Finally, I would like to thank my family and friends especially Veronica Silk whose presence was invaluable through graduate school and my grandmother who always found the words to encourage me in pursuing my dreams and aspirations.

Kirk J. Ziegler

December 2001

# Chemical Equilibria and Nanocrystal Synthesis in High Temperature Supercritical Solutions

Publication No. __________

Kirk Jeremy Ziegler, Ph.D.

The University of Texas at Austin, 2001

Supervisors: Keith P. Johnston and Brian A. Korgel

In supercritical water (SCW), reaction equilibrium constants may differ by several orders of magnitude from room temperature values due to changes in the solvent dielectric constant. While these changes have been well characterized for ionic acid-base reactions, non-ionic polar reaction equilibria in SCW have received little attention. Here, we have shown for several oxidation states of $NO_x$ species that polarity differences from reactants to products result in significant changes in equilibrium constants that scale with density. In addition, linear extrapolation of these equilibrium constants to zero density results in values which are very close to independent gas phase values.

Nitrate reaction equilibria provide the framework for the synthesis of copper nanocrystals in SCW. Aqueous copper nitrate ($Cu(NO_3)_2$) solutions when taken to supercritical conditions, hydrolyze to form large copper (II) oxide particles. Because of the low dielectric environment, SCW is a suitable solvent to employ organic capping ligands to control and stabilize the synthesis of nanocrystals. The presence of 1-hexanethiol results in reduction of copper (II) and produces copper nanocrystals approx. 7 nm in diameter. A proposed mechanism for sterically stabilized nanocrystal growth in SCW describes competing pathways of hydrolysis to large oxidized copper particles versus ligand exchange and arrested growth by thiols to produce small monodisperse Cu nanoparticles.

A new synthetic method was developed to produce organic-monolayer passivated silicon and germanium nanocrystals in solvents under supercritical conditions. By thermally degrading organosilane or organogermane precursors at high temperatures and pressures, sterically-stabilized nanocrystals could be obtained using octanol as a capping ligand. During the reaction, octanol binds to the nanocrystal surface through an alkoxide linkage to provide steric stabilization through the hydrocarbon chain. The absorbance and luminescence spectra of the nanocrystals exhibit significant size-dependent blue shifts in optical properties from bulk luminescence due to quantum confinement effects. High luminescence quantum yields are observed. The smallest nanocrystals exhibit discrete optical transitions, characteristic of quantum confinement effects for crystalline nanocrystals with a narrow size distribution.

## Table of Contents

## List of Figures

## List of Tables

# Chapter 1: Introduction

## 1.1 Background

The search for environmentally benign solvents [1] has raised the interest in supercritical fluids (SCFs) as replacements for hazardous organic solvents. The two most frequently used SCFs are supercritical $CO_2$ (sc-$CO_2$) and supercritical water (SCW) due to their abundancy and relative non-flammability and non-toxicity. Sc-$CO_2$ has the advantage that it has critical properties near ambient conditions ($T_c$ = 31 °C, $P_c$ = 72 bar) and can often be easily separated and recovered by depressurization, while SCW has the advantage of offering a wide range in dielectric constant leading to unique tunability of chemistry.

The interest in understanding chemical phenomena in aqueous solutions at elevated temperatures and pressures has grown significantly during the last decade [1-4]. Practical applications include hydrothermal growth of crystals, spraying of ceramics, and hydrothermal synthesis reactions. A promising application of supercritical water ($T_c$ = 374 °C, $P_c$ = 221 bar) is the treatment of organic wastes such as pulp and paper mill sludge, pharmaceutical biological wastes, and military wastes through oxidation (SCWO) [5]. SCWO converts organics primarily into $CO_2$ and $H_2O$. SCW is of interest for oxidation because of the high destruction efficiency due to faster reaction rates at high temperature and the nearly complete solubility of organics and oxygen resulting in rapid diffusion [6-8]. In addition, modest organic concentrations can make the process economically appealing due to auto-thermal operation [4]. However, despite practical interest in SCWO, key aspects of the process are not fully understood. Although recently much effort has been made in understanding acid-base chemistry in SCW, a firm knowledge of this chemistry is not yet available. These acid-base reactions play a central role in hydrothermal reactions such as oxidation and decomposition reactions, [7,9-11] and corrosion [12,13]. Significant efforts are also being made to understand hydrogen bonding [14-20] and the effects that solvation has on acid-base chemistry [21-25]. A firm knowledge of this solution chemistry will help yield the successful design and operation of SCWO reactors.

In addition to SCWO, many researchers have concentrated their efforts into the partial oxidation of waste streams. In this process, the waste stream is converted into useful products such as organic acids or can be used for the addition of oxygenated functional groups into hydrocarbons [4]. Examples include the conversion of methane to methanol [26-28] and cyclohexane to cyclohexanone [29]. A full understanding of these methods, however, requires a detailed knowledge of the reaction equilibria, which is usually unavailable.

The ability to control oxidation to obtain useful products has led to an increased perception that SCW can be used as a reaction medium. By controlling the parameters of the reaction (i.e. temperature, pressure, oxygen concentration), chemists can selectively choose the desired products. Furthermore, because of the tunability of this medium, the potential exists to eliminate by-products easing separation costs. For example, Korzenski and Kolis [30] have shown that the Diels-Alder reaction of 2,3-dimethyl-1,3-butadiene with acrylonitrile yields the product 3,4-dimethylcyclohex-3-enyl cyanide with a 100% yield. In addition, due to the high temperature and high diffusivity within SCW reactions can achieve nearly complete conversion in short periods of time. In the hydrolysis of ethyl acetate, nearly complete conversion to acetic acid and ethanol was achieved with residence times of 150 s [29].

## 1.2 Properties of Supercritical Fluids

At supercritical conditions, many of the properties of SCFs vary with density. Because SCFs are highly compressible near the critical point, small changes in pressure or temperature (see Fig. 1.1) cause large changes in the density and, therefore, offer the opportunity to manipulate the reaction environment in a supercritical solvent. In addition, many transport properties such as the viscosity and diffusivity as seen in Table 1.1 are typically between those of a liquid and a gas [4]. These differences allow reactions that are diffusion limited in the liquid phase to become much faster at supercritical conditions. Finally, SCFs have unique solubility properties. Species that are often insoluble at ambient conditions can become very soluble at supercritical conditions and, likewise, species that are soluble may become insoluble.

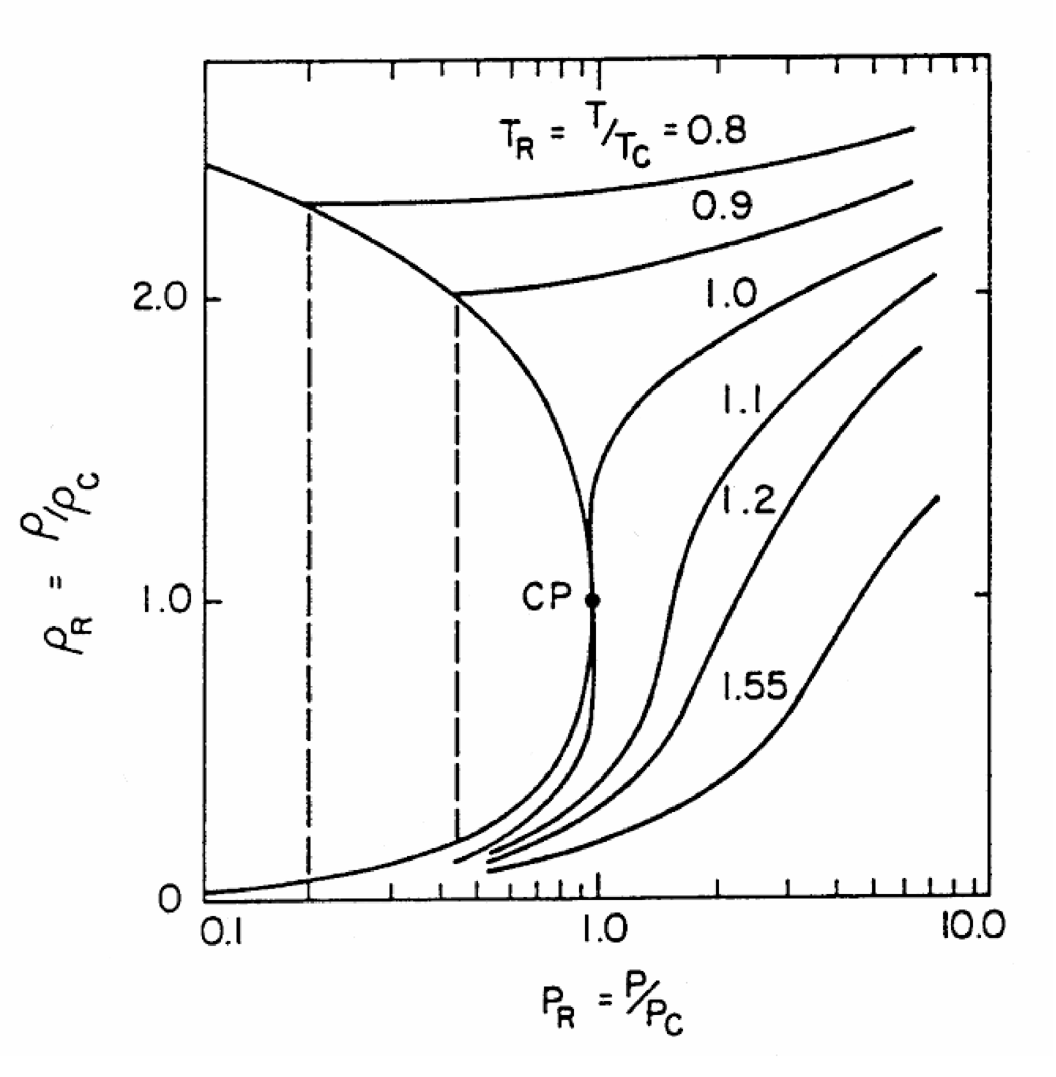

Fig. 1.1.  Phase diagram for supercritical fluids.

Table 1.1. Properties of Supercritical Fluids

| | Diffusion ($cm^2/s$) | Viscosity (g/cm/s) |
|---|---|---|
| Gases | $10^{-1}$ | $10^{-4}$ |
| SCFs | $10^{-3}$ | $10^{-3}$ |
| Liquids | $10^{-5}$ | $10^{-2}$ |

***1.21 Properties of Supercritical Water.*** Upon heating to supercritical conditions, water undergoes dramatic changes in density and the dielectric constant. These dramatic changes are what provide SCW with its interesting properties and advantages giving it both non-aqueous and aqueous characteristics. As mentioned for all supercritical fluids, small changes in temperature and pressure lead to large changes in the density. In SCW, these changes in density strongly affect the dielectric constant (see Fig. 1.2) and, hence, the solubilities of salts and the presence of ionic species, which play a central role in solvent effects on chemical reaction rate and equilibrium constants, phase equilibria, and corrosion. The dielectric constant is a measure of the ability of a solvent to separate charged species. Fig. 1.2 shows the dielectric constant of water, $\varepsilon$, as a function of temperature and pressure. At 250 bar, the dielectric constant drops from a room-temperature value of around 80, where it easily solubilizes salts, to values of 5-10 at near-critical temperatures and finally to 1-2 at 450 °C and above. Along the same isobar, the dissociation constant, $K_w$, falls from $10^{-14}$ at room temperature to $10^{-18}$ in the near-critical region and to $10^{-23}$ under supercritical conditions. This change is due to the changing solvent environment. Under supercritical conditions, the solvent is no longer able to solvate the charged species in reaction (1.1.) and is, hence, driven to the left causing a drop in the equilibrium constant $K_w$.

$$H_2O \leftrightarrows H^+ + OH^- \qquad (1.1)$$

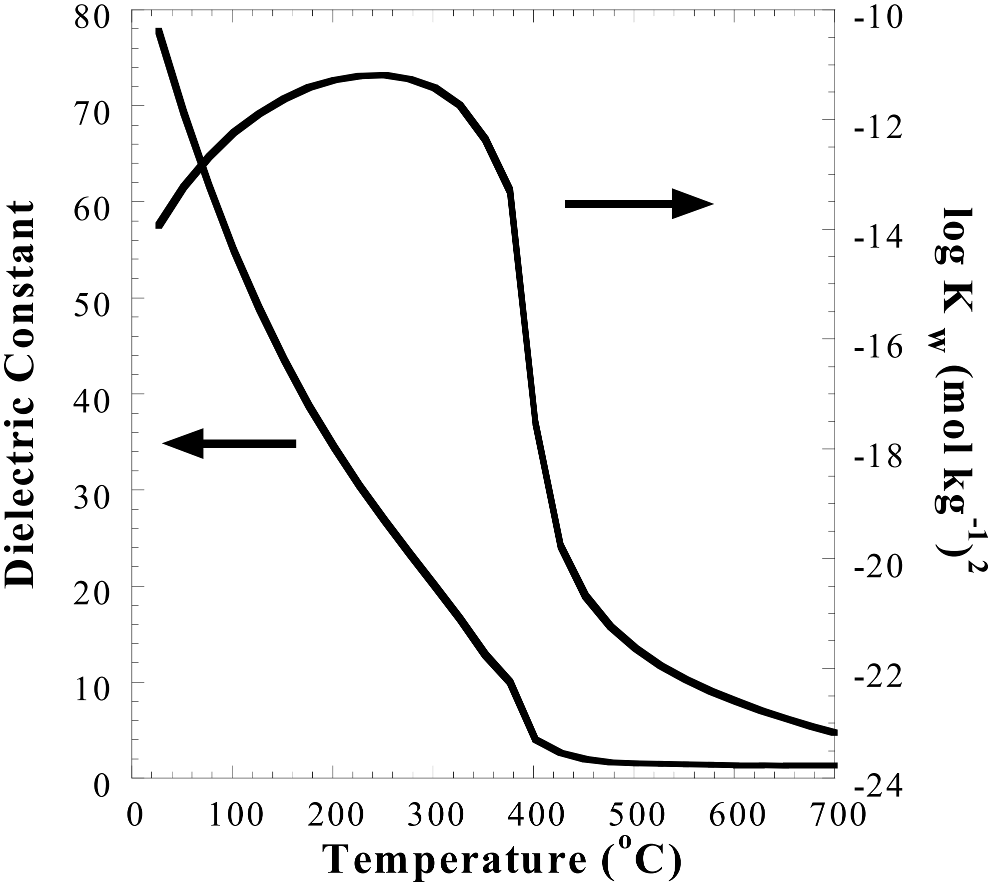

Fig. 1.2. Effect of temperature on the dielectric constant and the dissociation constant of water.

Furthermore, Raman spectra of deuterated water in the supercritical region show only a small residual amount of hydrogen bonding [31]. As a result, SCW acts as a non-polar dense gas, and its solvation properties resemble those of a low polarity organic.

Near the critical point, the solubility of organic compounds in water correlates strongly with density and is, thus, very pressure dependent in this region. Benzene solubility in water is a good example [8,32]. At 25 °C, benzene is sparingly soluble in water (0.07%), however the solubility rises to 35-wt% at 295 °C and 25 MPa, where the critical point of the benzene-water mixture is surpassed.

Conversely, the solubility of inorganic salts in SCW is very low. Many salts that have high solubilities in liquid water have extremely low solubilities in SCW. For example, NaCl solubility is about 37% at 300 °C and about 120 ppm at 550 °C and 25 Mpa; [33] $CaCl_2$ has a maximum solubility of 70-wt% at sub-critical temperatures and drops to 3 ppm at 500 °C and 25 Mpa [34]. The fact that inorganics are practically insoluble is consistent with a low dielectric constant for water of about 2 and an extremely low dissociation constant, $K_w$, of less than $10^{-22}$ at 500 °C and 25 MPa.

## 1.3 In-situ UV-vis for Measuring Reaction Equilibria

The measurement of reaction equilibria within supercritical fluids requires sophisticated *in-situ* methods due to the high pressure and occasional high temperature. Although there are some examples of pH electrodes [35] and conductivity electrodes [36-40] within supercritical fluids, spectroscopic methods have shown themselves to be the most versatile. Unlike some other supercritical fluids (for example $CO_2$), in which there have been many spectroscopic studies, [41-43] only a limited number of spectroscopic studies have been reported for aqueous solutions at sub-critical and supercritical conditions due to the challenges of high temperatures and pressures. Spectroscopic work in high temperature supercritical fluids is challenged not only by materials limitations, but also by features intrinsic to this unusual medium, particularly corrosion.

Chen *et al.* [44] presented a review of the experimental methods for measuring the thermodynamic properties of dissociation reactions of aqueous solutions at high temperatures and pressures. Current methods for studying reactions in SCW solutions include conductivity, potentiometry, and spectroscopy. The research group at Oak Ridge National Laboratory has measured thermodynamic properties for simple inorganic reactions studied by potentiometry up to 300 °C [45-50] and by conductivity up to 800 °C [36-39]. Raman and IR spectroscopy have been used primarily to determine kinetics and structural characteristics [9,10,51-55]. The difficulty in using this spectroscopic method is that the extinction coefficients are largely dependent on density and temperature [9,10,51,52] making it difficult to determine the concentration of the absorbing species and, hence, equilibrium constants.

UV-vis spectroscopy is ideal for the accurate determination of thermodynamic properties since extinction coefficients are only weakly dependent on temperature and pressure. While some reactions may be studied directly by UV-vis spectroscopy, [56-58] several species of interest do not absorb in this region and indirect methods are required. The traditional approach to characterizing these acid-base reactions is to measure the acidity of the solution. Macdonald et al [35] developed hydrothermal pH sensors composed of $ZrO_2$, Pd hydrides, and Ir oxides that could be used to characterize these reactions. Another means of determining the pH of solution is through the use of an indicator, which allows accurate determination of equilibrium constants [59-67] and, in addition, these probes offer insight into the molecular level interactions occurring in the solution.

***1.31 Titrations using pH indicators.*** Our group has investigated some organic indicators that have proven themselves to be successful in determining the pH of a supercritical solution and in accurately obtaining thermodynamic properties [61,68,69]. These indicators include β-naphthoic acid, acridine, s-collidine, and β-naphthol. These indicators cover a fairly broad pH range allowing many kinetic and equilibrium reactions to be studied in near critical and supercritical solutions.

To better understand the effects of SCW on chemical reactions at the molecular level, a spectroscopic approach is needed to investigate molecular interactions in the SCW phase, particularly by using organic probes. Recently, Bennett and Johnston [20] reported spectral shifts in the π-π* band of benzophenone and the n-π* band of acetone. This is the first time organic indicators have been used to study the solvation properties of SCW. This study has provided insight into the solvent strength of water, the clustering of water about an organic solute, and hydrogen bonding.

***1.32 Equilibria Studies using Chromophores.*** For systems with chromophores such as several metal ions, UV-vis spectroscopy may be used to study chemical equilibria directly without a pH indicator. Seward and co-workers have measured high temperature thermodynamic properties of chloride complexation of lead(II), and maganese(II) to 300 °C, and iron(II) to 200 °C [56-58]. Cr(VI) is of interest in hydrothermal oxidation because it is soluble and may be separated from high level nuclear wastes by hydrothermal oxidation of insoluble Cr(III) [70]. Also, oxidation of $Cr_2O_3$ is a reason why some stainless steels (e.g. SS 316) lose their corrosion resistance in oxidative hydrothermal environments [12].

The dissociation constants of $H_2CrO_4$ ($K_{a1}$) and $HCrO_4^-$ ($K_{a2}$) have been measured by UV-vis spectroscopy up to 420 °C [71]. The predominant species of Cr(VI) in alkaline (KOH) solutions at elevated temperatures were found to be chromate ($CrO_4^{2-}$), bichromate ($HCrO_4^-$), and, at temperatures above 260 °C, ($K^+$)($CrO_4^{2-}$) ion pairs. The molal concentration of $HCrO_4^-$ initially increases with temperature as expected due to the decrease in acidity of $K_{a2}$, but decreases again in the vicinity of water's critical point where the density decreases substantially. The decrease in $HCrO_4^-$ at high temperature and low density (dielectric constant) is counter-intuitive, but may be attributed to ($K^+$)($CrO_4^{2-}$) ion pairs, which become very favorable even in weakly alkaline solutions and eventually leads to $K_2CrO_4$ precipitation at 420 °C, where the Cr(VI) band becomes very small and noisy.

### 1.4 Nanocrystal Materials Synthesis

The study of reaction equilibria in high temperature aqueous solutions has resulted in an increased understanding of decomposition reactions, solubility, and solvation characteristics. These factors are key components in the development of synthetic methods for nanomaterials within SCFs, which provide knowledge of the parameters that control the morphology, particle size, and size distribution of nanoparticles. The effects of high temperature and density on reaction equilibria, solvation, and solubility may be expected to have a large effect on the properties and size of metals and semiconductors synthesized in SCFs. Since SCFs should enable great chemical flexibility and synthetic tunability as described above, it is desirable to use SCFs for highly controlled solution-phase synthetic methods. At low temperature, water-in-$CO_2$ microemulsions have been successfully utilized as ‘micro reactors’ in the production of silver [72] and cadmium sulfide [73] nanoparticles. Studies of particle formation of inorganic materials in SCW have recently become prevalent in the literature and have been reviewed [74]. Metal oxides have been prepared in SCW by the use of metal salts via a two-stage decomposition mechanism involving a hydrolysis and dehydration step [75]. However, these methods have had difficulties achieving nanoparticles that exhibit size-dependent properties due to agglomeration and coalescence.

The field of high temperature synthesis in supercritical fluids is now starting to address the production of nanomaterials with size-dependent properties. Dimensionality plays a central role in determining the physical properties of materials [76]. Electron interactions, for example, differ in three-dimensional bulk solids from those in two-dimensional (2D) and one-dimensional (1D) systems [76]. These differences can often lead to new phenomena. As technology rapidly shrinks toward the nanometer length-scale, understanding how dimensionality affects the electronic properties of semiconductors and metals has become technologically relevant. Material dimensions will restrict electron interactions resulting in an overall loss of energy level degeneracy in the electronic structure. These quantum confinement effects will lead to new electronic and optical properties, such as size-tunable excitation and luminescence energies. These new material properties might be exploited in a variety of new technologies including electronic, optical, medical, coatings, catalytic, memory, and sensor applications [77,78].

Nanoparticles exhibit properties different from that of a bulk material and these properties have been shown to be size dependent [78]. Particles of metals and semiconductors whose size is on the same order as the wavelength of the electron are of extraordinary interest since they behave electronically as zero-dimensional (0D) quantum dots [77]. Therefore, the classical laws of physics are no longer valid and have to be exchanged for quantum mechanics. Because of the appearance of discrete energetic states similar to molecular orbitals, semiconductor clusters have been called ‘artificial atoms’, and provide the unique opportunity to study semiconductor properties as they evolve from atoms to small molecules to a bulk crystal (See Fig. 1.3). Excellent examples of size-dependent discrete optical transitions exist for clusters of direct band gap semiconductors, such as CdSe [78,79] and InAs [80]. Size-dependent discrete optical transitions of indirect band gap materials, however, have not been exhibited. The phonon assistance required for an indirect transition (discussed below) reduces the probability of optical transitions. In addition, the optical properties of these materials are highly susceptible to surface states and trapped states. Therefore, it has been more difficult to obtain discrete bands in indirect band-gap materials.

The difficulty in achieving size-dependent optical properties for indirect band gap materials is due to the limitations of synthetic methods and control over

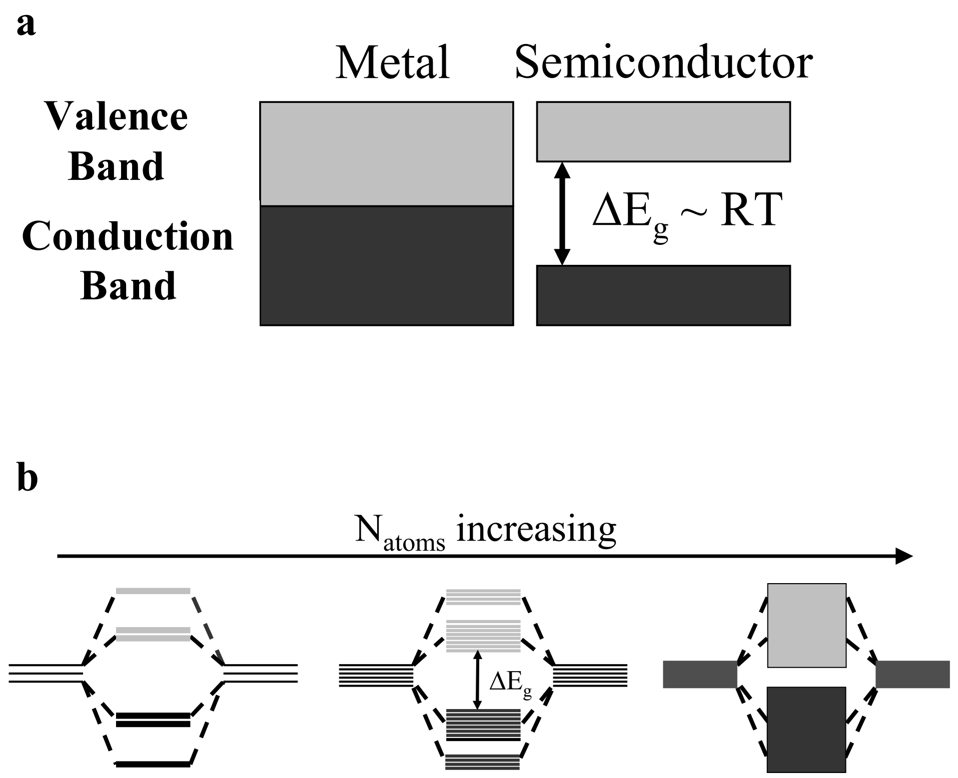

Fig. 1.3. Schematic of band structures for metals and semiconductors. (a) Standard depiction of the valence band and conduction band for metals and semiconductors. (b) Energy levels from a two atom model to a bulk semiconductor as N→ ∞. Note the intermediate stage where the energy level degeneracy has not completely formed the bulk band structures. This is considered quantum confinement of the energy levels from the bulk material.

particle size. The key ingredient to most successful methods for producing nanocrystals has been the use of capping ligands that bind to the particles surface and provide a steric barrier to aggregation as shown in Fig. 1.4. The capping ligands tend to exhibit the properties of surfactants: one end binds strongly to the particle surface while the opposite end interacts with the solvating fluid. In a good solvent, the ligands extend from the nanocrystal surface and provide steric stabilization, which typically limits size to the nanometer range and prevents unwanted agglomeration. The highly successful wet chemical techniques used to synthesize the group II-VI and III-V semiconductors cannot be applied to silicon or germanium, which require temperatures much higher than the boiling point of capping solvents to degrade the necessary precursors. Aerosol methods have produced silicon nanocrystals, however, the size distributions are broad and a thick oxide coating has been required to stabilize their structure.

Silicon and germanium are considered indirect band gap materials, which differ from direct band gap materials due to the energy bands that determine the valence band and the conduction band. Direct band gap materials have energy bands that do not require momentum changes ($k = 0$) for electron-hole recombination as shown in Fig. 1.5A. Indirect band gap materials shown in Fig. 1.5B, however, require phonon assistance for recombination to occur from the lowest lying energy band. In other words, momentum is not conserved ($k \neq 0$) and there must be some reorientation for electron-hole recombination to occur

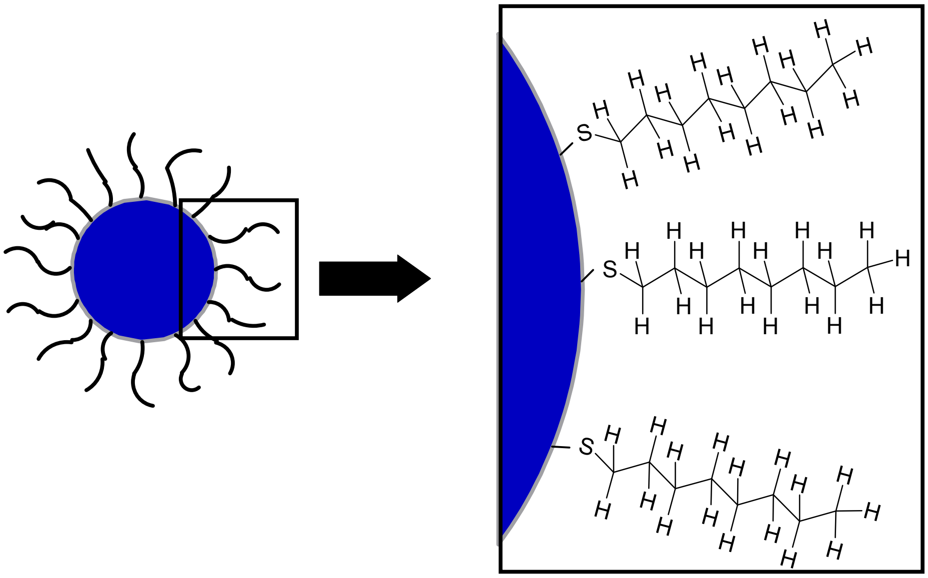

Fig. 1.4. Schematic of an organically-capped nanocrystal. The organic ligands shown are alkanethiols, which are typical ligands used in nanocrystal synthesis. However, other organics such as octanol and trioctylphosphine are often used.

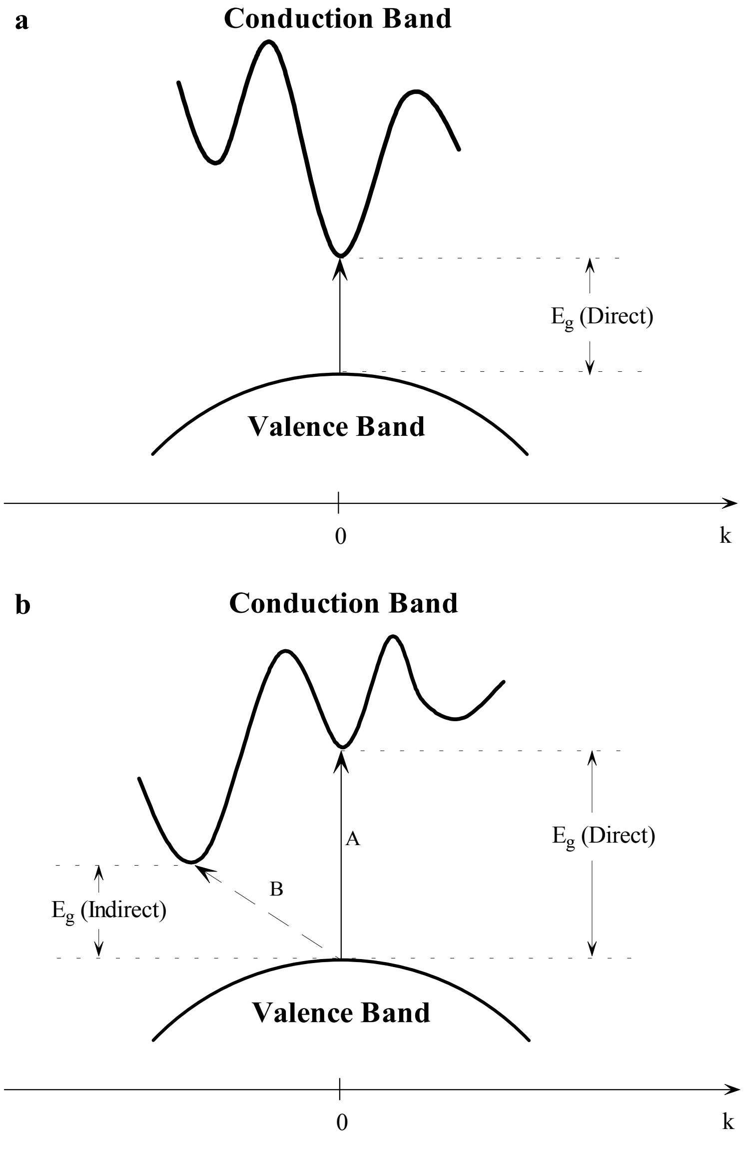

Fig. 1.5. Energy-band structures showing (a) direct optical transitions and (b) indirect optical transitions.

reducing the probability of recombination and subsequent luminescence. However, as dimensions are decreased to the nanometer level, the energy levels shift to higher energy due to quantum confinement and the probability of recombination resulting in luminescence may increase [78].

## 1.5 Objectives

The work here will focus on both fundamental reaction equilibria in SCW and high temperature synthesis reactions to produce metals and semiconductors in SCW and supercritical hydrocarbons. The *in-situ* spectroscopic studies will concentrate on reversible reactions in supercritical water and understanding the effects of solvation and dipole-dipole interactions on ionic acid-base and redox reactions. These studies often required extensive modeling and calculations to analyze the data. UV-vis spectroscopy was the primary tool used to study both the kinetics and the thermodynamic equilibria in these fundamental studies. Fundamental knowledge of the interactions of acids, bases, ions, and polar species within supercritical solvents helped guide the development of synthetic efforts to form nanoparticles. These synthetic studies focused on the kinetics of reactions leading to particle formation. These studies provide knowledge of the parameters that control the morphology, particle size, and size distribution of nanoparticles of great practical interest. Furthermore, some of the particles may have potential uses in electronic devices. The synthetic effort to produce copper nanocrystals in

SCW was greatly enhanced by the fundamental studies of chemical reaction equilibria, especially for nitrate species.

## 1.6 Organization of Dissertation

Reactions involving $NO_x$ species in the gas phase play a crucial role in nitric acid production, combustion, [81] and waste incineration. More recently $NO_x$ chemistry has been studied in SCWO [2,5]. Thermodynamics and kinetics favor significantly less $NO_x$ at the relatively low temperatures in SCWO compared with incineration where temperatures are typically 1200 °C or more [82]. In collaboration with Jerzy Chlistunoff, UV-vis spectroscopy was utilized in the quantitative measurement of the decomposition of aqueous $HNO_3$ solutions above 300°C, in some cases with added NaOH, $H_2O_2$, and/or $NaNO_2$, to form $NO_2$, $HNO_2$, NO, $N_2O$ and $O_2$ in Chapter 2. Individual bands corresponding to $HNO_2$ and $NO_2$ were deconvoluted from the spectra up to 400 °C and changes in the spectra are discussed. Although it was only possible to measure the absorbance of two of the twelve species by UV-vis spectroscopy, six equilibrium constants and two extinction coefficients could be optimized as discussed in Chapter 3. Linear extrapolation of the log K versus density plots to zero density results in values that are very close to independent gas-phase values. Furthermore, these reactions were shown to be dependent on the density (dielectric) of the solution with more polar species being favored at higher densities.

Chapter 3 discusses the optimization model developed to determine the equilibrium constants for dissociation, redox and disproportionation reactions involving nitric and nitrous acid, $NO_2$, NO, $N_2O$, and $O_2$ in SCW at the conditions discussed in Chapter 2. This constrained nonlinear programming (NLP) model is optimized using an implementation of the generalized reduced gradient (GRG) algorithm. Equilibrium constants and extinction coefficients are obtained with a minimal amount of experimental data that agrees well with published values. Significant improvements of these values are obtained with a Jackknife Statistical implementation. Computational difficulties are partially overcome by performing a logarithmic transformation of the constraining equations.

In Chapter 4, organic hydrocarbon capping ligands are used to stabilize the formation and quench the growth of copper nanocrystals in SCW. The change in the dielectric constant of water from values of 80 at room temperature to values below 5 at supercritical conditions allows complete miscibility of the organic capping ligand in an aqueous environment. Furthermore, the precursor has decreased solubility enhancing nucleation. The stabilizing ligands, in this case 1-hexanethiol, serve to quench the growth and also control the nanocrystal composition: copper oxide forms without ligands, while copper metal nanocrystals form in the presence of alkanethiol capping ligands. Furthermore, the processing conditions (i.e. precursor, pH, capping ligand) significantly affect the morphology and size of the nanocrystals formed in SCW, which is due to competing reaction pathways of hydrolysis and ligand exchange versus arrested growth.

In Chapter 5, silicon nanocrystals are formed using a SCF process in collaboration with Justin Holmes. Silicon nanocrystal synthesis with the narrow size distributions necessary to eliminate inhomogeneous broadening of the electronic properties has proven to be very difficult. A new wet chemical approach for silicon nanocrystals that utilizes the advantages of each of these approaches is described. The use of capping ligands for the precise control of particle size and the high temperatures of aerosol methods are combined in a supercritical method that successfully produces a wide distribution of particles sizes. The absorbance and photoluminescence excitation (PLE) spectra of the nanocrystals exhibit a significant blue shift in optical properties from the bulk band gap energy of 1.2 eV due to quantum confinement effects. The stable Si clusters show efficient blue (15 Å) or green (25-40 Å) band-edge photoemission with luminescence quantum yields up to 23 % at room temperature, and electronic structure characteristic of a predominantly indirect transition—despite the extremely small particle size. The smallest nanocrystals, 15 Å in diameter, exhibit discrete optical transitions, characteristic of quantum confinement effects for crystalline nanocrystals with a narrow size distribution.

Similar to the silicon nanocrystals produced in Chapter 5, germanium nanocrystals are produced by an arrested-growth method within supercritical octanol exhibiting size dependent properties and described in Chapter 6. While silicon was shown to have some size dependent features, germanium nanocrystals are expected to have more significant quantum confinement effects due to the smaller band gap. Indeed, the nanocrystals produced in Chapter 6 do show significant changes in the optical properties with size. The Ge crystals produced are size-polydisperse in nature; however, size-selectivity of these nanocrystals is obtained by the use of a chromatographic method. Luminescence of the nanocrystals is shown to be dependent on the size resulting in a blue-shift of the PL energy consistent with quantum confinement of the band gap energy and resulting in high quantum yields. UV-visible spectra are also size-dependent with smaller particles resulting in discrete optical features. In addition, these features are shown to be size-dependent characteristic of the loss of energy level degeneracy due to quantum confinement. At the smallest particle sizes, these features appear to behave similar to molecular absorbance with the density of the energy levels concentrated into just a few bands yielding high oscillator strengths further suggesting the idea that nanocrystals may be considered as ‘artificial’ atoms.

## References

(1) Caruana, C. M. *Chem. Eng. Progress* **1995**, *941*, 10-18.

(2) Tester, J. W.; Holgate, H. R.; Armellini, F. J.; Webley, P. A.; Killilea, W. R.; Hong, G. T.; Barner, H. E. *Supercritical Water Oxidation Technology: A Review of Process Development and Fundamental Research*; Tedder, D. W. and Pohland, F. G., Ed.; Am. Chem. Soc.: Washington, 1993; Vol. 518, pp 35-76.

(3) Shaw, R. W.; Brill, T. B.; Clifford, A. A.; Eckert, C. A.; Franck, E. U. *Chem. and Eng. News* **1991**, *69*, 26.

(4) Savage, P. E.; Gopalan, S.; Mizan, T. I.; Martino, C. J.; Brock, E. E. *AIChE J.* **1995**, *41*, 1723-1778.

(5) Gloyna, E. F.; Li, L. *Waste Manage.* **1993**, *13*, 379.

(6) Sealock, L. J.; Elliott, D. C.; Baker, E. G.; Butner, R. S. *Ind. Eng. Chem. Res.* **1993**, *32*, 1535.

(7) Klein, M. T.; Torry, L. A.; Wu, B. C.; Mentha, Y. G. **1990**, *Orlando, Florida*.

(8) Connolly, J. F. *J. Chem. Eng. Data* **1966**, *11*, 13.

(9) Schoppelrei, J. W., Kieke, M.L., Wang, X., Klein, M.T., Brill, T.B. *J.Phys.Chem.* **1996**, *100*, 14343.

(10) Schoppelrei, J. W., Brill, T.B. *J.Phys.Chem. A.* **1997**, *101*, 8593.

(11) Proesmans, P. I.; Luan, L.; Buelow, S. J. *Ind.Eng.Chem.Res.* **1997**, *36*, 1559.

(12) Kritzer, P.; Boukis, N.; Dinjus, E. *J. Supercritcal Fluids* **1999**, *15*, 205.

(13) Huang, S.; Daehling, K.; Carlson, T. E.; Taylor, P.; Wai, C.; Propp, A. *Am. Chem. Soc. Symp. Ser.* **1989**, *406*, 276.

(14) Chialvo, A. A.; Cummings, P. T. *J. Chem. Phys.* **1994**, *101*, 4466-4469.

(15) Gorbaty, Y. E.; Kalinichev, A. G. *J. Phys. Chem.* **1995**, *99*, 5336-5340.

(16) Gupta, R. B.; Panayoitou, C. G.; Sanchez, I. C.; Johnston, K. P. **1992**, *38*, 1243-1253.

(17) Gupta, R. B.; Combes, J. R.; Johnston, K. P. *J. Phys. Chem.* **1993**, *97*, 707-715.

(18) Gupta, R. B.; Johnston, K. P. *Fluid Phase Equilibria* **1994**, *99*, 135.

(19) Gupta, R. B.; Johnston, K. P. *Ind. Eng. Chem. Res.* **1994**, *33*, 2819.

(20) Bennett, G. E.; Johnston, K. P. *J.Phys.Chem.* **1994**, *98*, 441.

(21) Balbuena, P. B.; Johnston, K. P.; Rossky, P. J. *J. Phys. Chem.* **1996**, *100*, 2706.

(22) Flanagin, L. W.; Balbuena, P. B.; Johnston, K. P.; Rossky, P. J. *J. Phys. Chem. B* **1997**, *101*, 7998.

(23) Johnston, K. P.; Bennett, G. E.; Balbuena, P. B.; Rossky, P. J. *J. Am. Chem. Soc.* **1996**, *118*, 6746-6752.

(24) Luo, H.; Tucker, S. C. *J. Am. Chem. Soc.* **1995**, *117*, 11359-11360.

(25) Wood, R. H.; Quint, J. R.; Grolier, J.-P. E. *J. Phys. Chem.* **1981**, *85*, 3944-3949.

(26) Lee, J. H.; Foster, N. R. *J. Supercrit. Fluids* **1996**, *9*, 99-105.

(27) Hirth, T.; Schweppe, R.; Jahnke, S.; Bunte, G.; Eisenreich, N.; Krause, H. *High Pressure Chem. Eng.* **1996**.

(28) Savage, P. E.; Li, R.; Santini, J. T. *J. Supercrit. Fluids* **1994**, *7*, 135-144.

(29) Broll, D.; Kaul, C.; Kramer, A.; Krammer, P.; Richter, T.; Jung, M.; Vogel, H.; Zehner, P. *Angew. Chem.* **1999**, *Int. Ed.*, 2999- 3014.

(30) Korzenski, M. B.; Kolis, J. W. *Tetrahedron Lett.* **1997**, *38*, 5611-5614.

(31) Franck, E. U. *J. Solution Chem.* **1973**, *2*, 339-356.

(32) Rebert, C. J.; Kay, W. B. *AIChE J.* **1959**, *5*, 285.

(33) Pitzer, K. S. *J. Physical Chemistry* **1983**, *87*, 1120.

(34) *Solubility of Inorganic Compounds in Subcritical and Supercritical Water*; Martynova, O. I., Ed.; National Association of Corrosion Engineers: Houston, 1976.

(35) Macdonald, D. D.; Hettiarachchi, S.; Song, H.; Makela, K.; Emerson, R.; Ben-Haim, M. *J. Solution Chem.* **1992**, *21*, 849-881.

(36) Ho, P. C.; Palmer, D. A.; Mesmer, R. E. *J. Solution Chem.* **1994**, *23*, 997.

(37) Ho, P. C.; Palmer, D. A. *J.Solution Chem.* **1996**, *25*, 711.

(38) Ho, P. C.; Palmer, D. A. *Geochim.Cosmochim. Acta* **1997**, *61*, 3027.

(39) Frantz, J. D.; Marshall, W. L. *Amer. J. Sci.* **1984**, *284*, 651.

(40) Lee, C. T., Jr.; Bhargava, P.; Johnston, K. P. *J. Phys. Chem. B* **2000**, *104*, 4448-4456.

(41) Kim, S.; Johnston, K. P. *Ind. Eng. Chem. Res.* **1987**, *26*, 1206-1213.

(42) Johnston, K. P.; Kim, S.; Combes, J. **1989**, *Chapter 5*, 53-69.

(43) Brenecke, J. F.; Tomasko, D. L.; Peshkin, J.; Eckert, C. A. *J. Chem. Eng.* **1990**, *29*, 1682-1690.

(44) Chen, X.; Izatt, R. M.; Oscarson, J. L. *Chem.Rev.* **1994**, *94*, 467.

(45) Kettler, R. M.; Wesolowski, D. J.; Palmer, D. A. *J. Solution Chem.* **1995**, *24*, 385-407.

(46) Kettler, R. M.; Palmer, D. A.; Wesolowski, D. J. *J. Solution Chem.* **1995**, *24*, 65-87.

(47) Hitch, B. F.; Mesmer, R. E. *J. Solution Chem.* **1976**, *5*, 667-680.

(48) Patterson, C. S.; Slocum, G. H.; Busey, R. H.; Mesmer, R. E. *Geochim. Cosmochim. Acta* **1982**, *46*, 1653-1663.

(49) Patterson, C. S.; Busey, R. H.; Mesmer, R. E. *J. Solution Chem.* **1984**, *13*, 647-661.

(50) Capewell, S.; Hefter, G.; May, P. M. *J. Solution Chem.* **1998**, *27*, 865.

(51) Schoppelrei, J. W., Kieke, M.L., Brill, T.B. *J.Phys.Chem.* **1996**, *100*, 7463.

(52) Kieke, M. L.; Schooppelrei, J. W.; Brill, T. B. *J. Phys. Chem.* **1996**, *100*, 7455.

(53) Frantz, J. D. *Chemical Geology* **1998**, *152*, 211.

(54) Maiella, P. G.; Brill, T. B. *Appl.Spectroscopy* **1996**, *50*, 829.

(55) Spohn, P. D.; Brill, T. B. *J.Phys.Chem.* **1989**, *93*, 6224.

(56) Gammons, C. H.; Seward, T. M. *Geochim.Cosmochim.Acta* **1996**, *60*, 4295.

(57) Heinrich, C. A.; Seward, T. M. *Geochim.Cosmochim.Acta* **1990**, *54*, 2207.

(58) Seward, T. M. *Geochim.Cosmochim.Acta* **1984**, *48*, 121.

(59) Johnston, K. P.; Chlistunoff, J. B. *J. Supercritical Fluids* **1998**, *12*, 155.

(60) Xiang, T.; Johnston, K. P.; Wofford, W. T.; Gloyna, E. F. *Ind.Eng.Chem.Res.* **1996**, *35*, 4788.

(61) Wofford, W. T.; Gloyna, E. F.; Johnston, K. P. *Ind. Eng. Chem. Res.* **1998**, *37*, 2045.

(62) Huh, Y.; Lee, J.-G.; McPhail, D. C.; Kim, K. *J. Solution Chem.* **1993**, *22*, 651-661.

(63) Lee, I. J.; Jung, G. S.; Kim, K. *J. Solution Chem.* **1994**, *23*, 1283.

(64) Shin, T. W.; Kim, K.; Lee, I.-J. *J.Solution.Chem.* **1997**, *26*, 379.

(65) Park, S. N.; Kim, C. S.; Kim, M. H.; Lee, I.-J.; Kim, K. *J.Chem.Soc., Faraday Trans.* **1998**, *94*, 1421.

(66) Park, S.; Kim, H.; Kim, K.; Lee, J.; Lho, D.-S. *Pccp : physical chemistry, chemical physics, a* **1999**, *1*, 1893.

(67) Kim, M. H.; Kim, C. S.; Lee, H. W.; Kim, K. *J. Chem. Soc., Faraday Trans.* **1996**, *92*, 4951.

(68) Xiang, T.; Johnston, K. P. *J.Phys.Chem.* **1994**, *98*, 7915.

(69) Xiang, T.; Johnston, K. P. *J.Solution Chem.* **1997**, *26*, 13.

(70) Dell'Orco, P.; Foy, B.; Wilmanns, E.; Le, L.; Ely, J.; Patterson, K.; Buelow, S. *Hydrothermal Oxidation of Organic Compounds by Nitrate and Nitrite.*; Hutchenson, K. W., Foster, N.R., Ed.; American Chemical Society: Washington, D.C., 1995, pp 179-196.

(71) Chlistunoff, J. B.; Johnston, K. P. *J.Phys.Chem. B* **1998**, *102*, 3993.

(72) Ji, M.; Chen, X.; Wai, C. M.; Fulton, J. L. *J. Am. Chem. Soc.* **1999**, *121*, 2631.

(73) Holmes, J. D. B., Prashant A.; Korgel, Brian A.; Johnston, Keith P. *Langmuir* **1999**, *15*, 6613.

(74) Darr, J. A.; Poliakoff, M. *Chemical reviews* **1999**, *99*, 495.

(75) Adschiri, T.; Yamane, S.; Onai, S.; Arai, K. : Strasbourg, France, 1994; Vol. T3, pp 241.

(76) Peierls, R. E. *Ann. Inst. Henri Poincare* **1935**, *5*, 177.

(77) Schmid, G.; Baumle, M.; Geerkens, M.; Heim, I.; Osemann, C.; Sawitowski, T. *Chem. Soc. Rev.* **1999**, *28*, 179.

(78) Alivisatos, A. P. *Science* **1996**, *271*, 933.

(79) Murray, C. B.; Norris, D. J.; Bawendi, M. G. *J. Am. Chem. Soc.* **1993**, *115*, 8706.

(80) Banin, U.; Lee, C. J.; A.A., G.; Kadavanich, A. V.; Alivisatos, A. P.; Jaskolski, W.; Bryant, G. W.; Efros, A. L.; Rosen, M. *J. Chem. Phys.* **1998**, *109*, 2306.

(81) Miller, J. A.; Bowman, C. T. *Prog.Energy Combust.Sci.* **1989**, *15*, 287.

(82) Killilea, W. R.; Swallow, K. C.; Hong, G. T. In *2nd International Symposium on Supercritical Fluids*; Department of Chemical Engineering, Johns Hopkins University: Boston, MA, 1991; p 173-176.

# Chapter 2: Nitric/Nitrous Acid Equilibria in Supercritical Water †

## 2.1 Introduction

Reactions involving NO, $NO_2$, $H_2O$, $HNO_3$, $HNO_2$ and $O_2$ in the gas phase play a crucial role in nitric acid production, combustion [1], and waste incineration. These reactions have been studied extensively in both the gas phase and for a gas phase in contact with an aqueous phase, typically at temperatures below 100 °C [2-5]. The amount of $NO_x$ in exhaust gases may be lowered by catalytic reduction with $NH_3$ to form $N_2$, or conversely, $NO_x$ may be used to oxidize ammonia wastes to $N_2$ [6-8].

More recently $NO_x$ chemistry has been studied in hydrothermal oxidation (HO) (also called supercritical water oxidation (SCWO)). [9,10] In HO, an aqueous waste containing organics is oxidized by oxygen in supercritical water (SCW), i.e., at temperatures higher than 374 °C (typically around 500 °C and above 220 bar). Thermodynamics and kinetics favor significantly less $NO_x$ at the relatively low temperatures in HO compared with incineration where temperatures are typically 1200 °C or more [11]. Kinetic studies of oxidation reactions of organic compounds by nitrates suggested that the reactive species in SCW solutions of nitrates can be $NO_2$ [12]. Recently, it was suggested that nitrates present in certain

---

† The contents of this chapter appear in *J. Phys. Chem. A* **1999**, 103, 1678-1688.

high level and mixed nuclear wastes could be used as an oxidizing agent instead of oxygen in the HO pretreatment of these wastes [13-15]. It has been proposed that ammonium nitrate recovered from demilitarized rocket motors may be utilized as an oxidizing agent in HO [16]. $NO_x$ chemistry is also important in rapid hydrolysis of metal nitrates to form sub-micron metal oxide crystals [17,18].

Fundamental studies of nitrogen chemistry in SCW are relatively rare due to corrosion and the challenges from high pressures and temperatures. Brill and coworkers studied kinetics and mechanisms for decomposition reactions of a variety of nitrogen containing compounds in SCW including thermal decomposition of hydroxylammonium nitrate [19], urea and guanidinium nitrate [20], and ethylenediammonium dinitrate [21] by using FTIR and Raman spectroscopy. Spohn and Brill [22] studied ion pair formation in concentrated aqueous solutions of zinc, cadmium, lithium, and sodium nitrates up to 450 °C by Raman spectroscopy, which is very sensitive to contact interactions. The dissociation of nitric acid under hydrothermal conditions up to 250 °C was studied by Raman spectroscopy [23] and up to 319 °C from the heat of dilution of concentrated $HNO_3$ solutions [24]. Marshall and Slusher obtained $HNO_3$ dissociation constants indirectly from solubilities of magnesium sulfate [25] (up to 370 °C) and calcium sulfate [26] (up to 350 °C). However, Marshall and coworkers [26-28] found that nitric acid decomposes reversibly to nitrogen oxides and water at elevated temperatures even below the critical point of water [23,25,26].

Chemical reaction equilibria may be measured quantitatively in hydrothermal solution by UV-Vis spectroscopy. As demonstrated by Seward and coworkers [29-31] complex equilibria in hydrothermal solutions can be elucidated by spectral deconvolution techniques [29] and nonlinear regression procedures [29,31]. Chemical equilibria involving $H_2CrO_4$ and $HCrO_4^-$ were measured quantitatively up to 420 °C [32]. A series of relatively stable organic pH indicators has been developed to measure pH and monitor acid-base equilibria up to 420 °C [33-37]. These studies demonstrate that UV-Vis spectroscopy is well suited for obtaining quantitative equilibrium constants in SCW.

The objective of this work was to characterize and quantify chemical reaction equilibria involving nitric acid and its decomposition products with UV-Vis spectroscopy in SCW. Because of the possibility for severe corrosion, a new apparatus was developed in which the solutions contacted only titanium, gold, and sapphire and could be flushed rapidly. The results and discussion section begins with a description of changes in spectra resulting from adding NaOH, $H_2O_2$, $NaNO_2$ or mixtures of these compounds to $HNO_3$ solutions. Here the goal is to determine qualitatively which decomposition products are present based on these changes in spectra. Next, spectral deconvolution and peak assignment are discussed. From the areas of the deconvoluted spectra, a Large-Scale Generalized Reduced Gradient (LSGRG2) optimization model [38] was utilized to determine optimal values of the extinction coefficients and equilibrium constants in conjunction with the concentrations of the decomposition products. The density effect on equilibrium constants is discussed as a function of changes in polarity upon reaction. The equilibrium constants are also utilized to calculate speciation diagrams. Quantitative knowledge of chemical reaction equilibria of nitrogen chemistry is highly relevant to understanding hydrolysis and oxidation reactions, corrosion, materials science and separation processes in hydrothermal solution.

## 2.2 Experimental

The experimental apparatus was similar to one applied previously [32,39]. Spectra were obtained in a titanium optical cell equipped with two sapphire windows with an aperture of 5 mm and a path length of 1 cm. A modification was made to avoid pumping highly corrosive $HNO_3$ solutions through the HPLC pump (Fig. 2.1). The solutions were added to the top of a 11/16" i.d. x 1" o.d. 6 foot long stainless steel tube equipped with a stainless steel piston and polypropylene o-ring seals. Pure deionized water was pumped with an HPLC pump into the tube below the piston to displace the solution through a titanium pre-heater (0.03" i.d., 2 foot length) into the titanium optical cell. A bypass line was used to flush the cell with pure water. The typical time required to exchange the solution in the cell was around 3 minutes. After the cell was flushed with water or a fresh solution, the spectra were recorded. The spectrum for pure water (baseline) was measured immediately after the temperature attained its steady preset value. The spectra for the solutions were measured after additional

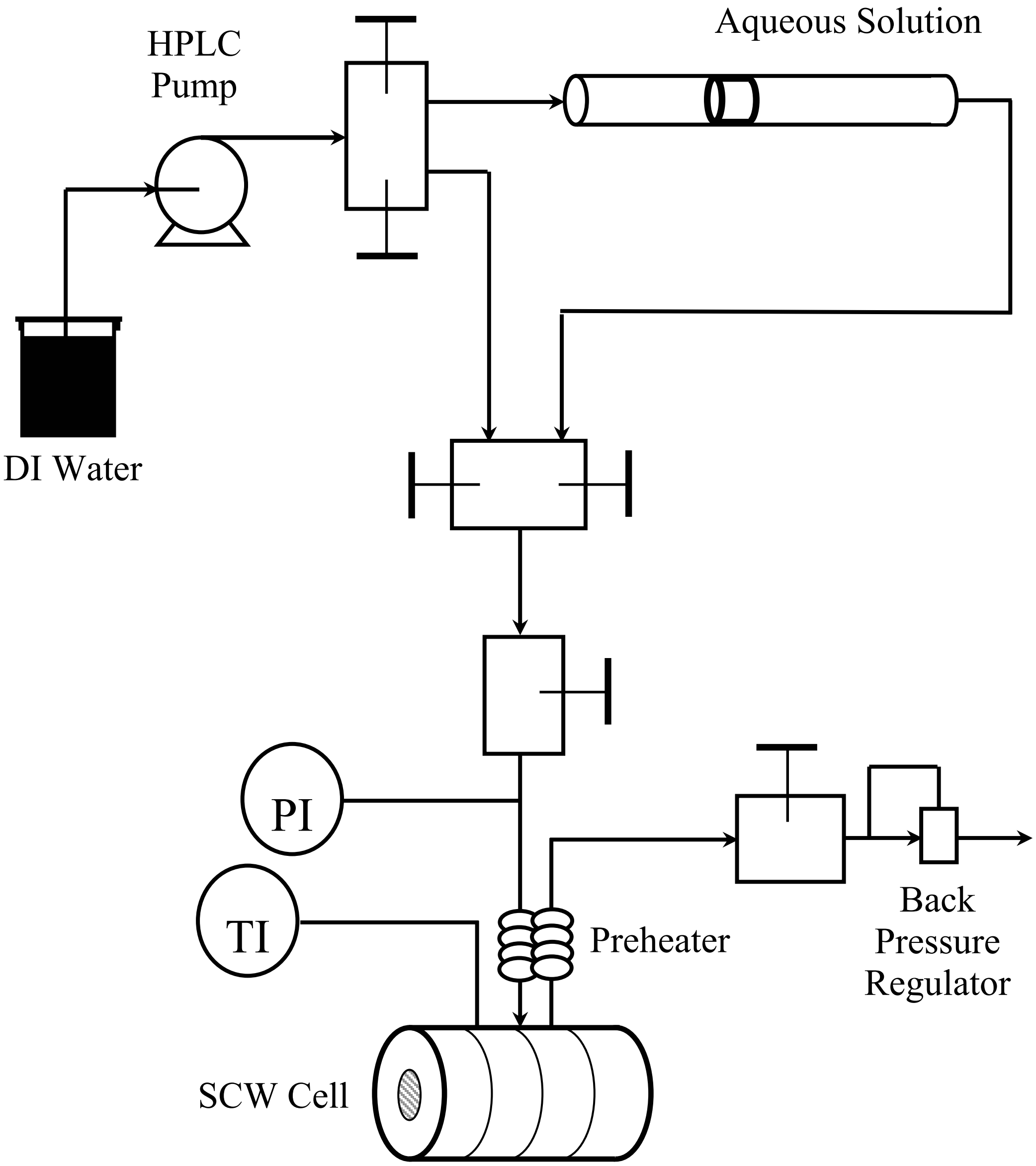

Fig. 2.1. Stopped flow apparatus for UV-vis spectroscopy of corrosive solutions in SCW.

flushing of the cell with 1 mL of the solution and re-equilibrating the temperature. Typically four spectra were recorded at different pressures without flushing the cell between experiments. The solution residence time, which did not exceed 6 minutes, was usually sufficiently short to produce only minor corrosion as well as negligible changes in the spectra.

Carbon dioxide free, approximately 0.5 M stock NaOH (analytical grade, EM Science) solution was prepared and standardized using generally accepted procedures [40]. A stock solution (approximately 0.5 M) of $HNO_3$ (70%, AR, Mallincrodt) was standardized by titration with the above NaOH standard solution. Approximately 0.25 M $NaNO_2$ solution was obtained by dissolving a sample of analytical grade $NaNO_2$ (EM Science) in a known volume of deionized water. Its concentration was determined by a classical Lunge method [41], i.e., by titration with a known volume of a standard $KMnO_4$ solution. This method is accurate to within 0.5 - 1 %. The NaOH and $NaNO_2$ stock solutions were prepared frequently, to reduce errors associated with absorption of $CO_2$ or decomposition ($NaNO_2$). Hydrogen peroxide (30%, EM Science) concentration was determined before each experiment by titration with a standard $KMnO_4$ solution [41].

With a few exceptions, the feed solutions were thoroughly deoxygenated by purging with nitrogen. The solutions containing $H_2O_2$ as well as mixtures of $HNO_3$ and $NaNO_2$ solutions were not deoxygenated, because of $H_2O_2$ decomposition upon shaking and evolution of NO, respectively. In these cases, however, the solutions were prepared immediately before each experiment in freshly deoxygenated water. After brief but thorough mixing, the solution was placed in the stainless steel tube and immediately isolated and pressurized. The estimated concentration of oxygen in these feed solutions was around $4\times10^{-5}$ mol $kg^{-1}$ based on the partial pressure of oxygen in air and the solubility of $O_2$ in water. Other details of experimental procedures can be found elsewhere [32].

## 2.3 Results and Discussion

***2.31 Concentrated $NaNO_3$ and $HNO_3$ solutions from 20 to 400 °C.*** The spectrum of nitrate ion in water is characterized by two principal bands as shown in Figure 2.2. The short wavelength band ($\lambda$=200.3 nm at ambient conditions) is very strong ($\varepsilon$=9600). While the high $\varepsilon$ of this band is beneficial, its $\lambda$ is not, since a variety of other species also absorb strongly here, including other $NO_x$ species, $OH^-$ via charge transfer to solvent, and the sapphire windows. The long wavelength band, centered at around 300 nm, is very weak with an extinction coefficient on the order of 7, which is too small to be of use.

The effect of temperature on the spectra of 0.0928 mol $kg^{-1}$ $HNO_3$ and 0.0928 mol $kg^{-1}$ $NaNO_3$ solutions is shown in Figure 2.2. Within limits of experimental error, the spectra of these solutions at room temperature are identical (Fig. 2.2a), in accordance with the fact that nitric acid is completely dissociated. However, an increase in temperature at a constant pressure of 34.5

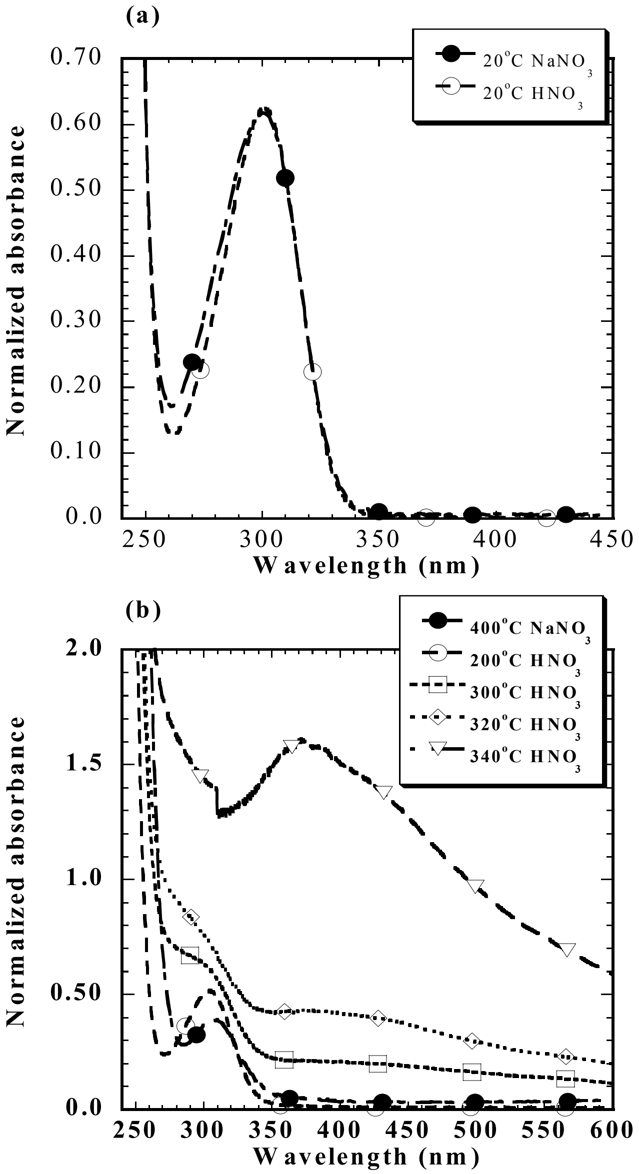

Fig. 2.2. Spectra of 0.0928 mol kg$^{-1}$ $HNO_3$ (filled symbols) and $NaNO_3$ (open symbols). Pressure 34.5 MPa.

MPa leads to changes in $HNO_3$ (open symbols) and $NaNO_3$ (filled symbols). While changes in $NaNO_3$ spectra up to 400 °C can be regarded as minor (Fig. 2.2b), temperature exerts a significant effect on the $HNO_3$ spectra. A temperature increase from 20 to 200 °C leads to increased overlap of the 300 nm and 200 nm bands. Since nitric acid becomes a weaker acid at elevated temperatures, these changes may reflect formation of molecular $HNO_3$.

At temperatures equal to or higher than 300 °C, an additional broad band centered around 370 nm, appears. This band grows significantly with temperature. While part of this increase is reversible and the nitrate band at 300 nm can be restored after cooling down the cell, the measured absorbance does not drop back to zero at wavelengths longer than those corresponding to the nitrate band. The reversible changes at temperatures greater than or equal to 300 °C represent reversible decomposition of nitric acid as previously suggested by Marshall and coworkers, based upon visual observation of $HNO_3$ samples in silica capillary tubes [27]. The residual absorption is still observed even after the cell is flushed with pure deionized water, due to the presence of a uniform brown deposit on the windows. The amount of the deposit increases with the nitric acid residence time in the cell. The brown deposit is believed to be titanium dioxide, which is formed when the hot solution containing Ti corrosion products contacts the cooler windows. Indeed, extensive use of the cell with these concentrated $HNO_3$ solutions resulted in formation of pits on the flat Ti surfaces remaining in contact with the gold seals. The corrosion led to serious leaks and irreproducible results due to inaccurate correction of the spectra for the baseline.

The corrosion of the cell and deposition of $TiO_2$ on the windows was curtailed by lowering the acid concentration to a level of $2\text{-}3\times10^{-2}$ mol kg$^{-1}$, which is also more suitable for equilibrium constant determinations. However, the changes occurring to the weak 300 nm band could no longer be accurately measured in our 1 cm cell. Fortunately, the light absorption by the $HNO_3$ decomposition products in the dilute $HNO_3$ solutions was sufficiently high to be measured quantitatively at temperatures exceeding 360 °C. Preliminary experiments revealed, however, that the spectra measured at 360 °C were not reproducible, because of either a relatively slow approach to equilibria or $TiO_2$ deposition. At 420 °C, on the other hand, leaks constituted a serious problem. At temperatures of 380 and 400 °C, equilibrium was achieved rapidly and leaks were minor, such that quantitative experiments could be performed.

***2.32 Spectra of nitric acid and its mixtures with sodium hydroxide, hydrogen peroxide and sodium nitrite at 380 and 400 °C.*** The experiments were grouped in five distinct classes depending on the feed solution composition (Table 2.1). The various classes were designed to manipulate the relative equilibrium concentrations of the nitrogen species, especially the oxidation states, in order to be able to obtain equilibrium constants from the spectra. The first

Table 2.1. Compositions of the classes of solutions studied.

| Class | $HNO_3$ mmol $kg^{-1}$ | NaOH mmol $kg^{-1}$ | $H_2O_2$ mol $kg^{-1}$ | $NaNO_2$ mmol $kg^{-1}$ |
|---|---|---|---|---|
| I | 7.736 - 38.68 | 0.0 | 0.0 | 0.0 |
| II | 19.34 | 1.237 - 12.37 | 0.0 | 0.0 |
| III | 23.20 | 0.0 | 0.182 – 0.931 | 0.0 |
| IV [a)] | 0.0 - 16.28 | 0.0 | 0.0 | 4.52 - 20.8 |
| V | 15.40 | 7.667 | 0.0 | 5.42 |
|  | 13.73 | 4.617 | 0.0 | 7.03 |

a) Total nitrogen concentration was 0.0208 mol $kg^{-1}$.

class consisted of pure nitric acid solutions (class I). In class II, these solutions were partially neutralized solutions with NaOH to form $NO_3^-$, which was shown above to be much more stable than $HNO_3$. Class III included $H_2O_2$ as an oxidant. Mixtures of $HNO_3$ + $NaNO_2$ were used in class IV to shift the oxidation states, while NaOH was added to this mixture in class V.

Typical spectra for a class I experiment are shown in Figure 2.3. In this class, spectra were time independent for times not exceeding 20 min. The spectra were reversible with changes in temperature and pressure, suggesting that decomposition products revert back to the starting material. The large asymmetric band at 385 nm decreases with an increase in density, especially at low densities. The band position, shape and fine structure are all very similar to that observed for $NO_2$ spectra in the gas phase [42-45]. However, these spectra do not correspond to $NO_2$ only. A distinct set of small peaks, whose relative contribution to the measured absorbance changes with temperature and pressure, can be seen on top of the large $NO_2$ band. The relative contribution from the set of small peaks decreases with increasing concentration (absorbance) of $NO_2$ resulting from decreasing solution density. A similar but somewhat weaker effect was also seen at a constant temperature and pressure when the $NO_2$ concentration increased due to an increase in the $HNO_3$ feed concentration. The fact that the relative contribution of the small peaks increases when the $NO_2$ concentration decreases suggests that these small peaks are not due to the presence of $N_2O_4$, i.e.,

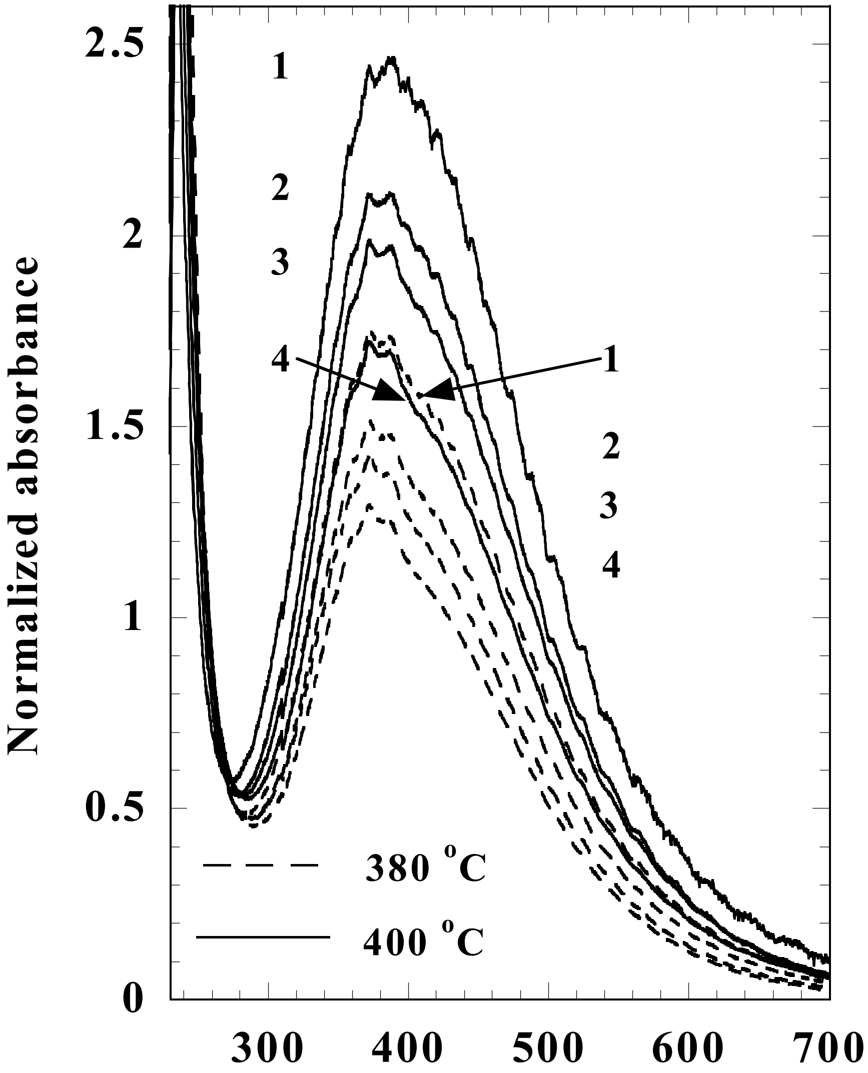

Fig. 2.3. Spectra of $3.868 \times 10^{-2}$ mol kg$^{-1}$ $HNO_3$ solutions at two temperatures and four pressures. Pressure (MPa): 27.6 (1); 31.0 (2); 34.5 (3); 41.3 (4). The spectra are corrected for density of water. Note similarity of spectrum 1 at 380 °C and spectrum 4 at 400 °C, which were obtained at similar densities, i.e., 0.506 and 0.533 g cm$^{-3}$ respectively.

$NO_2$ dimer. The dimerization reaction occurs to a limited extent at room temperature [3,42,46,47] in the gaseous phase, and the degree of dimerization decreases strongly with increasing temperature [46,47]. Thus dimerization is extremely unlikely at the high temperatures employed in this study. In addition, $N_2O_4$ absorbs light at shorter wavelengths and the absorption band does not exhibit any fine structure [42].

The general behavior observed for partially neutralized $HNO_3$ solutions (class II, Table 2.1) was very similar to that exhibited by pure nitric acid solutions. Solutions with equal feed concentrations of $H^+$ at ambient temperature, i.e., pure nitric acid solutions of concentration $m^o$ and partially neutralized $HNO_3$ solutions with an excess acid concentration equal to $m^o$, had almost identical spectra in supercritical water. This result is shown in Figure 2.4, where the integrated band areas in two wavelength ranges are plotted versus feed excess $H^+$ concentration. The band area, integrated over the wavelength range 450 - 600 nm, is believed to correspond to a single species ($NO_2$), because the ratios of absorbances measured at a given temperature and pressure for any two solutions were essentially independent of the wavelength in this range. In contrast, the area integrated over the wavelength range 330 - 450 nm includes the contribution from the substance(s) giving rise to the set of small peaks. As seen in Figure 2.4 and the associated spectra, this contribution, even though relatively small is similar for pure nitric acid solutions and partially neutralized $HNO_3$ solutions with equal excess $H^+$ feed concentration.

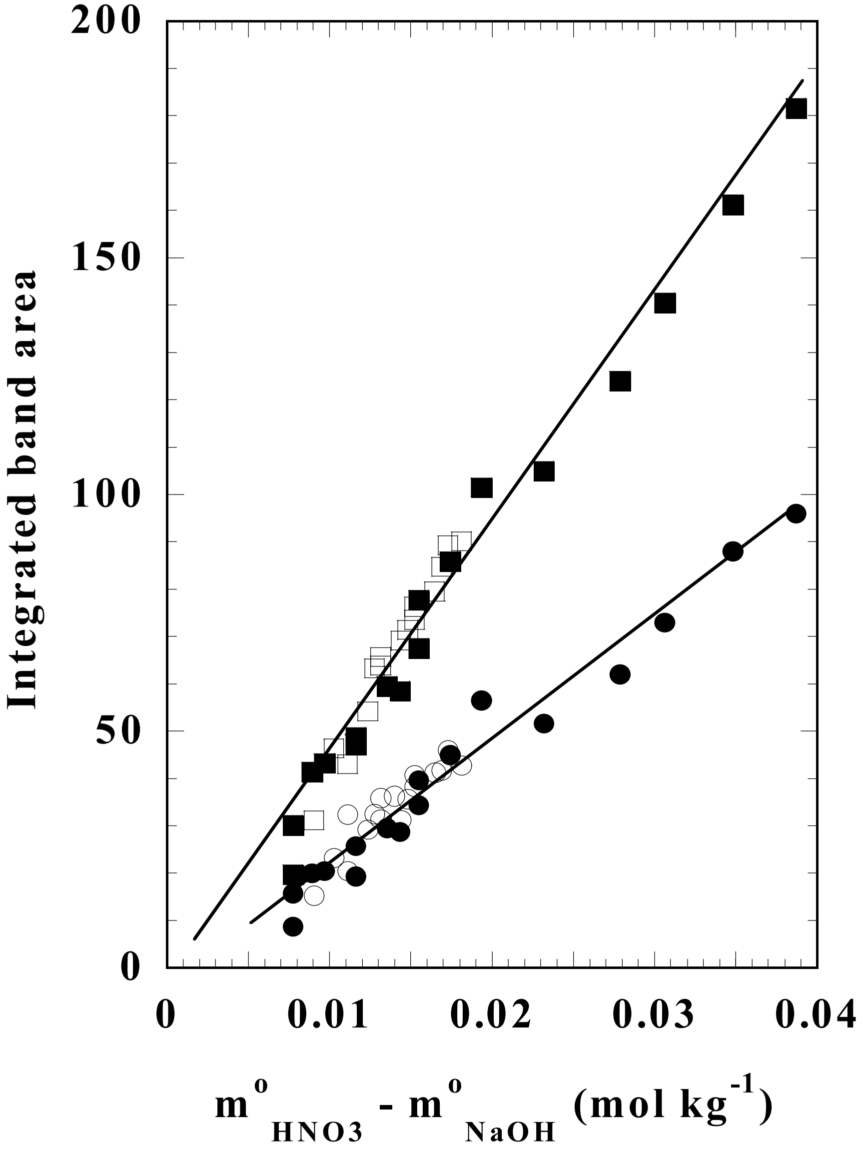

Fig. 2.4. The $NO_2$ band area integrated over 450 to 600 nm (bottom line) and 330 to 450 nm (top line) plotted against the concentration of nitric acid in pure nitric acid solutions (filled symbols) or excess of nitric acid in nitric acid/NaOH mixtures (open symbols). Temperature 380 °C. Pressure 27.6 MPa.

Addition of an excess oxidant such as $H_2O_2$, which decomposes to oxygen and water [48,49], to a 0.0232 mol kg$^{-1}$ $HNO_3$ solution removes the set of small peaks centered around 370 nm as shown in curves 3 and 4 of Figure 2.5 (class III, Table 2.1). The large $NO_2$ band is not affected significantly by $H_2O_2$. At 380 °C and all the pressures studied, the $NO_2$ band initially decreases and then increases slightly as the oxygen content increases. At 400 °C, the $NO_2$ band decreases monotonically as the feed $H_2O_2$ concentration increases from 0.18-0.93 mol kg$^{-1}$.

The stability of $NO_2$ versus the instability of the species represented by the set of small peaks in the presence of oxygen (curve 1 and 2 in Fig. 2.5) suggest that the yet unidentified species contains nitrogen in an oxidation state lower than +4. Among known $H_yNO_x$ ($x,y\geq0$) species only $NO_2^-$ and unstable $HNO_2$ (disproportionates to $HNO_3$ and NO) absorb light in this range [50-54]. Their spectra were measured at ambient conditions (Fig.2.6) and agreed well with literature data [50-54]. The positions, intensities and shapes of the spectra shown in Figure 2.6 strongly suggest that the set of small bands on top of the $NO_2$ band in hydrothermal $HNO_3$ solutions corresponds to the $HNO_2/NO_2^-$ couple.

The differences in the influence of oxygen on the $HNO_2/NO_2^-$ and $NO_2$ bands can be explained qualitatively in a simple manner in terms of the following equilibrium:

$$2\,NO_2 + H_2O \leftrightharpoons 2\,HNO_2 + 1/2\,O_2 \qquad (2.1)$$

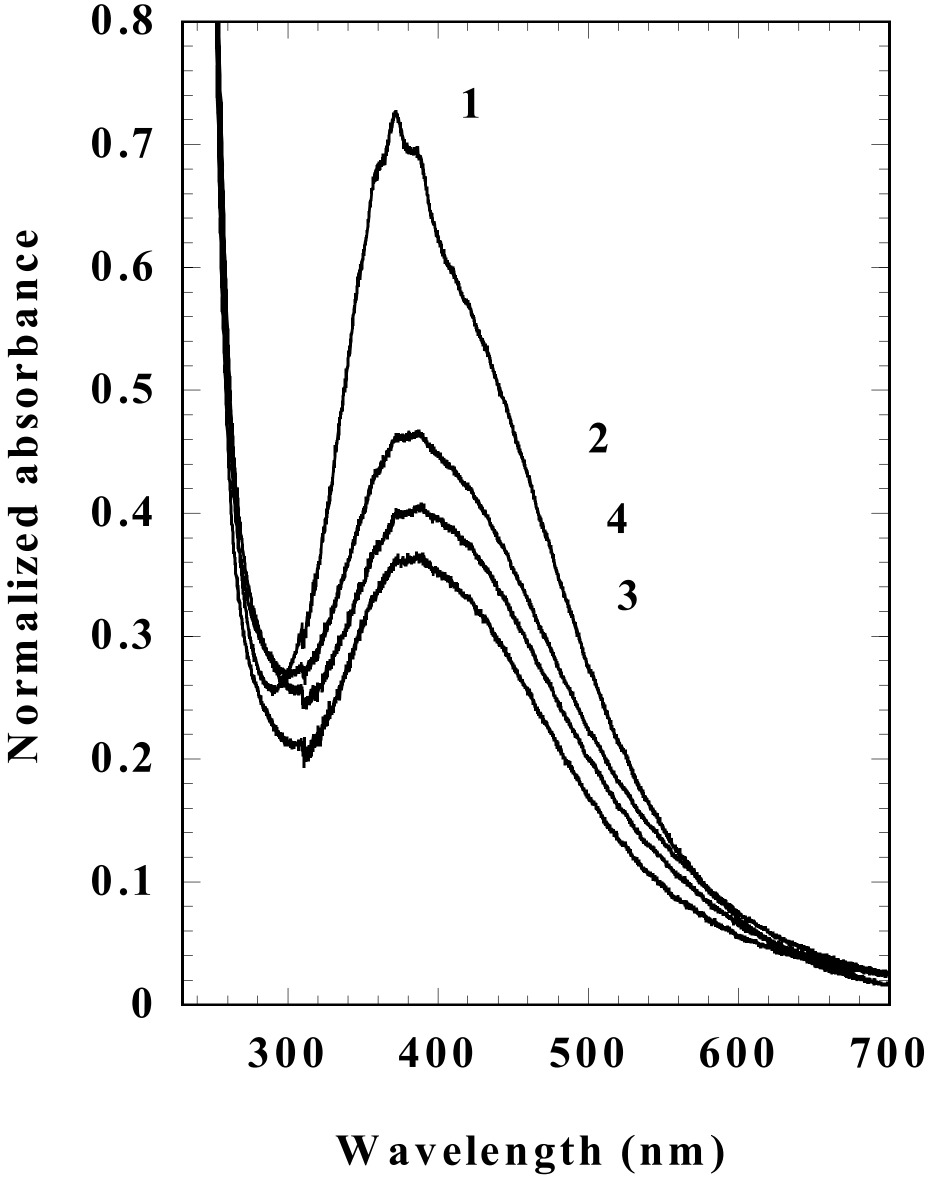

Fig. 2.5. Spectra of $2.320 \times 10^{-2}$ mol kg$^{-1}$ $HNO_3$ with addition of hydrogen peroxide. Temperature 380 °C. Pressure 41.3 MPa. Hydrogen peroxide concentration (mol kg$^{-1}$): 0.0 (1); 0.262 (2); 0.546 (3); 0.906 (4).

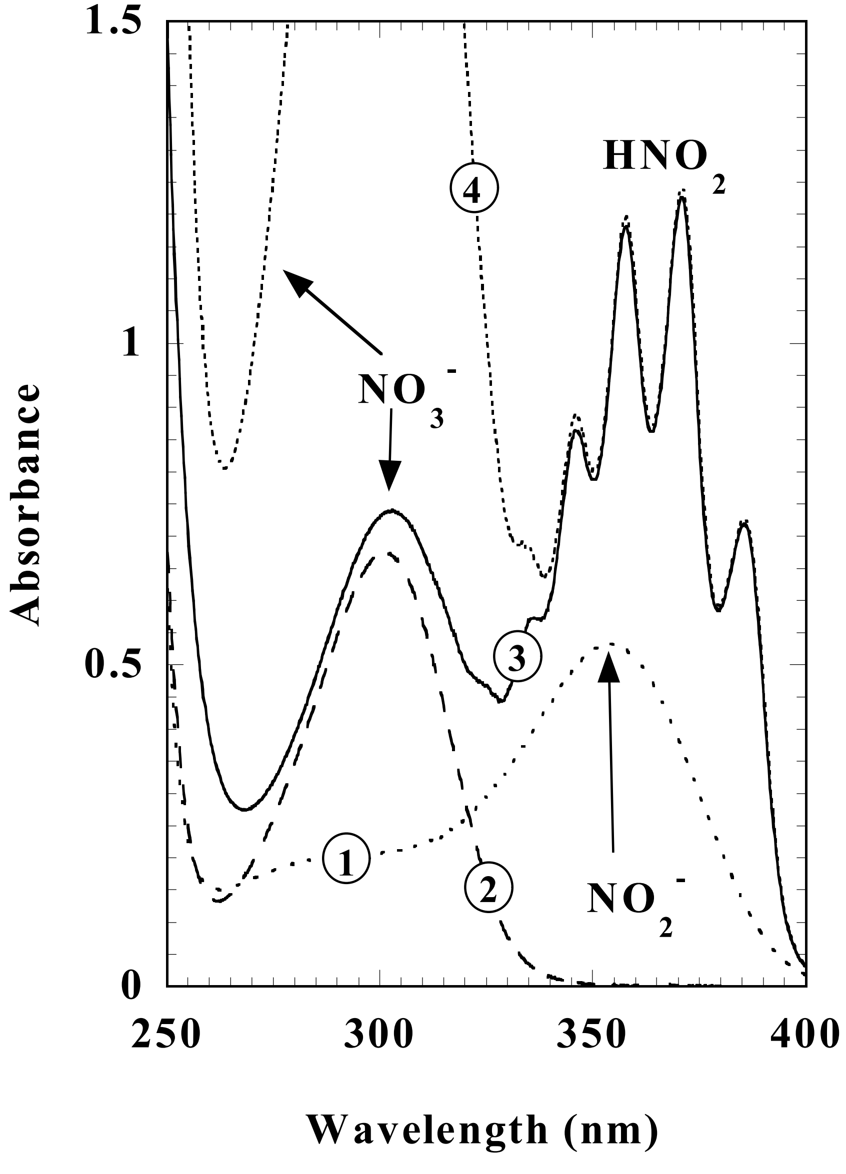

Fig. 2.6. Room temperature spectra of nitrates, nitrites, and the corresponding acids and assignment of the bands. (1) 2.26 × $10^{-2}$ mol $dm^{-3}$ $NaNO_2$; (2) 9.280 × $10^{-2}$ mol $dm^{-3}$ $NaNO_3$; (3) 2.26 × $10^{-2}$ mol $dm^{-3}$ $NaNO_2$ + 9.280 × $10^{-2}$ mol $dm^{-3}$ $HNO_3$; (4) 2.26 × $10^{-2}$ mol $dm^{-3}$ $NaNO_2$ + 0.4176 mol $dm^{-3}$ $HNO_3$.

Addition of oxygen shifts this equilibrium to the left and therefore explains the relative decrease of the $HNO_2/NO_2^-$ content versus that of $NO_2$ in Figure 2.5. One should note, however, that this explanation does not include $HNO_3$ as well as any nitrogen species with an oxidation state lower than +3, such as NO, which, as suggested by literature data [55], can also be present in our case. A more quantitative explanation, which includes these species, is given in the speciation diagrams below.

Figure 2.7 shows the effect of nitrite on the spectra of $HNO_3$ for a fixed total nitrogen concentration of 0.0208 mol $kg^{-1}$ (class IV). An increase in the $NaNO_2$ concentration leads to a significant decrease in the $NO_2$ band. At the same time, the set of small bands at 370 nm does not seem to be affected strongly for a molar ratio of $NaNO_2$ to $HNO_3$ up to 1:1. At higher $NaNO_2$ to $HNO_3$ ratios, the set of small bands ($HNO_2/NO_2^-$) is gradually replaced by a single band ($NO_2^-$) at a wavelength similar to that measured in pure $NaNO_2$ solution (curve 8). As could be expected for a salt of a relatively weak acid, sodium nitrite solution was found to be a rather strong base in supercritical water, as manifested by significant corrosion of the sapphire windows [32].

The observed changes in the spectra resulting from addition of $NaNO_2$ to nitric acid (Fig.2.7) further supports our assignment of the bands. Because the total nitrogen content is fixed, the amount of $HNO_3$ in the feed mixture decreases. Consequently products from the decomposition of $HNO_3$, i.e., $NO_2$ and

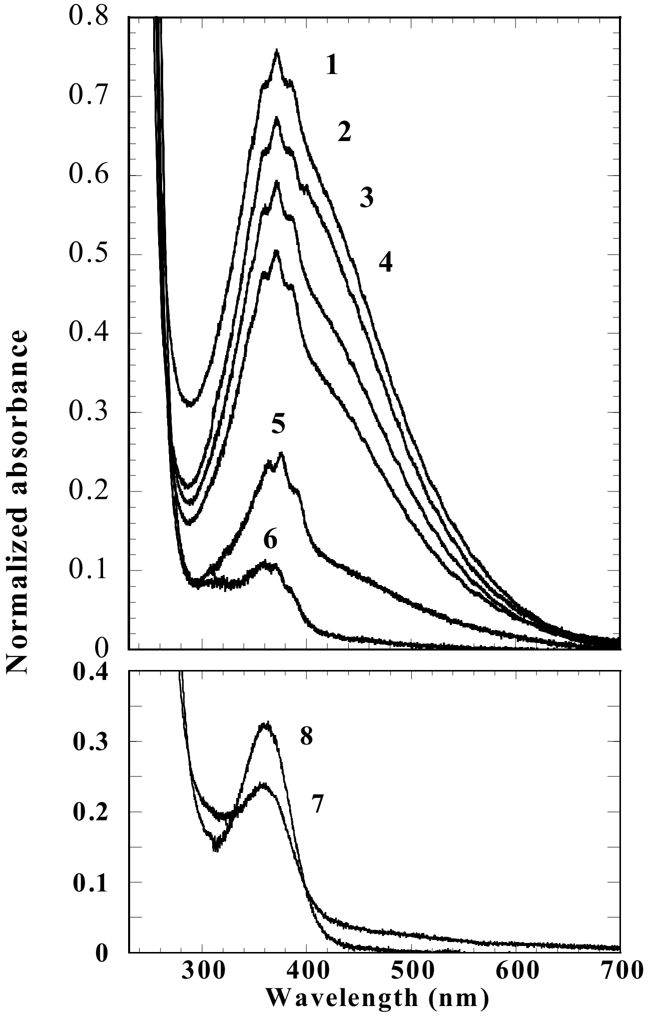

Fig. 2.7. Spectra of $HNO_3$/$NaNO_2$ mixtures with a total nitrogen content of 0.0208 mol $kg^{-1}$. Temperature 380 °C. Pressure 31.0 MPa. $NaNO_2$ molar fraction: 0.218 (1); 0.260 (2); 0.385 (3); 0.442 (4); 0.549 (5); 0.635 (6); 0.778 (7); 1.0 (8).

$HNO_2/NO_2^-$ decrease. However, the total nitrite concentration (small bands) does not decrease since the loss in $HNO_2/NO_2^-$ is compensated for by the greater amount of nitrite introduced in the feed. Alternatively, the same effects may be explained in terms of the net oxidation state of nitrogen in the mixture. The decrease in the net oxidation state of nitrogen in the feed mixture leads to the relative increase of the lower oxidation state ($HNO_2/NO_2^-$) versus that of the higher oxidation state ($NO_2$).

For mixtures with a high $NaNO_2$ to $HNO_3$ ratio (spectra 6 and 7 in Fig.2.7) the concentration of $NO_2$ is negligible. The composite $HNO_2/NO_2^-$ band is also much smaller than expected for pure $NO_2^-$ or $HNO_2$ solutions with identical total nitrogen content. While part of the nitrogen in these solutions can be in the form of $NO_3^-$, which has a weak absorption band around 300 nm (see Fig.2.6 and Fig.2.7 curve 6), other nitrogen species may also be present such as NO or $N_2O$ which absorb below 280 nm [56].

Experiments for mixtures of nitric acid, sodium hydroxide and sodium nitrite (class V) were performed to further increase the ratio of $HNO_2/NO_2^-$ to $NO_2$ over the values in class IV. As shown by the reaction,

$$2\,H^+ + 2\,NO_3^- \leftrightharpoons 2\,NO_2 + H_2O + 1/2\,O_2 \qquad (2.2)$$

the addition of a base (NaOH) may be expected to lower the $NO_2$, as was observed (not shown).

***2.33 Deconvolution of the spectra***. As shown in the preceding section, the only distinct bands in the measured spectra are those corresponding to $NO_2$ and $HNO_2/NO_2^-$. Among other species, which can absorb light in the visible and near-UV ranges are $HNO_3$, $NO_3^-$, $N_2O_4$, and $N_2O_3$. The steep increases in absorbance at wavelengths shorter than 280 nm cannot be used for analytical purposes, since so many nitrogen species absorb in this range. Above, we have already eliminated the possibility of $N_2O_4$.

The $HNO_3$ and $NO_3^-$ low energy bands are very weak [57] (Figs. 2.2 & 2.6). The absorbance of a 0.02 mol kg$^{-1}$ $HNO_3$ solution at 300 nm resulting from the presence of $HNO_3$ or $NO_3^-$ would not exceed 0.14 if there was no decomposition and assuming temperature independent extinction coefficients. Because a significant amount of $HNO_3$ decomposes, the remaining absorbance is too low to be determined accurately, especially after including effects due to the overlap with higher energy bands (Fig. 2.2), absorbance from decomposition products, and light scattering by the $TiO_2$ deposit on the windows. Consequently, we decided to exclude $NO_3^-$ and $HNO_3$ bands from spectral deconvolution.

$N_2O_3$ has a weak band ($\varepsilon \approx 20$) centered around 620 nm [58] and absorbs strongly in the UV region. The estimated extinction coefficient of $N_2O_3$ at 280 nm is 290 [59]. Since the measured absorbance at 280 nm did not exceed 0.4 in a $2\times10^{-2}$ mol kg$^{-1}$ $HNO_3$ solution, the maximum possible $N_2O_3$ concentration could not exceed $1.4\times10^{-3}$ mol kg$^{-1}$ resulting in a normalized absorbance of 0.03 at 620 nm. Similar calculations for $HNO_3/NaNO_2$ mixtures reveal that the absorbance due to $N_2O_3$ at 620 nm is also insignificant. In addition, gas phase data suggest that $N_2O_3$ should dissociate almost completely to NO and $NO_2$ at our temperatures [6,47,60,61]. As was the case for nitrate, we think that the $N_2O_3$ band at 620 nm, if present, is too small to be accurately measured and deconvoluted from the spectra.

Another species that was considered was the solvent separated ion pair $(H^+)(NO_2^-)$ or, in solutions containing $Na^+$, $(Na^+)(NO_2^-)$. These species will now be shown to be much less stable than $HNO_2$. The dissociation constant of nitrous acid under our experimental conditions can be roughly estimated to be on the order of $10^{-8}$ or less at 380 °C and solution densities in the range 0.5-0.6 g $cm^{-3}$ based on low temperature data [62-64] and comparison with other acids of comparable strength in supercritical water [65,66]. Dissociation constants for 1:1 alkali metal salts at densities from 0.5 to 0.6 g $cm^{-3}$ are typically between $10^{-1}$ and $10^{-2}$ at 380 °C [66,67]. Based on these equilibrium constants, comparable concentrations of $HNO_2$ and $(Na^+)(NO_2^-)$ would exist for $H^+$ to $Na^+$ equilibrium concentration ratios lower than $10^{-6}$, i.e., $H^+$ concentration on the order of $10^{-8}$ mol $kg^{-1}$, which is unlikely in acidic media. For similar reasons the concentration of $(H^+)(NO_2^-)$ may be expected to be insignificant. Therefore, we chose to exclude $(H^+)(NO_2^-)$, and $(Na^+)(NO_2^-)$ bands from the spectral deconvolution.

Our final procedure was to deconvolute the spectra with only five Gaussian peaks, four of them representing $HNO_2$ and one representing $NO_2$. Fixed widths and positions were used for the $HNO_2$ bands as determined from the spectra where $HNO_2$ bands were the strongest (see above). A wavenumber range of $3\times10^4$ - $5\times10^4$ $cm^{-1}$ (333 - 500 nm) was used to achieve an accurate fit for the asymmetric $NO_2$ peak. The position and width of this peak was allowed to vary. Extensive calculations revealed that the $NO_2$ peak position peak width varied randomly (Table 2.2), most likely because of the large peak width and the imperfect baseline correction. Spectra obtained from class IV experiments with a $NaNO_2$ to $HNO_3$ ratio higher than approximately 1:1 (curves 6-8 in Fig. 2.7) were excluded, since these solutions obviously contained nitrites whose bands interfered with these of $HNO_2$. The parameters for the $HNO_2$ bands were averages of the values obtained from deconvoluting individual spectra; typical results of deconvolution are quite accurate as shown in Figure 2.8. As shown in Table 2.2, the ratio of each band to band 2 was relatively constant indicating only one species produced the fine structure and that the fits were quite accurate. An exception is $H_2O_2$ class III experiments where nitrous acid peaks were extremely small (Fig.2.5) and the errors were correspondingly large (Table 2.2).

The rest of this section describes other deconvolution techniques that were unsuccessful and not adopted. Because the $NO_2$ band was extremely broad, it was attempted to fit the band with two Gaussian bands. However, the changes in the positions and widths of these bands were unacceptably large. As indicated by the

Table 2.2. Deconvolution of the spectra with five Gaussian peaks at 380 - 400 °C and 27.6 - 41.3 MPa [a].

| Band | Species | $\lambda$ nm | $1/\lambda$ $cm^{-1}$ | Peak Width $cm^{-1}$ | Peak area ratio [b] class I | class II [c] | class III [d] | class IV |
|---|---|---|---|---|---|---|---|---|
| 1 | $NO_2$ | 385 ± 7 | | 1134 ± 48 | | | | |
| 2 | $HNO_2$ | 386.1 | 25900 | 50 | 1 | 1 | 1 | 1 |
| 3 | $HNO_2$ | 371.7 | 26900 | 90 | 0.33 ± 0.04 | 0.32 ± 0.07 | 0.25 ± 0.09 | 0.34 ± 0.03 |
| 4 | $HNO_2$ | 358.4 | 27900 | 70 | 0.64 ± 0.10 | 0.65 ± 0.16 | 0.99 ± 1.00 | 0.70 ± 0.11 |
| 5 | $HNO_2$ | 348.4 | 28700 | 130 | 0.58 ± 0.20 | 0.69 ± 0.23 | 2.31 ± 7.21 | 0.69 ± 0.14 |

[a] The errors listed are mean standard deviations. [b] Peak area relative to band 2. [c] After removing four data points, which deviated strongly from the mean. [d] Significant scatter in these data result from the extremely small nitrous acid bands in the presence of oxygen.

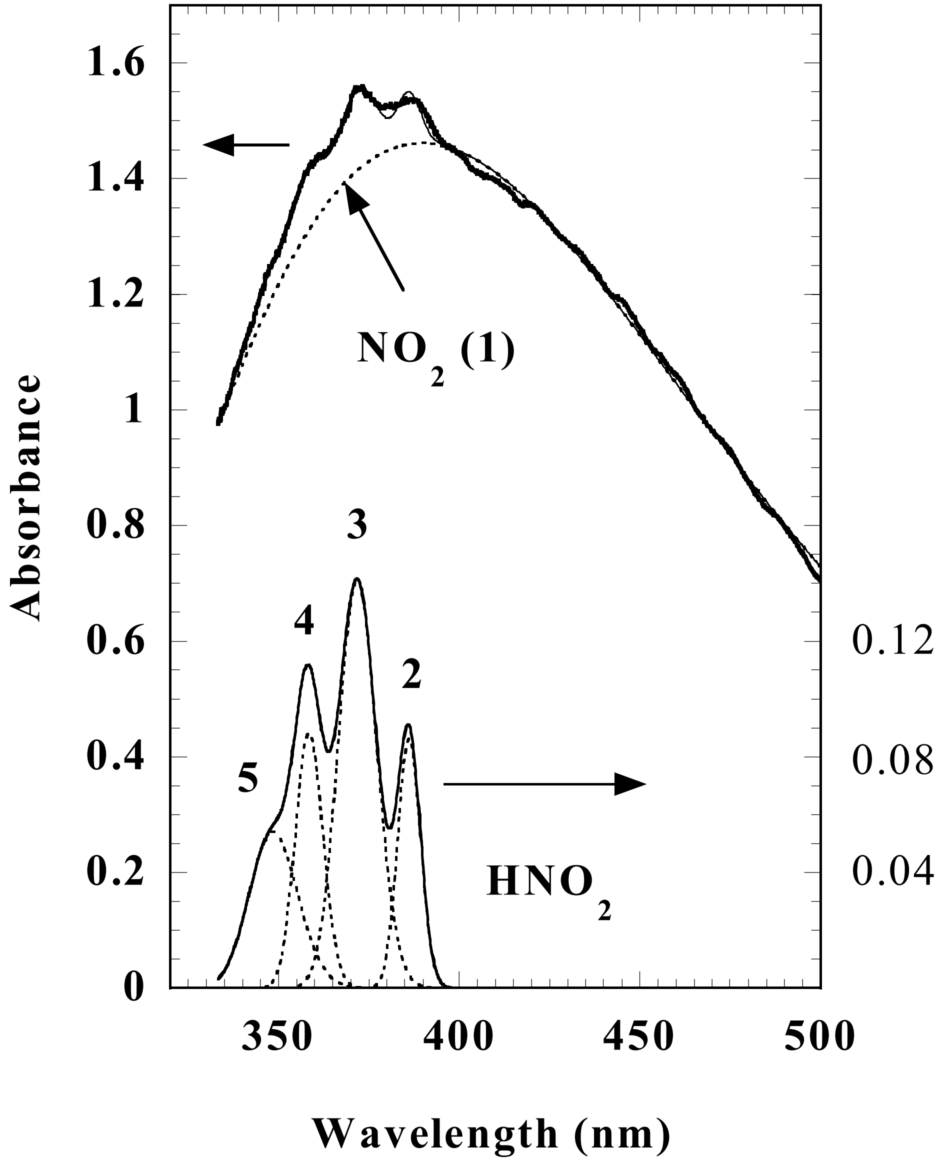

Fig. 2.8. Peak fitting results for a 0.03480 mol kg$^{-1}$ $HNO_3$ solution at 27.6 MPa and 380 °C. The individual bands obtained from the fitting are drawn with dotted lines. Thick and thin full lines in the upper portion of the graph represent the measured and fitted spectra, respectively.

spectra measured for $NaNO_2/HNO_3$ mixtures (see Fig.2.7), the content of $NO_2^-$ in some of these solutions could potentially be significant. Therefore, it was also attempted to fit the spectra with six Gaussian peaks representing a single $NO_2$ band, the four strongest $HNO_2$ bands, and a single $NO_2^-$ band (see Fig. 2.6). However, consistent peak positions and widths were obtained only for the four peaks representing $HNO_2$ in spectra where the $HNO_2$ bands were the strongest. Because the single $NO_2^-$ band was not different enough from the $NO_2$ band, it was not possible to deconvolute reliable values of $NO_2^-$ over a wide pH range. Therefore, spectra were not deconvoluted in this study in solutions where the $NaNO_2$ to $HNO_3$ ratio in the feed was greater than 1.22:1.

***2.34 Determination of the equilibrium constants.*** Among possible decomposition products of nitric acid, only $NO_2$ and $HNO_2$ could be observed in our spectra. Their concentrations, however, could not be determined directly, since their extinction coefficients are unknown under hydrothermal conditions. The $NO_2$ extinction coefficients in the gas phase have been determined accurately [43-45,68-71] and are strongly dependent upon temperature [45,70]. The $NO_2$ band fine structure is significantly reduced in SCW, especially at higher densities (see above). Data are unavailable for nitrous acid extinction coefficients versus temperature, most likely due to the low stability of the acid at low temperatures. However, since measured absorbances are unique functions of extinction coefficients and all the equilibria in the system, both the extinction coefficients and the equilibrium constants may be optimized numerically to the experimental data [29,30]. While details of the numerical method are described in Chapter 3, the basic method and assumptions are presented here.

The equilibrium between most probable species may be represented by the following basic set of reactions:

$$HNO_3 \leftrightharpoons H^+ + NO_3^- \tag{2.3}$$

$$2\ HNO_3 \leftrightharpoons H_2O + 2\ NO_2 + \tfrac{1}{2}\ O_2 \tag{2.4}$$

$$2\ NO_2 + H_2O \leftrightharpoons HNO_3 + HNO_2 \tag{2.5}$$

$$2\ HNO_2 \leftrightharpoons H_2O + 2\ NO + \tfrac{1}{2}\ O_2 \tag{2.6}$$

$$2\ NO \leftrightharpoons N_2O + \tfrac{1}{2}\ O_2 \tag{2.7}$$

$$H_2O \leftrightharpoons OH^- + H^+ \tag{2.8}$$

$$NaOH \leftrightharpoons Na^+ + OH^- \tag{2.9}$$

$$(Na^+)(NO_3^-) \leftrightharpoons Na^+ + NO_3^- \tag{2.10}$$

Less important reactions are:

$$(Na^+)(NO_2^-) \leftrightharpoons Na^+ + NO_2^- \tag{2.11}$$

$$2\ NO_2 \leftrightharpoons N_2O_4 \tag{2.12}$$

$$HNO_2 \leftrightharpoons H^+ + NO_2^- \tag{2.13}$$

$$2\ HNO_2 \leftrightharpoons N_2O_3 + H_2O \tag{2.14}$$

$$N_2O_3 \leftrightharpoons NO + NO_2 \tag{2.15}$$

For reasons specified immediately below, these equilibria (Equations 2.11-2.15) were not considered in our model. As explained above, reactions (2.11) and

(2.12) do not occur to a significant extent under our experimental conditions. Due to the low dissociation constant of nitrous acid, reaction (2.13) is shifted far to the left in all the acidic solutions. At ambient conditions, reaction (2.14) occurs to a significant extent in strongly acidic dehydrating media [52,53,72] but it is not likely to generate significant quantities of $N_2O_3$ under our experimental conditions because of reaction (2.15) as discussed above. The following set of equations defined the equilibrium constants in our model:

$$K_a m_{HNO_3} - m_{H^+} m_{NO_3^-} \gamma_{\pm}^2 = 0 \tag{2.16}$$

$$K_4 m_{HNO_3}^2 - m_{NO_2}^2 m_{O_2}^{1/2} = 0 \tag{2.17}$$

$$K_5 m_{NO_2}^2 - m_{HNO_3} m_{HNO_2} = 0 \tag{2.18}$$

$$K_6 m_{HNO_2}^2 - m_{NO}^2 m_{O_2}^{1/2} = 0 \tag{2.19}$$

$$K_7 m_{NO}^2 - m_{N_2O} m_{O_2}^{1/2} = 0 \tag{2.20}$$

$$K_w - m_{H^+} m_{OH^-} \gamma_{\pm}^2 = 0 \tag{2.21}$$

$$K_b m_{NaOH} - m_{Na^+} m_{OH^-} \gamma_{\pm}^2 = 0 \tag{2.22}$$

$$K_{d,ip} m_{NaNO_3} - m_{Na^+} m_{NO_3^-} \gamma_{\pm}^2 = 0 \tag{2.23}$$

where $K_a$ is the dissociation constant of nitric acid, $K_w$ is the ion product of water [73], $K_b$ is the inverse of the sodium hydroxide association constant as determined by Ho and Palmer [74], and $K_{d,ip}$ is the $(Na^+)(NO_3^-)$ ion pair dissociation constant. The subscripts defining the remaining equilibrium constants refer to the later part of the reaction numbers in the equations above. It was assumed that the individual ionic activity coefficients are not sensitive to specific properties of ions and can be approximated by the mean ionic activity coefficient, $\gamma_\pm$, given by Pitzer [75]:

$$\ln\gamma_\pm = -A_\varphi\left[\frac{\sqrt{I}}{1+1.2\sqrt{I}} + \frac{2}{1.2}\ln(1+1.2\sqrt{I})\right] \tag{2.24}$$

where $A_\varphi$ is the Debye-Huckel parameter [75], and $I$ is the ionic strength given by:

$$I = \frac{1}{2}\sum_i m_i z_i^2 \tag{2.25}$$

where $m_i$ and $z_i$ are the molalities and charges of all the ionic species in solution.

The model also included:

a charge balance:

$$m_{Na^+} + m_{H^+} - m_{NO_3^-} - m_{OH^-} = 0 \tag{2.26}$$

a sodium mass balance:

$$m^0_{NaOH} + m^0_{NaNO_2} - m_{Na^+} - m_{NaOH} - m_{(Na^+)(NO_3^-)} = 0 \tag{2.27}$$

a nitrogen mass balance:

$$\begin{aligned} &m^0_{HNO_3} + m^0_{NaNO_2} - m_{HNO_3} - m_{NO_3^-} - m_{HNO_2} \\ &- m_{NO_2} - m_{NO} - 2m_{N_2O} - m_{(Na^+)(NO_3^-)} = 0 \end{aligned} \tag{2.28}$$

and a redox balance:

$$m_{O_2} - \frac{1}{2}(m^0_{H_2O_2} - m^0_{NaNO_2} + m_{HNO_2}) - \frac{1}{4}(m_{NO_2} + 3m_{NO}) - 2m_{N_2O} = 0 \tag{2.29}$$

The equilibrium constants and extinction coefficients were fitted through a Large-Scale Generalized Reduced Gradient (LSGRG2) optimization routine [38].

To properly scale the equations to aid optimization, a logarithmic transformation was made for each equation as described in Chapter 3. The optimization was carried out on eight data sets corresponding to the different temperatures and pressures. Initially, all concentrations, extinction coefficients, and equilibrium constants were not bounded. These values were further refined by reducing the bounds of the variables to achieve more linear behavior in the log of the equilibrium constants versus density. Typically, the final values for the equilibrium constants were at least half an order of magnitude away from a bound.

Integrated areas of $NO_2$ and $HNO_2$ bands from deconvolution of the spectra were used in the determination of the equilibrium constants. The optimization was performed by using Equations (2.16)-(2.29) as constraints and the equilibrium constants, species concentrations, ionic strength, and activity coefficient as variables. Each of the eight data sets (T,P) included 35-48 experiments from classes I-IV (see Chapter 3). This resulted in the simultaneous solution of 497-679 variables by using 490-672 equations as constraints. The objective function was chosen to be:

$$\min\phi = w_1 \sum_{i=1}^{N} \left( A_{NO_{2,measured}} - \varepsilon_{NO_2} l m_{NO_2} \right)^2 + w_2 \sum_{i=1}^{N} \left( A_{HNO_{2,measured}} - \varepsilon_{HNO_2} l m_{HNO_2} \right)^2 \qquad (2.30)$$

where $\varepsilon_{NO_2}$, and $\varepsilon_{HNO_2}$ are the integrated extinction coefficients. The $HNO_2$ residuals were weighted so as to be the same order of magnitude as the $NO_2$ residuals; $w_1$ and $w_2$ were chosen to be 10 and 1000, respectively. This approach allowed the small integrated area of $HNO_2$ to affect the final equilibrium values. Further improvements on the model were achieved by applying a statistical procedure called the jackknife. Table 2.3 lists values of the equilibrium constants and molar absorptivities of $NO_2$ and $HNO_2$ obtained from this optimization. For a discussion of local optima and estimates on the error associated with these values see Chapter 3.

Figure 2.9 shows dissociation constants for nitric acid and the $(Na^+)(NO_3^-)$ ion pair plotted against the water density. Similarly to other strong acids, $HNO_3$ becomes a much weaker acid at high temperatures in supercritical water. Part of this effect is due to the exothermic character of $HNO_3$ dissociation at moderate and high densities. The second part is due to the isobaric decrease of water density and dielectric constant, which favor the associated species, i.e., $HNO_3$. The nitric acid dissociation constants at 380 °C agree well with the data of Marshall and Slusher obtained from calcium and magnesium sulfate solubilities in nitric acid solutions [25,26] at densities down to 0.45 g $cm^{-3}$ (See Fig 2.9a). However, this new spectroscopic technique offers a means to measure equilibrium constants at very low densities, in this case down to 0.24 g $cm^{-3}$.

Table 2.3. Equilibrium constants for the reactions (2.3)-(2.7), and (2.10) and integrated extinction coefficients for $NO_2$ and $HNO_2$ from optimization of the measured $NO_2$ and $HNO_2$ absorbances [a].

| T °C | P MPa | $10^4$ $K_{HNO_3}$ mol $kg^{-1}$ | $K_4$ (mol $kg^{-1})^{0.5}$ | $10^2$ $K_5$ | $10^2$ $K_6$ (mol $kg^{-1})^{0.5}$ | $K_7$ (mol $kg^{-1})^{0.5}$ | $10^2$ $K_{d,ip}$ mol $kg^{-1}$ | $10^5$ $\varepsilon_{NO_2}$ [b] (kg $mol^{-1}$ $cm^{-1}$)$cm^{-1}$ | $10^5$ $\varepsilon_{HNO_2}$ [b] (kg $mol^{-1}$ $cm^{-1}$)$cm^{-1}$ |
|---|---|---|---|---|---|---|---|---|---|
| 380 | 27.6 | 18.2 | 1.09 | 2.98 | 3.83 | $4.65\times10^{-2}$ | 4.65 | 6.24 | 1.43 |
| | 31.0 | 5.15 | 0.231 | 6.30 | 7.23 | $2.36\times10^{-2}$ | 12.3 | 6.40 | 1.77 |
| | 34.5 | 4.20 | 0.168 | 5.28 | 12.5 | $2.56\times10^{-2}$ | 5.13 | 6.05 | 2.39 |
| | 41.4 | 5.64 | 0.086 | 8.67 | 6.76 | $0.47\times10^{-2}$ | 16.6 | 6.04 | 2.16 |
| 400 | 27.6 | 0.006 | 24.4 | 0.05 | 41.6 | 490.91 | 0.003 | 7.06 | 7.46 |
| | 31.0 | 0.041 | 2.47 | 0.60 | 30.9 | 12.39 | 0.615 | 6.32 | 3.74 |
| | 34.5 | 0.586 | 1.06 | 2.17 | 22.8 | 0.53 | 0.582 | 6.68 | 2.08 |
| | 41.4 | 5.65 | 0.333 | 5.45 | 12.2 | $7.14\times10^{-2}$ | 5.15 | 7.08 | 1.82 |

[a] Class V experiments were not used in deconvolution.

[b] Integrated extinction coefficient with respect to wavenumber ($cm^{-1}$).

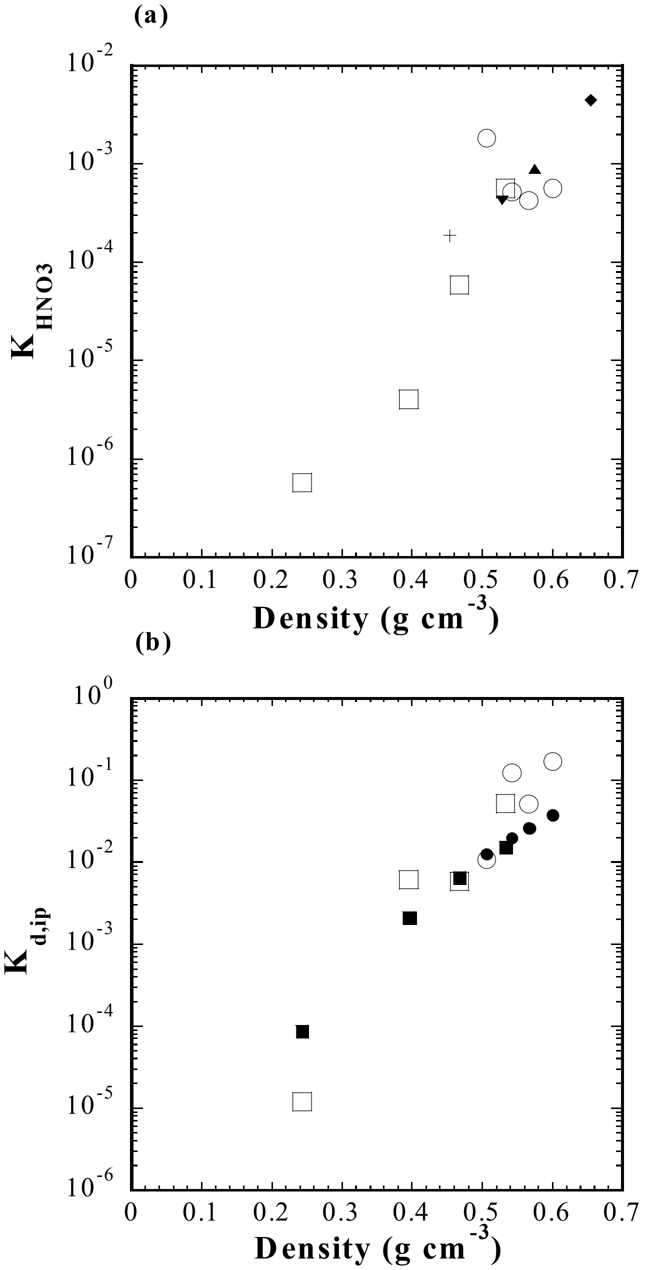

Fig. 2.9. Dissociation constants of $HNO_3$ and the $(Na^+)(NO_3^-)$ ion pair at 380 °C (circles) and 400 °C (rectangles) plotted against solution density. (a) Literature data [25] for dissociation of saturated $HNO_3$ at 325 (◆), 350 (▲), 360 (▼), and 370 °C (✚) are also presented. (b) For comparison the literature data [76] for the dissociation of NaCl are also presented at identical temperatures and pressures (filled symbols).

The dissociation constants for $(Na^+)(NO_3^-)$ ion pair are close to corresponding data for NaCl, KCl, KOH, NaOH [67,74,76]. The change in $K_{d,ip}$ with a decrease in density (Fig.2.9b) reflects increased interionic interactions in low dielectric permittivity media.

Figures 2.10-2.13 show the equilibrium constants for reactions (2.4)-(2.7) plotted against the water density together with the gas phase values calculated from existing thermodynamic data [61]. Reactions (2.4)-(2.7) are non-ionic, and density effects on equilibrium constants are smaller than these observed for ionic reactions [77]. Linear extrapolation of the log K versus density plots to zero density results in values which are very close to the gas phase data, a result which supports our methodology. Relatively linear plots of log K vs. $\rho$ (in some cases log $\rho$) have been observed previously for equilibrium constants in hydrothermal solutions [73].

The hydration of neutral molecules in SCW is most likely limited to the first coordination shell and is relatively weak [39,78,79]. For polar molecules like $HNO_3$ and $NO_2$, the density effect is likely to be influenced more by the solvation energies resulting from dipole-dipole interactions than from partial molar volume changes [80]. The dipole moments for polar molecules in Equations (2.4)-(2.7) are 2.17 ($HNO_3$), 1.423 (cis- $HNO_2$), 1.855 (trans- $HNO_2$), 0.313 ($NO_2$), 0.159 (NO), 0.167 ($N_2O$), and 1.854 ($H_2O$) [81]. A net decrease of dipole moment is observed for reactions (2.4), (2.6), and (2.7) on the basis of the stoichiometries. The

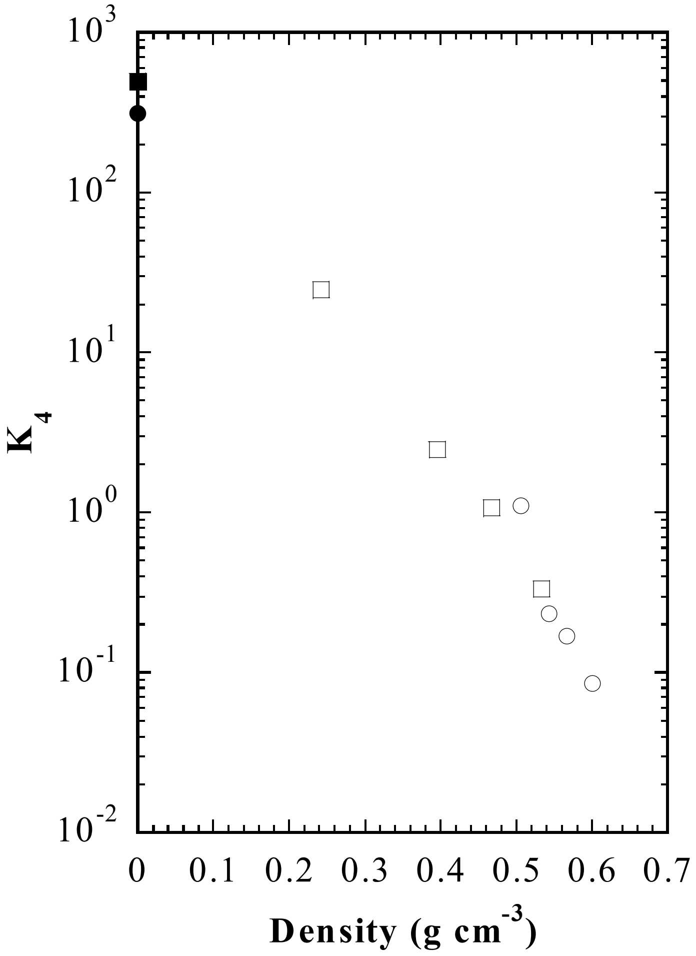

Fig. 2.10. Equilibrium constants for the reactions (2.4) in supercritical water at 380 °C (circles) and 400 °C (rectangles) plotted against solution density. For comparison, gas phase data [61] calculated from thermochemical data are also presented (filled symbols).

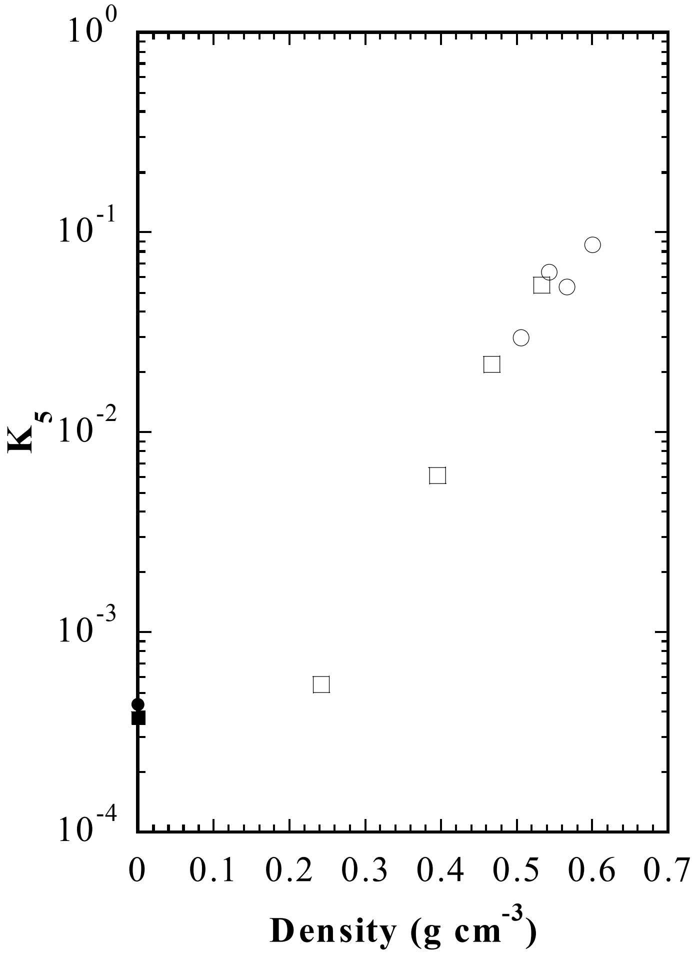

Fig. 2.11. Equilibrium constants for the reactions (2.5) in supercritical water at 380 °C (circles) and 400 °C (rectangles) plotted against solution density. For comparison, gas phase data [61] calculated from thermochemical data are also presented (filled symbols).

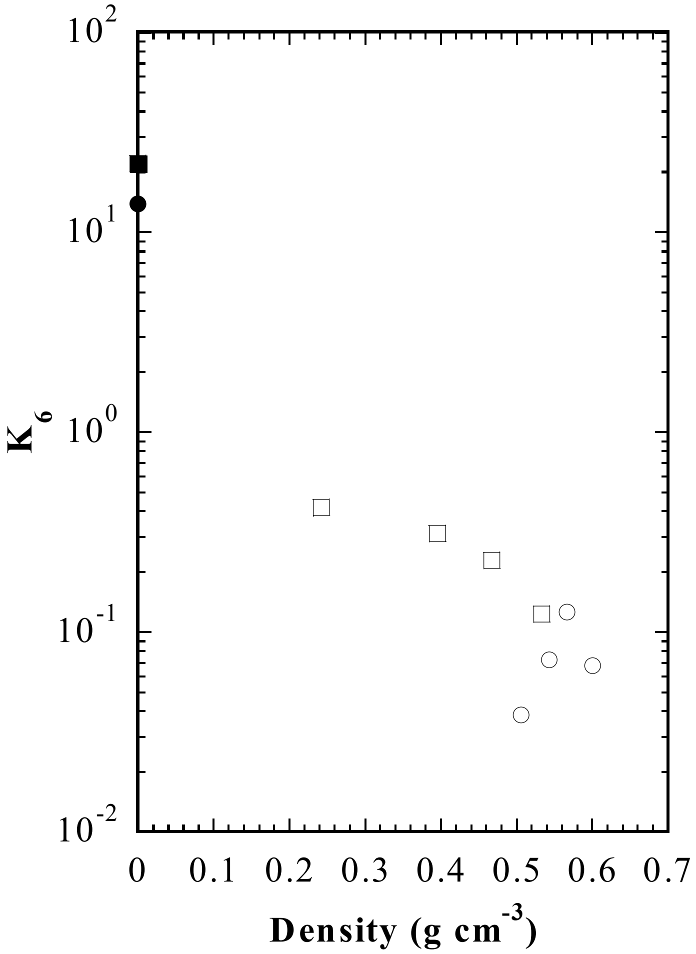

Fig. 2.12. Equilibrium constants for the reactions (2.6) in supercritical water at 380 °C (circles) and 400 °C (rectangles) plotted against solution density. For comparison, gas phase data [61] calculated from thermochemical data are also presented (filled symbols).

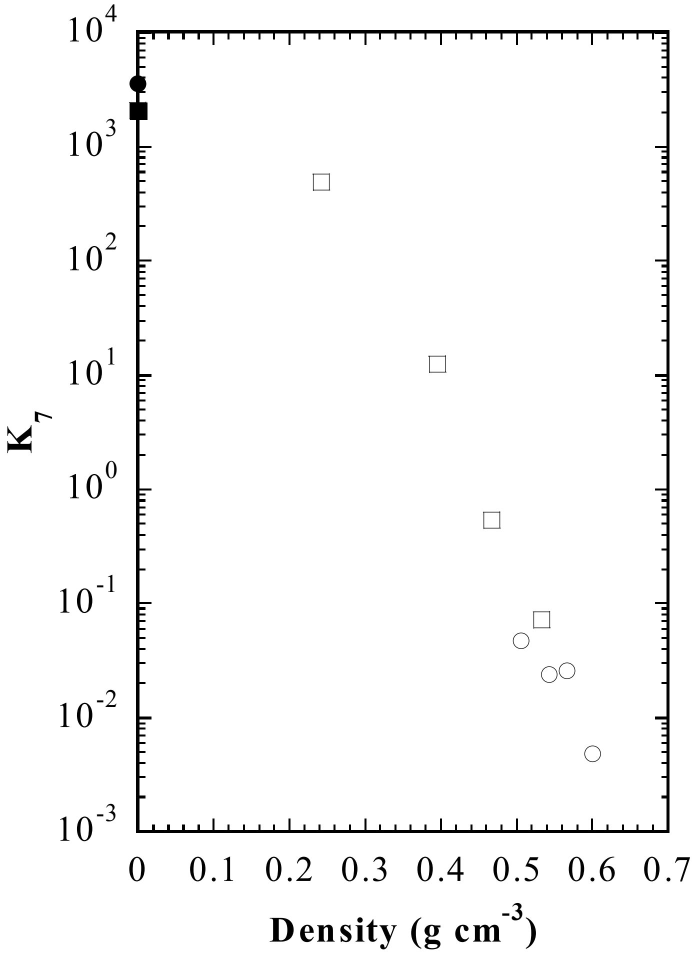

Fig. 2.13. Equilibrium constants for the reactions (2.7) in supercritical water at 380 °C (circles) and 400 °C (rectangles) plotted against solution density. For comparison, gas phase data [61] calculated from thermochemical data are also presented (filled symbols).

observed decrease of the equilibrium constants with increasing density (dielectric constant) for these three reactions is consistent with this decrease in polarity. Similarly, the observed increase of the equilibrium constant for the disproportionation reaction (2.5) is consistent with the net increase in polarity upon the reaction.

***2.35 Speciation diagrams based on the regressed equilibrium constants.*** The concentrations of the various species in equilibrium were calculated from Equations (2.16)-(2.29) on the basis of the feed concentrations and equilibrium constants regressed from the model. The results obtained at 380 °C and 31 MPa for three classes (I, III, and IV) are presented in Figures 2.14-2.16, respectively. For pure nitric acid solutions (class I, Fig.2.14) the concentration of each species increases in approximately the same manner with an increase in the feed $HNO_3$ concentration. This result is consistent with the relatively constant $HNO_2$ to $NO_2$ molar ratio in Figure 2.4.

The addition of $H_2O_2$ reduces the decomposition of $HNO_3$ modestly (Fig.2.15). The relative decrease in the concentrations of the products follows the order $N_2O$ (from $10^{-6}$ to $10^{-10}$ mol kg$^{-1}$, not shown) > NO > $HNO_2$ > $NO_2$, a result consistent with the oxidation states of nitrogen. The weak decrease in $NO_2$ concentration shown in Figure 2.15 was not observed experimentally over the whole range of $H_2O_2$ concentrations. A decrease followed by a small increase of the $NO_2$ content was actually observed at 380 °C (Fig.2.5) but not at 400 °C. This

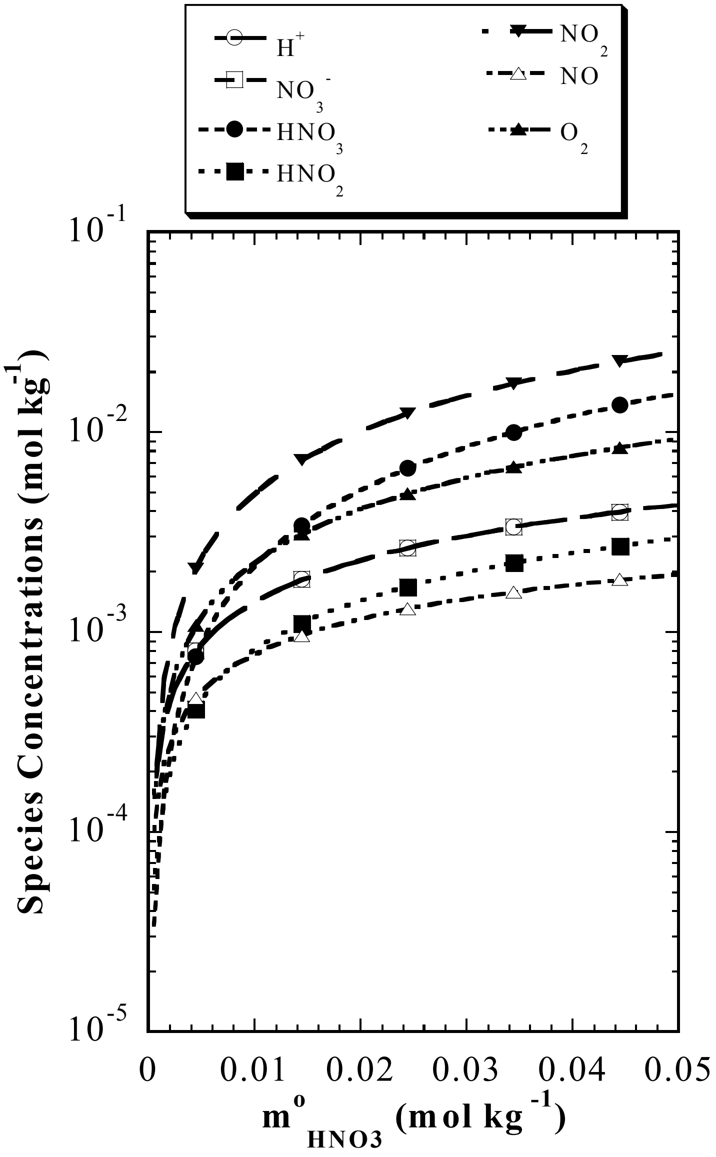

Fig. 2.14. Speciation diagram of the major species in class I experiments at 380 °C and 31.0 MPa.

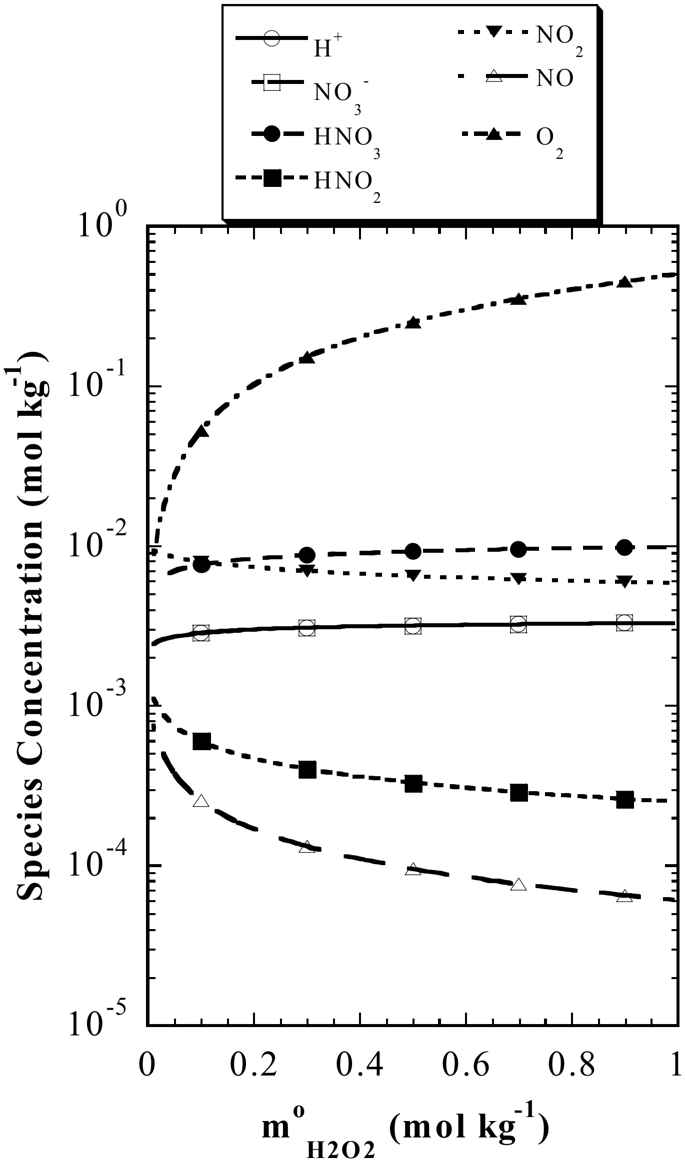

Fig. 2.15. Speciation diagram of the major species in class III experiments at 380 °C and 31.0 MPa. The initial concentration of $HNO_3$ is 0.0232 mol kg$^{-1}$.

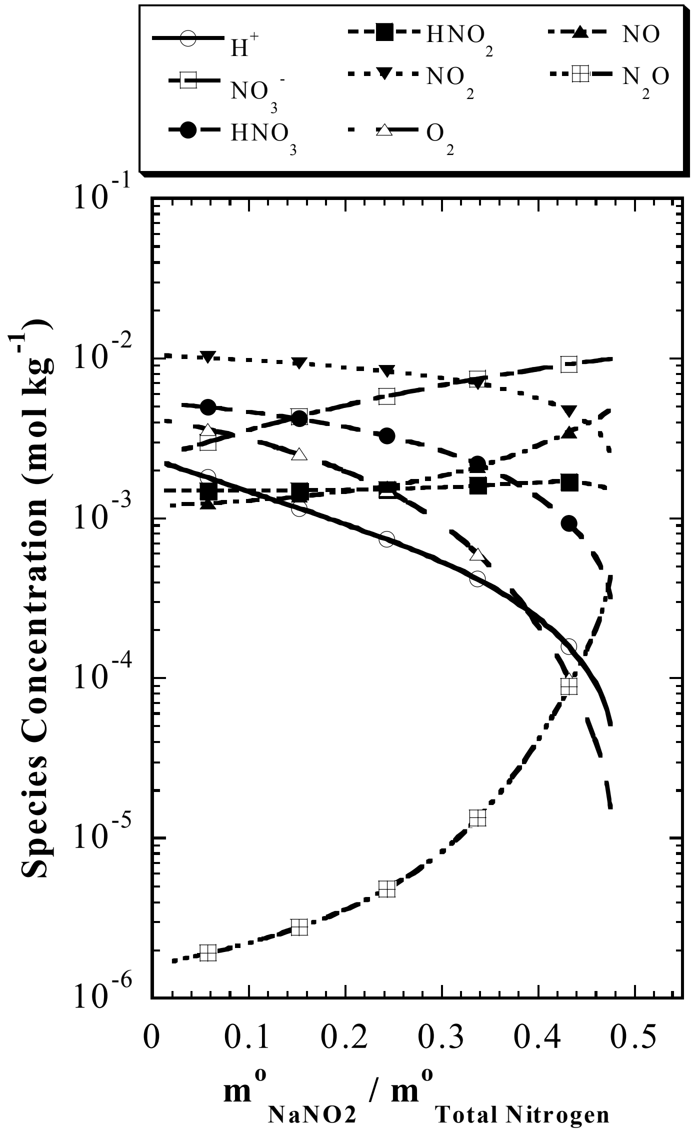

Fig. 2.16. Speciation diagram of the major species in class IV experiments at 380 °C and 31.0 MPa. Total nitrogen concentration is 0.0208 mol $kg^{-1}$.

behavior may result in part from the error introduced in correcting the measured absorbances (Fig.2.5) for density when the actual solution density is approximated by the water density at the same T and P. Electrolytes increase the density, and the actual concentration of ions increases upon addition of $H_2O_2$ (Fig.2.15). Therefore, the density corrected absorbances will be progressively overestimated as the $H_2O_2$ feed concentration increases.

Addition of $NaNO_2$ to a $HNO_3$ solution (Fig.2.16) leads to a significant increase in the $N_2O$ and NO concentrations, and to a substantial decrease in Fig. 2.16. Speciation diagram of the major species in class IV experiments at 380 °C and 31.0 MPa. Total nitrogen concentration is 0.0208 mol $kg^{-1}$.oxygen concentration. These changes may be understood easily. Addition of an N(+3) species ($NaNO_2$) to a solution of N(+5) species ($HNO_3$) destabilizes products with an oxidation state higher than +3 ($NO_2$, sum of nitrate ion and nitric acid) and stabilizes products with an oxidation state lower than +3 ($N_2O$, NO). A relatively constant concentration is observed for $HNO_2$. The small increase in $NO_3^-$ concentration upon addition of $NaNO_2$ is caused by an increase in $OH^-$ concentration (from $10^{-10}$ to $10^{-8}$ mol $kg^{-1}$, not shown) resulting from the decrease in the $HNO_3$ feed concentration and increase in $NaNO_2$, which exhibits basic properties.

The quantitative predictions of our model (see above, Figs. 2.14-2.16) agree very well with the measured $HNO_2$ and $NO_2$ absorbance bands. Examples include the roughly proportional increase of both $HNO_2$ and $NO_2$ bands generated by an increase in $HNO_3$ concentration (Figs.2.4 and 2.14); the relative effect of oxygen on the $NO_2$ and $HNO_2$ bands (Figs.2.5 and 2.15); and the weak sensitivity of the $HNO_2$ band in the $HNO_3$ / $NaNO_2$ mixtures to the solution composition (Figs.2.7 and 2.16).

The predictions of the model for the species whose absorbances were not measured directly also appear to be realistic. Class IV (mixtures of $HNO_3$ and $NaNO_2$) experiments (Fig. 2.7) suggested that significant amounts of a species with a nitrogen oxidation state lower than +3 were formed. Indeed, a significant contribution from NO is predicted by the model (Fig.2.16). Concentration changes for other species including $HNO_3$, $NO_3^-$, $N_2O$, oxygen, and the ion pairs NaOH and $(Na^+)(NO_3^-)$ follow trends, which may be expected from the feed solution composition and/or oxidation state of nitrogen.

## 2.4 Conclusions

Chemical equilibria in nitric acid solutions in SCW may be measured directly from the absorbance bands of $NO_2$ and $HNO_2$ from 380 °C to 400 °C by UV-Vis spectroscopy. These absorbance bands are similar to those at ambient temperature, except the fine structure of $NO_2$ is far less than in the gas phase. All of the spectra appear to be nearly completely reversible upon cooling. Equilibrium constants for reactions (2.3)-(2.7), and (2.10) can be determined by optimization of the measured and calculated absorbances of $NO_2$ and $HNO_2$.

Other important decomposition products that do not absorb in the wavelengths studied include $O_2$, NO, and in mixtures of $HNO_3$ and $NaNO_2$, $N_2O$.

The equilibrium constants for all the reactions change with water density in the direction expected, on the basis of the change in polarity. In most cases, the measured equilibrium constants are in good agreement with the gas phase value when extrapolated to zero density. While the behavior of ionic reactions (2.3) and (2.10) may be quantified in terms of a modified Born model, [33,36] non-ionic reactions (2.4)-(2.7) require other types models to predict solvation effects [78]. These models are useful for extrapolation of the equilibrium constants to even higher temperatures, which are also of interest in hydrothermal technology.

## 2.5 References

(1) Miller, J. A.; Bowman, C. T. *Prog.Energy Combust.Sci.* **1989**, *15*, 287.

(2) Wendel, M. M.; Pigford, R. L. *A.I.Ch.E. Journal* **1958**, *4*, 249.

(3) England, C.; Corcoran, W. H. *Ind.Eng.Chem., Fundam.* **1974**, *13*, 373.

(4) Kaiser, E. W.; Wu, C. H. *J.Phys.Chem.* **1977**, *81*, 187.

(5) Kaiser, E. W.; Wu, C. H. *J.Phys.Chem.* **1977**, *81*, 1701.

(6) Odenbrand, C. U. I.; Andersson, L. A. H.; Brandin, J. G. M.; Lundin, S. T. *Appl.Catalysis* **1986**, *27*, 363.

(7) Kiovsky, J. R.; Koradia, P. B.; Lim, C. T. *Ind.Eng.Chem.Prod.Res.Dev.* **1980**, *19*, 218.

(8) Kato, A.; Matsuda, S.; Kamo, T.; Nakajima, F.; Kuroda, H.; Narita, T. *J.Phys.Chem.* **1981**, *85*, 4099.

(9) Tester, J. W.; Holgate, H. R.; Armellini, F. J.; Webley, P. A.; Killilea, W. R.; Hong, G. T.; Barner, H. E. *Supercritical Water Oxidation Technology: A Review of Process Development and Fundamental Research*; Tedder, D. W. and Pohland, F. G., Ed.; Am. Chem. Soc.: Washington, 1993; Vol. 518, pp 35-76.

(10) Gloyna, E. F.; Li, L. *Waste Manage.* **1993**, *13*, 379.

(11) Killilea, W. R.; Swallow, K. C.; Hong, G. T. In *2nd International Symposium on Supercritical Fluids*; Department of Chemical Engineering, Johns Hopkins University: Boston, MA, 1991; p 173-176.

(12) Dell'Orco, P. C. PhD Dissertation, University of Texas at Austin, 1994.

(13) Dell'Orco, P. C.; Foy, B. F.; Robinson, J. M.; Buelow, S. J. *Haz.Waste Haz.Mat.* **1993**, *10*, 221.

(14) Dell'Orco, P.; Foy, B.; Wilmanns, E.; Le, L.; Ely, J.; Patterson, K.; Buelow, S. *Hydrothermal Oxidation of Organic Compounds by Nitrate and Nitrite.*; Hutchenson, K. W., Foster, N.R., Ed.; American Chemical Society: Washington, D.C., 1995, pp 179-196.

(15) Oldenborg, R.; Robinson, J. M.; Buelow, S. J.; Dyer, R. B.; Anderson, G.; Dell'Orco, P. C.; Funk, K.; Willmanns, E.; Knutsen, K. "Hydrothermal Processing of Inorganic Components of Hanford Tank Wastes. Los Alamos National Laboratories report LA-UR-94:3233," Los Alamos National Laboratories, 1994.

(16) Proesmans, P. I.; Luan, L.; Buelow, S. J. *Ind.Eng.Chem.Res.* **1997**, *36*, 1559.

(17) Adschiri, T.; Kanazawa, K.; Arai, K. *J.Am.Ceram.Soc.* **1992**, *75*, 1019.

(18) Adschiri, T.; Kanazawa, K.; Arai, K. *J.Am.Ceram.Soc.* **1992**, *75*, 2615.

(19) Schoppelrei, J. W., Brill, T.B. *J.Phys.Chem. A.* **1997**, *101*, 8593.

(20) Schoppelrei, J. W., Kieke, M.L., Wang, X., Klein, M.T., Brill, T.B. *J.Phys.Chem.* **1996**, *100*, 14343.

(21) Maiella, P. G.; Brill, T. B. *Appl.Spectroscopy* **1996**, *50*, 829.

(22) Spohn, P. D.; Brill, T. B. *J.Phys.Chem.* **1989**, *93*, 6224.

(23) Ratcliffe, C. I.; Irish, D. E. *Can.J.Chem.* **1985**, *63*, 3521.

(24) Oscarson, J. L.; Gillespie, S. E.; Izatt, R. M.; Chen, X.; Pando, C. *J.Solution Chem.* **1992**, *21*, 789-801.

(25) Marshall, W. L.; Slusher, R. *J.inorg.nucl.Chem.* **1975**, *37*, 2165.

(26) Marshall, W. L.; Slusher, R. *J.inorg.nucl.Chem.* **1975**, *37*, 1191.

(27) Marshall, W. L.; Jones, E. V. *J.inorg.nucl.Chem.* **1974**, *36*, 2313.

(28) Barton, C. J.; Hebert, G. M.; Marshall, W. L. *J.inorg.nucl.Chem.* **1961**, *21*, 141.

(29) Seward, T. M. *Geochim.Cosmochim.Acta* **1984**, *48*, 121.

(30) Heinrich, C. A.; Seward, T. M. *Geochim.Cosmochim.Acta* **1990**, *54*, 2207.

(31) Gammons, C. H.; Seward, T. M. *Geochim.Cosmochim.Acta* **1996**, *60*, 4295.

(32) Chlistunoff, J. B.; Johnston, K. P. *J.Phys.Chem. B* **1998**, *102*, 3993.

(33) Xiang, T.; Johnston, K. P. *J.Phys.Chem.* **1994**, *98*, 7915.

(34) Xiang, T.; Johnston, K. P.; Wofford, W. T.; Gloyna, E. F. *Ind.Eng.Chem.Res.* **1996**, *35*, 4788.

(35) Xiang, T.; Johnston, K. P. *J.Solution Chem.* **1997**, *26*, 13.

(36) Ryan, E. T.; Xiang, T.; Johnston, K. P.; Fox, M. A. *J.Phys.Chem. A* **1997**, *101*, 1827.

(37) Shin, T. W.; Kim, K.; Lee, I.-J. *J.Solution.Chem.* **1997**, *26*, 379.

(38) Smith, S.; Lasdon, L. *Journal on Computing* **1992**, *4*, 1.

(39) Bennett, G. E.; Johnston, K. P. *J.Phys.Chem.* **1994**, *98*, 441.

(40) *Official Methods of Analysis of AOAC International*; 16th ed.; AOAC International: Arlington, 1995; Vol. II.

(41) Kolthoff, I. M.; Sandell, E. B. *Textbook of Quantitative Inorganic Analysis*; 3rd ed.; The Macmillan Company: New York, 1952.

(42) Hall, T. C.; Blacet, F. E. *J.Chem.Phys.* **1952**, *20*, 1745.

(43) Norris, M. S.; Fleck, S. A.; Lichtenfels, D. H. *Anal.Chem.* **1955**, *27*, 1565.

(44) Schneider, W.; Moortgat, G. K.; Tyndall, G. S.; Burrows, J. P. *J.Photochem.Photobiol.* **1987**, *40*, 195.

(45) Mihalcea, R. M.; Baer, D. S.; Hanson, R. K. *Appl.Optics* **1996**, *35*, 4059.

(46) Chao, J.; Wilhott, R. C.; Zwolinski, B. J. *Thermochim.Acta* **1974**, *10*, 359.

(47) Hisatsune, I. C. *J.Phys.Chem.* **1961**, *65*, 2249.

(48) McLane, C. K. *J.Chem.Phys.* **1949**, *17*, 379.

(49) Takagi, J.; Ishigure, K. *Nuc.Sci.Eng.* **1985**, *89*, 177.

(50) Strickler, S. J.; Kasha, M. *J.Phys.Chem. or J.Am.Chem.Soc.* **1963**, *85*, 2899.

(51) Longstaff, J. V. L.; Singer, K. *J.Chem.Soc.* **1954**, 2604.

(52) Bunton, C. A.; Stedman, G. *J.Chem.Soc.* **1958**, 2440.

(53) Bayliss, N. S.; Watts, D. W. *Aust.J.Chem.* **1956**, *9*, 319.

(54) Bennet, M. R.; Brown, G. M.; Maya, L.; Posey, F. A. *Inorg.Chem.* **1982**, *21*, 2461.

(55) Wikstrom, M. M.; Nobe, K. *I&EC Process Design and Development* **1965**, *4*, 191.

(56) Sponer, H.; Bonner, L. G. *J.Chem.Phys.* **1940**, *8*, 33.

(57) Friend, J. A.; Lyons, L. E. *J.Chem.Soc.* **1959**, 1572.

(58) Mason (Banus), J. *J.Chem.Soc.* **1959**, 1288.

(59) Beattie, I. R.; Vosper, A. J. *J.Chem.Soc.* **1961**, 2106.

(60) Verhoek, F. H.; Daniels, F. *J.Am.Chem.Soc.* **1931**, *53*, 1250.

(61) Chase, M. W., Jr.; Davies, C. A.; Downey, J. R., Jr.; Frurip, D. J.; McDonald, R. A.; Syverud, A. N. *JANAF Thermochemical Tables*; Third ed.; American Chemical Society and the American Institute of Physics for the National Bureau of Standards:, 1985; Vol. 14.

(62) Lumme, P.; Lahermo, P.; Tummavuori, J. *Acta Chem. Scand.* **1965**, *19*, 2175.

(63) Lumme, P.; Tummavuori, J. *Acta Chem.Scand.* **1965**, *19*, 617.

(64) Tummavuori, J.; Lumme, P. *Acta Chem.Scand.* **1968**, *22*, 2003.

(65) Mesmer, R. E.; Marshall, W. L.; Palmer, D. A.; Simonson, J. M.; Holmes, H. F. *J.Solution Chem.* **1988**, *17*, 699.

(66) Chen, X.; Izatt, R. M.; Oscarson, J. L. *Chem.Rev.* **1994**, *94*, 467.

(67) Ho, P. C.; Palmer, D. A. *Geochim.Cosmochim. Acta* **1997**, *61*, 3027.

(68) Dixon, J. K. *J.Chem.Phys.* **1940**, *8*, 157.

(69) Nakayama, T.; Kitamura, M. Y.; Watanabe, K. *J.Chem.Phys.* **1959**, *30*, 1180.

(70) Corcoran, T. C.; Beiting, E. J.; Mitchell, M. O. *J.Mol.Spectrosc.* **1992**, *154*, 119.

(71) Armerding, W.; Walter, J.; Ruger, C.; Spiekermann, M.; Comes, F. J. *Ber.Bunsenges.Phys.Chem.* **1993**, *97*, 1440.

(72) Singer, K.; Vamplew, P. A. *J.Chem.Soc.* **1956**, 3971.

(73) Marshall, W. L.; Franck, E. U. *J.Phys.Chem.Ref.Data* **1981**, *10*, 1.

(74) Ho, P. C.; Palmer, D. A. *J.Solution Chem.* **1996**, *25*, 711.

(75) Pitzer, K. S. *Ion Interaction Approach. Theory and Data Correlation*, 1991, pp 75-153.

(76) Ho, P. C.; Palmer, D. A.; Mesmer, R. E. *J. Solution Chem.* **1994**, *23*, 997.
(77) Balbuena, P. B.; Johnston, K. P.; Rossky, P. J. *J. Phys. Chem.* **1996**, *100*, 2706.

(78) Luo, H.; Tucker, S. C. *J. Phys. Chem.* **1997**, *101*, 1063.

(79) Sitkoff, D.; Sharp, K. A.; Honig, B. *J.Phys.Chem.* **1994**, *98*, 1978.

(80) Ji, Q.; E.M.E.; van Eldik, R.; Johnston, K. P.; Goates, S. R.; Lee, M. L. *J.Phys.Chem.* **1995**, *99*, 13461.

(81) *CRC Handbook of Chemistry and Physics*; 78th. ed.; CRC Press: Boca Raton, 1997.

# Chapter 3: Optimization Models for Determining Nitric Acid Equilibria in Supercritical Water †

## 3.1 Introduction

Nitrogen chemistry involving $HNO_3$, $HNO_2$, $NO_2$, and other $NO_x$ species has been studied extensively at low temperatures in the gas phase and in liquid phases [1-4]. This chemistry is important in the fields of combustion and pollution prevention due to the harmful nature of $NO_x$ compounds [5-8]. Hydrothermal oxidation (HO), or supercritical water oxidation (SCWO), [9,10] produces less $NO_x$ species than incineration due to thermodynamic and kinetic arguments [11]. However, studies of nitrogen chemistry in SCW are rare due to high pressures, temperatures, and corrosion of reaction vessels. The dissociation constant of $HNO_3$ has been studied by Raman spectroscopy up to 250 °C [12], by heats of dilution up to 319 °C [13], and indirectly from solubilities of calcium sulfate up to 350 °C [14] and magnesium sulfate up to 370 °C [15].

Chemical equilibria may be measured quantitatively in SCW by UV-Vis spectroscopy. A series of relatively stable pH indicators has been developed to measure the pH in SCW and study acid-base chemistry [16-20]. However, in the presence of a strong oxidizer like $HNO_3$, these indicators would be unstable. In the case of Cr(VI), acid-base chemistry was studied by directly measuring $HCrO_4^-$ and $CrO_4^{2-}$ bands [21].

---

† The contents of this chapter appear in *Comput. Chem.* **1999**, 23, 421-434.

Optimization techniques have been widely used to estimate equilibrium concentrations, equilibrium constants, and extinction coefficients in chemical and phase equilibrium problems [22,23]. Several papers focus on accurately determining the equilibrium concentrations and ensuring convergence of chemical and phase equilibrium optimization problems [24-29]. Lingane and Hugus have determined extinction coefficients and formation constants of iron(II)—iron(III)—chloride systems in DMSO as well as mercury(II)—iodide systems in DMSO [30]. Roman and Gonzalez have studied kinetics of triphenyltetrazolium chloride by absorption spectroscopy determining the extinction coefficients and concentrations to obtain the rate constant [31]. Garcia *et al.* used spectrophotometric data to determine extinction coefficients and protonation constants of p-nitroaniline, 4-(2-phyridylazo)-resorcinol and salycilic acid [32]. D'Angelo and Collette have devised a method to determine the site-specific tautomeric and zwitterionic microspecies equilibrium constants [33]. At high temperatures, Seward and coworkers have determined the equilibrium constants in the formation of lead(II) chloride complexes up to 300 °C [34], manganese(II) chloride complexes up to 300 °C [35], and iron(II) chloride complexes up to 200 °C [36].

In Section 3.2 of this paper, we formulate an optimization model that describes the equilibrium of nitrogen chemistry in SCW, and show how it can be used to compute least squares estimates of unknown equilibrium constants and extinction coefficients by using UV-Vis spectroscopic measurements obtained in Chapter 2. The present work focuses on the development and results of this optimization model, which was described only briefly in Chapter 2. Section 3.3 discusses the optimizer used, a generalized reduced gradient (GRG) algorithm that is capable of solving large problems, the FORTRAN implementation of the model, a statistical Jackknife implementation of the model, and implementation of the model in the algebraic modeling language GAMS [37]. GAMS and similar languages like AMPL [38] are readily available, and are convenient and powerful tools for solving such problems. Section 3.4 describes algorithm performance and how some computational difficulties were overcome. The results obtained from both the FORTRAN implementation and the Jackknife Statistical implementation are described in Section 3.5 with a discussion of the standard error of the equilibrium constants and extinction coefficients. Section 3.6 applies a regression to allow extrapolation to other regimes in supercritical water.

## 3.2 Model Formulation

UV-Vis spectra were measured previously by using varying concentrations of nitric acid, sodium hydroxide, hydrogen peroxide, and sodium nitrate at 380 °C and 400 °C and various pressures as described in Chapter 2. They were then deconvoluted to yield the bands corresponding to $NO_2$ and $HNO_2$.

The absorbance of the $NO_2$ and $HNO_2$ bands at any given wavelength, $\lambda$, can be described by Beer's Law:

$$A_{NO_2}(\lambda) = \varepsilon_{NO_2}(\lambda) \cdot l \cdot m_{NO_2} \qquad (3.1)$$

$$A_{HNO_2}(\lambda) = \varepsilon_{HNO_2}(\lambda) \cdot l \cdot m_{HNO_2} \qquad (3.2)$$

where $A_k$ is the absorbance of the band for species $k$, $\varepsilon_k$ is the extinction coefficient for the band, $l$ is the pathlength of absorbance, and $m_k$ is the molal concentration of species $k$.

The first step in preparing the model was to formulate a set of reactions that describe the spectroscopic results for the decomposition equilibria of nitric acid discussed in Chapter 2. While certain species contained chromophores, several other species were transparent in the UV-Vis region. In Chapter 2, we proposed the following reaction scheme:

$$HNO_3 \leftrightharpoons H^+ + NO_3^- \qquad (3.3)$$

$$2\ HNO_3 \leftrightharpoons H_2O + 2\ NO_2 + \tfrac{1}{2}\ O_2 \qquad (3.4)$$

$$2\ NO_2 + H_2O \leftrightharpoons HNO_3 + HNO_2 \qquad (3.5)$$

$$2\ HNO_2 \leftrightharpoons H_2O + 2\ NO + \tfrac{1}{2}\ O_2 \qquad (3.6)$$

$$2\ NO \leftrightharpoons N_2O + \tfrac{1}{2}\ O_2 \qquad (3.7)$$

$$(Na^+)(NO_3^-) \leftrightharpoons Na^+ + NO_3^- \qquad (3.8)$$

$$H_2O \leftrightharpoons H^+ + OH^- \qquad (3.9)$$

$$NaOH \leftrightharpoons Na^+ + OH^- \qquad (3.10)$$

This set of equilibria is governed by the following equilibrium equations:

$$K_a m_{HNO_3}(i) - m_{H^+}(i) m_{NO_3^-}(i) \gamma_{\pm}^2(i) = 0 \tag{3.11}$$

$$K_4 m_{HNO_3}^2(i) - m_{NO_2}^2(i) m_{O_2}^{1/2}(i) = 0 \tag{3.12}$$

$$K_5 m_{NO_2}^2(i) - m_{HNO_3}(i) m_{HNO_2}(i) = 0 \tag{3.13}$$

$$K_6 m_{HNO_2}^2(i) - m_{NO}^2(i) m_{O_2}^{1/2}(i) = 0 \tag{3.14}$$

$$K_7 m_{NO}^2(i) - m_{N_2O}(i) m_{O_2}^{1/2}(i) = 0 \tag{3.15}$$

$$K_{d,ip} m_{NaNO_3}(i) - m_{Na^+}(i) m_{NO_3^-}(i) \gamma_{\pm}^2 = 0 \tag{3.16}$$

$$K_w - m_{H^+}(i) m_{OH^-}(i) \gamma_{\pm}^2(i) = 0 \tag{3.17}$$

$$K_b m_{NaOH}(i) - m_{Na^+}(i) m_{OH^-}(i) \gamma_{\pm}^2(i) = 0 \tag{3.18}$$

In the above, $K_w$ is the ion product of water given by Marshall and Franck [39] and $K_b$ is the dissociation constant of sodium hydroxide given by Ho and Palmer [40]. All other $K$'s are to be determined by fitting the model to experimental data. $K_a$ is the dissociation constant of nitric acid, and $K_{d,ip}$ is the ion pair $(Na^+)(NO_3^-)$ dissociation constant. The index $i$ represents the experiment number, $m_k(i)$ are the molal concentrations of species $k$ in experiment $i$, and $\gamma_{\pm}(i)$ is the mean ionic activity coefficient in experiment $i$. The subscripts for the equilibrium constants in Equations (3.11)-(3.16) correspond to Reactions (3.3)-(3.8).

In addition to the equilibrium expressions, the model includes a charge balance:

$$m_{Na^+}(i) + m_{H^+}(i) - m_{NO_3^-}(i) - m_{OH^-}(i) = 0 \tag{3.19}$$

a mass balance on sodium:

$$m^o_{NaOH}(i) + m^o_{NaNO_2}(i) - m_{Na^+}(i) - m_{NaOH}(i) - m_{NaNO_3}(i) = 0 \tag{3.20}$$

where $m_k^o$ ($i$) is the initial molal concentration of species $k$ in experiment $i$.

a mass balance on nitrogen:

$$\begin{aligned} & m^o_{HNO_3}(i) + m^o_{NaNO_2}(i) - m_{HNO_3}(i) - m_{NO_3^-}(i) - m_{HNO_2}(i) \\ & - m_{NO_2}(i) - m_{NO}(i) - 2m_{N_2O}(i) - m_{NaNO_3}(i) = 0 \end{aligned} \tag{3.21}$$

and a stoichiometric redox balance on oxygen that can be derived straightforwardly from a stoichiometric table based on feed concentrations, reactant stoichiometries, and the conversions for reactions (3.4)-(3.7):

$$\begin{aligned} & m_{O_2}(i) - \frac{1}{2}\left(m^o_{H_2O_2}(i) - m^o_{NaNO_2}(i) + m_{HNO_2}(i)\right) \\ & - \frac{1}{4}\left(m_{NO_2}(i) + 3m_{NO}(i)\right) - 2m_{N_2O}(i) = 0 \end{aligned} \tag{3.22}$$

Note that the initial concentration of $HNO_2$ is equivalent to the initial concentration of $NaNO_2$ due to it's weak acidity (pKa ≈ 8) and the fact that all the solutions are acidic due to high concentrations of $HNO_3$.

In writing (3.11), and (3.16)-(3.18), we have assumed that individual ionic activity coefficients are not sensitive to specific properties of ions and can be replaced by the mean ionic activity coefficient, $\gamma_{\pm}$, given by Pitzer [41]:

$$\ln \gamma_{\pm}(i) + A_{\varphi}\left[\frac{\sqrt{I(i)}}{1+1.2\sqrt{I(i)}} + \frac{2}{1.2}\ln\left(1+1.2\sqrt{I(i)}\right)\right] = 0 \qquad (3.23)$$

where $A_{\varphi}$ is the Debye-Huckel parameter, and $I(i)$ is the ionic strength given by:

$$I(i) - \frac{1}{2}\left[m_{Na^+}(i) + m_{H^+}(i) + m_{NO_3^-}(i) + m_{OH^-}(i)\right] = 0 \qquad (3.24)$$

In the equations above, the values of the equilibrium constants and concentrations $m_k\,(i)$ can span several orders of magnitude, with the smallest on the order of $10^{-10}$. This poor scaling of the variables makes accurate solution of these equations and estimation of the unknown parameters numerically difficult. As noted by several authors [22,42], this situation is partially remedied by taking the logarithms of both sides of Equations (3.11)-(3.18), and using a new set of variables equal to the logs of the concentrations and equilibrium constants. This eases the variable scaling problems, and (3.11)-(3.18) are linear in the new variables. Defining

$x_k(i) = \log m_k(i)$ if $k$ is a chemical species

$x_e = \log e$ if $e$ is an equilibrium constant, i.e. $e = K_a$

$x_{\gamma\pm}(i) = \log \gamma_{\pm}(i)$

as the logs of the equilibrium constants, concentrations, and mean ionic activity coefficients, the transformed equations are:

$$x_{K_a} + x_{HNO_3}(i) - x_{H^+}(i) - x_{NO_3^-}(i) - 2x_{\gamma_\pm}(i) = 0 \tag{3.25}$$

$$x_{K_4} + 2x_{HNO_3}(i) - 2x_{NO_2}(i) - \frac{1}{2}x_{O_2}(i) = 0 \tag{3.26}$$

$$x_{K_5} + 2x_{NO_2}(i) - x_{HNO_3}(i) - x_{HNO_2}(i) = 0 \tag{3.27}$$

$$x_{K_6} + 2x_{HNO_2}(i) - 2x_{NO}(i) - \frac{1}{2}x_{O_2}(i) = 0 \tag{3.28}$$

$$x_{K_7} + 2x_{NO}(i) - x_{N_2O}(i) - \frac{1}{2}x_{O_2}(i) = 0 \tag{3.29}$$

$$x_{K_{d,ip}} + x_{NaNO_3}(i) - x_{Na^+}(i) - x_{NO_3^-}(i) - 2x_{\gamma_\pm}(i) = 0 \tag{3.30}$$

$$\log K_w - x_{H^+}(i) - x_{OH^-}(i) - 2x_{\gamma_\pm}(i) = 0 \tag{3.31}$$

$$\log K_b + x_{NaOH}(i) - x_{Na^+}(i) - x_{OH^-}(i) - 2x_{\gamma_\pm}(i) = 0 \tag{3.32}$$

the charge balance constraint:

$$10^{x_{Na^+}(i)} + 10^{x_{H^+}(i)} - 10^{x_{NO_3^-}(i)} - 10^{x_{OH^-}(i)} = 0 \tag{3.33}$$

the mass balance on sodium constraint:

$$\begin{aligned} & m^o_{NaOH}(i) + m^o_{NaNO_2}(i) - 10^{x_{Na^+}(i)} \\ & -10^{x_{NaOH}(i)} - 10^{x_{NaNO_3}(i)} = 0 \end{aligned} \tag{3.34}$$

the mass balance on nitrogen constraint:

$$\begin{aligned} &m^o_{HNO_3}(i) + m^o_{NaNO_2}(i) - 10^{x_{HNO_3}(i)} - 10^{x_{NO_3^-}(i)} - 10^{x_{HNO_2}(i)} \\ &-10^{x_{NO_2}(i)} - 10^{x_{NO}(i)} - 2\cdot 10^{x_{N_2O}(i)} - 10^{x_{NaNO_3}(i)} = 0 \end{aligned} \tag{3.35}$$

the stoichiometric redox balance on oxygen constraint:

$$\begin{aligned} &10^{x_{O_2}(i)} - \frac{1}{2}\left(m^o_{H_2O_2}(i) - m^o_{NaNO_2}(i) + 10^{x_{HNO_2}(i)}\right) \\ &-\frac{1}{4}\left(10^{x_{NO_2}(i)} + 3\cdot 10^{x_{NO}(i)}\right) - 2\cdot 10^{x_{N_2O}(i)} = 0 \end{aligned} \tag{3.36}$$

Pitzer's mean ionic activity coefficient constraint:

$$x_{\gamma_\pm}(i) + \frac{A_\varphi}{2.303}\left[\frac{\sqrt{I(i)}}{1+1.2\sqrt{I(i)}} + \frac{2}{1.2}\ln\left(1+1.2\sqrt{I(i)}\right)\right] = 0 \tag{3.37}$$

and the ionic strength constraint:

$$I(i) - \frac{1}{2}\left[10^{x_{Na^+}(i)} + 10^{x_{H^+}(i)} + 10^{x_{NO_3^-}(i)} + 10^{x_{OH^-}(i)}\right] = 0 \tag{3.38}$$

For the $NO_2$ and $HNO_2$ bands, integration of the absorption band (Eq.3.1 and 3.2) for each species over the wavelengths 333-500 nm as described in Chapter 2 yields an integrated absorbance, $S_k$. Rewriting the integrated absorbance in terms of the new variables $x$, the objective function was chosen to be the squared sum of residuals:

$$\begin{aligned} \min\phi = w_1 &\sum_{i=1}^{N}\left(S_{NO_2,measured}(i) - l\cdot 10^{x_{E_{NO_2}} + x_{NO_2}(i)}\right)^2 + \\ w_2 &\sum_{i=1}^{N}\left(S_{HNO_2,measured}(i) - l\cdot 10^{x_{E_{HNO_2}} + x_{HNO_2}(i)}\right)^2 \end{aligned} \tag{3.39}$$

where $w_1$ and $w_2$ are weighting factors to ensure that both the $NO_2$ and $HNO_2$ band have equal importance in determining the optimum ($w_1 = 10$ and $w_2 = 1000$), and $x_{Ek}$ are the logs of the *integrated* extinction coefficients.

The goal of the optimization is to obtain values of the vector, $\theta$, containing the eight variables $K_a$, $K_4$, $K_5$, $K_6$, $K_7$, $K_{d,ip}$, $E_{NO_2}$, and $E_{HNO_2}$ which minimize the objective, $\phi$. However, to do so, the values for all the variables $x_k(i)$, $x_{\gamma\pm}(i)$, and $I(i)$ must be determined. If values are assigned to the above vector, the $x$ and $I$ variables may be determined independently for each experiment $i$ by solving the square system of nonlinear equations (3.25)-(3.38) numerically. The objective (3.39) may then be viewed as a function of the eight primary decision variables, and could be minimized using an unconstrained minimization procedure [34-36]. However, the $x$ and $I$ values determined by this numerical approach would contain considerable numerical error, and would be computed to at best single precision accuracy (7 or 8 significant digits). Virtually all unconstrained minimizers require the gradient of the objective, and this gradient will be approximated by finite differencing, since the objective is an implicit function of the eight primary variables. Since the computed objective is only available to single precision, the gradient estimates will have only half this accuracy, which severely limits the attainable accuracy of the parameter estimates, as well as optimizer speed and reliability.

Thus we have chosen to treat this problem as one of constrained optimization, retaining (3.25)-(3.38) as constraints, rather than using them to eliminate variables. This greatly increases problem size, but leaves it well within the capabilities of available NLP software, such as LSGRG2 [43], CONOPT [44], and MINOS [45]. In this extended form, the problem has $14 \times N$ equality constraints and $(14 \times N + 8)$ variables, where $N$ is the number of experiments. For 45 experiments, this is 630 constraints and 638 variables. One can then compute analytic derivatives of the objective and constraints to full double precision accuracy, or have an algebraic modeling system like GAMS [37] or AMPL [38] compute them automatically. In our experiments, the model was coded both in FORTRAN (with derivatives approximated by finite differencing) and in GAMS. Upper and lower bounds were imposed on all variables, to restrict them to physically meaningful values during the iterations.

## 3.3 Model Implementation

The optimization was carried out on eight data sets (A-H) corresponding to optimizations performed at the different temperatures and pressures. For example, the optimization at 380 °C and 276 bar will correspond to data set A as shown in Table 3.1. Each data set (T, P) included 35-48 experiments with varying initial concentrations of reactants, $m_k^o\ (i)$, divided up into four distinct

Table 3.1. Breakdown of the number of experiments used in optimization.

| Experiment Type | Data Set | | | | | | | | | | | | | | | |
|---|---|---|---|---|---|---|---|---|---|---|---|---|---|---|---|---|
| | A | | B | | C | | D | | E | | F | | G | | H | |
| | °C | bar | °C | bar | °C | bar | °C | bar | °C | bar | °C | bar | °C | bar | °C | bar |
| | 380 | 276 | 380 | 310 | 380 | 345 | 380 | 414 | 400 | 276 | 400 | 310 | 400 | 345 | 400 | 414 |
| Class I | 11 | | 12 | | 12 | | 8 | | 12 | | 12 | | 11 | | 6 | |
| Class II | 15 | | 17 | | 17 | | 14 | | 16 | | 17 | | 15 | | 11 | |
| Class III | 8 | | 8 | | 8 | | 8 | | 8 | | 8 | | 8 | | 8 | |
| Class IV | 11 | | 11 | | 11 | | 11 | | 7 | | 10 | | 10 | | 10 | |
| Total No. Experiment | 45 | | 48 | | 48 | | 41 | | 43 | | 47 | | 44 | | 35 | |
| No. Variables | 638 | | 679 | | 679 | | 581 | | 609 | | 665 | | 623 | | 497 | |
| No. Equations | 630 | | 672 | | 672 | | 574 | | 602 | | 658 | | 616 | | 490 | |

classes of experiments. The first class consisted of pure $HNO_3$ solutions (Class I). In Class II, these solutions were partially neutralized with NaOH to form $NO_3^-$, which was shown to be more stable than $HNO_3$ in Chapter 2. Class III included $H_2O_2$ as an oxidant. Finally, mixtures of $HNO_3$ and $NaNO_2$ were used in Class IV to shift the oxidation states. Due to the difficulty in experimentation, smaller data sets were obtained at higher temperatures and pressures. As mentioned in Chapter 2, basic solutions could result in the presence of $NO_2^-$. Therefore, only experiments that had pH from 2 to 6 were utilized in the optimization. This resulted in optimizations with 497-679 variables and 490-672 constraints. The number of nonzero elements in the Jacobian matrix varied between approximately 1850-2600.

***3.31 FORTRAN Model.*** Our FORTRAN implementation uses a sparsity-exploiting implementation of the GRG algorithm called LSGRG2, described in Smith and Lasdon [43]. The constraints and objective are coded in a user-provided subroutine, and the optimizer is called from a user-coded calling program. This program reads the data on the initial concentrations $m_k^o$ ($i$) and the measured absorbances, computes the right hand sides of the equalities, sets bounds on the variables, sets optimizer tolerances and options, calls the optimizer, and writes output reports on the results. In the function evaluation routine, we account for the fact that some of the experiments involve no initial sodium compounds, so reaction (3.10), $NaOH \leftrightarrows Na^+ + OH^-$ is excluded for these experiments, as is the corresponding equilibrium constraint (3.32) and the sodium mass balance constraint (3.34). The concentrations of $Na^+$, NaOH, and $(Na^+)(NO_3^-)$ are also fixed to zero for these experiments.

***3.32 GAMS Model.*** Although the numerical results of Section 3.51 are generated using the FORTRAN implementation, the model was also coded in the algebraic modeling language GAMS. The additional effort required to do this was not large (3 to 4 man-days), and GAMS allowed us to check our FORTRAN results using two other NLP solvers, MINOS [45] and CONOPT2 [44]. Since GAMS computes analytic derivatives of all problem functions, we hoped we might obtain more accurate results, but solutions obtained by the FORTRAN and GAMS systems on two of the eight data sets were quite similar. GAMS also provides a compact, precise, and understandable representation of the model, and it and similar languages, e.g. AMPL [38] are widely available.

***3.33 Bootstrap and Jackknife Statistical Model.*** As with any numerical procedure for model parameter estimation, it is important to have an understanding of the sensitivity of the parameter estimates to the experimental data used to determine their values. Since this is a constrained nonlinear least squares model, the standard confidence intervals and significance tests associated with linear regression do not apply. To estimate the variability in the parameter estimates, a statistical procedure called the Jackknife [46] was applied based on the FORTRAN implementation.

The Jackknife is actually an approximation of the Bootstrap estimate of bias and the standard error. Both the Bootstrap and the Jackknife are statistical procedures that resample the original data set and allow the determination of how this resampled data set changes the observed parameter estimates, $\theta$, where $\theta$ is the vector of eight model parameters estimated as described above. The Jackknife is a simple technique that takes the original data set and obtains a new sample by eliminating one observation at a time. Let **Y** be the vector of all experimental data at a particular temperature and pressure, and define **Y***(i)* as the vector of experimental data for all experiments *except* the *i*th:

$$\mathbf{Y}(i) = \left(y_1, y_2, \ldots y_{i-1}, y_{i+1}, \ldots y_N\right) \tag{3.40}$$

resulting in *N* new samples. Each of these defines an instance of the optimization model described in Section 3.2, and each was solved using the LSGRG2 FORTRAN optimization routine described above in Section 3.31. The optimal vector of eight parameters associated with the experimental data **Y***(i)* is defined as $\hat{\theta}(i)$. For example, data set A has 45 experiments as seen in Table 3.1. The first Jackknife replication, $\hat{\theta}(1)$, is the optimization solution to experiments 2-45; $\hat{\theta}(2)$ is the optimization solution to experiments 1, 3-45 and so on resulting in 45 replications. The Jackknife estimate of standard error for the *j*th element of $\hat{\theta}(i)$, $\hat{\theta}_j(i)$, can then be defined as [46]:

$$se_j = \left[\frac{N-1}{N}\sum_{i=1}^{N}\left(\hat{\theta}_j(i) - avg_j\right)^2\right]^{1/2} \qquad j = 1,8 \tag{3.41}$$

where

$$avg_j = \sum_{i=1}^{N} \hat{\theta}_j(i) \big/ N \qquad\qquad j = 1,8 \qquad\qquad (3.42)$$

The Jackknife Statistical procedure was used on all eight data sets and showed the effect that a single experimental data point could have on the parameter estimates. The final estimates obtained from the FORTRAN implementation optimizations described in Section 3.31 were used as warm starting points for the Jackknife approach.

## 3.4 Numerical Difficulties and Algorithm Performance

***3.41 FORTRAN Implementation.*** The balance constraints (3.33)-(3.36) and the ionic strength constraint (3.38) are badly scaled because the terms of the form $10^x$ are numerically small (ranging from $10^{-2}$ to $10^{-10}$), as are their derivatives. This causes numerical difficulties for any NLP algorithm (i.e. slow convergence, stopping at an infeasible point, or failure to determine an accurate solution), and also requires that these equations be satisfied to a very tight tolerance. Hence all FORTRAN runs used the LSGRG2 scaling option, which determines row and column scale factors so that the Jacobian matrix at the initial point has nonzero elements, which are close to unity. For example, runs using data set A and no scaling failed, stopping at a substantially infeasible point due to repeated failures of the LSGRG2 Newton sub-algorithm to converge.

Experiments showed that it was best to solve each problem with the default feasibility tolerance of $1\times10^{-4}$, then re-solve it from that solution with a tolerance of $1\times10^{-8}$. This tactic required only one fourth the number of iterations as runs which used $1\times10^{-8}$ throughout, and was also more reliable, eliminating several terminations due to small fractional changes in the objective function or failure by a line search to improve the objective.

In most cases, the optimization stopped at points, which satisfied the Kuhn-Tucker conditions to within the optimality tolerance (default value $1\times10^{-4}$) (see Table 3.2). However, in some instances, a second run, starting from the final point of the previous run, made significant further progress. Since all runs used scale factors computed at their starting point, the final solution of the previous run might not meet the Kuhn-Tucker conditions (to within the specified tolerances) for a scaled problem with sharply different scale factors. To alleviate this problem, the Jacobian was re-scaled every 200 iterations.

Table 3.2 shows LSGRG2 computational effort and reason for termination for 12 typical runs. All calculations were performed on a Digital Semiconductor 500 MHz workstation using the Digital Unix 4.06 Operating System and the Unix 0.5.22 FORTRAN compiler. In the “Experiment” column, “A”, “B”, etc. indicate which of the eight data sets (corresponding to different pressure-temperature combinations described above) was involved. A “1” following that letter (i.e.

Table 3.2. Computational Results of FORTRAN Optimization Implementations.

| | Problem Size | | Reason for | Iterations | Computation |
|---|---|---|---|---|---|
| Experiment | Variables | Constraints | Termination | | Time (sec) |
| A.1 | 679 | 672 | KT | 679 | 221 |
| A.2 | 679 | 672 | KT | 104 | 36 |
| B.1 | 679 | 672 | KT | 715 | 230 |
| B.2 | 679 | 672 | KT | 128 | 43 |
| E.1 | 609 | 602 | LS | 802 | 268 |
| E.2 | 609 | 602 | FC | 148 | 56 |
| E.3 | 609 | 602 | KT | 90 | 33 |
| F.1 | 665 | 658 | FC | 1979 | 603 |
| F.2 | 665 | 658 | KT | 171 | 53 |
| F.3 | 665 | 658 | KT | 166 | 53 |
| G.1 | 623 | 616 | FC | 789 | 217 |
| G.2 | 623 | 616 | KT | 132 | 38 |

| | |
|---|---|
| FC: | Fractional Change in the objective less than $1\times10^{-4}$ for 15 consecutive iterations |
| LS: | Line Search failure after re-scaling the objective |
| KT: | Kuhn-Tucker conditions met within $1\times10^{-4}$ |

A.1) indicates a run on data set "A" with a relatively poor starting point, while a "2" indicates that the starting point was the optimal solution of the previous data set, which is much closer to the final solution. A "3" indicates a run started with the final solution of the "2" run of the same data set. Cold starts (e.g. A.1) required several hundred iterations (> 679) and sometimes did not yield the optimum, stopping due to fractional changes in the objective, line searches which failed to improve the objective, or a Kuhn-Tucker point which later runs showed to be a local but not global optimum. Warm starts (e.g. A.2), however, required significantly fewer iterations (< 171) and obtained an optimum near the previous one. In a few cases, the optimum was determined through three or more optimizations, typically when the optimization terminated due to failed line searches or fractional changes in the objective. Calculation times were under 10 minutes.

For some data sets, runs using several different initial guesses terminated at points with different objective values, where the Kuhn-Tucker conditions were satisfied to within tight tolerances. These are almost surely local optima, since Kuhn-Tucker points that are not local minima are not stable attractors of a GRG algorithm. Typically, the objective values at these local optima differed by approximately 5-10% from the lowest value found. The optimal values for $K_a$, $K_4$, $K_5$, $K_6$, $K_7$, $K_{d,ip}$, $E_{NO_2}$, and $E_{HNO_2}$, at most of these were "out of line" with the corresponding values for the other data sets, since they did not show a smooth and consistent variation with density. Starting at the optimal solution of a "good" previous run mitigated this problem, and produced the results described below.

The optimal objective value was least sensitive to the equilibrium constant $K_{d,ip}$ , and estimates of its optimal value varied widely from one data set to another. Because this equilibrium constant is determined without the direct spectral measurement of any of the species in the reaction, it is subject to larger errors. Furthermore, the concentration of the ion pair only reaches significant values at very high concentrations of NaOH (Class II) or $NaNO_2$ (Class IV). The Class IV experiments had the largest errors, due to the large amount of decomposition products, and the large changes in chemistry that occur (See Chapter 2).

***3.42 Jackknife Statistical Implementation.*** In addition to the problems mentioned above, we encountered further difficulties in obtaining the Jackknife results. Most data sets required tuning of the weighting factors, $w_1$ and $w_2$, changing the optimality tolerance from $10^{-4}$ to $10^{-3}$, and altering the initial feasibility tolerance to $1\times10^{-8}$. In addition, the variable bounds were widened to allow the optimizer to return a wider range of estimates. Often the estimates obtained from the Jackknife had 1-5 vectors, $\hat{\theta}(i)$, that had one or more variables at a boundary. These vectors were removed from the data before the standard error was determined if the values would significantly alter the average. In data sets at higher temperature or lower density (E-H), the warm start values of some equilibrium constants were also altered slightly to yield better replications.

As might be expected, performing multiple optimizations required significant computation time but this was significantly reduced by using warm starts. In addition, without the warm starts, this procedure would probably have failed due to reasons mentioned above (local optima, line search failures, and terminations due to small fractional changes in the objective).

## 3.5 Model Solution

***3.51 FORTRAN Implementation.*** The initial solutions of the data sets were used to observe general trends of the logs of the equilibrium constants with respect to density, which contained some numerical anomalies due to the presence of local optima. Subsequent optimizations refined the boundaries to reflect the expected density trends observed for a majority of the data sets. In cases where smooth trends were already observed, those equilibrium constants were fixed to allow the optimizer to concentrate on other constants. In some cases, tighter bounds were also placed on certain species concentrations that varied significantly from the norm. Typically, the final values for the equilibrium constants were at least half an order of magnitude away from a bound. With the exception of $K_{d,ip}$, whose optimal value was difficult to determine accurately as described above, the differences in the log $K$ were typically small.

Linear extrapolations of log $K_4$ and log $K_5$ to zero density agreed well with the gas phase data and did not require subsequent optimizations to improve the trend with density. The same is true for Reactions (3.6) and (3.7) at 380 °C. However, the extrapolations were less satisfactory at 400 °C. Reactions (3.4) and (3.5) include $NO_2$ directly. Due to the large concentration and large peak area of $NO_2$, smooth plots for these reactions are observed, consistent with gas phase data. Reaction (3.6) contains only one species that is directly measured ($HNO_2$), but neither $NO_2$ nor $HNO_2$ appear in Reaction (3.7). In addition, due to the reduction of nitrogen species, the concentration of $HNO_2$ decreases with increasing temperature and decreasing density resulting in very small concentrations at 400 °C (not shown). Because $K_6$ appeared to be under-predicted and $K_7$ appeared be over-predicted, we imposed tighter bounds on the concentration of NO at higher temperatures, but only achieved slight improvement.

The extinction coefficients versus wavelength for $NO_2$ and $HNO_2$ are plotted in Figures 3.1 and 3.2, respectively. These extinction coefficients were determined by using the absorbance of the individual bands obtained from deconvolution and their concentrations determined by this optimization. The extinction coefficient for $NO_2$ at 380 °C and 276 bar (data set A) resembles that at room temperature in the gas phase [47-50] with the exception of the fine structure

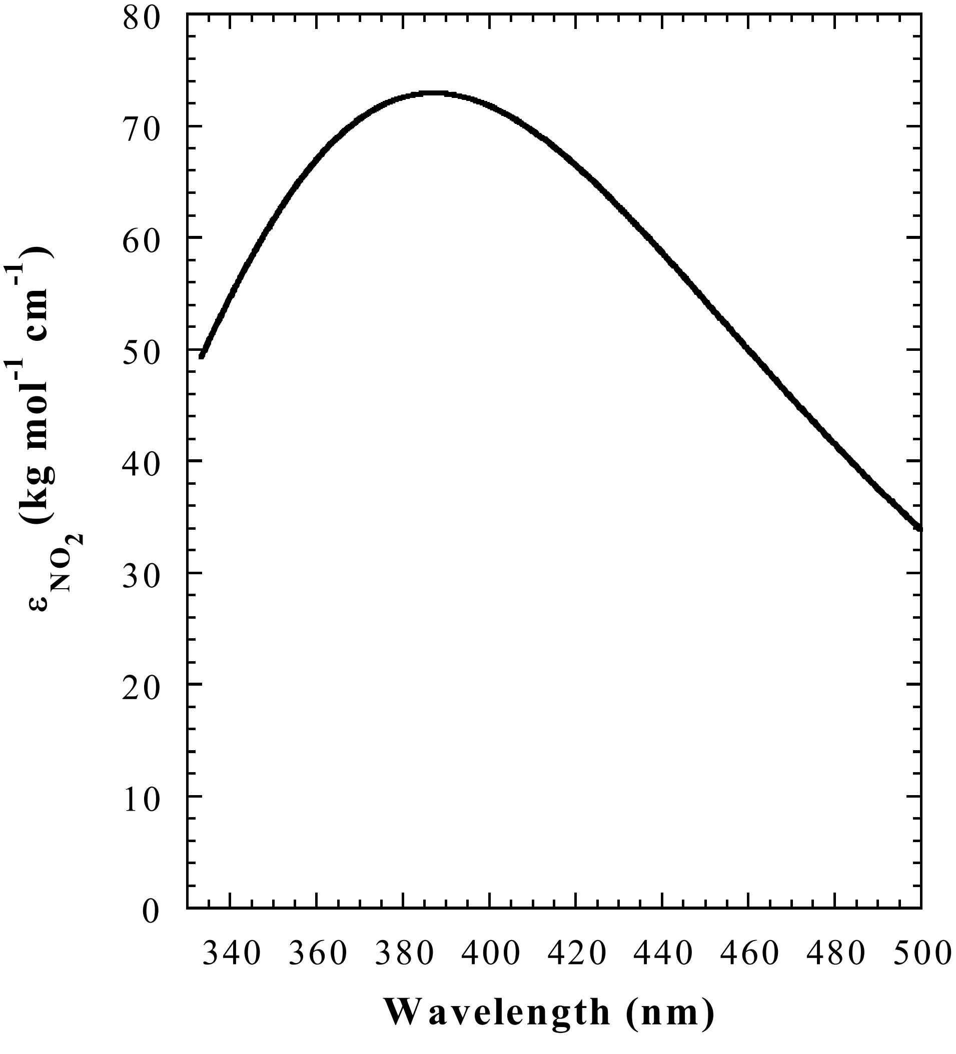

Fig. 3.1. Molal extinction coefficient for $NO_2$ determined by using the results from deconvolution and optimization at 380°C and 276 bar.

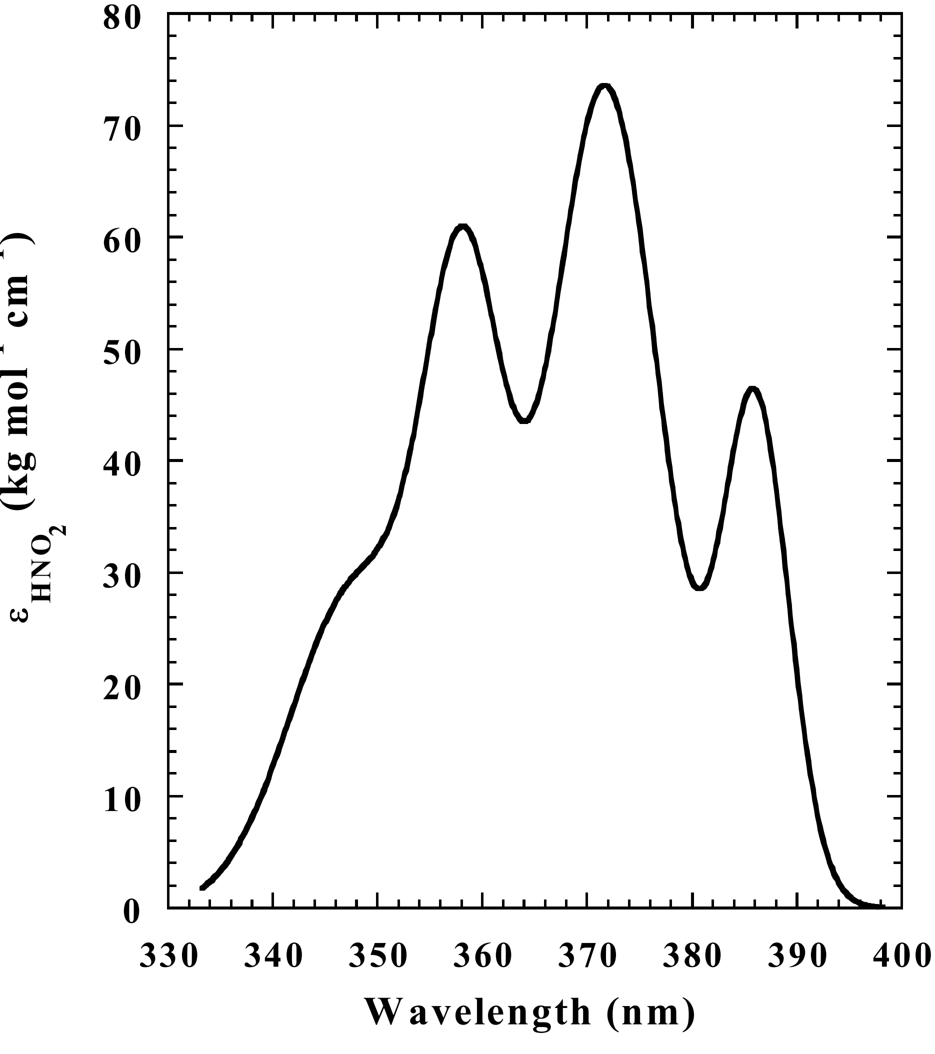

Fig. 3.2. Molal extinction coefficient for $HNO_2$ determined by using the results from deconvolution and optimization at 380°C and 276 bar.

observed for the gas phase. At the maximum peak height of 385 nm, the value for the extinction coefficient of approximately 73 kg mol$^{-1}$ cm$^{-1}$ is smaller than the room temperature gas phase value of 150-170 kg mol$^{-1}$ cm$^{-1}$ [47-50]. A similar net decrease in this extinction coefficient of approximately 50% was previously observed in gas phase results by Mihalcea *et al.* from a temperature of 25 °C to 250 °C [50].

The extinction coefficient for $HNO_2$ at 380 °C and 276 bar (data set A) also resembles that at room temperature [51-54], except that the weakest band was not observed in our deconvolution technique. Due to the weak $\varepsilon$ and low concentration of $HNO_2$, it was difficult to estimate an *integrated* extinction coefficient for this species. In nearly all cases, the optimization gave a value that rested on the chosen boundaries. Only in data set A was the optimization able to obtain a value strictly within these bounds. A desirable result was that attempts to optimize the data without the use of the $HNO_2$ band offered solutions to the equilibria, but without consistent trends with density (not shown). Also, the optimized molal extinction coefficient of $HNO_2$ was approximately 15,000 kg mol$^{-1}$ cm$^{-1}$, a physically unrealistic result [51,54]. Clearly, the $HNO_2$ band should be included and the extinction coefficient of data set A was chosen to be constant in data sets B-H.

***3.52 Jackknife Statistical Implementation.*** The results of the Jackknife Statistical Optimization were dependent on reasonably accurate results of the

FORTRAN implementation in Section 3.51 and are given in Figures 3.3-3.9 and in Table 3.3. An asymmetric confidence interval can be constructed using the bootstrap-*t* interval method with a 95% confidence interval [46]. As can be seen in Table 3.4, the Jackknife average is often close to the FORTRAN optimization. However, it can differ from the computed estimate, $\theta$, significantly as in data sets E and F, where $K_6$ changes by more than an order of magnitude. The most prominent improvements from the Jackknife Statistical Optimization approach have been the increase in the number of data sets that follow consistent trends with density. These changes can be seen for the logs of the equilibrium constants $K_6$ and $K_7$ in Figures 3.7-3.8 and in Table 3.4. As mentioned in Section 3.51, $K_6$ and $K_7$ at 400°C appeared to have been under-estimated and over-estimated, respectively. The results from the Jackknife procedure seem to support this argument.

Figures 3.3 and 3.4 show the effect of water density on the dissociation constant of nitric acid and the dissociation of the ion pair $(Na^+)(NO_3^-)$, respectively. As expected for a strong acid, $K_a$ decreases with decreasing density. This decrease is due to the exothermic character of the reaction as well as the isobaric decrease of the dielectric constant, which favors the associated species, $HNO_3$. It can be expected that the results for $K_a$ will have more error associated with them than for $K_4$ and $K_5$, as seen in data sets A and F in Figure 3.3, since

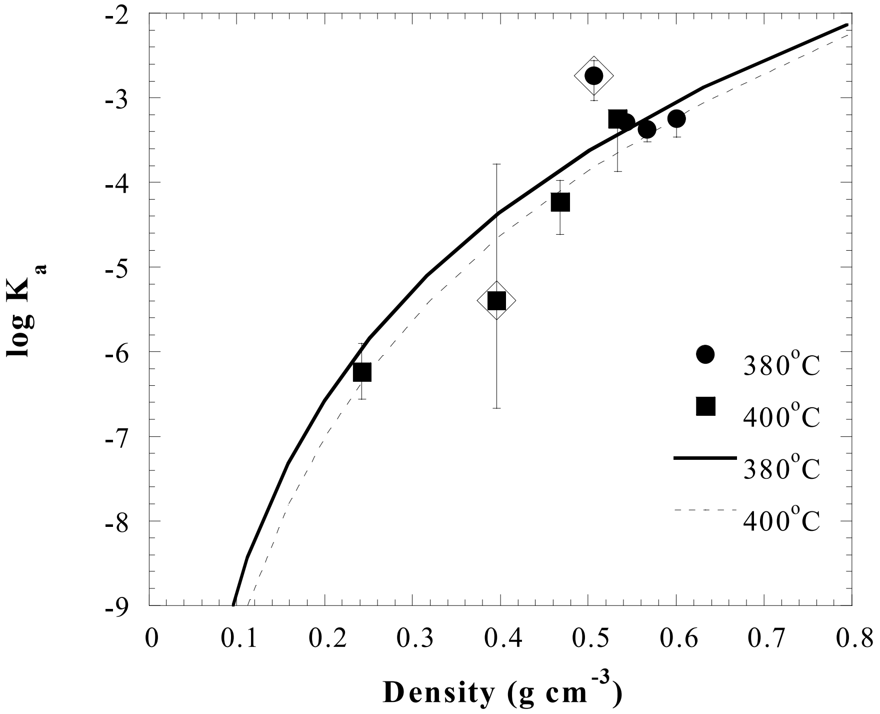

Fig. 3.3. Jackknife Statistical Optimization estimates of the dissociation constant of nitric acid in supercritical water at 380 °C (●) and 400 °C (■). The lines are regressed with Equation (3.43) at 380 °C and 400 °C. Those data sets that were excluded in the regression are denoted by (◇).

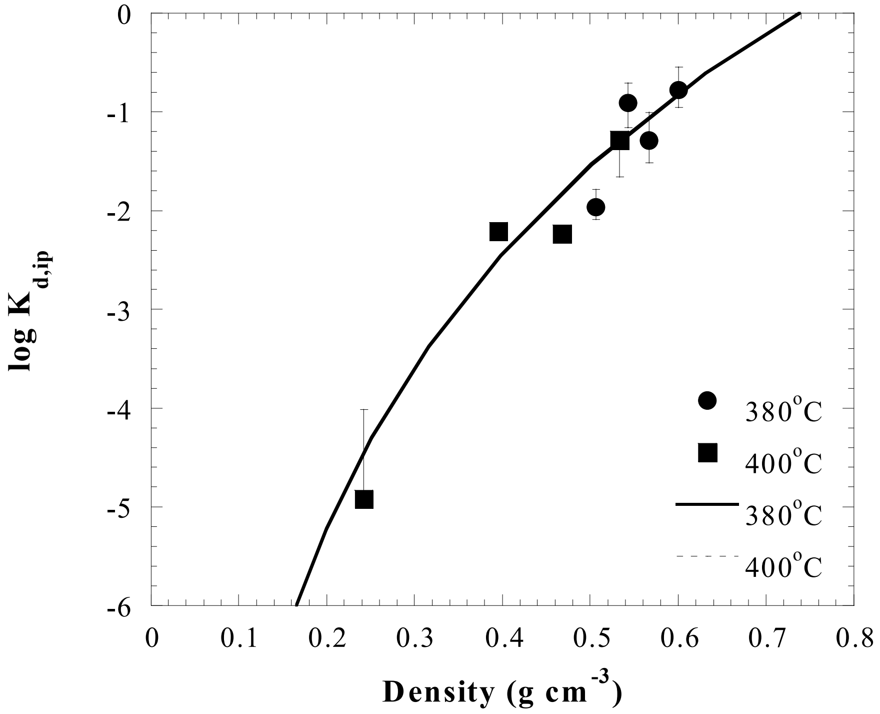

Fig. 3.4. Jackknife Statistical Optimization estimates of the dissociation constant of the solvent separated ion pair $(Na^+)(NO_3^-)$ in supercritical water at 380 °C (●) and 400 °C (■). The lines are regressed with Equation (3.43) at 380 °C and 400 °C.

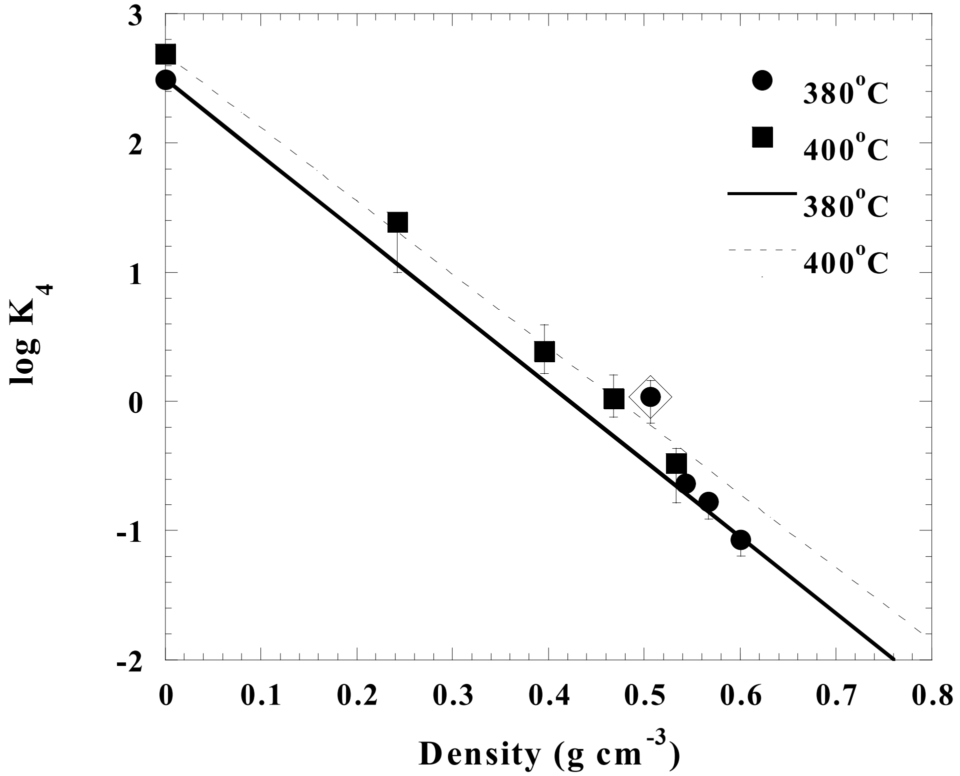

Fig. 3.5. Jackknife Statistical Optimization estimates of the equilibrium constant of Reaction (3.4) in supercritical water at 380 °C (●) and 400 °C (■). For comparison, gas phase data calculated from the JANAF Thermochemical Tables [55] are also presented. The lines are regressed with Equation (3.45) at 380 °C and 400 °C. Those data sets that were excluded in the regression are denoted by (◇).

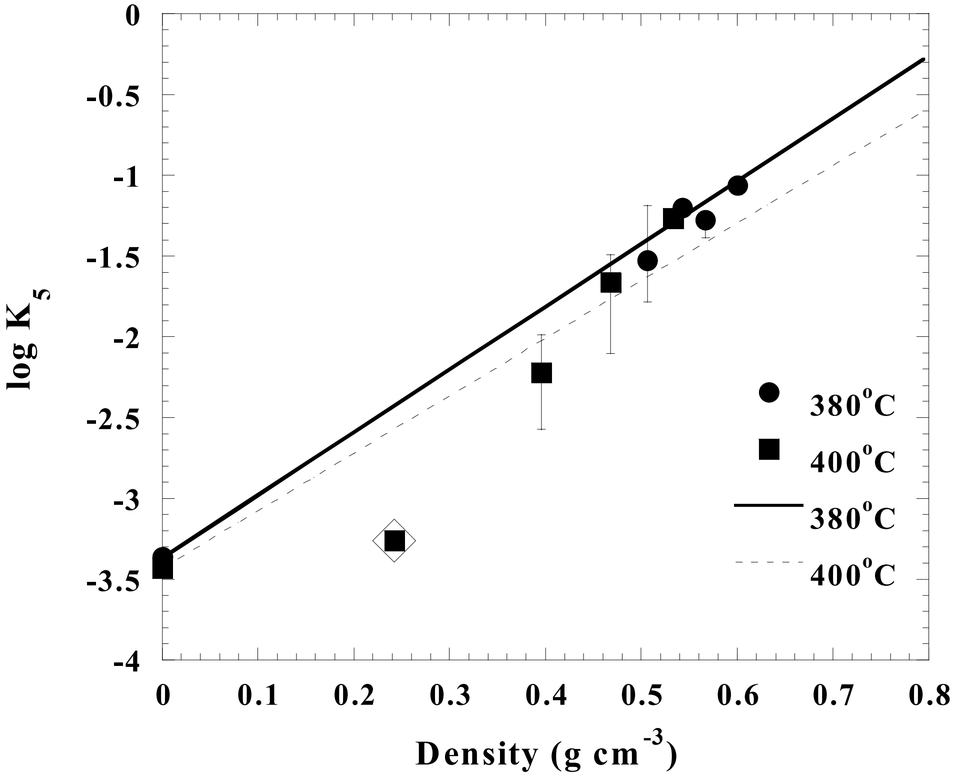

Fig. 3.6. Jackknife Statistical Optimization estimates of the equilibrium constant of Reaction (3.5) in supercritical water at 380 °C (●) and 400 °C (■). For comparison, gas phase data calculated from the JANAF Thermochemical Tables [55] are also presented. The lines are regressed with Equation (3.45) at 380 °C and 400 °C. Those data sets that were excluded in the regression are denoted by (◇).

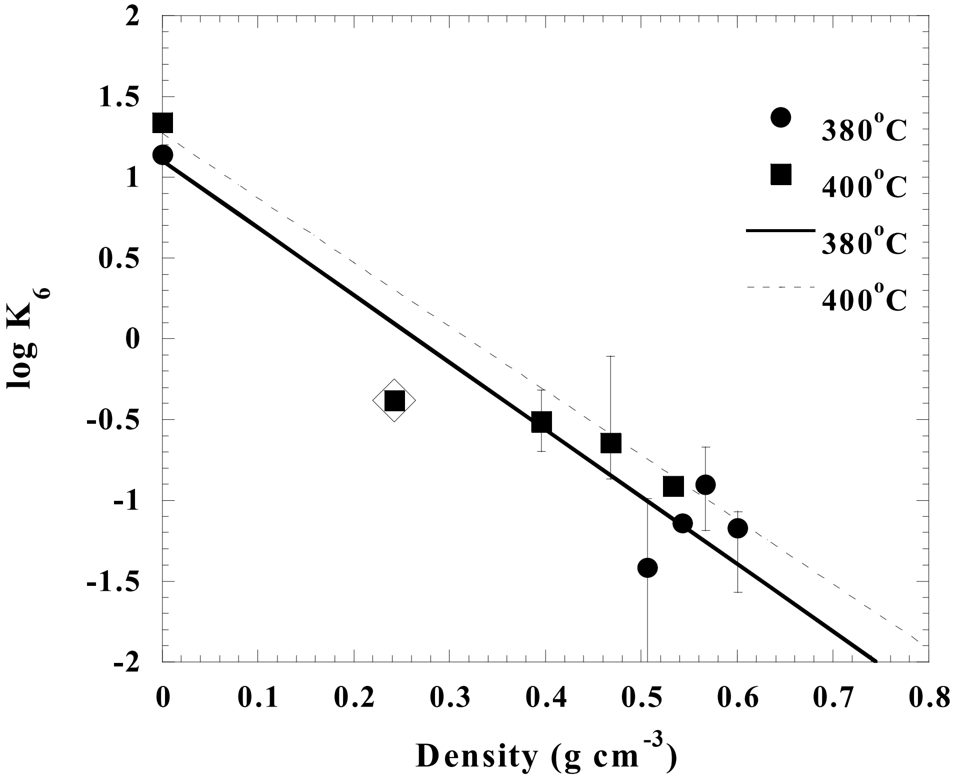

Fig. 3.7. Jackknife Statistical Optimization estimates of the equilibrium constant of Reaction (3.6) in supercritical water at 380 °C (●) and 400 °C (■). For comparison, gas phase data calculated from the JANAF Thermochemical Tables [55] are also presented. The lines are regressed with Equation (3.45) at 380 °C and 400 °C. Those data sets that were excluded in the regression are denoted by (◇).

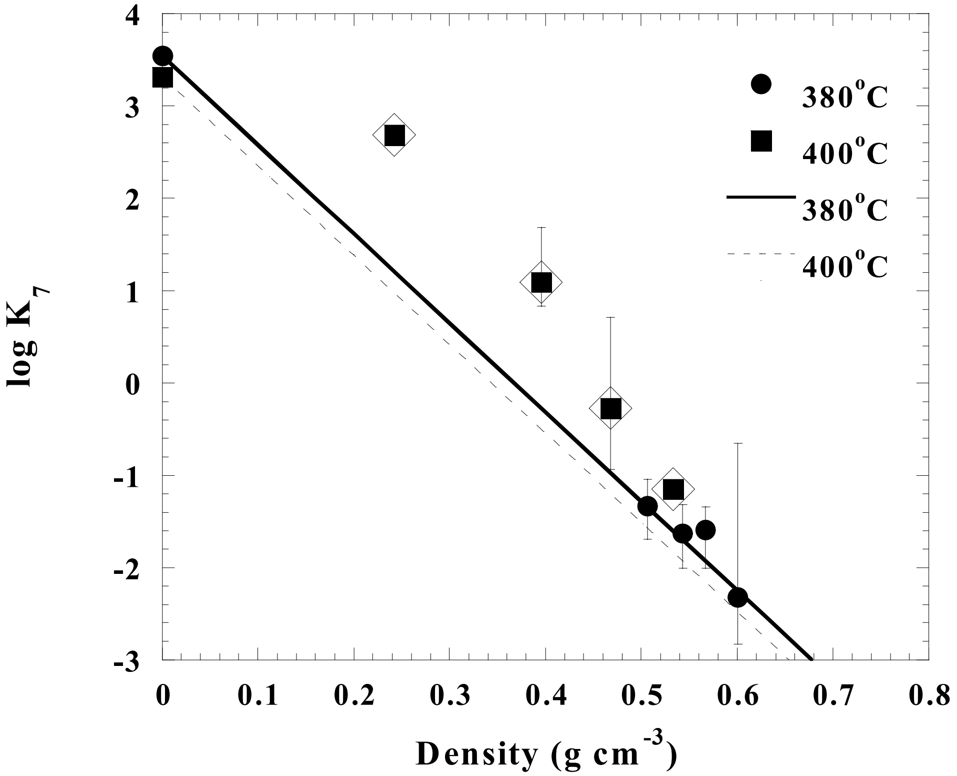

Fig. 3.8. Jackknife Statistical Optimization estimates of the equilibrium constant of Reaction (3.7) in supercritical water at 380 °C (●) and 400 °C (■). For comparison, gas phase data calculated from the JANAF Thermochemical Tables [55] are also presented. The lines are regressed with Equation (3.45) at 380 °C and 400 °C. Those data sets that were excluded in the regression are denoted by (◇).

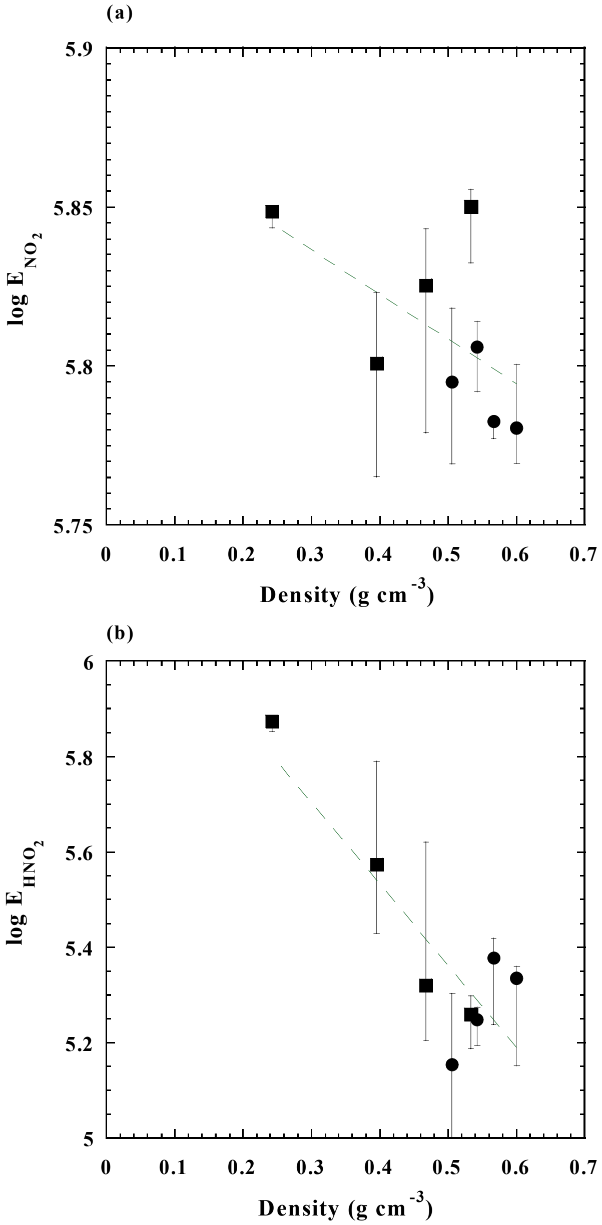

Fig. 3.9. Effect of density on the *integrated* molal extinction coefficient of (a) $NO_2$ between 333-500 nm and (b) $HNO_2$ between 333-400 nm at 380 °C (●) and 400 °C (■). The error bars are determined using the Jackknife Statistical Optimization.

Table 3.3. Averages and asymmetric confidence intervals determined by the Jackknife Statistical procedure using the bootstrap-*t* interval method.

| Data Set | log $K_a$ | log $K_4$ | log $K_5$ | log $K_6$ | log $K_7$ | log $K_{d,ip}$ | log $E_{NO2}$ | log $E_{HNO2}$ |
|---|---|---|---|---|---|---|---|---|
| | -2.741 | 0.038 | -1.526 | -1.417 | -1.333 | -1.333 | 5.795 | 5.154 |
| A | -0.29 | -0.20 | -0.26 | -0.80 | -0.36 | -0.12 | -0.03 | -0.33 |
| | +0.18 | +0.12 | +0.34 | +0.43 | +0.29 | +0.18 | +0.02 | +0.15 |
| | -3.288 | -0.637 | -1.201 | -1.141 | -1.628 | -0.911 | 5.806 | 5.247 |
| B | -0.07 | -0.04 | -0.04 | -0.04 | -0.37 | -0.25 | -0.01 | -0.05 |
| | +0.08 | +0.03 | +0.02 | +0.02 | +0.31 | +0.20 | +0.01 | +0.03 |
| | -3.377 | -0.775 | -1.277 | -0.902 | -1.592 | -1.290 | 5.782 | 5.378 |
| C | -0.15 | -0.14 | -0.11 | -0.28 | -0.42 | -0.23 | -0.01 | -0.14 |
| | +0.05 | +0.02 | +0.05 | +0.23 | +0.25 | +0.29 | +0.00 | +0.04 |
| | -3.249 | -1.068 | -1.062 | -1.170 | -2.324 | -0.780 | 5.781 | 5.334 |
| D | -0.22 | -0.13 | -0.06 | -0.40 | -0.51 | -0.18 | -0.01 | -0.18 |
| | +0.04 | +0.03 | +0.04 | +0.10 | +1.68 | +0.23 | +0.02 | +0.03 |
| | -6.241 | 1.388 | -3.263 | -0.381 | 2.691 | -4.492 | 5.849 | 5.873 |
| E | -0.32 | -0.39 | -0.03 | -0.02 | -0.04 | -0.47 | -0.01 | -0.02 |
| | +0.34 | +0.05 | +0.00 | +0.01 | +0.00 | +0.48 | +0.00 | +0.00 |
| | -5.392 | 0.392 | -2.219 | -0.510 | 1.093 | -2.211 | 5.801 | 5.573 |
| F | -1.28 | -0.17 | -0.36 | -0.19 | -0.26 | -0.01 | -0.04 | -0.14 |
| | +1.61 | +0.20 | +0.23 | +0.19 | +0.59 | +0.00 | +0.02 | +0.22 |
| | -4.232 | 0.025 | -1.663 | -0.642 | -0.273 | -2.235 | 5.825 | 5.319 |
| G | -0.38 | -0.15 | -0.44 | -0.22 | -0.66 | -0.01 | -0.05 | -0.11 |
| | +0.26 | +0.18 | +0.17 | +0.53 | +0.99 | +0.01 | +0.02 | +0.30 |
| | -3.248 | -0.478 | -1.264 | -0.914 | -1.146 | -1.288 | 5.850 | 5.260 |
| H | -0.62 | -0.31 | -0.02 | -0.05 | -0.08 | -0.37 | -0.02 | -0.07 |
| | +0.03 | +0.11 | +0.02 | +0.05 | +0.00 | +0.01 | +0.01 | +0.04 |

Table 3.4. $\Delta \log K_i$ between FORTRAN Optimization and Jackknife Statistical Optimization [a].

| Data Set | $\Delta \log K_a$ | $\Delta \log K_4$ | $\Delta \log K_5$ | $\Delta \log K_6$ | $\Delta \log K_7$ | $\Delta \log K_{d,ip}$ |
|---|---|---|---|---|---|---|
| A | 0.04 | 0.01 | 0.01 | -0.07 | -0.21 | 0.53 |
| B | -0.10 | -0.03 | -0.06 | 0.24 | -0.50 | 0.42 |
| C | -0.20 | -0.05 | -0.19 | 0.60 | 0.30 | 1.02 |
| D | -0.19 | -0.03 | -0.17 | 0.50 | -1.04 | 1.46 |
| E | -0.70 | -0.18 | -0.61 | — | -0.13 | -0.89 |
| F | -1.06 | -0.15 | -0.35 | 1.15 | -0.74 | 0.00 |
| G | -0.77 | -0.19 | -0.06 | 0.59 | -0.90 | -0.03 |
| H | -0.78 | -0.31 | 0.00 | 0.01 | 0.07 | -0.06 |

[a] $\Delta \log K_i = \log K_{\text{Jackknife}} - \log K_{\text{FORTRAN}}$

$HNO_3$, $H^+$, and $NO_3^-$ are not measured spectroscopically. However, our results have been shown to agree well with the data of Marshall and Slusher [15] at 325 °C, 350 °C, 360 °C, and 370 °C at saturated pressures (See Chapter 2). Likewise, the decrease in $K_{d,ip}$ with decreasing density represents the increased ion pairing expected in low dielectric media. The data for this ion pair agree well with similar ion pairs in supercritical water, NaOH, NaCl, KOH, and KCl [40,56,57], as shown previously in Chapter 2.

Figures 3.5-3.8 represent non-ionic reactions that are expected to have smaller density effects than the ionic reactions discussed above. The most important effect is likely due to the solvation of polar species like $HNO_3$ and $NO_2$ (See Chapter 2). By analysis of Figures 3.3-3.9, it can be seen that some values have significant error bars determined from the bootstrap-*t* interval method, whereas others have very little. In addition, some of the error bars are asymmetric and heavily skewed in one direction, i.e. log $K_{d,ip}$ for data set E (Fig.3.4). Those values with large error bars are associated with an objective function for the data set that is relatively insensitive to the particular equilibrium constant. In other words, large changes in this equilibrium constant have only a small effect on the objective function, because the other equilibrium constants hold more "weight" in this particular optimization. The skewed values indicate that the deviations were in a particular direction, typically in a direction that corresponds to the trend shown by the other data sets. It should be pointed out that this method does not show all the error associated with the experimental and optimization procedures. For example, the error for log $K_5$ in data set E appears to be significant with regards to the regression applied in Section 6 described below, but minimal error due to the optimization. This does not necessarily imply that this is the correct value for the equilibrium constant but that it is the correct value determined by the optimization.

Figure 3.9 shows that the *integrated* extinction coefficients of (a) $NO_2$ and (b) $HNO_2$ decrease slightly with density. This trend was not noticeable with the FORTRAN Optimization technique, since values were obtained for only one data set. However, the Jackknife Statistical Optimization offered substantial improvement in that values could be optimized for all data sets.

### 3.6 Regression of Equilibrium Constants

The equation of Marshall and Frank [39] has been used previously for fitting experimental dissociation constants [16,18,40,56,57]:

$$\log K = a + bT^{-1} + cT^{-2} + dT^{-3} + k \log \rho \qquad (3.43)$$

where

$$k = e + fT^{-1} + gT^{-2} \qquad (3.44)$$

Using the final solution sets obtained from the Jackknife estimates, and the data from Marshall and Slusher [15] at saturated conditions, the parameters for $K_a$, and $K_{d,ip}$, were obtained by nonlinear regression and are given in Table 3.5. These parameters were used to obtain the log $K$ at various densities and are plotted in Figures 3.3 and 3.4 for the isotherms at 380 °C and 400 °C. For $K_{d,ip}$, the temperature effect is very small, and a single regression fits both temperatures (Fig. 3.4).

For the non-ionic reactions given in Reactions (3.4)-(3.7), Equation (3.44) cannot be used due to the asymptote caused by log $\rho$ at zero density. Therefore, Equation (3.44) was modified to account for the apparent linearity observed for these reactions with density:

$$\log K = a + bT^{-1} + cT^{-2} + dT^{-3} + k\rho \tag{3.45}$$

where $k$ is given by Equation (3.45). The solution sets determined through the Jackknife Statistical Optimization (with noted exceptions in Table 3.5) as well as the gas phase data at 300 °C, 350 °C, 380 °C, 400 °C, and 425 °C were used to determine the regression parameters for these equilibrium constants. The isotherms at 380 °C and 400 °C are plotted in Figures 3.5-3.8 and agree excellently with the optimization values. For the equilibrium constant $K_7$, the values at 400 °C should have been lower than those at 380 °C based on the gas phase data, therefore, data sets E-H were removed.

Table 3.5. Parameters [a] for Equilibrium Constants in Equations (3.43) [b] and (3.45) [c].

| | log $K_a$ [b] | log $K_{d,ip}$ [b] | log $K_4$ [c] | log $K_5$ [c] | log $K_6$ [c] | log $K_7$ [c] |
|---|---|---|---|---|---|---|
| $a$ | -3.74 | 1.24 | 9.06 | -5.53 | 6.75 | -4.14 |
| $b$ | 1529.7 | — | -4291.1 | 1412.8 | -3691.0 | 5018.9 |
| $e$ | 25.07 | 9.24 | 1.69 | -7.02 | 1.80 | -9.66 |
| $f$ | -11538.7 | — | -4960.9 | 7124.0 | -3897.4 | — |
| Data Sets Removed | A,F | — | A | E | E | E-H |

[a] Parameters $c$, $d$, and $g$ were determined to be zero in all cases

## 3.7 Conclusions

Nitrogen oxide chemical equilibria can be modeled in supercritical water through the use of general-purpose nonlinear programming algorithms. Six equilibrium constants and two extinction coefficients were optimized accurately with direct spectroscopic measurement of only two of the twelve species. The best results were obtained in cases where a species that appears directly in a given reaction had a significant absorbance, as in the case of the $NO_2$ band and equilibrium constants $K_4$ and $K_5$. However, the inclusion of a small absorbance of another species, $HNO_2$, can offer additional valuable input for the determination of other equilibrium constants ($K_6$, $K_7$, $K_a$, $K_{d,ip}$).

The Jackknife Statistical method offers insight into the effect that a single data set has on the estimated parameter values. In many cases, it resulted in an average log $K$ that more closely resembled the expected values from the trends observed with water density. As expected, those equilibrium constants that were directly tied to experimental absorbances had the smallest error bars. This procedure also allowed determination of the *integrated* extinction coefficient of $HNO_2$ for all data sets, which could not be determined accurately with the optimization based on the FORTRAN implementation. However, the solutions to those optimizations greatly aided in the accurate solution of the Jackknife Statistical Optimizations.

## 3.8 References

(1) Wendel, M. M.; Pigford, R. L. *A.I.Ch.E. Journal* **1958**, *4*, 249.

(2) England, C.; Corcoran, W. H. *Ind.Eng.Chem., Fundam.* **1974**, *13*, 373.

(3) Kaiser, E. W.; Wu, C. H. *J.Phys.Chem.* **1977**, *81*, 187.

(4) Kaiser, E. W.; Wu, C. H. *J.Phys.Chem.* **1977**, *81*, 1701.

(5) Miller, J. A.; Bowman, C. T. *Prog.Energy Combust.Sci.* **1989**, *15*, 287.

(6) Odenbrand, C. U. I.; Andersson, L. A. H.; Brandin, J. G. M.; Lundin, S. T. *Appl.Catalysis* **1986**, *27*, 363.

(7) Kiovsky, J. R.; Koradia, P. B.; Lim, C. T. *Ind.Eng.Chem.Prod.Res.Dev.* **1980**, *19*, 218.

(8) Kato, A.; Matsuda, S.; Kamo, T.; Nakajima, F.; Kuroda, H.; Narita, T. *J.Phys.Chem.* **1981**, *85*, 4099.

(9) Tester, J. W.; Holgate, H. R.; Armellini, F. J.; Webley, P. A.; Killilea, W. R.; Hong, G. T.; Barner, H. E. *Supercritical Water Oxidation Technology: A Review of Process Development and Fundamental Research*; Tedder, D. W. and Pohland, F. G., Ed.; Am. Chem. Soc.: Washington, 1993; Vol. 518, pp 35-76.

(10) Gloyna, E. F.; Li, L. *Waste Manage.* **1993**, *13*, 379.

(11) Killilea, W. R.; Swallow, K. C.; Hong, G. T. In *2nd International Symposium on Supercritical Fluids*; Department of Chemical Engineering, Johns Hopkins University: Boston, MA, 1991; p 173-176.

(12) Ratcliffe, C. I.; Irish, D. E. *Can.J.Chem.* **1985**, *63*, 3521.

(13) Oscarson, J. L.; Gillespie, S. E.; Izatt, R. M.; Chen, X.; Pando, C. *J.Solution Chem.* **1992**, *21*, 789-801.

(14) Marshall, W. L.; Slusher, R. *J.inorg.nucl.Chem.* **1975**, *37*, 1191.

(15) Marshall, W. L.; Slusher, R. *J.inorg.nucl.Chem.* **1975**, *37*, 2165.

(16) Xiang, T.; Johnston, K. P. *J.Phys.Chem.* **1994**, *98*, 7915.

(17) Xiang, T.; Johnston, K. P.; Wofford, W. T.; Gloyna, E. F. *Ind.Eng.Chem.Res.* **1996**, *35*, 4788.

(18) Xiang, T.; Johnston, K. P. *J.Solution Chem.* **1997**, *26*, 13.

(19) Ryan, E. T.; Xiang, T.; Johnston, K. P.; Fox, M. A. *J.Phys.Chem. A* **1997**, *101*, 1827.

(20) Shin, T. W.; Kim, K.; Lee, I.-J. *J.Solution.Chem.* **1997**, *26*, 379.

(21) Chlistunoff, J. B.; Johnston, K. P. *J.Phys.Chem. B* **1998**, *102*, 3993.

(22) Smith, W. R.; Missen, R. W. *Chemical Reaction Equilibrium Analysis: Theory and Algorithms*; John Wiley & Sons, Inc.: New York, 1982.

(23) Inczedy, J. *Analytical Applications of Complex Equilibria*; John Wiley & Sons: New York, 1976.

(24) Shapiro, N. Z.; Shapley, L. S. *J. Soc. Indust. Appl. Math.* **1965**, *13*, 353.

(25) Clasen, R. J. *Operations Research* **1984**, *32*, 70.

(26) Myers, A. K.; Myers, A. L. *J. Chem. Phys.* **1986**, *84*, 5787.

(27) Song, W.; Larson, M. *Chemical Engineering Science* **1991**, *46*, 2513.

(28) Jiang, Y.; Smith, W. R.; Chapman, G. R. *SIAM J. Optimization* **1995**, *5*, 813.

(29) McDonald, C. M.; Floudas, C. A. *Computers chem. Engng* **1995**, *19*, 1111.

(30) Lingane, P. J.; Hugus, Z. Z. *Inorganic Chem.* **1970**, *9*, 757.

(31) Roman, E. S.; Gonzalez, M. C. *J. Phys. Chem.* **1989**, *93*, 3532.

(32) Garcia, M. C.; Ramis, G.; Mongay, C. *Spectrochimica Acta* **1982**, *38A*, 1005.

(33) D'Angelo, J. C.; Collette, T. W. *Anal. Chem.* **1997**, *69*, 1642.

(34) Seward, T. M. *Geochim.Cosmochim.Acta* **1984**, *48*, 121.

(35) Gammons, C. H.; Seward, T. M. *Geochim.Cosmochim.Acta* **1996**, *60*, 4295.

(36) Heinrich, C. A.; Seward, T. M. *Geochim.Cosmochim.Acta* **1990**, *54*, 2207.

(37) Brooke, A.; Kendrich, D.; Meeraus, A. *GAMS: A User's Guide*; Boyd and Fraser: Danvers, MA, 1992.

(38) Fourer, R.; Gay, G.; Kernighan, B. *AMPL: A Modeling Language for Mathematical Programming*; Boyd and Fraser: Danvers, MA, 1993.

(39) Marshall, W. L.; Franck, E. U. *J.Phys.Chem.Ref.Data* **1981**, *10*, 1.

(40) Ho, P. C.; Palmer, D. A. *J.Solution Chem.* **1996**, *25*, 711.

(41) Pitzer, K. S. *Ion Interaction Approach. Theory and Data Correlation*, 1991, pp 75-153.

(42) Liebman, J.; Lasdon, L.; Schrage, L.; Warren, A. *Modeling and Optimization with GINO*; Scientific Press: Palo Alto, CA, 1986.

(43) Smith, S.; Lasdon, L. *Journal on Computing* **1992**, *4*, 1.

(44) Drud, A. *Journal on Computing* **1992**, *6*, 207.

(45) Murtagh, B. A.; Saunders, M. A. *Mathematical Programming Study* **1982**, *16*, 84.

(46) Efron, B.; Tibshirani, R. J. *An Introduction to the Bootstrap*; Chapman & Hall: New York, 1993.

(47) Hall, T. C.; Blacet, F. E. *J.Chem.Phys.* **1952**, *20*, 1745.

(48) Norris, M. S.; Fleck, S. A.; Lichtenfels, D. H. *Anal.Chem.* **1955**, *27*, 1565.

(49) Dixon, J. K. *J.Chem.Phys.* **1940**, *8*, 157.

(50) Mihalcea, R. M.; Baer, D. S.; Hanson, R. K. *Appl.Optics* **1996**, *35*, 4059.

(51) Longstaff, J. V. L.; Singer, K. *J.Chem.Soc.* **1954**, 2604.

(52) Bayliss, N. S.; Watts, D. W. *Aust.J.Chem.* **1956**, *9*, 319.

(53) Singer, K.; Vamplew, P. A. *J.Chem.Soc.* **1956**, 3971.

(54) Longstaff, J. V. L.; Singer, K. *J.Chem.Soc.* **1954**, 2610.

(55) Chase, M. W., Jr.; Davies, C. A.; Downey, J. R., Jr.; Frurip, D. J.; McDonald, R. A.; Syverud, A. N. *JANAF Thermochemical Tables*; Third ed.; American Chemical Society and the American Institute of Physics for the National Bureau of Standards:, 1985; Vol. 14.

(56) Ho, P. C.; Palmer, D. A. *Geochim.Cosmochim. Acta* **1997**, *61*, 3027.

(57) Ho, P. C.; Palmer, D. A.; Mesmer, R. E. *J. Solution Chem.* **1994**, *23*, 997.

# Chapter 4: Synthesis of Organic Monolayer-Stabilized Copper Nanocrystals in Supercritical Water †

## 4.1 Introduction

At the nanometer length-scale, material dimensions lead to quantum confinement effects that give rise to unique electronic and optical properties useful for a variety of new technologies including, electronic, optical, medical, coatings, catalytic, memory and sensor applications [1]. A variety of wet chemical methods have been developed for nanocrystal synthesis. The main issues are control over particle size and size distribution, surface passivation and core crystallinity. Metal nanocrystals, such as silver and gold, can be synthesized at room temperature [2,3]; whereas, semiconductor nanocrystals, such as CdSe [4] and InAs [5], must be grown at high temperatures in high boiling point solvents to achieve crystalline cores and well-defined shape. The key ingredient in all of these methods is the use of capping ligands that bind to particle surfaces and provide a steric barrier to aggregation. The capping ligands tend to exhibit the properties of surfactants: one end binds strongly to the particle surface while the opposite end interacts with the solvating fluid. In a good solvent, the ligands extend from the nanocrystal surface and provide steric stabilization, which

---

† The contents of this chapter appear in *J. Am. Chem. Soc.* **2001**, 123, 7797-7803.

typically limits size to the nanometer range and prevents unwanted agglomeration.

Supercritical fluids (SCFs) offer several processing advantages over conventional solvents, which has led to increased use in materials chemistry [6-9] and more specifically, nanocrystal synthesis [8-16]. Supercritical $CO_2$ and supercritical water (SCW), for example, are chemically stable and environmentally benign. SCFs exhibit the combined characteristics of both gas and liquid solvents to provide a medium with densities characteristic of liquids, and gas-like viscosities and diffusivities. Thus, mass transfer rates approach those in gases, while solvation properties resemble those of conventional liquid solvents. Furthermore, supercritical fluids exhibit unique *tunable* solvation characteristics, as subtle changes in pressure and temperature in SCFs alter the solvent density. This property might be utilized to improve many aspects of nanocrystal processing—such as size-selective separations, synthesis and self-assembly.

In water, the dielectric constant dramatically decreases ($\varepsilon \approx 5$) when heated and pressurized above the critical point ($T_c = 374$ °C, $P_c = 221$ bar), which decreases the solubility of salts and increases the solubility of organics [17]. In certain applications, such as the supercritical water oxidation of organic wastes, the precipitation of salt particles is undesirable because it leads to reactor plugging and corrosion problems [17,18]. Recent efforts, however, have been made to control particle formation in SCW to create useful materials such as ceramics, coatings, and catalysts, with a variety of particulate chemistries being produced by hydrolyzing metal nitrates or metal acetates in sub-critical [13,14,19] or supercritical water [8,15,16,20,21]. For example, metal oxides have been prepared in SCW using metal nitrate salts, which decompose via a two-step mechanism of hydrolysis and dehydration [20-23]. The high temperature of SCW promotes crystallization, which eliminates the need for post-process annealing. Different particle sizes and morphologies have been obtained with changes in reaction time, temperature, and pressure [22,24-29]. Additionally, the nature of the anion can affect the oxidation state of the metal, possibly as a result of oxidative mechanisms involving decomposition products of the precursor [22]. These results suggest that oxidants/reductants can be added to the reaction mixture to influence the product chemistry as has been recently shown by the addition of oxalic acid to copper hydroxycarbonate [16]. Nanometer particle size control (i.e. < 10 nm diameters), however, is difficult to achieve under these conditions due to agglomeration and coalescence and has only recently been demonstrated [14].

Near ambient temperatures, many approaches have been developed to control nanocrystal size. These rely on the use of either stabilizing ligands to bind nanocrystal surfaces or the use of compartmentalized heterogeneous media, such as micellar solutions, to control growth [30-36]. These ideas have recently been extended to SCFs with general success. Water-in-sc-$CO_2$ microemulsions have been used as 'micro reactors' to produce cadmium sulfide [10] and silver [37] nanocrystals, while copper nanocrystals have been prepared in water-in-sc-ethane and water-in-propane microemulsions [35,36]. Arrested precipitation methods have also recently been used in SCFs to produce sterically stabilized silicon nanocrystals (in sc-octanol and sc-hexane) [11] and silver, platinum, and iridium nanocrystals (in sc-$CO_2$) [38]. The key to this work has been the identification of suitable capping ligands for the SCF environment.

Here we report our finding that organic hydrocarbon capping ligands can be used to stabilize nanocrystal formation in SCW. We also find that the stabilizing ligands, in this case 1-hexanethiol, control the nanocrystal composition: copper oxide forms without ligands, while copper metal nanocrystals form in the presence of alkanethiol capping ligands. Furthermore, the processing conditions (i.e. precursor, pH, capping ligand) significantly affect the morphology and size of the nanocrystals formed in SCW, which is due to competing reaction pathways of hydrolysis and ligand exchange versus arrested growth.

## 4.2 Experimental

***4.21 Nanocrystal synthesis***. Copper (II) nitrate hemipentahydrate (Aldrich), copper (II) acetate monohydrate (Acros), and 1-hexanethiol (95%, Aldrich) were used as received without further purification. The experimental apparatus consisted of a pumping system and a 7/8″ I.D. × 4″ long 316 stainless steel reaction cell (10 mL) described in Fig. 4.1. For reactions without thiols, the cell was initially loaded at ambient conditions with 1.0 mL of pure water. For reactions with thiols, 900 μL of pure water with 100 μL of 1-hexanethiol was used (initial water:thiol mole ratio ≈ 70:1). The cell was sealed and heated to 400 °C and ~173 bar using heating tape (Barnstead/Thermolyne) and an Omega temperature controller. The cell temperature was measured with a K-type thermocouple (Omega). A 0.02 M copper precursor solution was injected into the cell via 1/16″ I.D. stainless steel tubing by an HPLC pump (Beckman Model 100A) at 4 mL/min until the operating pressure reached 413 bar. The solution reacts immediately upon entering the reactor, as observed visually in a separate experiment with an optical cell [39,40]. The products precipitate upon cooling the reaction. The nanocrystals were removed from the cell with either deionized water (uncapped particles) or chloroform (organic capped particles). In the case of the thiol-capped nanocrystals, unreacted precursor was removed by extraction with water. The nanoparticles were filtered (Fisher, qualitative P5) to remove large agglomerates of uncapped nanocrystals and dried using a rotary evaporator (Buchi). The nanocrystals re-disperse in either deionized water (uncapped particles) or chloroform (organic capped particles).

***4.22 Phase behavior of supercritical water and 1-hexanethiol***. The water and 1-hexanethiol phase equilibria were studied in a titanium grade 2 optical cell

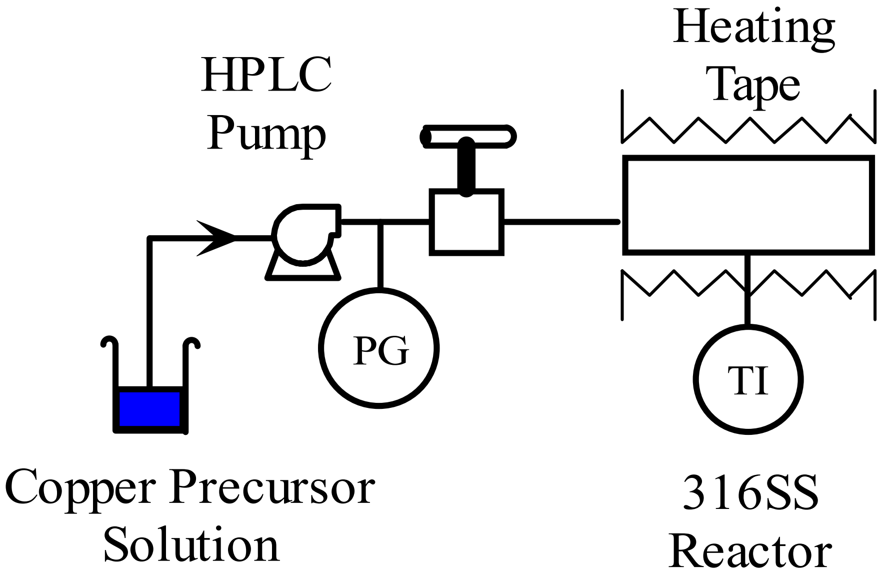

Fig. 4.1. Schematic of the high-temperature stainless steel reactor.

equipped with sapphire windows. Under the reaction conditions of 400 °C and ~ 413 bar (50 μL 1-hexanethiol in 150 μL of water), water and 1-hexanethiol are miscible. This miscibility is consistent with the phase diagram for n-alkanes in water (n-pentane and n-heptane [41]).

***4.23 Characterization methods***. Gas chromatography (GC) measurements of hexanethiol were recorded with a Hewlett-Packard 5890A Gas Chromatograph. Fourier-transform infrared (FTIR) spectroscopy measurements were performed using a Perkin-Elmer Spectrum 2000 spectrometer with the nanoparticles dispensed on PTFE cards. Low resolution transmission electron microscopy (TEM) images were obtained on a JEOL 200CX transmission electron microscope operating with a 120 kV accelerating voltage, while high resolution transmission electron microscopy (HRTEM) images and selected area electron diffraction (SAED) patterns were obtained with a GATAN digital photography system on a JEOL 2010 transmission electron microscope with 1.7 Å point to point resolution operated with a 200 kV accelerating voltage. All samples were prepared on Electron Microscope Sciences 200 mesh carbon coated aluminum grids by dispersing suspended nanoparticles onto the grid and evaporating the solvent. The measured lattice separations were indexed against standards [42] for copper, $Cu_2O$, and CuO. UV-visible absorbance spectroscopy was performed using a Varian Cary 300 UV-vis spectrophotometer with the capped-nanoparticles dispersed in chloroform. X-ray photoelectron spectroscopy

(XPS) was performed on a Physical Electronics XPS 5700, with a monochromatic Al x-ray source ($K_\alpha$ excitation at 1486.6 eV). For XPS, the samples were deposited on a silicon wafer (cleaned with a 50:50 mixture of methanol: HCl), vacuum-dried at 25°C to remove all residual solvent, and stored under nitrogen.

## 4.3 Results

The nanocrystals synthesized in SCW were characterized using several techniques, including TEM, XPS, EDS, and SAED. Several factors, including precursor concentration, solution pH, capping ligand, and the type of precursor, affect the crystal structure, size, morphology, and degree of agglomeration of the nanocrystals. Tables 4.1 and 4.2 summarize all results.

***4.31 Copper and copper oxide particle formation in supercritical water (no capping ligands)***. Fig. 4.2 shows TEM images of size-polydisperse particles formed using $Cu(NO_3)_2$. Particle diameters range from 8 to 35 nm with an average diameter of 16.7 nm. High-resolution TEM (HRTEM) (Fig. 4.2a) reveals relatively spherical and crystalline particles. Although some individual particles can be seen on the TEM grid after deposition (Fig. 4.2b), a significant amount of aggregation has occurred (Fig. 4.2c). SAED revealed that the particle cores are tenorite copper (II) oxide (CuO) (Fig. 4.7). The lattice spacing in the HRTEM images (such as those in Fig. 4.2a) of 2.53 Å, are also consistent with the bulk value of 2.51 Å for the <002> or <-111> lattice spacing in tenorite CuO. XPS,

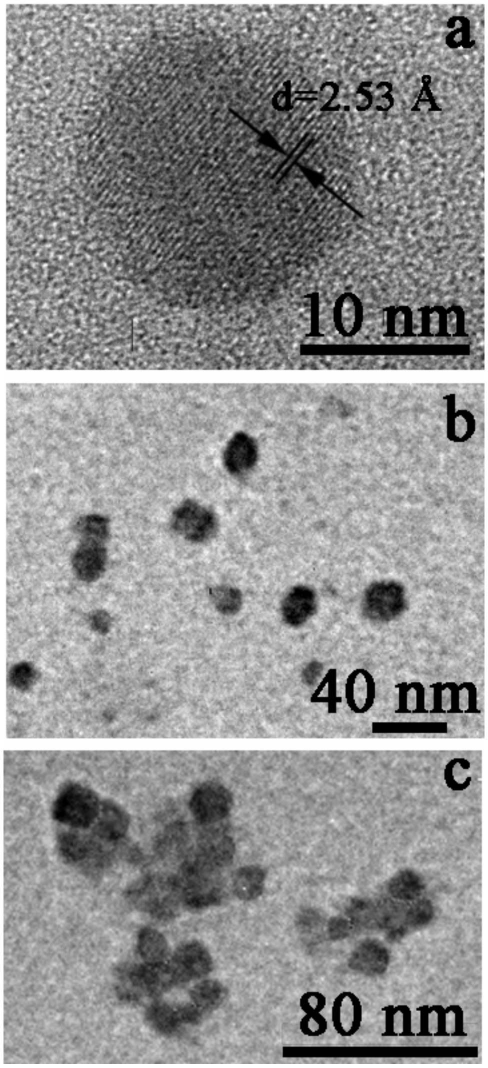

Fig. 4.2. (a) High-resolution; and (b) and (c) Low-resolution TEM images CuO nanoparticles synthesized via $Cu(NO_3)_2$ in SCW without capping ligands.

shown in Fig. 4.8a, further confirmed that particles formed using $Cu(NO_3)_2$ without thiol were composed of CuO: the Cu 2p core level binding energy of 933.7 eV is characteristic of $Cu^{II}$ cations, and the satellite or shake-up regions for $Cu^{2+}$ at 945 and 965 eV [43] result from electron transfer to the core hole to yield $d^9$ character [44]. All of these techniques indicate $Cu(NO_3)_2$ degradation in SCW yields CuO particles.

When using $Cu(CH_3COO)_2$ as the precursor, particles form with a larger average diameter of 30.9 nm and a broader distribution ranging from 10 to 97 nm (Fig. 4.3) than those formed using $Cu(NO_3)_2$. The particles exhibit an octahedral morphology (projected as cubic in Fig. 4.3a or as hexagonal in Fig. 4.3c) and a greater tendency to agglomerate (Fig. 4.3b and 4.3c). SAED (Fig. 4.7) shows that the particles contain Cu cores. Many HRTEM images of the $Cu(CH_3COO)_2$ system (such as Fig. 4.5a), however, reveal both copper (I) oxide ($Cu_2O$) (3.07 Å compared to 3.02 Å for the <110> lattice spacing) as well as copper metal nanocrystals. XPS in Fig. 4.8 show Cu 2p core level binding energy characteristic of elemental copper or $Cu_2O$. Unfortunately, from XPS data alone it is difficult to distinguish the copper oxidation state between $Cu^0$ and $Cu^I$ due to the effects of crystal size and surface coverage on the binding energy [45]. However, it appears that $Cu(CH_3COO)_2$ degradation in SCW yields a mixture of Cu and $Cu_2O$ particles.

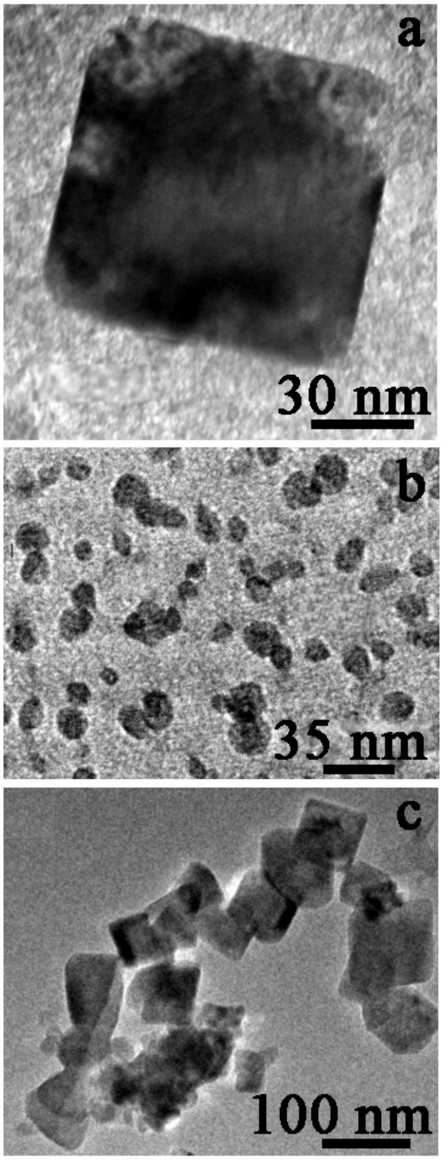

Fig. 4.3. (a) High-resolution; and (b) low-resolution TEM images of slightly agglomerated, uncapped $Cu_2O$ or elemental copper nanoparticles; and (c) TEM images of highly agglomerated, uncapped $Cu_2O$ or elemental copper nanoparticles synthesized via $Cu(CH_3COO)_2$ in SCW. Note in (a) and (c) the appearance of different morphologies.

***4.32 Formation of ligand-stabilized copper nanocrystals in supercritical water***. 1-hexanethiol was added to the reactor as a capping ligand to control particle growth in SCW. Although alkanethiols do not dissolve in water at room temperature, 1-hexanethiol dissolves in supercritical water at the concentrations studied (see above) [41]. GC analysis of water/1-hexanethiol mixtures confirmed that the organic capping ligands were stable in SCW under the reaction conditions explored. For residence times up to 30 min, 1-hexanethiol did not decompose. After 45 min, decomposition product concentrations could be detected on the order of 10 to 100 times smaller than the initial 1-hexanethiol concentration.

Nanocrystals formed using $Cu(NO_3)_2$ in the presence of 1-hexanethiol with a starting solution pH of 3.4 have an average diameter of 7.0 nm with crystalline cores and spherical shape, as shown in Fig. 4.4. The nanocrystal surfaces rarely touch in the TEM image due to the bulky capping ligand layer surrounding each particle (Fig. 4.4b). The average size and the size distribution (3 to 15 nm) of these nanoparticles are smaller than those of the uncapped particles (16.7 nm) by a factor of more than two. SAED of the nanocrystals (Fig. 4.7) show that the nanocrystal cores are composed of elemental Cu. The HRTEM images, such as Fig. 4.4a, reveal d-spacings of 1.87 Å (compared to 1.81 Å for the <200> lattice spacing) characteristic of copper. Furthermore, the Cu 2p core level binding energies consistent with elemental copper appear in the XPS data [45]. The

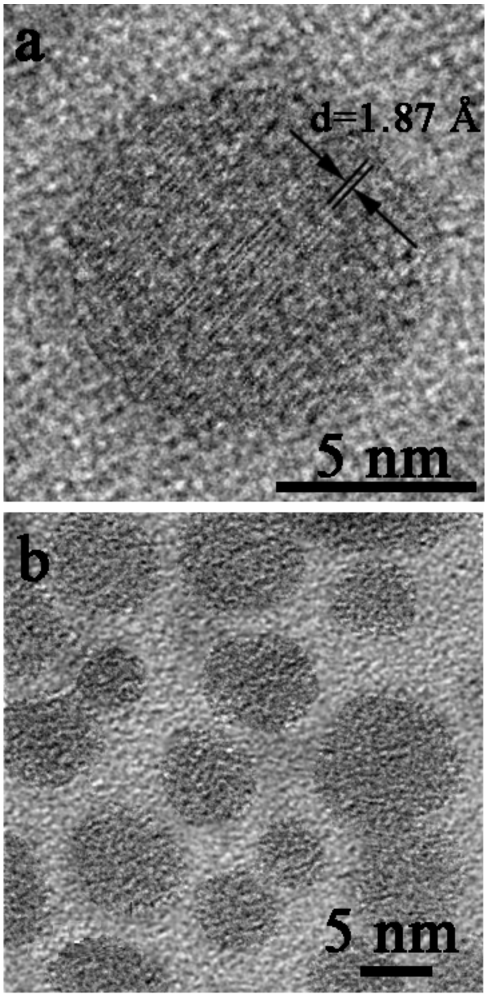

Fig. 4.4. (a) High-resolution; and (b) low-resolution TEM images of 1-hexanethiol stabilized copper nanoparticles synthesized via $Cu(NO_3)_2$ in SCW. Note that the nanoparticles are stabilized and not agglomerated despite the close proximity.

spherical nanocrystal shape is consistent with icosahedra formation, which is well known for copper nanocrystals smaller than about 7 nm [46-48]. Room temperature UV-visible absorbance spectra in Fig. 4.9 are characteristic of Cu nanocrystals, [32,33] as the surface plasmon resonance for bulk copper metal (2.15 eV (560 nm) to 2.2 eV (580 nm)) is noticeably absent. Based on Mie theory, the surface plasmon resonance for copper nanocrystals is expected to have strong broadening for particles smaller than 100 Å [33]. Increasing the reaction temperature to 425 °C and 450 °C resulted in an increase in the average particle diameter (7.8 nm and 9.2 nm, respectively).

TEM images of copper nanocrystals formed with $Cu(CH_3COO)_2$ precursor in the presence of 1-hexanethiol at a starting solution pH of 5.25 under identical pressure, temperature and concentration as the nitrate system above, are shown in Fig. 4.5. The addition of the capping ligand has little effect on the average size (33.8 nm), size distribution, morphology, and oxidation state of the particles. Despite the apparent lack of an effect on size and morphology, the ligands are nonetheless bound to the particle surface. FTIR spectra in Fig. 4.6 show the characteristic methyl and methylene stretches of the capping ligands after removal of all unbound ligands from the sample; however, these capping ligands apparently do not effectively prevent agglomeration or quench growth. A longer capping ligand (1-dodecanethiol) helped stabilize a small amount of particles (not shown), but most of the particles agglomerated as with 1-hexanethiol.

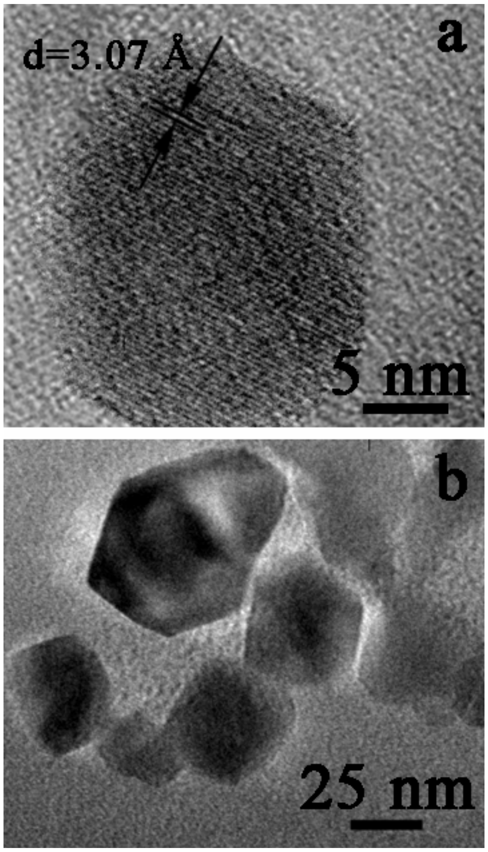

Fig. 4.5. (a) High-resolution; and (b) low-resolution TEM images of 1-hexanethiol stabilized copper nanoparticles synthesized via $Cu(CH_3COO)_2$ in SCW. Note that the particles are not stabilized and highly agglomerated despite being passivated with a capping-ligand.

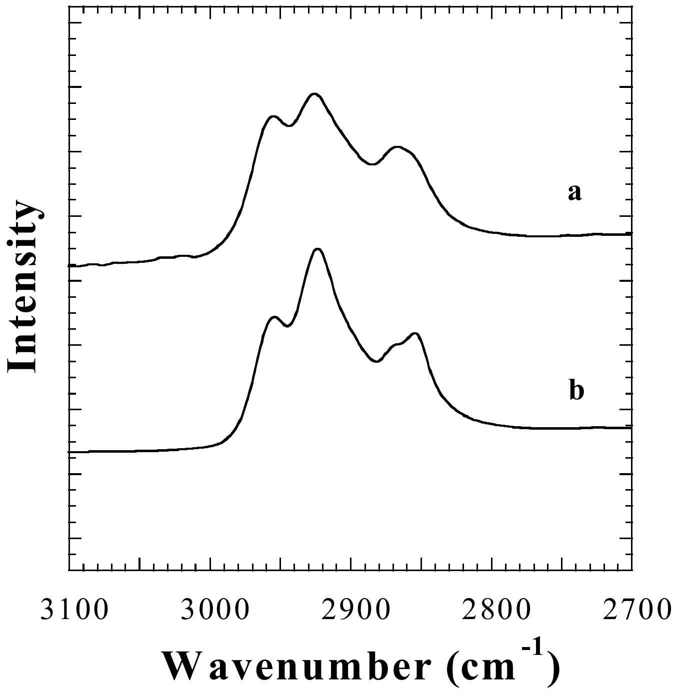

Fig. 4.6. FTIR spectra of 1-hexanethiol capped nanoparticles synthesized via (a) $Cu(NO_3)_2$ and (b) $Cu(CH_3COO)_2$. Spectra are offset for clarity.

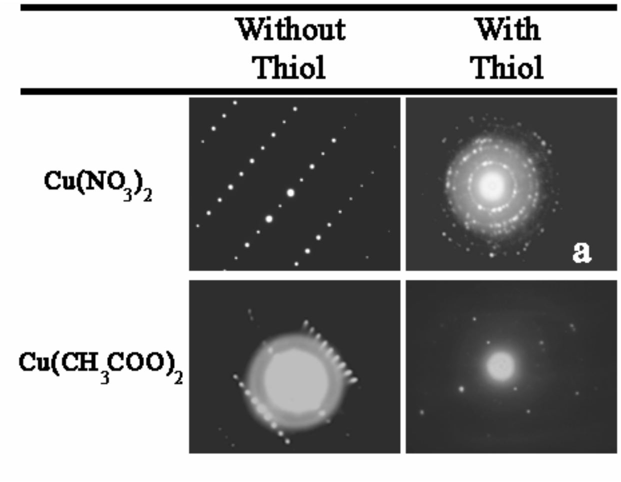

Fig. 4.7. Electron diffraction images of nanoparticles synthesized via $Cu(NO_3)_2$ and $Cu(CH_3COO)_2$ with and without the use of 1-hexanethiol as a capping-ligand in SCW. (a) Note that the electron diffraction image here yields rings and not the single crystal patterns observed for the other nanoparticles. This is due to the small size of these nanoparticles (5 to 11 nm) and the inability to focus the electron beam on a single crystal.

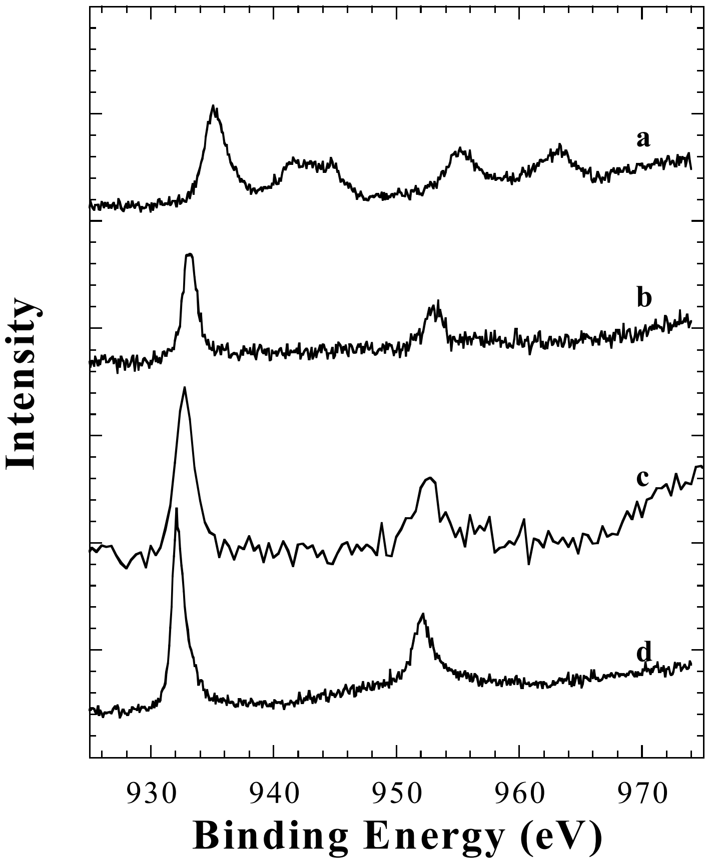

Fig. 4.8. XPS of uncapped particles produced via (a) $Cu(NO_3)_2$ and (b) $Cu(CH_3COO)_2$; XPS scan of organically capped nanoparticles produced with (c) $Cu(NO_3)_2$ and (d) $Cu(CH_3COO)_2$. All scans are offset for clarity. Cu 2p core level binding energy for copper (II) at 934 eV and copper (0) at 932 eV.

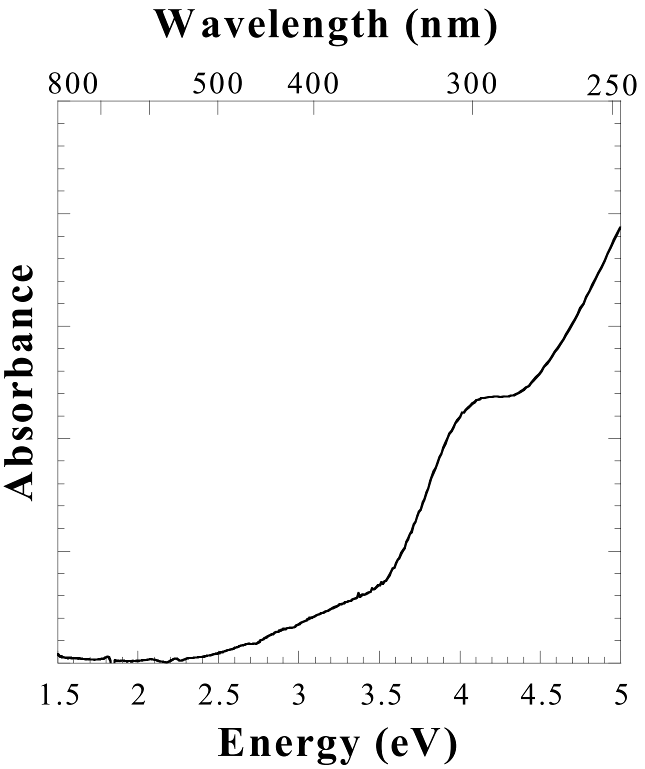

Fig. 4.9. Room temperature UV-visible spectra of organically capped copper nanoparticles synthesized via $Cu(NO_3)_2$ and 1-hexanethiol.

Since the reaction mechanism may involve hydrated and hydroxylated complexes, pH differences could be the source of the significant variations in particle formation using the acetate and nitrate precursors. For example, Baes and Mesmer [49] have shown at room temperature that $Cu^{II}$ exists as hydrated $Cu^{2+}$ at acidic conditions and as $Cu_2(OH)_2^{2+}$ under basic conditions ($pH > 4$). Differences in hydration could be present at higher temperatures, although they have not been studied. Particles formed using $Cu(NO_3)_2$ after raising the pH to 6.0 with NaOH appeared very similar to those produced with $Cu(CH_3COO)_2$ at a pH of 5.25, with 45.0 nm average particle diameter and size distribution of 13 to 187 nm. Cu nanocrystals synthesized using 2 mM $Cu(NO_3)_2$ with a starting pH of 4.59 were also large (40.8 nm) with a broad size distribution. Experiments using $Cu(CH_3COO)_2$ after lowering the pH to 2.66 with $HNO_3$, however, yielded large agglomerated particles with an average particle diameter of 47.4 nm and a size distribution of 11 to 133 nm. Therefore, both pH and the nature of the anions affects nanocrystal formation.

It is worth noting that mixing $Cu(NO_3)_2$ and 1-hexanethiol at room temperature produced a yellow precipitate likely due to the formation of a copper-thiol complex. When heated to 400 °C and ~ 413 bar, this mixture produced large spherical or ellipsoidal size-polydisperse particles 36.1 nm in diameter ranging 9 to 80 nm (Fig. 4.10). The particles exhibit little aggregation on the TEM grid with unique morphologies compared to the synthesis with $Cu(CH_3COO)_2$.

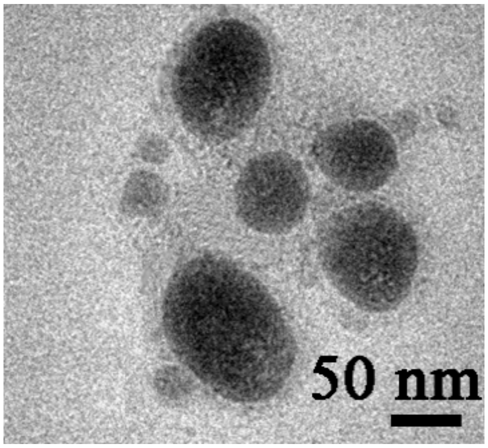

Fig. 4.10. Low-resolution TEM images of stabilized copper particles synthesized via a copper-thiol complex in SCW.

Table 4.1. Nanocrystal Formation in Supercritical Water. [a]

| | Starting Material | Conc (mM) | Temp (°C) | Initial Pressure (bar) [b] | Capping Ligand | pH at room Temp | Average Diameter (nm) | Distribution (nm) | Product |
|---|---|---|---|---|---|---|---|---|---|
| A | $Cu(NO_3)_2$ | 20 | 400 | 200 | — | 3.40 | 16.7 | 8 – 35 | CuO |
| B | $Cu(CH_3COO)_2$ | 20 | 400 | 200 | — | 5.25 | 30.9 | 10 – 97 | Cu, $Cu_2O$ |
| C | $Cu(NO_3)_2$ | 20 | 400 | 200 | $C_6SH$ | 3.40 | 7.0 | 3 – 15 | Cu |
| D | $Cu(NO_3)_2$ | 20 | 425 | 220 | $C_6SH$ | 3.40 | 7.8 | 4 – 14 | Cu |
| E | $Cu(NO_3)_2$ | 20 | 450 | 240 | $C_6SH$ | 3.40 | 9.2 | 4 – 15 | Cu |
| F | $Cu(CH_3COO)_2$ | 20 | 400 | 200 | $C_6SH$ | 5.25 | 33.8 | 10 – 89 | Cu, $Cu_2O$ |
| G | $Cu(CH_3COO)_2$ | 20 | 400 | 200 | $C_{12}SH$ | 5.25 | 26.5 | 10 – 68 | Cu, $Cu_2O$ |
| H | $Cu(NO_3)_2$ | 2 | 400 | 200 | $C_6SH$ | 4.59 | 40.8 | 12 – 111 | |
| I | $Cu(NO_3)_2$ [c] | — | 400 | 200 | $C_6SH$ | — | 36.1 | 9 – 80 | |
| J | $Cu(NO_3)_2$ + NaOH | 20 | 400 | 200 | $C_6SH$ | 6.00 | 45.0 | 13 – 187 | |
| K | $Cu(CH_3COO)_2$ + $HNO_3$ | 20 | 400 | 200 | $C_6SH$ | 2.66 | 47.4 | 11 – 133 | |

[a] All reactions were performed with 900 μL of pure water and 100 μL of thiol unless otherwise noted.

[b] Based on PVT data for pure water.

[c] Copper nitrate (0.02-M) and 1-hexanethiol were mixed before heating and pressurizing. A reaction occurred immediately resulting in the formation of a yellow solid.

Table 4.2. Growth Analysis of Nanocrystal Formation in Supercritical Water.

| | Product | Predominant Structure | Agglomeration | Average Diameter (nm) | Distribution Moment $\mu_1$ | Distribution Moment $\mu_3$ | Growth Mechanism |
|---|---|---|---|---|---|---|---|
| A | CuO | Icosahedral | Moderate | 16.7 | 1.23 | 0.90 | Diffusion |
| B | Cu, $Cu_2O$ | Octahedral | High | 30.9 | 1.75 | 0.76 | Coagulation |
| C | Cu | Icosahedral | Low | 7.0 | 1.19 | 0.92 | Diffusion |
| D | Cu | Icosahedral | Low | 7.8 | 1.08 | 0.96 | Diffusion |
| E | Cu | Icosahedral | Low | 9.2 | 1.14 | 0.94 | Diffusion |
| F | Cu, $Cu_2O$ | Octahedral | High | 33.8 | 1.40 | 0.84 | Coagulation |
| G | Cu, $Cu_2O$ | Octahedral | High | 26.5 | 1.27 | 0.88 | Coagulation |
| H | | Mixture | Moderate | 40.8 | 1.44 | 0.83 | Coagulation |
| I | | Ellipsoidal | Low | 36.1 | 1.40 | 0.86 | Coagulation |
| J | | Mixture | Moderate | 45.0 | 1.67 | 0.75 | Coagulation |
| K | | Mixture | High | 47.4 | 1.38 | 0.86 | Coagulation |

***4.33 Growth analysis of particle formation*.** After nucleation, the particles may grow either by condensation (diffusion-limited growth) or by fusion of the metal cores (coagulation) [38,50-52]. Analysis of the moments of the size distribution provides insight into the growth mechanism. The first moment, $\mu_1 = r_3/r_h$, and the third moment, $\mu_3 = r_1/r_3$, describe the polydispersity of the sample. The moments are functions of the arithmetic mean radius $r_1 = \sum r_i / N_\infty$, the cube-mean radius $r_3 = \sqrt[3]{\sum r_i^3 / N_\infty}$, and the harmonic mean radius $r_h = N_\infty / \sum 1/r_i$, where $N_\infty$ is the total number of particles in the sample. Values of $\mu_1 > 1.25$ and $\mu_3 < 0.905$ indicate that growth occurs by coagulation, whereas diffusion-limited growth occurs when $\mu_1$ and $\mu_3$ approach unity [38,50-52]. In the case of the experiments with $Cu(NO_3)_2$ at pH ~ 3, $\mu_1$ and $\mu_3$ approach unity (Tables 4.1 and 4.2 summarize the size distribution analysis of all the experiments), which suggests that growth occurs through a diffusion limited mechanism of Cu atom diffusion to nucleated particles. In nearly all other experiments, growth occurs primarily through coagulation of metal cores and broad size distributions result.

## 4.4 Discussion

The precursors, $Cu(NO_3)_2$ and $Cu(CH_3COO)_2$, produce qualitatively different nanocrystals. Without alkanethiol, the nitrate precursor yields spherical

CuO particles approximately 17 nm in diameter. The acetate precursor gives 30 to 40 nm diameter octahedral particles with mixed Cu and $Cu_2O$ composition. In the presence of alkanethiol, $Cu(NO_3)_2$ gives 7 nm diameter spherical Cu nanocrystals; whereas, there is little change in the nanocrystal size and shape when using $Cu(CH_3COO)_2$. Below, we describe the mechanistic factors that lead to these differences. The mechanism can be viewed as a competition between hydrolysis to large oxidized copper particles versus ligand exchange and arrested growth by thiols to produce small monodisperse nanoparticles.

Recently, Fulton *et al.* [53] used X-ray absorption fine structure (XAFS) to determine that ion-pairing and hydrolysis mechanisms for $Cu^I$ and $Cu^{II}$ in SCW are temperature dependent:

$$[Cu(H_2O)_6]^{2+} + m(NO_3^-) \xrightarrow{350\,^\circ C > T > 100\,^\circ C} [Cu(H_2O)_{6-m}(NO_3^-)_m]^{2-m} + mH_2O \qquad (4.1)$$

$$[Cu(H_2O)_6]^{2+} + m(NO_3^-) \xrightarrow{T > 400\,^\circ C} CuO + 2H^+ + 5H_2O + m(NO_3^-) \qquad (4.2)$$

Above 400 °C, hydrolysis results in CuO formation. Adschiri *et al*. have also described metal oxide formation in SCW using metal nitrates [54,55] as a two-step hydrolysis and dehydration reaction [20,21]. Based on these studies, copper nitrate hydrolysis, in the absence of alkanethiol, may be described by pathway I in Fig. 4.11, which leads to nucleation of the oxide, CuO.

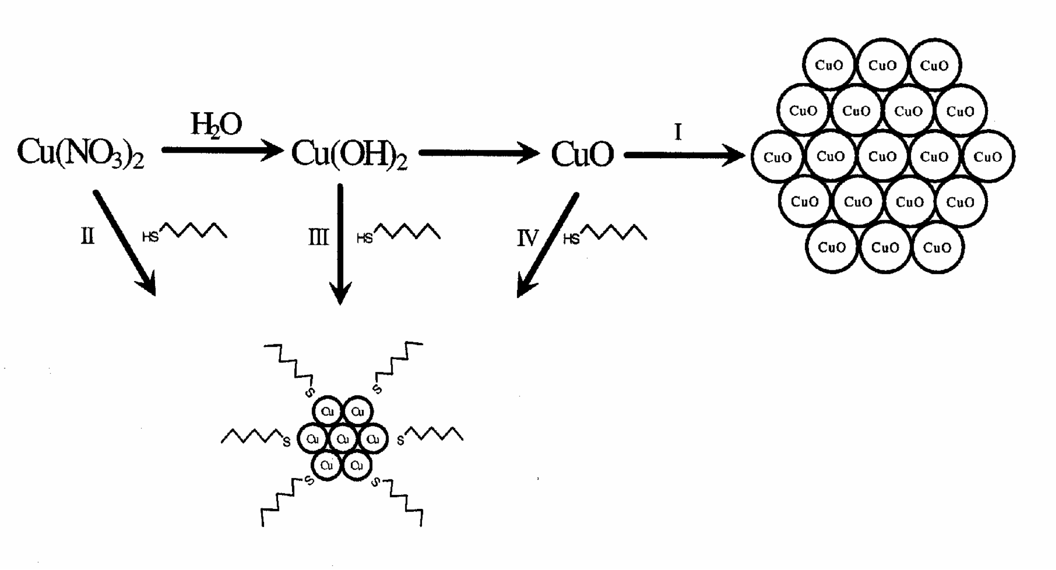

Fig. 4.11. Proposed schematic representation of reaction mechanism for the formation of organically capped copper nanoparticles in supercritical water via $Cu(NO_3)_2$.

In the presence of 1-hexanethiol, ligand exchange of thiol for anions and thiol-induced $Cu^{II}$ reduction can lead to Cu particles by pathways II, III, and possibly IV shown in Fig. 4.11. Pathways II and III compete with the hydrolysis/dehydration pathway. This mechanism is consistent with the observed effects of anion, pH and thiol ligand on particle size, size distribution and oxidation state as discussed below.

***4.41 Ligand effects***. When alkanethiol is added to the $Cu(NO_3)_2$ solutions during nanocrystal formation, Cu nanocrystals result in lieu of CuO. Although the nitrate ion serves as an oxidizing agent in SCW [54,55] to favor CuO, the thiol participates in $Cu^{II}$ reduction to $Cu^0$ during nanocrystal formation through either reaction pathway II, III, or IV in Fig. 4.11. The steric stabilization provided by alkanethiol results in diameters half the size of those produced without capping ligands.

Previous investigators have shown that during the self-assembly of alkanethiol monolayers on monolithic CuO surfaces, the alkanethiol reduces the oxide surface to copper metal before binding through the following mechanism [56,57]:

$$2\ HSC_xH_{2x+1} + CuO \rightarrow (SC_xH_{2x+1})_2 + Cu + H_2O \qquad (4.3)$$

$$HSC_xH_{2x+1} + Cu \rightarrow C_xH_{2x+1}SCu + \tfrac{1}{2}\ H_2 \qquad (4.4)$$

If CuO particles, which are highly insoluble in SCW, nucleated and grew via reaction pathway I, the thiol would have limited ability to reduce the CuO in the cores of the growing nanocrystals. Cu nanocrystals may be produced through pathway IV only if reduction occurs before significant growth of CuO crystals takes place. Because the nanocrystals formed from $Cu(NO_3)_2$ in the presence of thiol exhibit Cu crystalline cores with few lattice defects (as confirmed by HRTEM and XPS), it is unlikely that these cores came from previously grown CuO nuclei or small nanocrystals. Furthermore, the Cu nanocrystal size distributions in experiments C-E are consistent with diffusion-limited growth by copper atom addition to growing Cu nanocrystals rather than the aggregation of uncapped CuO particles. Therefore, $Cu^{II}$ reduction likely occurs prior to nanocrystal growth via pathway II, or III.

In sub-critical studies, alkanethiol has been found to reduce $Cu_2O$ to elemental copper through the reaction mechanism [56,57]:

$$2\ HSC_xH_{2x+1} + Cu_2O \rightarrow 2C_xH_{2x+1}SCu + H_2O \qquad (4.5)$$

The alkanethiol, however, does not appear to readily aid the reduction of $Cu_2O$ to elemental copper when $Cu(CH_3COO)_2$ is used as the precursor for nanocrystal growth in SCW. In addition, thiol does not appear to affect the size or morphology of the nanocrystals. Nevertheless, FTIR spectra show that the thiol binds to the particle surface to stabilize the particles in organic solutions, whereas, uncapped particles precipitate within minutes. It appears that the thiol binding rate cannot compete with the particle growth rate when $Cu(CH_3COO)_2$ is used as the precursor.

***4.42 pH and anion effects***. In the absence of thiol, $Cu(CH_3COO)_2$ produces particles that consist of a mixture of copper metal and $Cu_2O$, in contrast with CuO particles produced using $Cu(NO_3)_2$. These results are consistent with Poliakoff *et al.* [8] whom have shown that the hydrolysis of metal-organic complexes, in contrast with metal salts, produces reduced metal oxides or metal particles. Complexes of coinage metals, such as copper, are particularly susceptible to reduction [8].

A key difference between the $Cu(NO_3)_2$ and $Cu(CH_3COO)_2$ solutions is the pH prior to nanocrystal formation. Although the pH is unknown for these systems in SCW, the relative pH may follow approximate trends at ambient conditions, based on previous in situ measurements for related systems [39,40]. In sub-critical water, the Pourbaix diagram indicates that Cu is favored at low pH and oxidized copper species at higher pH due to reactions with OH ligands [58]. Our results are consistent with this trend, in that Cu alone is formed only in the $Cu(NO_3)_2$ experiments with thiol at low pH, and oxidized species are present at higher pH values. For example, when NaOH was added to raise the pH to 6.0, approximately 45 nm diameter octahedral Cu and $Cu_2O$ nanocrystals were produced. Here, the thiol was less effective in reducing the copper and stabilizing the particles. Both of these trends would be consistent with greater selectivity towards hydrolysis, due to an increase in pH, relative to pathway II.

The effects of pH and anion structure are further described in the experiment where $HNO_3$ was added to $Cu(CH_3COO)_2$. Despite having a pH similar to those in experiments with $Cu(NO_3)_2$ only, that yielded small nanocrystals, these crystals were quite large (47 nm in diameter) and included $Cu_2O$. Clearly, these changes are not due to pH alone. Thus, it is likely that the complexation of acetate anion to copper inhibits ligand exchange reactions with thiol and the ability of thiol to reduce and stabilize the growing particles, relative to the case of the nitrate ion. The possibility of a copper(II) acetate dimmer, which is known to be stable at ambient temperature, could also influence the hydrolysis and ligand capping reaction pathways.

### 4.5 Conclusions

Organic alkanethiol capping ligands can be used successfully to stabilize Cu nanocrystal formation in supercritical water. The formation of the organically capped nanocrystals occurs in a miscible mixture of organic thiols and water at supercritical conditions. Despite the highly destructive environment of supercritical water, the alkanethiol was relatively stable for the length of the reaction. Competitive pathways are present between hydrolysis to large polydisperse oxidized particles and ligand exchange and arrested growth favoring smaller Cu nanocrystals. $Cu(NO_3)_2$ was found to be a suitable precursor to produce 7 nm diameter Cu nanocrystals at low starting pH with alkanethiol. Higher pH increased particle sizes and led to $Cu_2O$ along with Cu. The alkanethiol plays a key role in stabilization and quenching particle growth. The alkanethiol also controls the oxidation state of the nanocrystals by reducing $Cu^{II}$ to $Cu^0$; in the absence of thiol, the nitrate precursor yields CuO particles. When $Cu(CH_3COO)_2$, was used as a precursor with or without alkanethiol, large particles, 10 to 30 nm in diameter, are produced with a mixture of Cu and $Cu_2O$. In the proposed mechanism for nanocrystal synthesis, larger more oxidized particles are produced via a hydrolysis route, which are favored by higher pH, and less effective early ligand exchange by thiol. The $Cu(NO_3)_2$ precursor at low pH favors early thiol ligand exchange and arrested growth, which competes with hydrolysis. Analyses of the moments of the particle size distributions further support a competitive mechanism between hydrolysis to large polydisperse oxidized particles favored by aggregation, and arrested growth of low polydispersity Cu particles smaller than 10 nm by diffusion-limited growth.

## 4.6 References

(1) Alivisatos, A. P. *Science* **1996**, *271*, 933.

(2) Brust, M.; Walker, M.; Bethell, D.; Schiffrin, D. J.; Whyman, R. *J. Chem. Soc. Chem. Comm.* **1994**, 801-802.

(3) Leff, D. V.; Ohara, P. C.; Heath, J. R.; Gelbart, W. M. *J. Phys. Chem.* **1995**, *99*, 7036-7041.

(4) Murray, C. B.; Norris, D. J.; Bawendi, M. G. *J. Am. Chem. Soc.* **1993**, *115*, 8706.

(5) Banin, U.; Lee, C. J.; A.A., G.; Kadavanich, A. V.; Alivisatos, A. P.; Jaskolski, W.; Bryant, G. W.; Efros, A. L.; Rosen, M. *J. Chem. Phys.* **1998**, *109*, 2306.

(6) Gogotsi, Y. G.; Yoshimura, M. *Nature* **1994**, *367*, 628.

(7) Watkins, J. J.; Blackburn, J. M.; McCarthy, T. J. *Chem. Mater.* **1999**, *11*, 213-215.

(8) Darr, J. A.; Poliakoff, M. *Chemical reviews* **1999**, *99*, 495.

(9) Savage, P. E.; Gopalan, S.; Mizan, T. I.; Martino, C. J.; Brock, E. E. *AIChE J.* **1995**, *41*, 1723-1778.

(10) Holmes, J. D. B., Prashant A.; Korgel, Brian A.; Johnston, Keith P. *Langmuir* **1999**, *15*, 6613.

(11) Holmes, J. D.; Ziegler, K. J.; Doty, R. C.; Pell, L. E.; Johnston, K. P.; Korgel, B. A. *J. Am. Chem. Soc.* **2001**, *123*, 3743-3748.

(12) Holmes, J. D.; Johnston, K. P.; Doty, R. C.; Korgel, B. A. *Science* **2000**, *287*, 1471.

(13) Cabanas, A.; Darr, J. A.; Lester, E.; Poliakoff, M. *Chem. Commun.* **2000**, 901-902.

(14) Cabanas, A.; Darr, J. A.; Lester, E.; Poliakoff, M. *J. Mater. Chem.* **2001**, *11*, 561-568.

(15) Galkin, A. A.; Kostyuk, B. G.; Lunin, V. V.; Poliakoff, M. *Angew. Chem. Int. Ed.* **2000**, *39*, 2738-2740.

(16) Galkin, A. A.; Kostyuk, B. G.; Kuznetsova, N. N.; Turakulova, A. O.; Lunin, V. V.; Polyakov, M. s. *Kinetics and Catalysis* **2001**, *42*, 154-162.

(17) Gloyna, E. F.; Li, L. *Waste Management* **1993**, *13*, 379-394.

(18) Kritzer, P.; Boukis, N.; Dinjus, E. *J. Supercritcal Fluids* **1999**, *15*, 205.

(19) Goia, D. V.; Matijevic, E. *New J. Chem.* **1998**, *22*, 1203-1215.

(20) Adschiri, T.; Kanazawa, K.; Arai, K. *J.Am.Ceram.Soc.* **1992**, *75*, 1019.

(21) Adschiri, T.; Kanazawa, K.; Arai, K. *J.Am.Ceram.Soc.* **1992**, *75*, 2615.

(22) Adschiri, T.; Yamane, S.; Onai, S.; Arai, K. : Strasbourg, France, 1994; Vol. T3, pp 241.

(23) Adschiri, T.; Hakuta, Y.; Arai, K. *Ind. Eng. Chem. Res.* **2000**, *29*, 4901-4907.

(24) Matijevic, E. *J. Colloid Interface Sci.* **1987**, *117*, 593-595.

(25) Matijevic, E. *Chem. Mater.* **1993**, *5*, 412-426.

(26) McFayden, P.; Matijevic, E. *J. Colloid Interface Sci.* **1973**, *44*, 95.

(27) Tamura, H.; Matijevic, E. *J.Colloid. Interface Sci.* **1982**, *90*, 100-109.

(28) Hirano, M.; Etsuro, K. *J. Mater. Sci. Lett.* **1996**, *15*, 1249-1250.

(29) Hirano, M.; Etsuro, K. *J. Am. Ceram. Soc.* **1996**, *79*, 777-780.

(30) Lisiecki, I.; Pileni, M., P. *J. Am. Chem. Soc.* **1993**, *115*, 3887-3896.

(31) Lisiecki, I.; Bjorling, M.; Motte, L.; Ninham, B.; Pileni, M. P. *Langmuir* **1995**, *11*, 2385-2392.

(32) Lisiecki, I.; Pileni, M. P. *J. Phys. Chem.* **1995**, *99*, 5077-5082.

(33) Lisiecki, I.; Billoudet, F.; Pileni, M., P. *J. Phys. Chem.* **1996**, *100*, 4160-6.

(34) Lisiecki, I.; Filankembo, A.; Sack-Kongehl, H.; Weiss, K.; Pileni, M., P.; Urban, J. *Phys. Rev. B: Condens. Matter Mater. Phys.* **2000**, *61*, 4968-4974.

(35) Cason, J.; Roberts, C. *J. Phys. Chem. B* **2000**, *104*, 1217.

(36) Cason, J. P.; Khambaswadkar, K.; Roberts, C. B. *Ind. Eng. Chem. Res.* **2000**, *39*, 4749-4755.

(37) Ji, M.; Chen, X.; Wai, C. M.; Fulton, J. L. *J. Am. Chem. Soc.* **1999**, *121*, 2631.

(38) Shah, P. S.; Johnston, K. P.; Korgel, B. A. *submitted* **2001**.

(39) Xiang, T.; Johnston, K. P. *J.Phys.Chem.* **1994**, *98*, 7915.

(40) Xiang, T.; Johnston, K. P. *J.Solution Chem.* **1997**, *26*, 13.

(41) Connolly, J. F. *J. Chem. Eng. Data* **1966**, *11*, 13.

(42) Urban, J.; Sack-Kongehl, H.; Weiss, K. *Catalysis Letters* **1997**, *49*, 101-108.

(43) Chusuei, C. C.; Brookshier, M. A.; Goodman, D. W. *Langmuir* **1999**, *15*, 2806-2808.

(44) Borgohain, K.; Singh, J., B.; Rama Rao, M., V.; Shripathi, T.; Mahamuni, S. *Phys. Rev. B: Condens. Matter Mater. Phys.* **2000**, *61*, 11093-11096.

(45) Carley, A. F.; Dollard, L. A.; Norman, P. R.; Pottage, C.; Roberts, M. W. *J. Electron Spectrosc.* **1999**, *98-99*, 223-233.

(46) Olynick, D. L.; Gibson, J. M.; Averback, R. S. *Appl. Phys. Lett.* **1996**, *68*, 343-345.

(47) Gillet, M. *Surf. Sci.* **1977**, *67*, 139-157.

(48) Urban, J.; Sack-Kongehl, H.; Weiss, K. *Z. Phys. D* **1996**, *36*, 73-83.

(49) Baes, C. F., Jr.; Mesmer, R. E. *The Hydrolysis of Cations*; Wiley: New York, 1976.

(50) Friedlander, S. K.; Wang, C. S. *J. Colloid Interf. Sci.* **1966**, *22*, 126-132.

(51) Pich, J.; Friedlander, S. K.; Lai, F. S. *Aerosol Science* **1970**, *1*, 115-126.

(52) Swift, D. L.; Friedlander, S. K. *J. Colloid Interf. Sci.* **1964**, *19*, 621-647.

(53) Fulton, J. L.; Hoffman, M. M.; Darab, J. G.; Palmer, B. J.; Stern, E. A. *J. Phys. Chem. A* **2000**, *104*, 11651-11663.

(54) Chlistunoff, J.; Ziegler, K. J.; Lasdon, L.; Johnston, K. P. *J. Physical Chem.* **1999**, *103*, 1678.

(55) Ziegler, K. J.; Chlistunoff, J.; Lasdon, L.; Johnston, K. P. *Computers and Chemistry* **1999**, *27*, 421.

(56) Ron, H.; Cohen, H.; Matlis, S.; Rappaport, M.; Rubinstein, I. *J. Phys. Chem.* **1998**, *102*, 9861.

(57) Sung, M. M.; Sung, K.; Kim, C. G.; Lee, S. S.; Kim, Y. *J. Phys. Chem. B* **2000**, *104*, 2273-2277.

(58) Beverskog, B.; Puigdomenech, I. *J. Electrochem. Soc.* **1997**, *144*, 3476-3483.

# Chapter 5: Highly Luminescent Silicon Nanocrystals With Discrete Optical Transitions †

## 5.1 Introduction

Semiconductor cluster properties depend on size. For example, quantum confinement effects lead to unique electronic and optical properties, such as size-tunable excitation and luminescence energies with an overall loss of energy level degeneracy [1]. By studying the discrete energetic states that appear, these clusters can provide a test of our current understanding of quantum mechanics. Examples of size-dependent discrete optical transitions exist for clusters of direct band gap semiconductors, such as CdSe [1,2] and InAs [3]. This loss of energy level degeneracy, however, has not previously been observed in the optical properties of Si nanocrystals [4-14]. Why is Si different? Fig. 5.1 shows the Brillouin zone and band structure for bulk Si. In Si, the lowest lying $\Gamma \rightarrow X$ energetic transition violates conservation of momentum; therefore, light absorption requires phonon assistance, resulting in a very low transition probability [15]. Consequently, bulk Si photoluminescence is very weak. Quantum confinement in Si nanocrystals [4-14,16,17] and porous Si [18] leads to enhanced luminescence efficiencies with quantum yields that have reached as high as 5% at room temperature [4-7] and blue-shifted "band gap" energies. However, in sharp contrast to their direct

---

† The contents of this chapter appear in *J. Am. Chem. Soc.* **2001**, 123, 3743-3748.

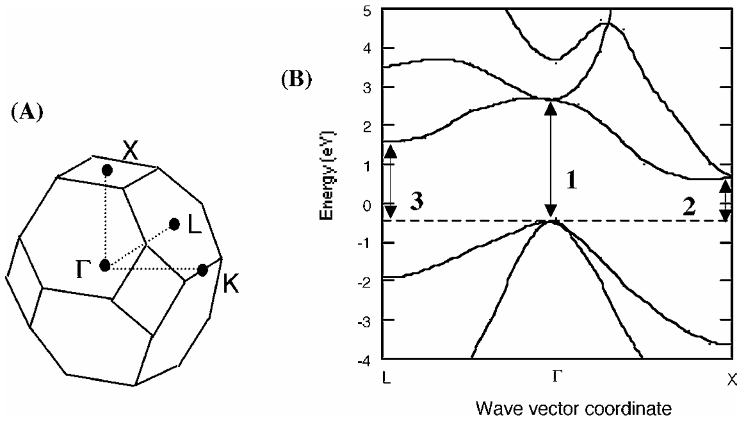

Fig. 5.1. (A) Brillouin zone for the diamond lattice. (B) Bulk band structure for Si. The arrows indicate the energies of the direct Γ→Γ (**1**) transition, and the indirect phonon-assisted Γ→L (**3**), Γ→X (**2**) transitions. Note that the direct transition at k=0 (the Γ→Γ transition) is a saddle point. Ramakrishna and Friesner [19] predicted that the indirect transitions increase in energy with decreased quantum dot size, with a slight red-shift in the direct transition energy. This prediction arises from the qualitative difference between the parabolic conduction band structure of a direct semiconductor and the saddle-point conduction band structure of the indirect semiconductor.

semiconductor counterparts, Si nanocrystals have not displayed discrete electronic transitions in the absorbance and photoluminescence excitation (PLE) spectra [4-14]. Without experimental evidence to the contrary, one might argue that even the smallest quantum dots of Si, with its indirect band gap, will not exhibit discrete electronic transitions at room temperature due to the phonon-assisted continuum occurring across the excitation spectra. This would have important implications on the development of quantum electronic devices utilizing Si.

Non-lithographic strategies are required to create Si quantum dots with the necessary dimensions (< 5 nm diameter) to exhibit quantum confinement effects at room temperature. The highly successful wet chemical techniques used to synthesize Group II-VI and III-V semiconductors have not been readily applied to Si, largely due to the high temperatures required to degrade the necessary precursors, which exceed the boiling points of available capping solvents. Furthermore, the covalent bonding of Si requires temperatures higher than the II-VI materials to achieve highly crystalline cores. Moderate progress has been made using alternative solution-phase reduction of Si salts [8-14] and aerosol [4-7] methods. These methods, however, have produced nanocrystals with extremely broad size distributions, which would smear any discrete size-dependent optical features in the absorbance and PLE spectra. Furthermore, the aerosol methods have required a thick oxide coating to stabilize their structure [4-7], which has been shown recently to significantly affect the photoluminescence (PL) energies of porous Si [20]. Recently, we demonstrated that nanocrystal steric stabilization in a supercritical solvent is possible [21]. Here, we demonstrate that by using a Si surface-passivating solvent heated and pressurized above its critical point, the necessary temperatures can be reached to degrade the Si precursor while maintaining solvation of the capping ligand to arrest particle growth (Fig. 5.2); thus, combining the best assets of both the aerosol and wet chemical approaches. The high temperature of 500 °C promotes Si crystallization. The additional advantage of using a supercritical (sc) solvent over a conventional solvent is the high diffusion coefficient, on the order of $10^{-3}$ to $10^{-4}$ $cm^2$ $s^{-1}$, [22] enabling the rapid reactant diffusion necessary to achieve diffusion-limited growth for the narrowest particle size distributions possible [23]. Using this method, relatively size-monodisperse, highly stable Si nanocrystals ranging from 15 Å to 40 Å in diameter are produced.

This article presents the structural, chemical, and optical characterization of the Si nanocrystals produced using this method, with transmission electron microscopy (TEM), energy dispersive X-ray spectroscopy (EDS), Fourier transform infrared spectroscopy (FTIR), UV-visible absorbance and luminescence (both PL and PLE) spectroscopy data. The Si nanocrystals consist of crystalline cores coated by hydrocarbon ligands bound through covalent alkoxide bonds with the nanocrystal surface. The nanocrystals luminesce with size-tunable color, from

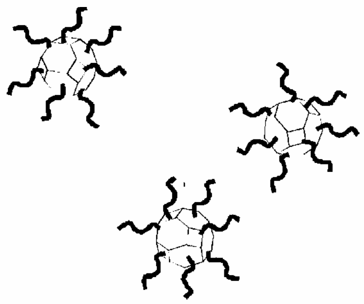

Fig. 5.2. Illustration of sterically stabilized nanocrystals. Flexible organic molecules, such as alkanes, provide repulsive interactions between other nanocrystals in solution; thus, preventing uncontrolled particle growth and aggregation. The crystalline semiconductor core tends to be well-defined and faceted.

the blue (15 Å diameter) to the green (25-40 Å diameter). Discrete optical transitions also appear in the absorbance and PLE spectra of the 15 Å diameter nanocrystals, which is consistent with quantum confinement effects in semiconductors.

## 5.2 Experimental Section

Diphenylsilane and anhydrous 1-octanol and hexane, packaged under nitrogen, were obtained from Aldrich Chemical Company (St. Louis, MO) and stored in a nitrogen glove box.

Organic-passivated Si nanocrystals were prepared by thermally degrading diphenylsilane in mixtures of octanol and hexane (octanol:$T_c$ = 385 °C, $P_c$ = 34.5 bar; hexane: $T_c$ = 235 °C, $P_c$ = 30 bar) well above the critical point at 500 °C and 345 bar in an inconnell high-pressure cell as shown in Fig. 5.3. The presence of Si particles was observed by the formation of a yellow solution; no color change was observed in the absence of diphenylsilane. When diphenylsilane was degraded in the presence of sc-ethanol rather than sc-octanol, the solution quickly turned from orange to brown and then clear as polydisperse micron-sized Si particles formed and settled on the walls of the reaction vessel [24]. This result suggests that, unlike ethanol, the bound octanol chains provide sufficient steric stabilization to prevent aggregation. The sc-octanol quenches the reaction and passivates the Si nanocrystal surface.

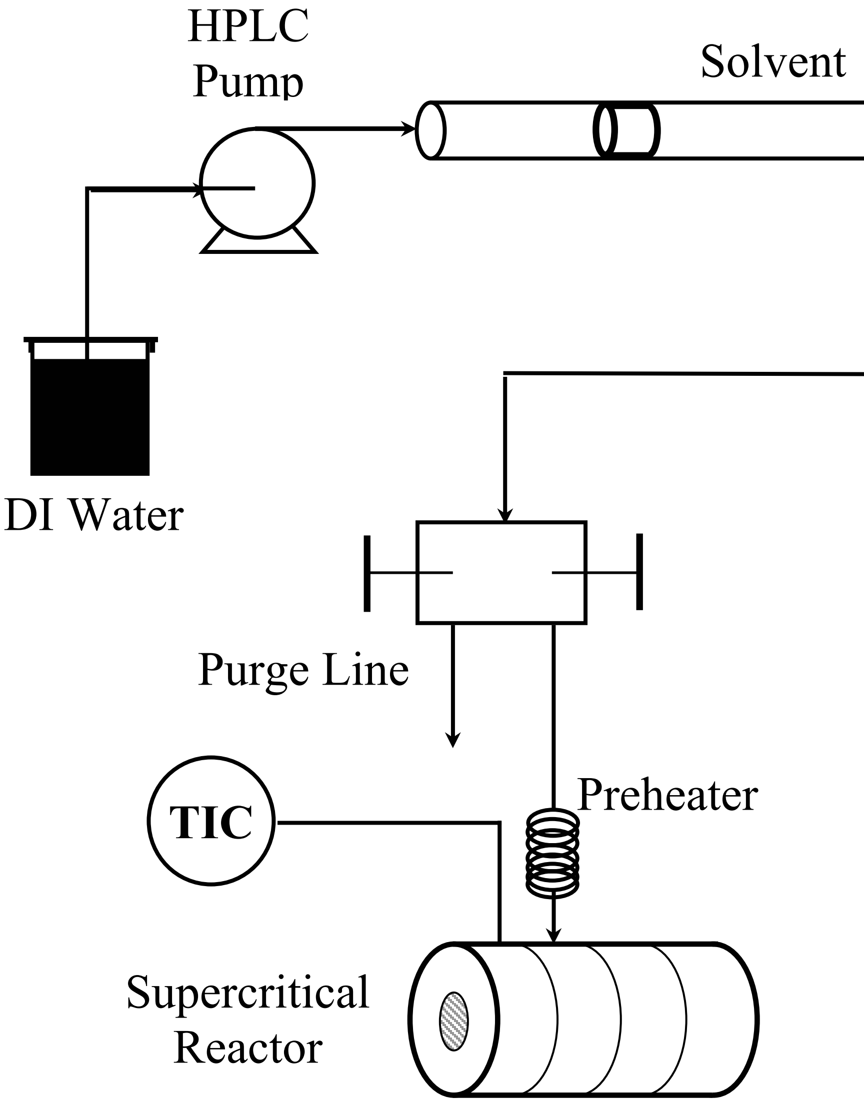

Fig. 5.3. Schematic of the supercritical reaction apparatus used in the batch production of Si nanocrystals.

A typical preparation begins inside a glove box. Diphenylsilane solution (250-500 mM in octanol) is loaded into an inconnell high-pressure cell (0.2 ml) and sealed under a nitrogen atmosphere. After removing the cell from the glove box, it is attached via a three-way valve to a stainless steel high-pressure tube (~ 40 $cm^3$) equipped with a stainless steel piston. Deionized water is pumped into the back of the piston using an HPLC pump (Thermoquest) to inject oxygen-free octanol through an inlet heat exchanger and into the reaction cell to the desired pressure, between 140-345 bar. The cell is covered with heating tape (2 ft) and heated to 500 °C (±0.2 °C) within 15-20 minutes using a platinum resistance thermometer and a temperature controller. The reaction proceeds at these conditions for 2 hours. Chloroform is used to extract the Si nanoparticles from the cell upon cooling and depressurization. The nanocrystal dispersion is subsequently dried and the organic-stabilized Si nanocrystals are redispersed in hexane or chloroform. The small 15 Å diameter particles also redisperse in ethanol. The larger Si nanocrystals, with slightly broader size distributions are produced by increasing the Si:octanol mole ratio using hexane as a solvent; a typical Si:octanol mole ratio is 1000:1. The reaction yield in percent conversion of Si precursor to Si incorporated in the nanocrystals varies from 0.5% to 5%.

A JEOL 2010 transmission electron microscope with 1.7 Å point to point resolution operating with a 200 kV accelerating voltage with a GATAN digital photography system was used for transmission electron microscopy. *In situ* elemental analysis was performed on the nanocrystals using an Oxford energy dispersive spectrometer. Electron diffraction images were obtained using the JEOL 2010 operating at 200 kV. Absorbance spectra were recorded using a Varian Cary 500 UV-Vis-NIR spectrophotometer with Si nanocrystals dispersed in ethanol or hexane. The extinction coefficients ε, were determined for the nanocrystals from the relationship between the measured absorbance ($A=\varepsilon \cdot c \cdot l$), the path length ($l$=10 cm), and the Si concentration determined from dry weights. The quantity $\varepsilon \cdot c$, is the absorption coefficient, $\alpha$. Luminescence measurements were performed using a SPEX Fluorolog-3 spectrophotometer. The PL and PLE spectra were corrected using quinine sulfate as a standard. Quantum yields were calculated by comparison with 9,10-Diphenylanthracene. FTIR measurements were obtained with a Perkin-Elmer Spectrum 2000 FTIR spectrometer. FTIR spectra were acquired from dried films of silicon nanocrystals deposited on Zinc Selenide windows.

## 5.3 Results and Discussion

***5.31 Synthesis and Characterization.*** Fig. 5.4 shows a TEM image of an organic-monolayer stabilized 40 Å diameter Si nanocrystal. The particle exhibits a crystalline core with a well-defined faceted surface. The lattice spacing is 3.1

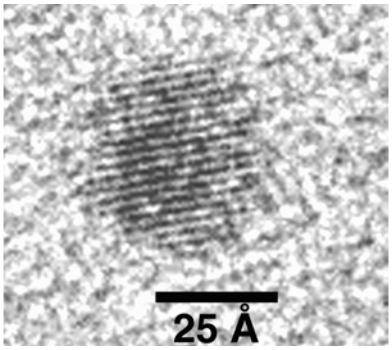

Fig. 5.4. High resolution TEM image of a 40 Å diameter Si nanocrystal. The lattice spacing of 3.1 Å is consistent with the (111) separation in the Si diamond-like lattice. The adsorbed organic capping layer is not visible in the TEM image. The faceted surface indicates that the nanocrystals were grown in a controlled environment.

Å, characteristic of the distance separating the (111) planes in diamond-like Si. Si nanocrystal formation likely propagates through a radical mechanism as shown below [25]:

$$(\mathrm{Ph})_2\mathrm{SiH}_2 \rightarrow (\mathrm{Ph})_2\mathrm{SiH}\bullet \tag{5.1}$$

$$2\ (\mathrm{Ph})_2\mathrm{SiH}\bullet \rightarrow \mathrm{H}(\mathrm{Ph})_2\mathrm{Si} - \mathrm{Si}(\mathrm{Ph})_2\mathrm{H} \quad . \tag{5.2}$$

The benzene rings help stabilize the diphenyl silane radical intermediates by delocalizing the electron charge. These free radicals can react to form Si-Si bonds. The octanol molecules subsequently displace the phenyl groups and cap the Si particle surface.

Size-monodisperse 15 Å diameter Si nanocrystals were obtained by reacting diphenylsilane in pure octanol with subsequent redispersion in ethanol. A fraction of the sample is made up of larger Si nanocrystals that form during the reaction that do not resuspend in ethanol due to their hydrophobicity; whereas, the extreme surface curvature of the 15 Å diameter nanocrystals provides ethanol with “access” to the polar Si-O-C capping layer termination to enable the size-selective dispersion of 15 Å diameter Si nanocrystals. The 15 Å diameter nanocrystals are barely perceptible in TEM images obtained with samples dispersed on a carbon-coated TEM grid (Fig. 5.5). In Fig. 5.5A, a low-resolution image of an aggregate of these 15 Å diameter nanocrystals also shows that the sample contains little size variation. For comparison, TEM images in Fig. 5.5 of

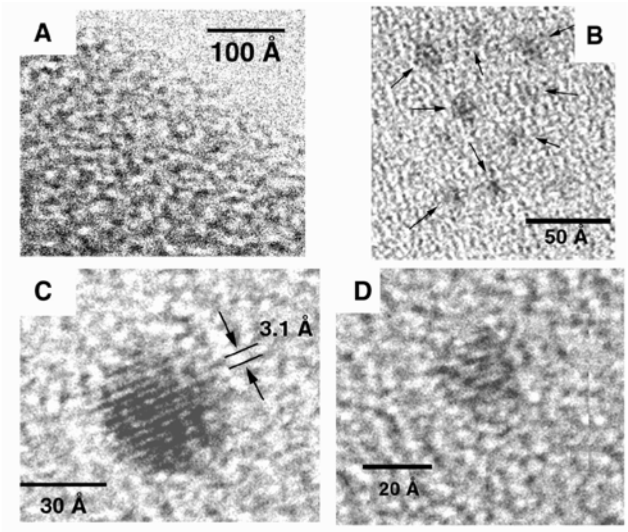

Fig. 5.5. TEM images of Si nanocrystals. (A) Low resolution TEM image of an aggregate of 15 Å diameter Si nanocrystals extended out from the edge of a carbon film. EDS of the aggregate (Fig. 5.6) confirmed that the nanocrystals were Si. (B) High resolution TEM image of several 15 Å diameter Si nanocrystals. (C) and (D) High resolution images of 35 and 25 Å diameter sterically stabilized Si nanocrystals. The lattice planes are visible in the 25 Å diameter nanocrystals.

larger Si nanocrystals with diameters ranging from 25 to 35 Å produced by performing the synthesis in sc-hexane with increased Si:octanol mole ratios clearly reveal highly crystalline cores and faceted surfaces. Crystalline lattice planes are observed in nanocrystals as small as 25 Å. Electron diffraction from these nanocrystals (Fig. 5.6) also confirms that the nanocrystals consist of crystalline Si cores with diamond lattice structure.

A variety of other techniques were used to characterize the Si nanocrystals, including energy dispersive X-ray spectroscopy (EDS), X-ray photoelectron spectroscopy (XPS), Fourier transform infra-red spectroscopy (FTIR), UV-vis absorbance and PL and PLE spectroscopy. *In-situ* EDS measurements shown in Fig. 5.7 of the nanocrystals imaged by TEM revealed Si in high abundance with the presence of oxygen and carbon as well. A quantitative analysis of the elemental ratios was not possible since the supporting substrate was carbon containing a measurable amount of residual oxygen. XPS, however, provides an elemental analysis of the particles, which gives an indication of how the nanocrystals are capped with the organic ligands.

Fig. 5.8 shows XPS data for 15 Å diameter Si nanocrystals, which reveals that the sample contains a Si:C ratio of 0.70:1. Using a shell approximation, $d_p = a_{Si}\left(3N_{Si}/4\pi\right)^{1/3}$, where $a_{Si}$ is the lattice constant (5.43 Å), the number of Si atoms $N_{Si}$, in a nanocrystal can be calculated. Particles with 15 Å diameter ($d_p$)

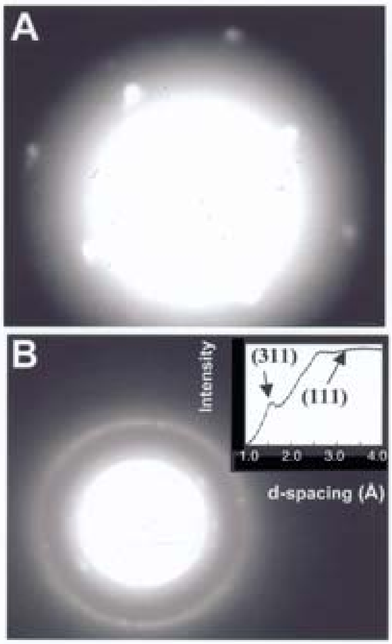

Fig. 5.6. Electron diffraction images and data for Si nanocrystals: (A) Diffraction pattern from a few Si nanocrystals with (200), (400), and (511) orientation; (B) Diffraction of many Si nanocrystals predominantly (111) and (311) oriented (Inset: measured d-spacings of 1.6 Å and 3.2 Å correspond to the (311) and (111) lattice spacings in Si).

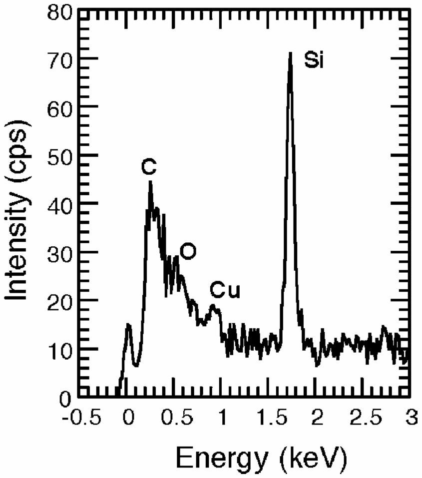

Fig. 5.7. EDS data of the nanocrystals imaged by TEM in Fig. 5.4A. The copper peak results from the copper TEM grid used as the material support.

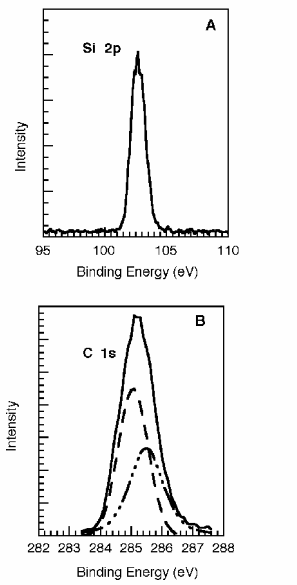

Fig. 5.8. XPS of the 15 Å diameter Si nanocrystals deposited on a graphite substrate: (A) Si 2p region in the spectra; modified area is 592.2 counts. (B) C 1s region (——) and its deconvoluted peaks from the graphite substrate (— —), and the capping ligand (— . . . —). The modified area of the C 1s curve due to the capping ligand is 850.5 counts. The silicon to carbon ratio (Si:C) is 0.70:1.

have approximately 88 atoms. The Si:C ratio determined from XPS can be used to calculate approximately the area occupied on the nanocrystal surface by each capping ligand. With the Si:C ratio equal to 0.7, the 15 Å cluster with 88 core Si atoms has 125 C atoms surrounding it. Each ligand has 8 carbons. Therefore, each particle is surrounded by approximately 16 capping ligands. Dividing the particle surface area by 16 indicates that each ligand occupies an average of 44 $Å^2$. This value is about twice that expected for a close-packed monolayer of ligands surrounding the nanocrystals. Therefore, XPS indicates that the ligands coat the nanocrystals with approximately 50% surface coverage. An estimate of the surface coverage of the largest 20 Å diameter nanocrystals in the sample size distribution gives an area per molecule of 33 $Å^2$, for approximately 70% surface coverage.

FTIR spectra show that the nanocrystals are most likely terminated with a combination of hydrogen and hydrocarbon chains, bound through an alkoxide (Si-O-C) linkage. In Fig. 5.9, the four characteristic methylene and terminal methyl stretching modes $\tilde{\nu}_{a(\mathrm{CH_2})} = 2928\ \mathrm{cm^{-1}}$, $\tilde{\nu}_{s(\mathrm{CH_2})} = 2855\ \mathrm{cm^{-1}}$, $\tilde{\nu}_{a(\mathrm{CH_3,ip})} = 2954.5\ \mathrm{cm^{-1}}$, $\tilde{\nu}_{s(\mathrm{CH_3,FR})} = 2871\ \mathrm{cm^{-1}}$, reveal that a hydrocarbon steric layer has indeed adsorbed to the particle surface. The notable absence of the hydroxyl stretch ($\tilde{\nu}_{(\mathrm{O-H})} = 3300\ \mathrm{cm^{-1}}$) and the presence of the strong doublet corresponding to the Si-O-$CH_2$- stretching modes, $\tilde{\nu}_{(\mathrm{Si\text{-}O\text{-}CH_2\text{-}})}$=1100-1070 $\mathrm{cm^{-1}}$, suggests covalent

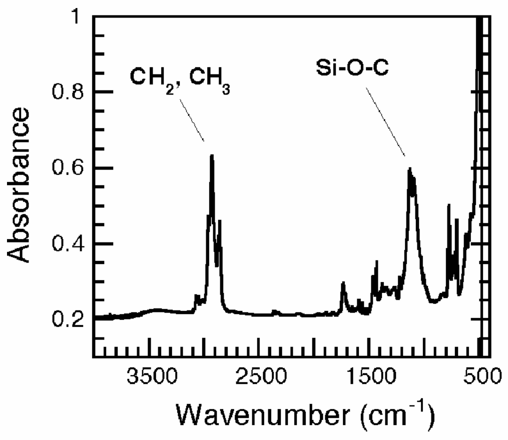

Fig. 5.9. FTIR spectra of Si nanocrystals on a ZnSe window. The spectra reveal that the sterically stabilizing hydrocarbon chains are covalently linked to the Si surface through alkoxide linkages. These covalent linkages give rise to highly stable optical properties in the presence of ambient oxygen and water.

alkoxide bonding to the Si nanocrystal surface [26,27]. Siloxane Si-O-Si stretches typically occur at slightly lower wave number (1085 and 1020 $cm^{-1}$); however, the presence of residual oxide on the nanocrystal surfaces cannot be completely excluded based on this data alone. The absence of the very strong characteristic aryl-Si stretching mode, at $\tilde{\nu}_{(\text{Si-Ph})} = 1125 - 1090\ \text{cm}^{-1}$, confirms precursor degradation. The lack of the strong $\tilde{\nu}_{(\text{Si-C-Si})} = 1080 - 1040\ \text{cm}^{-1}$ stretching mode eliminates the possibility that the nanoparticles consist of a Si-C core, or that the alkane layer is directly adsorbed to the Si surface. Strong Si TO (transverse optical) phonon bands occur between 450 and 520 $cm^{-1}$, indicating that the particles are composed of Si only [28,29]. Strong peaks between 750 to 850 $cm^{-1}$ and subtle absorption peaks in the range 2100 to 2300 $cm^{-1}$ can possibly be assigned to a variety of Si-H stretching modes [26,27]. There is also a possible carbonyl stretch at $\tilde{\nu} \cong 1700\ \text{cm}^{-1}$ which could result from octanol adsorption through a Si-C=O linkage if alcohol oxidation to the aldehyde occurs. Based on the XPS and FTIR data, the nanocrystal surface is coated mostly by the hydrocarbon ligands. However, the remaining 30% to 50% of the surface is coated with a combination of hydrogen, Si-C=O, and possibly a small portion of oxide.

***5.32 Optical Properties.*** The Si nanocrystals photoluminesce as shown in Fig. 5.10 with overall quantum yields as high as 23% at room temperature.

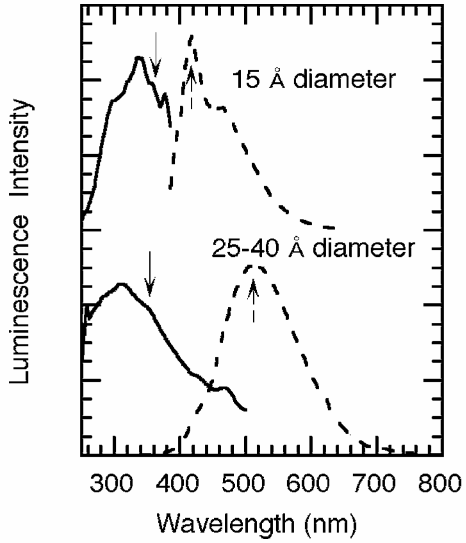

Fig. 5.10. Room temperature PL (solid lines, excitation energy denoted by solid arrows) and PLE (dashed lines, detection energy denoted by dashed arrows) spectra of Si nanocrystals. The spectra of 15 Å diameter nanocrystals are compared with spectra of slightly larger particles with a broader size distribution.

Several closely spaced discrete features appear in the PLE spectra of the 15 Å diameter nanocrystals, which are mirrored by a few meV in the absorbance spectra in Fig. 5.11. As shown in Fig. 5.10, the nanocrystals exhibit size-dependent PL and PLE spectra, with the smaller nanocrystals (15 Å diameter) emitting in the near-UV and the larger nanocrystals (25 to 40 Å diameter) emitting green light (see Fig. 5.12). For all sizes, the absorption coefficient $\alpha$, was found to increase quadratically with incident energy, $\alpha \sim \left[h\nu - E_g\right]^2$, near the absorption edge (Fig. 5.13)—characteristic of a predominantly indirect transition [15]. Fig. 5.13 compares the extinction coefficients for bulk Si with those measured for the 15 Å diameter nanocrystals. The indirect $\Gamma \rightarrow X$ transition remains the lowest energy transition, increasing from 1.2 eV (bulk Si) to 1.9 eV due to quantum confinement. It should be noted that it appears that the direct $\Gamma \rightarrow \Gamma$ transition has *red* shifted to 3.2 eV from 3.4 eV and the $L \rightarrow L$ transition energy has blue-shifted from 4.4 eV to 4.7 eV, in *quantitative* agreement with empirical pseudopotential calculations by Ramakrishna and Friesner [19], although these assignments cannot be made conclusively. Further comparison of the extinction coefficients measured for the nanocrystals with values for bulk Si reveals an overall lifting of the critical point degeneracies (direct transitions at k = 0 and away from k = 0), as predicted by both empirical pseudopotential [19] and tight-binding [30,31] calculations, and an oscillator strength enhancement. These results

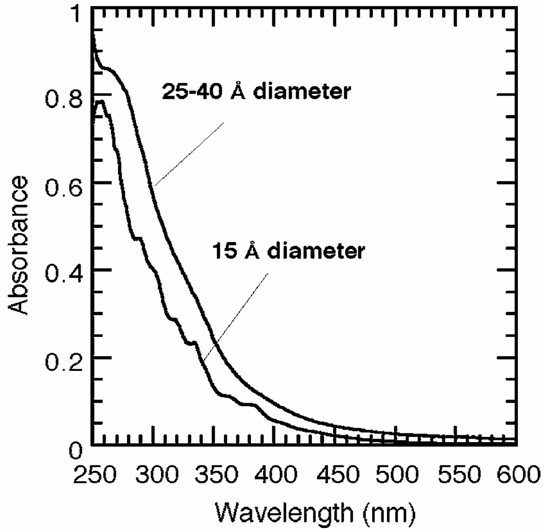

Fig. 5.11. Room temperature absorbance spectra of Si nanocrystals formed under supercritical conditions in the presence of octanol. The absorbance spectra were insensitive to solvent polarity, indicating that the absorbance is due to an exciton state and not a charge-transfer transition between bound ligands. Note the blue shift in the absorbance edge, and the appearance of discrete optical transitions in the spectra of the 15 Å diameter nanocrystals compared to the larger, more polydisperse nanocrystals.

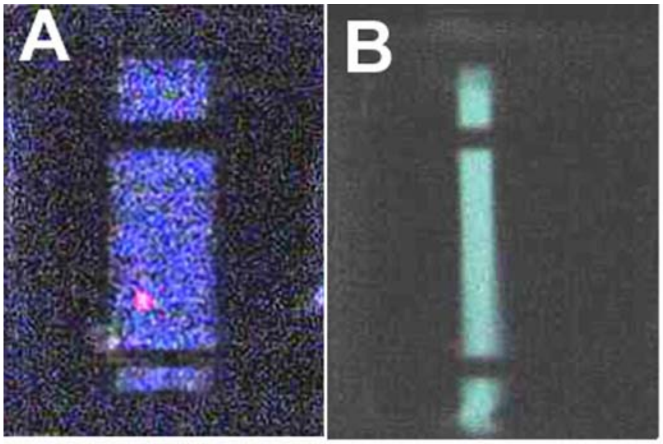

Fig. 5.12. Photographic image of the luminescent Si nanocrystals excited at 320 nm in hexane: (A) 15 Å diameter Si nanocrystals; (B) 25-40 Å diameter nanocrystals. The smaller nanocrystals emit in the near-UV and appear deep blue, whereas the larger particles appear blue-green.

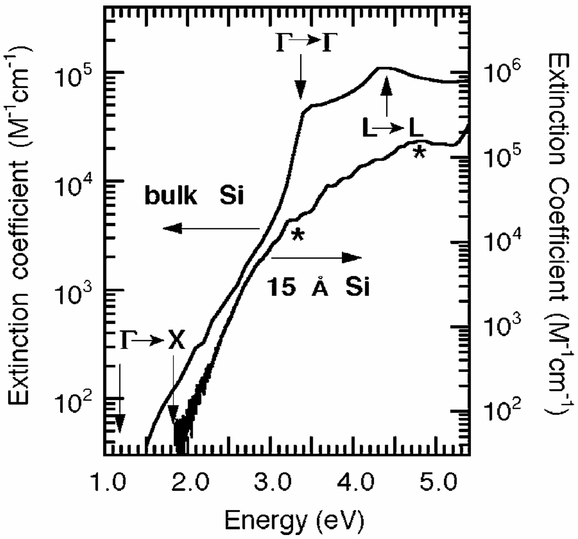

Fig. 5.13. Extinction coefficients plotted on a log scale for bulk Si and those measured for 15 Å Si nanocrystals formed by arrested precipitation in supercritical octanol. The absorption edge corresponds to the indirect Γ→X transition and the two peaks in the bulk Si spectra correspond to the Γ→Γ and L→L critical points at 3.4 eV and 4.3 eV, respectively. Note the apparent blue shift of the Γ→X and L→L transitions in the nanocrystals due to quantum confinement and the apparent red shift of the Γ→Γ transition, as predicted by Ramakrishna and Friesner [19].

contrast the spectra for slightly larger, more polydisperse Si nanocrystals, ranging in size from 25 to 40 Å in diameter in Fig. 5.11, which exhibit monotonically increasing featureless absorbance spectra. A slight exciton peak, however, does seem to appear in the PLE spectra in Fig. 5.10 for the larger nanocrystals at 2.6 eV (470 nm). The Si nanocrystal PL was remarkably stable in the presence of atmospheric oxygen, especially when considering the sensitivity of the optical properties of porous-Si to surface chemistry, such as oxidation [20,32]. The sc-technique provides Si nanocrystals with sufficiently robust surface passivation to prevent strong interactions between the Si cores and the surrounding solvent to enable efficient luminescence from Si. Comparison between the PL and PLE spectra in Fig. 5.10 reveals a Stokes shift of approximately 100 meV with respect to the lowest energy peak in the PLE spectra. The relatively broad PL peak has a characteristic lifetime of 2 nsec, indicates that various nonradiative processes are important in the nanocrystals. It is worth noting that the low energy PL peak observed by Brus, *et al.* [4-7] for ~20 Å diameter oxide-coated Si nanocrystals at 1.6 eV was not observed in any of these samples.

The origin of the photoluminescence in Si nanocrystals is quite complex and remains actively debated. The PL spectra in Fig. 5.10 is clearly size dependent, with the larger particles emitting lower energy light than the smaller particles, consistent with the general perception of quantum confinement effects in Si. The PL from Si nanocrystals, however, has been shown to be highly sensitive to surface chemistry, especially the presence of oxide on the nanocrystal surface [20,32]. Indeed, the PL spectra of the 15 Å diameter nanocrystals is complicated by the presence of two prominent peaks in the 15 Å nanocrystal spectra as shown in Fig. 5.10: one at 2.95 eV (419 nm) and one at 2.65 eV (467 nm). Furthermore, the PL was found to depend on the excitation wavelength, with 3.4 eV (363 nm) excitation yielding the highest quantum yield and the sharpest PL. Increasing the excitation energy from 3.4 eV to 4.4 eV (281 nm) led to a decrease in the intensity of the highest energy feature with respect to the low energy "satellite" peak, and a decrease in the overall quantum yield. Although we cannot assign these peaks conclusively at this time, we propose that the higher energy peak is intrinsic to quantum confinement in Si nanocrystals and the lower energy peak results from the presence of oxygen on the particle surface, as proposed for porous Si [20]. Wolkin, *et al.* [20] calculated that the PL energy due to intrinsic quantum confinement in Si can in some cases differ from the PL energy due to surface states, specifically Si=O. For nanocrystals greater than 3 nm in diameter, the intrinsic and surface state emission energies are the same, with emission at 2 eV (620 nm) [20]. However, 15 Å diameter nanocrystals were predicted to give rise to intrinsic PL at 2.8 eV, and surface state PL resulting from the presence of oxygen at 2.3 eV (537 nm) [20]. The PL spectra of the Si nanocrystals shown in Fig. 5.10 are consistent with this interpretation. It should be noted, however, that peak splitting due to separate direct and phonon-assisted absorption and emission events, has been observed by Calcott *et al.* [33] for porous Si and may provide an alternative explanation.

### 5.4 Conclusions

Sc-octanol serves as an effective capping ligand for the synthesis of Si nanocrystals. Significant quantities of stable, well-passivated nanocrystals can be produced in a simple batch reactor. The smallest size-monodisperse 15 Å diameter Si nanocrystals exhibit previously unobserved discrete electronic absorption and luminescence transitions due to quantum confinement effects. This study also confirms that Si clusters as small as 15 Å in diameter still behave as indirect semiconductors. This supercritical route for nanostructure formation might be applied to other materials, such as Si nanowires, [34] that require high temperatures for crystal formation and the solvation of capping ligands.

### 5.5 References

(1) Alivisatos, A. P. *Science* **1996**, *271*, 933.

(2) Murray, C. B.; Norris, D. J.; Bawendi, M. G. *J. Am. Chem. Soc.* **1993**, *115*, 8706.

(3) Banin, U.; Lee, C. J.; A.A., G.; Kadavanich, A. V.; Alivisatos, A. P.; Jaskolski, W.; Bryant, G. W.; Efros, A. L.; Rosen, M. *J. Chem. Phys.* **1998**, *109*, 2306.

(4) Wilson, W. L.; Szajowski, P. F.; Brus, L. E. *Science* **1993**, *262*, 1242.

(5) Littau, K. A.; Szajowski, P. J.; Muller, A. J.; Kortan, A. R.; Brus, L. E. *J. Phys. Chem.* **1993**, *97*, 1224.

(6) Brus, L. E. *J. Phys. Chem.* **1994**, *98*, 3575.

(7) Brus, L. E.; Szajowski, P. F.; Wilson, W. L.; Harris, T. D.; Schuppeler, S.; Citrin, P. H. *J. Am. Chem. Soc.* **1995**, *117*, 2915.

(8) Batson, P. E.; Heath, J. R. *Phys. Rev. Lett.* **1993**, *71*, 911.

(9) Heath, J. R. *Science* **1992**, *258*, 1131.

(10) Bley, R. A.; Kauzlarich, S. M. *J. Am. Chem. Soc.* **1996**, *118*, 12461.

(11) Yang, C.-S.; Bley, R. A.; Kauzlarich, S. M.; Lee, H. W. H.; Delgado, G. R. *Journal of the american chemical society* **1999**, *121*, 5191.

(12) Van Buuren, T.; Dinh, L. N.; Chase, L. L.; Siekhaus, W. J.; Terminello, L. J. *Phys. Rev. Lett.* **1998**, *80*, 3803.

(13) Wilcoxon, J. P.; Samara, G. A. *Appl. Phys. Lett.* **1999**, *74*, 3164.

(14) Wilcoxon, J. P.; Samara, G. A.; Provencio, P. N. *Phys. Rev. B* **1999**, *60*, 2704.

(15) Sze, S. M. *Physics of Semiconductor Devices*; 2nd ed.; Wiley: New York, 1981.

(16) Furukawa, S.; Miyasato, T. *Phys. Rev. B* **1988**, *38*, 5726.

(17) Takagai, H.; Ogawa, H.; Yamzaki, Y.; Ishizaki, A.; Nakagiri, T. *Appl. Phys. Lett.* **1990**, *56*, 2379.

(18) Canham, L. T. *Appl. Phys. Lett.* **1990**, *57*, 1046.

(19) Ramakrishna, M. V.; Friesner, R. A. *J. Chem. Phys.* **1992**, *96*, 873.

(20) Wolkin, M. V.; Jorne, J.; Pauchet, P. M.; Allan, G.; Delerue, C. *Phys. Rev. Lett.* **1999**, *82*, 197.

(21) Shah, P. S.; Holmes, J. D.; Doty, R. C.; Johnston, K. P.; Korgel, B. A. *J. Am. Chem. Soc.* **2000**, *122*, 4245.

(22) McHugh, M. A.; Krukonis, V. J. *Supercritical Fluids Extraction: Principles and Practice*; 2nd ed.; Butterworth-Heinman: MA, 1993.

(23) Reiss, H. *J. Chem. Phys.* **1951**, *19*, 482.

(24) Barj, M.; Bocquet, J. F.; Chhor, K.; Pommier, C. *J. Mater. Sci.* **1992**, *27*, 2187.

(25) March, J. *Advanced Organic Chemistry: Reactions, Mechanisms, and Structure*; 4th ed.; Wiley: New York, 1992.

(26) Pretsch, E.; Clerc, T.; Seibl, J.; Simon, W. *Tables of Spectral Data for Structure Determination of Organic Compounds*; Springer-Verlag: Berlin, 1942.

(27) Socrates, G. *Infrared Characteristic Group Frequencies Tables and Charts*; John Wiley & Sons: New York, 1994.

(28) Giannozzi, P.; de Gironcoli, S.; Pavone, P.; Baroni, S. *Phys. Rev. B* **1991**, *43*, 7231.

(29) Scholten, A. J.; Akimov, A. V.; Dijkhuis, J. I. *Phys. Rev. B* **1993**, *47*, 13910.

(30) Hill, N. A.; Whaley, K. B. *Phys. Rev. Lett.* **1995**, *75*, 1130.

(31) Hill, N. A.; Whaley, K. B. *J. Electron. Mat.* **1996**, *25*, 269.

(32) Lauerhaas, J. M.; Sailor, M. J. *Science* **1993**, *261*, 1567.

(33) Calcott, P. D. J.; Nash, K. J.; Canham, L. T.; Kane, M. J.; Brumhead, D. *J. Phys.: Condens. Matter* **1993**, *5*, L91.

(34) Holmes, J. D.; Johnston, K. P.; Doty, R. C.; Korgel, B. A. *Science* **2000**, *287*, 1471.

# Chapter 6: Synthesis of Germanium Nanocrystals within a Supercritical Fluid Yielding Size-Dependent Properties †

## 6.1 Introduction

At the nanometer length-scale, material dimensions lead to quantum confinement effects that give rise to unique electronic and optical properties useful for a variety of new technologies including, electronic, optical, medical, coatings, catalytic, memory, and sensor applications [1]. A variety of wet chemical methods have been developed for nanocrystal synthesis. The main issues are control over particle size and size distribution, surface passivation and core crystallinity. Metal nanocrystals, such as silver and gold, can be synthesized at room temperature; [2,3] whereas, semiconductor nanocrystals, such as CdSe [4] and InAs [5], must be grown at high temperatures in high boiling point solvents to achieve crystalline cores and well-defined shape.

Recently, quantum confinement was observed in silicon nanocrystals produced in supercritical octanol [6]. The Si nanocrystals exhibited a loss of energy level degeneracy in their optical properties resulting from quantum confinement, which has not previously been observed in the optical properties of germanium nanocrystals. Similar to silicon nanocrystals, the lowest lying $\Gamma \rightarrow L$ energetic

---

† Portions of this chapter are being prepared for a manuscript.

transition violates conservation of momentum; therefore, light absorption requires phonon assistance, resulting in a very low transition probability (see Figure 6.1). Consequently, bulk silicon and germanium photoluminescence is very weak. Previous attempts to produce germanium nanocrystals inside $SiO_2$ matrices exhibited photoluminescence [7-9] as well as a solution phase method [10,11]. Several of these methods have exhibited changes in the photoluminescence dependent on size, but the source of this luminescence is highly debated and is often attributed to surface states and trapped states [9,12-14]. Furthermore, while silicon nanocrystals remained an indirect band gap semiconductor even at sizes near 15 Å [6], germanium nanocrystals may be more likely to undergo a transition to a direct band gap semiconductor since Ge is nearly a direct band gap semiconductor in the bulk, unlike Si in which $\Gamma \rightarrow X$ (1.2 eV) vs. $\Gamma \rightarrow \Gamma$ (3.1 eV) [8,15-17] (see Figure 6.1).

Supercritical fluids (SCFs) offer several processing advantages over conventional solvents, which have led to its increased use in materials chemistry [18-21] and more specifically, for nanocrystal synthesis. [6,20-25] SCFs exhibit the combined characteristics of both gas and liquid solvents to provide a medium with densities characteristic of liquids, and gas-like viscosities and diffusivities. Thus, mass transfer rates approach those in gases, while solvation properties resemble those of conventional liquid solvents. Furthermore, supercritical fluids exhibit unique *tunable* solvation characteristics, as subtle changes in pressure and

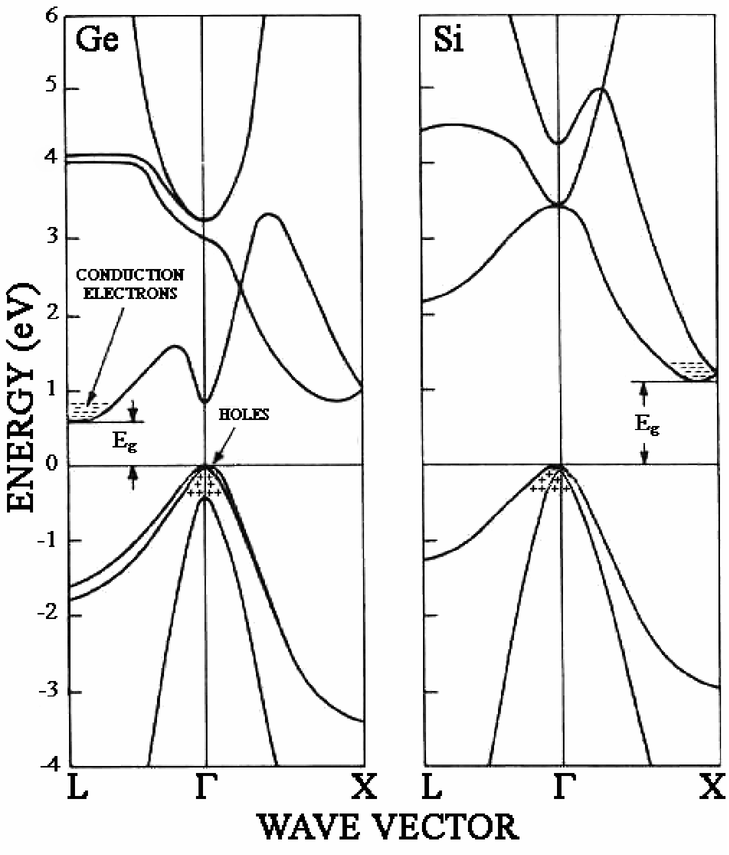

Fig. 6.1. Energy-band structures of bulk silicon and germanium. (+) Holes in the valence band. (—) Electrons in the conduction band.

temperature in SCFs alter the solvent density. This property might be utilized to improve many aspects of nanocrystal processing—such as size-selective separations [26], synthesis [6,22-25], and self-assembly.

Here we report our finding that germanium nanocrystals formed in an arrested-growth method within supercritical octanol exhibit size dependent optical properties. These nanocrystals consist of highly crystalline cores with few defects, surrounded by an organic layer of $C_8$ hydrocarbon chains bound through an alkoxide layer. These chains serve as a steric stabilizer preventing unwanted agglomeration and also aid in quenching the growth of the crystals. Transmission electron microscopy (TEM), energy dispersive X-ray spectroscopy (EDS), X-ray photoelectron spectroscopy (XPS), selected area electron diffraction (SAED), Fourier transform infrared spectroscopy (FTIR), UV-visible absorbance and photoluminescence were used to analyze the structural, chemical, and optical properties of these crystals. The Ge crystals produced are size-polydisperse in nature; however, size-selectivity of these nanocrystals is obtained by the use of a chromatographic method. Luminescence of the nanocrystals is shown to be dependent on the size with smaller particles resulting in a blue-shift of the PL energy consistent with quantum confinement of the band gap energy and resulting in high quantum yields. UV-visible spectra are also size-dependent with smaller particles resulting in discrete optical features. In addition, these features are shown to be size-dependent characteristic of the loss of energy level degeneracy due to quantum confinement. At the smallest particle sizes, these features appear to behave similar to molecular absorbance with the density of the energy levels concentrated into just a few bands yielding high oscillator strengths further suggesting the idea that nanocrystals may be considered as ‘artificial’ atoms [1].

## 6.2 Experimental Section

***6.21 Nanocrystal synthesis***. Tetraethyl germane was obtained from Aldrich Chemical Company (St. Louis, MO) and de-oxygenated by freeze-pump-thaw, while anhydrous 1-octanol was packaged under nitrogen (Aldrich) and stored in a nitrogen glove box. Organic-passivated germanium nanocrystals were prepared by thermally degrading tetraethyl germane in pure 1-octanol ($T_c$ = 385 °C; $P_c$ = 34.5 bar) well above the critical point at 450 °C and above 482 bar. These reactions were performed in either a 1 mL 316 stainless steel or a 10 mL 316 stainless steel reactor. The 1 mL reactors can be seen in Figure 6.2 and consist of a batch cell with a standard LM6 HIP gland and plug (High Pressure Equipment, Erie, PA). These reactors (7/32″ I.D and ¾″ O.D.) can then be placed inside a preheated brass block (8″ × 1 ½″ × 3″) heated by four cartridge heaters (Omega, Stamford, CT) and thermostated with a platinum resistance thermocouple (Omega) and a temperature controller (Omega). An aluminum shell filled with insulation surrounds the brass-heating block and maintains the

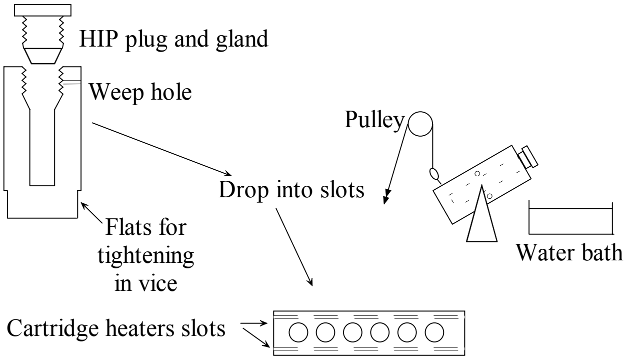

Fig. 6.2. Schematic of high-temperature batch reactors.

temperature. Once the reaction is complete, a pulley can be utilized to cause the batch cells to fall from the heating block into a water bath. A polycarbonate barricade was placed in front of the apparatus for safety.

The 10 mL reaction cell is based on a similar design. It consists of a reactor (7/16″ I.D. and 1 ¾″ O.D.—hex shaped) purchased from HIP utilizing a reducer to 1/16″ tubing. Due to the large volume, this reactor was attached to a Heise (Stratford, CT) digital pressure gauge and a rupture disc rated for approximately 10,000 psia. The cell is covered with heating tape and heated to 450 °C in approx. 30-45 minutes to within 5 °C using a platinum resistance thermometer inserted into the reactor wall and an Omega temperature controller. For safety, the reactor was mounted inside a 5-gallon solvent cabinet (Lab Safety Supply, Janesville, WI) and purged with nitrogen to remove oxygen and any combustible gases caused by potential leaks. Once again, a polycarbonate shield was placed in front of the apparatus.

A 250 mM tetraethyl germane in octanol precursor solution was loaded into either a 1 mL or 10 mL reactor to achieve a supercritical solvent density of approx. 0.5-0.8 g $cm^{-3}$ and sealed under a nitrogen atmosphere. After the cell is removed from the glove box it is heated by either the brass-heating block or mounted inside the solvent cabinet and heated by heating tape (Barnstead/Thermolyne) and insulated. Once the reactor had achieved the desired reaction temperature, the reaction was allowed to proceed for 30 min. Upon cooling, chloroform was used to extract the germanium nanocrystals from the cell yielding a pale yellow to dark brown solution. The particles were subsequently dried using a rotary evaporator (Buchi, Flawil, Switzerland) and vacuum oven (VWR, West Chester, PA) to remove excess octanol and re-dispersed in hexane, chloroform, or toluene. Size-selectivity was performed using a chromatography column filled with Bio-Beads® (Bio-Rad Laboratories, Hercules, CA), typically resulting in 15-20 fractions.

***6.22 Bio-bead preparation***. Bio-Beads® (200-400 mesh, 8% crosslinked styrene divinylbenzene copolymer) were swollen by placing the beads in six times the resin weight in THF for a period of several hours. The chromatography column was then filled with the resin slurry and the packing material was allowed to settle resulting in a bed volume of approximately 50 mL. The eluent was then changed from THF to chloroform by flushing the column with a minimum of three bed volumes of chloroform. A short segment of sand was added to the top of the column to prevent the packing material from floating in the eluent. Size-polydisperse Ge nanoparticles were then dispersed in a small volume of chloroform (~1 mL) and added to the top of the column. The eluent flow rate through the column was enhanced by applying moderate air pressure to the top of the column, resulting in a flow rate of approximately 2 mL/min. In accordance with size-exclusion chromatography, the smaller particles had a longer path to travel because of diffusion into the porous beads and consequently flowed through the column at a slower rate, while larger particles flow through the column at faster rates. This permitted the separation of the size-polydisperse sample into several fractions (15-20) of size-monodisperse nanoparticles.

***6.23 Characterization methods*.** A JEOL 2010 transmission electron microscope with 1.7 Å point to point resolution operating with a 200 kV accelerating voltage with a GATAN digital photography system was used for transmission electron microscopy. All samples were prepared on Electron Microscope Sciences 200 or 400-mesh carbon coated copper grids by dispersing suspended nanoparticles onto the grid and evaporating the solvent. *In-situ* elemental analysis was performed on the nanocrystals using a LEO 1530 SEM operated at 10kV with an iXRF energy dispersive spectrometer. Electron diffraction images were obtained using the JEOL 2010 operating at 200 kV. Absorbance spectra were recorded using a Varian Cary 500 UV-Vis-NIR spectrophotometer with germanium nanocrystals dispersed in chloroform. Luminescence measurements were performed using a Fluorolog fluorometer (Jobin Yvon SPEX division, Edison, NJ) with a cooled PMT (Products for Research, Inc, Danvers, MA) and a Xenon short arc lamp operated at 950V. The quantum efficiencies of PL spectra were determined using quinine bisulfate as a standard. FTIR measurements were obtained with a Perkin-Elmer Spectrum 2000 FTIR spectrometer with the nanoparticles dispensed on PTFE cards. X-ray photoelectron spectroscopy (XPS) was performed on a Physical Electronics XPS 5700, with a monochromatic Al X-ray source ($K_\alpha$ excitation at 1486.6 eV). For

XPS, the samples were deposited on a silicon wafer (cleaned with a 50:50 mixture of methanol: HCl), vacuum-dried at 25°C to remove all residual solvent, and stored under nitrogen.

## 6.3 Results and Discussion

***6.31 Synthesis and characterization.*** Figure 6.3 shows HRTEM images of octanol-capped germanium nanoparticles of various sizes. As can be seen by the HRTEM images, the particles have a crystalline core and show no defects. The lattice spacing is shown to be 2.10 Å and 2.78 Å characteristic of the β-Sn tetragonal form of germanium for the <220> and <201> plane, respectively (compared to 2.11 Å and 2.73 Å [27]). Selected area electron diffraction (SAED) shown in Figure 6.3d confirms the presence of the tetragonal phase. In addition, to the planes noted above, the <102> plane was visible at 3.02 Å compared to 3.00 Å [27]. The presence of a tetragonal phase is consistent with the high pressure phase [27] of germanium crystals as well as the crystal formation witnessed for many germanium nanocrystals smaller than 4 nm [14,28,29] and has even been attributed to the source of photoluminescence in these germanium nanocrystals [14].

The germanium nanocrystals are formed by thermally decomposing the precursor tetraethyl germane (TEG) within supercritical octanol at temperatures above 450°C and pressures above 482 bar (7000 psia). The supercritical environment allows the use of an arrested growth synthesis by maintaining a

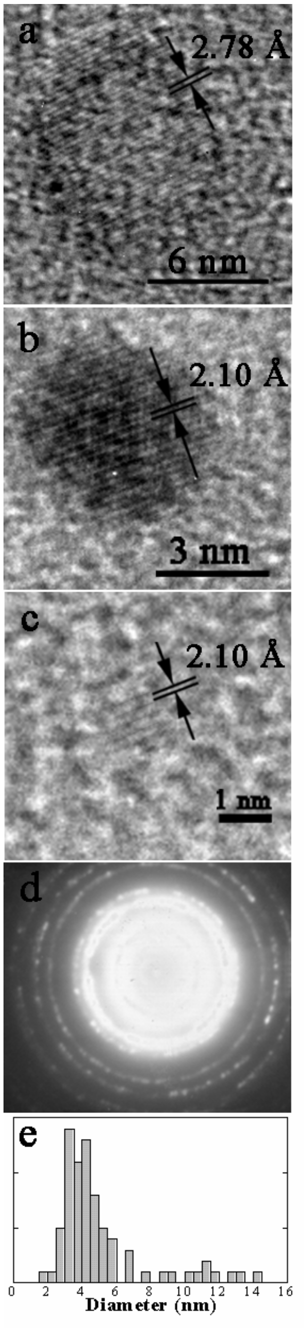

Fig. 6.3. HRTEM images of octanol-capped germanium nanocrystals of (a) 12 nm; (b) 5.5 nm; (c) 1.5 nm; (d) SAED of crystal; and (e) histogram of distribution.

solvent environment (ρ ~ 0.5 to 0.8 g $cm^{-3}$) even at the high temperature required for precursor degradation in Group IV semiconductors. The organic capping ligand, 1-octanol, then quenches the growth and stabilizes the formation of germanium nanocrystals by bonding to the surface through an alkoxide linkage with an extended hydrocarbon chain, as shown below, which interacts with the solvent making it soluble in common organic solvents.

The nanocrystals produced were size-polydisperse with diameters ranging from 15 Å to 140 Å as can be seen in the histogram in Figure 6.3e. The polydispersity is in contrast to previous results with silicon nanocrystals [6] that showed the formation of size-monodisperse samples of nanocrystals. The cause of this-polydispersity may be attributed to several factors. First, the strength of the alkoxide bond could affect the polydispersity. Indeed, Si-O-C bonds are stronger bonds than Ge-O-C (~185 kcal/mol vs. ~155 kcal/mol), which could result in a decreased ability of the capping ligand to quench the growth for germanium nanocrystals [30,31]. In addition, the kinetics and growth mechanisms may be vastly different. While little is known about the kinetics of organosilanes and organogermanes at high temperatures, previous work in other SCFs has shown that the growth mechanism may be by coagulation or condensation [24,25]. Coagulation mechanisms tend to achieve more size polydisperse particles while condensation mechanisms achieve monodisperse size distributions. It was also shown in the synthesis of copper nanocrystals in supercritical water that changes in pH could alter the mechanism of growth [25] and it is plausible that other factors such as temperature and density may also affect these mechanisms. Furthermore, the densities applied in the synthesis described here are more liquid-like than those previously used, which may affect reaction kinetics as well as the stabilization of the nanocrystals produced. While kinetics and growth mechanisms will control the size distribution of crystals produced, changes in density can have significant effects on the size of nanocrystals that can be stabilized within a supercritical fluid [26]. Finally, Wu and Yang [32] have shown that the melting point of germanium nanowires is significantly depressed from the bulk value (930°C) for diameters between 20 to 50 nm (as low as 450°C), which may have effects on the sizes of nanoparticles produced.

A variety of other techniques were used to characterize the Ge nanocrystals, including energy dispersive X-ray spectroscopy (EDS), X-ray photoelectron spectroscopy (XPS), Fourier transform infra-red spectroscopy (FTIR), UV-vis absorbance, and PL and PLE spectroscopy. *In-situ* EDS measurements of the nanocrystals shown in Figure 6.4 revealed germanium in high abundance with the presence of oxygen and carbon as well. XPS data shown in Figure 6.5 for monodisperse Ge nanocrystals approx. 2 nm in diameter confirms the EDS results. The corrected XPS area of the germanium ($2p_{3/2}$) peak compared to the area of the carbon peak results in a Ge:C ratio of approx. 0.3:1.

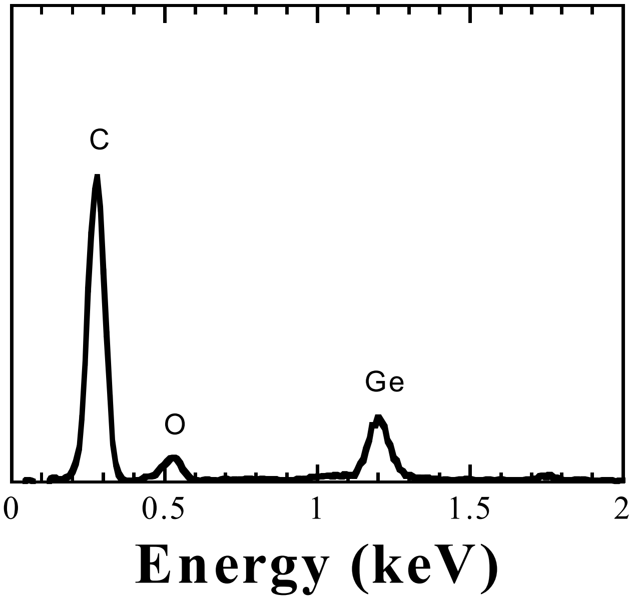

Fig. 6.4. EDS data for germanium nanocrystals.

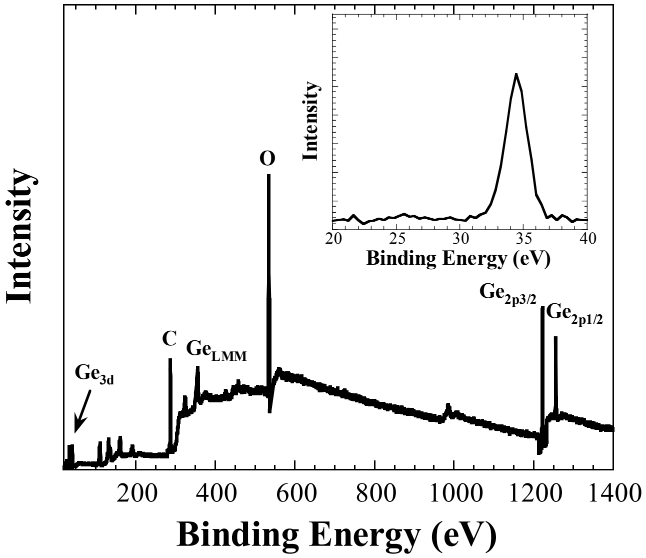

Fig. 6.5. XPS data for 2 nm germanium nanocrystals on a silicon substrate. Inset shows the 3d orbital of germanium. Note that the high oxygen count is likely due to the presence of $SiO_2$ on the substrate.

Using a shell approximation, $N_{Ge} = \dfrac{32\pi\left(d_p/2\right)^3}{3\cdot a_{Ge}^2\cdot c_{Ge}}$, where $a_{Ge}$ and $c_{Ge}$ are the lattice constants of tetragonal Ge (5.93 Å and 6.98 Å, respectively), the number of Ge atoms, $N_{Ge}$, in a nanocrystal can be estimated. Particles 20 Å in diameter ($d_p$) have approximately 137 atoms. The Ge:C ratio determined from XPS can be used to calculate the approximate area occupied on the nanocrystal surface by each capping ligand. With the Ge:C ratio equal to 0.3, a 20 Å cluster with 137 core Ge atoms has 455 C atoms surrounding it. Since each octanol ligand has 8 carbons, approximately 57 capping ligands surround each particle. Dividing the particle surface area by 57 indicates that each ligand occupies an average of 22 Å$^2$, which approaches 100% coverage for a close-packed monolayer of ligands surrounding the nanocrystals.

The data for the 3d orbital of pure germanium is expected to be approx. 29-30 keV. As seen in the inset of Figure 6.5, the energy is nearly 34-35 keV. If an oxide were present, the energy would be expected to shift nearly 2 keV. Therefore, it is apparent that there is another cause of the shift. Based on other peaks present, such as silicon (substrate), it is apparent that there is charging on the surface. This charging results in the shifting of the binding energy by as much as 8-10 keV in some cases. Further complications arise from the effects of small nanocrystals and surface coverage. Carley et al. [33] have shown that binding energies can be shifted by nearly 1 keV based on surface coverage alone. The effects of nanocrystal size on binding energy are less understood. Due to the small size of the nanocrystals (approx. 2 nm), there are a significant amount of surface atoms. As stated above, the ligand coverage approaches 100%; therefore, many of the surface atoms will be bound to oxygen through the alkoxide linkage to the capping ligand (~35-50% of all atoms). These bonds would be expected to cause shifts in the binding energy of a significant portion of the germanium atoms present. Therefore, it is difficult to obtain the exact oxidation state of the germanium from XPS data alone.

FTIR spectra in Figure 6.6 show that the nanocrystals are most likely terminated with hydrocarbon chains, bound through an alkoxide (Ge-O-C) linkage. The spectra show the characteristic methyl and methylene stretches (2800 to 3000 $cm^{-1}$) of the capping ligands after removal of all unbound ligands from the sample. The notable absence of the hydroxyl stretch for octanol (~3300 $cm^{-1}$), and the presence of the peaks at 1155 $cm^{-1}$, 1210 $cm^{-1}$, and 640 $cm^{-1}$ corresponding to the Ge-O-C- stretching modes [34], suggests covalent alkoxide bonding to the Ge nanocrystal surface. Germanium oxide stretches are expected to occur at 770 to 910 $cm^{-1}$ [11,34-36]. Although the presence of an oxide cannot be excluded based on the FTIR data alone, it appears that if an oxide is present that its concentration would be small as these oxide stretches are expected to have very strong intensity [11].

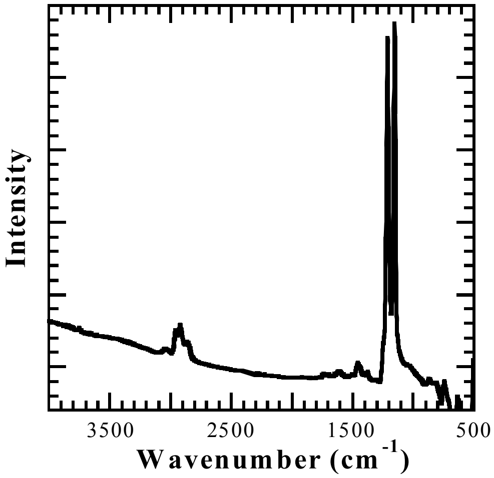

Fig. 6.6. FTIR spectra of octanol-capped germanium nanocrystals. The relative intensities of the peaks were varied between samples; however, this is likely due to changes in the mean particle size.

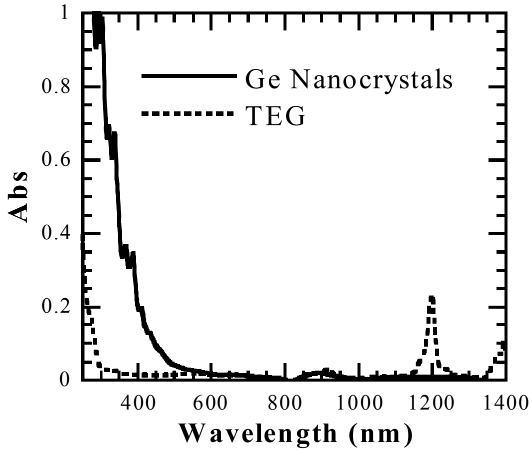

Fig. 6.7. Room temperature UV-Vis-NIR spectra of octanol-capped germanium nanocrystals and 0.75 M TEG in chloroform.

Precursor degradation is confirmed by the absorbance spectra in the near-IR range. As seen in Figure 6.7, pure TEG in chloroform (0.75M) is seen to have strong absorbance peaks at approximately 1200 and 1400 nm. However, the Ge nanocrystals formed have no absorbance in the near-IR. In addition, the fine structure apparent in the UV-visible absorbance for smaller nanocrystals (discussed below) cannot be due to the precursor.

***6.32 Optical properties***. By using the chromatography method described above, several fractions were obtained from a size polydisperse sample. The fractions obtained have noticeable changes in color with the larger particles appearing to be a deep gold while smaller particles appear pale yellow. All fractions of germanium obtained were shown to photoluminesce with quantum yields as high as 5% for the smallest nanocrystals shown in Figure 6.8. While changes in the peak position are not noticed, the intensity of the luminescence (quantum yield) is shown to increase as the particles approach smaller sizes. Discrete features can be seen in the PLE shown in Figure 6.9 which mirror the features witnessed in the absorbance spectra shown in Figure 6.10 within a few meV.

As can be seen in Figure 6.8, there is a significant blue shift of the PL of nanocrystals from the bulk values of ~1200 nm to values of ~400 nm. In addition, as the size of the nanocrystals get smaller, the PL quantum yield increases and the PL sharpens to a narrow band eventually resulting in distinct features in the spectra. The spectra exhibit three distinct peaks located at approx. 3.25 eV, 3.10

eV, and 2.95 eV. This separation of approx. 0.15 eV is equivalent to an IR stretch of approx. 1210 $cm^{-1}$, which corresponds to the alkoxide stretch for Ge-O-C as noted above.

UV-visible absorption spectra of these solutions show size-dependent features as well. In Figure 6.10, the UV-visible absorbance of several fractions is compared. For the nanocrystals larger than 66 Å, the absorption shows no distinct features and has an absorption edge at lower energies (high wavelength) as expected. Despite the fact that these particles are quite large (12.7 nm), they still exhibit some quantum confinement effects as witnessed in the PL and UV-vis spectra, which is consistent with the Bohr radius for germanium nanocrystals of 11.5 nm [37]. However, as the size of the nanocrystals decreases to values below 66 Å, the absorption edge of the UV-vis spectra is blue-shifted. In addition, there are distinct features that become apparent in the spectra similar to features observed for silicon nanocrystals [6]. Further decreases in size result in a blue-shift of these distinct features consistent with quantum confinement and a loss of degeneracy of the energy levels. Furthermore, at the smallest sizes, these features appear to look like spectra of molecules as witnessed by the growth of the feature at ~340 nm relative to the other features, which is likely due to the convergence of energy bands into a single band with high oscillator strength.

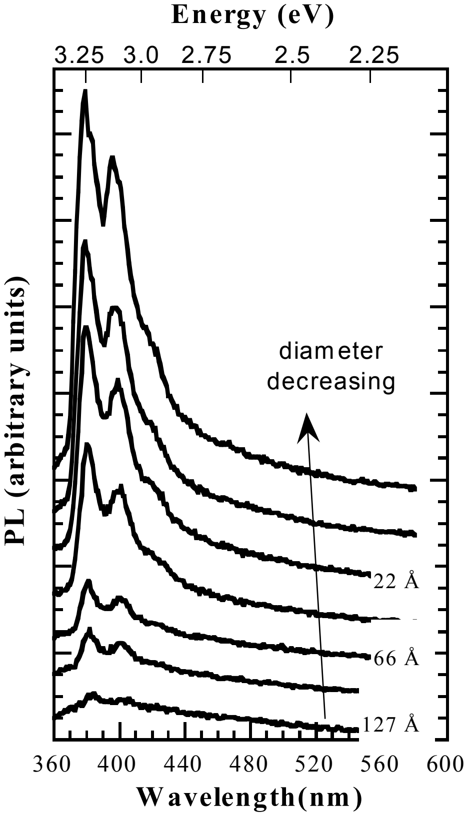

Fig. 6.8. Size-dependent room temperature PL of germanium nanocrystals excited at 338 nm.

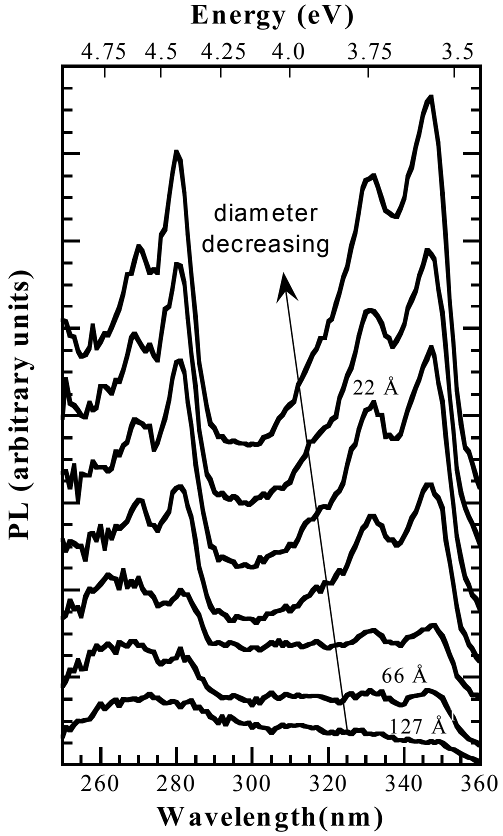

Fig. 6.9. Size-dependent room temperature PLE of germanium nanocrystals with emission at 380 nm

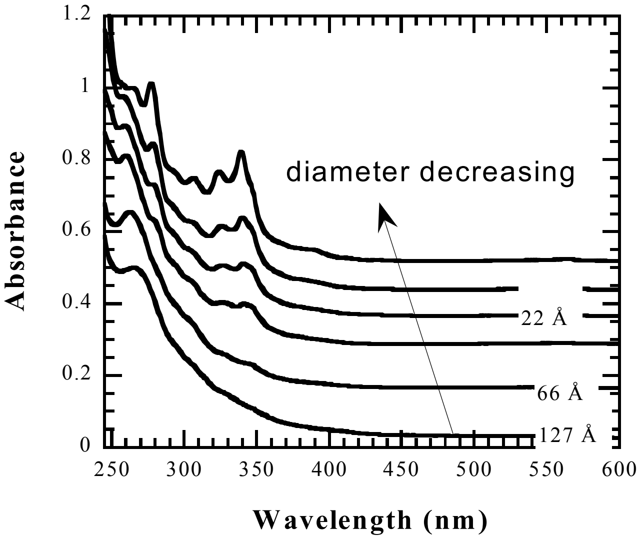

Fig. 6.10. Size-dependent room temperature UV-visible absorbance of germanium nanocrystals. Note the appearance of distinct features for the smallest nanocrystals and the peak shifts to higher energies. All spectra are offset such that the absorbance at 600 nm is approx. zero.

## 6.4 Conclusions

Germanium nanocrystals are produced by an arrested-growth method within supercritical octanol exhibiting size dependent properties. Due to the high pressure associated with this arrested-growth method, the germanium nanocrystals form a tetragonal lattice structure, which has been arguably attributed to the PL in germanium nanocrystals [14]. The Ge crystals produced are size-polydisperse in nature; however, size-selectivity of these nanocrystals is obtained by the use of a chromatographic method. While silicon was shown to have some size dependent features, germanium nanocrystals are shown to have more significant quantum confinement effects due to the smaller band gap as witnessed in the optical properties. Luminescence of the nanocrystals is shown to be size-dependent resulting in a blue-shift of the PL energy consistent with quantum confinement of the band gap energy and resulting in quantum yields of 5%. UV-visible spectra are also size-dependent with smaller particles resulting in discrete optical features. In addition, these features are shown to be size-dependent characteristic of the loss of energy level degeneracy due to quantum confinement. At the smallest particle sizes, these features appear to behave similar to molecular absorbance with the density of the energy levels concentrated into just a few bands yielding high oscillator strengths further suggesting the idea that nanocrystals may be considered as ‘artificial’ atoms.

## 6.5 References and Notes

(1) Alivisatos, A. P. *Science* **1996**, *271*, 933.

(2) Brust, M.; Walker, M.; Bethell, D.; Schiffrin, D. J.; Whyman, R. *J. Chem. Soc. Chem. Comm.* **1994**, 801-802.

(3) Leff, D. V.; Ohara, P. C.; Heath, J. R.; Gelbart, W. M. *J. Phys. Chem.* **1995**, *99*, 7036-7041.

(4) Murray, C. B.; Norris, D. J.; Bawendi, M. G. *J. Am. Chem. Soc.* **1993**, *115*, 8706.

(5) Banin, U.; Lee, C. J.; A.A., G.; Kadavanich, A. V.; Alivisatos, A. P.; Jaskolski, W.; Bryant, G. W.; Efros, A. L.; Rosen, M. *J. Chem. Phys.* **1998**, *109*, 2306.

(6) Holmes, J. D.; Ziegler, K. J.; Doty, R. C.; Pell, L. E.; Johnston, K. P.; Korgel, B. A. *J. Am. Chem. Soc.* **2001**, *123*, 3743-3748.

(7) Paine, D. C.; Caragianis, C.; Kim, T. Y.; Shigesato, Y.; Ishahara, T. *Appl. Phys. Lett.* **2842**, *62*, 2842-2844.

(8) Okamoto, S.; Kanemitsu, Y. *Phys. Rev. B* **1996**, *54*, 16421-16424.

(9) Maeda, Y. *Phys. Rev. B* **1995**, *51*, 1658-1670.

(10) Taylor, B. R.; Kauzlarich, S. M.; Lee, H. W. H.; Delgado, G. R. *Chem. Mater.* **1998**, *10*, 22-24.

(11) Taylor, B. R.; Kauzlarich, S. M.; Delgado, G. R.; Lee, H. W. H. *Chem. Mater.* **1999**, *11*, 2493-2500.

(12) Zacharias, M.; Fauchet, P. M. *Appl. Phys. Lett.* **1997**, *71*, 380-382.

(13) Niquet, Y. M.; Allan, G.; Delerue, C.; Lannoo, M. *Appl. Phys. Lett.* **2000**, *77*, 1182-1184.

(14) Kanemitsu, Y.; Uto, H.; Masumoto, Y.; Maeda, Y. *Appl. Phys. Lett.* **1991**, *61*, 2187-2189.

(15) Peng, C. S.; Huang, Q.; Cheng, W. Q.; Zhou, J. M.; Zhang, Y. H.; Sheng, T. T.; Tung, C. H. *Phys. Rev. B* **1998**, *57*, 8805-8808.

(16) Reboredo, F. A.; Zunger, A. *Phys. Rev. B* **2000**, *62*, R2275-R2278.

(17) Reboredo, F. A.; Zunger, A. *Phys. Rev. B* **2001**, *63*, 235314.

(18) Gogotsi, Y. G.; Yoshimura, M. *Nature* **1994**, *367*, 628.

(19) Watkins, J. J.; Blackburn, J. M.; McCarthy, T. J. *Chem. Mater.* **1999**, *11*, 213-215.

(20) Darr, J. A.; Poliakoff, M. *Chemical reviews* **1999**, *99*, 495.

(21) Savage, P. E.; Gopalan, S.; Mizan, T. I.; Martino, C. J.; Brock, E. E. *AIChE J.* **1995**, *41*, 1723-1778.

(22) Holmes, J. D. B., Prashant A.; Korgel, Brian A.; Johnston, Keith P. *Langmuir* **1999**, *15*, 6613.

(23) Holmes, J. D.; Johnston, K. P.; Doty, R. C.; Korgel, B. A. *Science* **2000**, *287*, 1471.

(24) Shah, P. S.; Husain, S.; Johnston, K. P.; Korgel, B. A. *submitted* **2001**.

(25) Ziegler, K. J.; Doty, R. C.; Johnston, K. P.; Korgel, B. A. *J. Am. Chem. Soc.* **2001**, *123*, 7797-7803.

(26) Shah, P. S.; Holmes, J. D.; Johnston, K. P.; Korgel, B. A. *in preparation* **2001**.

(27) Bundy, F. P.; Kasper, J. S. *Science* **1963**, *139*, 340-341.

(28) Pizzagalli, L.; Galli, G.; Klepeis, J. E.; Gygi, F. *Phys. Rev. B* **2001**, *63*, 165324.

(29) Rath, S.; Sato, S.; Ono, H.; Nozaki, S.; Morisaki, H. *Mater. Chem. Phys.* **1998**, *54*, 244-246.

(30) Taugbol, K.; Augdahl, E.; Sara, A. N. *Acta Chem. Scand.* **1967**, *21*, 817-819.

(31) Sanderson, R. T. *Chemical Bonds and Bond Energy*; 2nd ed.; Academic Press: New York, 1976; Vol. 21.

(32) Wu, Y.; Yong, P. *Adv. Mater.* **2001**, *13*, 520-523.

(33) Carley, A. F.; Dollard, L. A.; Norman, P. R.; Pottage, C.; Roberts, M. W. *J. Electron Spectrosc.* **1999**, *98-99*, 223-233.

(34) Inagaki, N.; Mitsuuichi, M. *J. Polym. Sci.* **1983**, *21*, 2887-2895.

(35) Gazicki, M.; Ledzion, R.; Mazurczyk, R.; Pawlowski, S. *Thin Solid Films* **1998**, *322*, 123-131.

(36) Theobald, M.; Baclet, P.; Legaie, O.; Durand, J. *J. Vac. Sci. Technol. A* **2001**, *19*, 118-123.

(37) Wilcoxon, J. P.; Provencio, P. P.; Samara, G. A. *Phys. Rev. B* **2001**, *64*, 035417.

# Chapter 7: Conclusions and Recommendations

## 7.1 Conclusions

***7.11 Polar reactions in supercritical water.*** In Chapter 2, the equilibrium study of several polar reactions involving nitrogen-containing species in SCW was presented. Similar to the case for reactions of ionic species, these reactions are effected by the density (dielectric constant) of SCW. The equilibrium constants for these polar reactions changed between 1-3 orders of magnitude over a density range of 0.25-0.6 g cm$^{-3}$. Whereas these changes are smaller than for ionic reactions, they are significant. As observed for ionic reactions, where reactions shift to associated species due to the low dielectric medium, the polar reactions involving nitrogen oxides were shown to shift to less polar species. Interestingly, independent gas phase values determined from thermochemical data [1] may help in the prediction of equilibrium constants in SCW. It was shown that extrapolation of the equilibrium constants to zero density results in values very close to gas phase values. Furthermore, it was shown that nitrogen chemistry could be controlled in SCW to yield significantly less $NO_x$ species than conventional incineration methods.

***7.12 Optimization model for study of complex reaction equilibria.*** A number of previously studied reactions in SCW focused on equilibrium studies of ionic dissociation reactions [2,3] or kinetic studies of decomposition reactions [4].

This is due to the difficulty in obtaining *in-situ* measurements at high temperatures where corrosion becomes significant. Typically, equilibrium studies have been limited to pH studies of ionic reactions [5,6] or studies of reactions involving chromophores [7,8]. The study of reaction equilibria of nitrogen oxides within SCW described in Chapter 2 was made possible by the development of an optimization model. Despite measuring the concentration of only two species directly, six equilibrium constants and two extinction coefficients were obtained. This model was based on the Non-linear Optimization model developed by Lasdon et al. [9] called GRG2. The study of nitrogen decomposition reactions within SCW was complicated by the fact that multiple reactions were coupled, requiring the simultaneous solution of nearly 400-600 equations and 400-600 variables. Further complications exist due to the wide variance of the values of the variables; molal concentrations were on the order of $10^{-4}$ or smaller, while equilibrium constants could be $10^{5}$ to $10^{-5}$. To alleviate these problems, all equations and variables were transformed to a logarithmic scale easing the scaling problem and making some of the restraint equations linear in nature. The procedures outlined in Chapter 3, make the study of complex reaction systems within supercritical fluids or other media possible.

***7.13 Synthesis of organic-capped nanocrystals within supercritical water.*** The use of SCW as a solvent for particle synthesis has several benefits. Besides being environmentally friendly, the solvent can be easily controlled through changes in density (dielectric) allowing reaction rates, diffusion, and ion-pairing reactions to be manipulated for the desired morphology or size of nanocrystals. Furthermore, the high temperature enhances crystallization and the solvent does not degrade like some common organic solvents at these temperatures. In addition, because organics become miscible at supercritical conditions, organic capping ligands can be used to quench and stabilize growth. These nanocrystals are then soluble in common organic solvents at room temperature, where they can easily be manipulated for deposition onto surfaces. In Chapter 4, SCW was utilized for the synthesis of copper nanocrystals capped with 1-hexanethiol. This alkanethiol was shown to stabilize particles and quench particle growth in a narrow size distribution between 3 and 15 nm through a diffusion limited growth mechanism. Furthermore, a competing reaction mechanism between hydrolysis and ligand exchange reactions allows factors such as the pH, and precursor to have substantial effects on the particle size and morphology.

***7.14 Synthesis of nanocrystals exhibiting quantum confinement effects.*** Although the synthesis of nanocrystals exhibiting size dependent optical properties due to quantum confinement have previously been reported [10-12], these size dependent changes have not been witnessed in two of the most technologically important semiconductors—silicon and germanium. In Chapter 5 and Chapter 6, size dependent properties for silicon and germanium nanocrystals are outlined. These nanocrystals are formed in an arrested-growth method within supercritical octanol at temperatures exceeding 450 °C, which is required for precursor degradation. The high temperatures required for these semiconductors makes them ideal for supercritical fluids as conventional liquid methods are difficult at these temperatures. Other methods such as laser ablation often lead to thick oxide layers. The optical properties of these nanocrystals show a significant blue shift of the photoluminescence from the bulk as might be expected for quantum confined nanocrystals of silicon and germanium [13] and are dependent on the size of the nanocrystals. Furthermore, the quantum yield obtained with these nanocrystals is high.

## 7.2 Recommendations for further study

***7.21 Study of complex reaction equilibria.*** The successful application of optimization methods in the study of complex nitrate equilibria in Chapter 2 and Chapter 3 has expanded the field of reaction equilibria in SCW for further studies of similar species of interest. Several other species involved in oxidation type equilibria such as perchlorates and sulfates are of interest in the destruction of waste streams and sludges. Further study of non-ionic polar reactions should also verify that equilibrium constants appear to be linearly dependent on the solvent density and that they may be extrapolated to independent gas-phase equilibrium values.

***7.22 Stabilize organic-capped particles within supercritical water.*** Because the stabilization of nanocrystals within SCW is an important step in their formation, key aspects of this mechanism should be further studied. While the synthesis of copper nanocrystals within SCW discussed in Chapter 4 suggests that these nanocrystals are soluble in supercritical water, the time scale of the stabilization and the effect of density have yet to be determined. These factors can play significant roles in the growth of nanocrystals, agglomeration, and yield. In addition, this knowledge may be applicable in the size selective precipitation of nanocrystals. Because the solvent conditions can be easily manipulated from a water-like solvent to an organic-like solvent with changes in the dielectric (density), the pressure can be tuned to allow the selective solubilization of various sizes of nanocrystals. Finally, this study would help to answer more fundamental questions about the stability of colloids in supercritical fluids and the factors that control them.

***7.23 Synthesis of core-shell nanocrystals within supercritical fluids.*** The synthesis of layered materials at nano-scale dimensions will be useful for future devices. By passivating a quantum dot with a higher band-gap material, further control over the particle optoelectronic properties are made possible. Although Yang and Kauzlarich have demonstrated the ability to form germanium (core)/silicon (shell) nanocrystals [14], these nanocrystals were only passivated with a short alkyl chain resulting in significant agglomeration and the effect of particle size was not studied. Furthermore, studies of core-shell structures are complicated by the ability to characterize these systems. However, the Transmission Electron Microscope being built for the Texas Materials Institute will have the ability to perform holography, which is a valuable tool in identifying phase shifts related to the materials present. Therefore, from these holographic images the core and shell structure becomes easily visible [14] allowing the potential to study size effects of core/shell germanium/silicon nanoparticles.

## 7.3 References

(1) Chase, M. W., Jr.; Davies, C. A.; Downey, J. R., Jr.; Frurip, D. J.; McDonald, R. A.; Syverud, A. N. *JANAF Thermochemical Tables*; Third ed.; American Chemical Society and the American Institute of Physics for the National Bureau of Standards:, 1985; Vol. 14.

(2) Xiang, T.; Johnston, K. P. *J.Phys.Chem.* **1994**, *98*, 7915.

(3) Xiang, T.; Johnston, K. P. *J.Solution Chem.* **1997**, *26*, 13.

(4) Broll, D.; Kaul, C.; Kramer, A.; Krammer, P.; Richter, T.; Jung, M.; Vogel, H.; Zehner, P. *Angew. Chem.* **1999**, *Int. Ed.*, 2999- 3014.

(5) Mesmer, R. E.; Marshall, W. L.; Palmer, D. A.; Simonson, J. M.; Holmes, H. F. *J.Solution Chem.* **1988**, *17*, 699.

(6) Ho, P. C.; Palmer, D. A.; Mesmer, R. E. *J. Solution Chem.* **1994**, *23*, 997.

(7) Schoppelrei, J. W., Brill, T.B. *J.Phys.Chem. A.* **1997**, *101*, 8593.

(8) Schoppelrei, J. W., Kieke, M.L., Wang, X., Klein, M.T., Brill, T.B. *J.Phys.Chem.* **1996**, *100*, 14343.

(9) Smith, S.; Lasdon, L. *Journal on Computing* **1992**, *4*, 1.

(10) Alivisatos, A. P. *Science* **1996**, *271*, 933.

(11) Murray, C. B.; Norris, D. J.; Bawendi, M. G. *J. Am. Chem. Soc.* **1993**, *115*, 8706.

(12) Banin, U.; Lee, C. J.; A.A., G.; Kadavanich, A. V.; Alivisatos, A. P.; Jaskolski, W.; Bryant, G. W.; Efros, A. L.; Rosen, M. *J. Chem. Phys.* **1998**, *109*, 2306.

(13) Takagahara, T.; Takeda, K. *Phys. Rev. B* **1992**, *46*, 15578-15581.

(14) Yang, C.-S.; Kauzlarich, S. M.; Wang, Y., C. *Chem. Mater.* **1999**, *11*, 3666-3670.

# Appendix A: Nitrate Optimization Program

This FORTRAN subroutine was written to determine the equilibrium constants involved in the decomposition equilibria of nitric acid in supercritical water and the extinction coefficients of $NO_2$ and $HNO_2$. It is implemented within a Non-linear programming Model called GRG (Smith and Lasdon, 1992). All equilibria equations, mass balances, and charge balances are written as constraints on the optimization. The objective is defined as the difference between the calculated absorbance and the measured absorbance of $NO_2$ and $HNO_2$.

```
c     last updated: 6/15/98


C     SET PROBLEM SIZE AND OBJECTIVE
      IMPLICIT  DOUBLE PRECISION(A-H,O-Z),INTEGER(I,J,L,M,N)
      INTEGER DATA
C *   DATA -- NUMBER OF DATA POINTS TO BE FITTED                    *
      PARAMETER (DATA = 45)
      PARAMETER (NCORE = 750000)
c     NCORE PREVIOSLY = 250000 small scale
      PARAMETER (NNVARS = 16*DATA + 10)
      PARAMETER (NFUN   = 16*DATA + 1)
      PARAMETER (NNOBJ = 16*DATA + 1)
      PARAMETER (MAXBAS = NFUN)
      PARAMETER (MAXHES = NNVARS)

      COMMON /DBUG/ DEBUG
      LOGICAL DEBUG
      COMMON /IOUNIT/ IOIN, IOOUT, IODUMP, IOERR, IOTERM
      COMMON /MYSTUF/H,Ab1,Ab2,m0hno3,m0base,m0nano2,m0h2o2,Na
      COMMON /MYSTUF2/DATAPTS
      COMMON /MYSTUF3/kw,kbase,t,rho,A,conf1,conf2

      INTEGER*4 LVARS(NNVARS)
      CHARACTER*8 RAMCON, RAMVAR
      LOGICAL INPRNT,OTPRNT
      DIMENSION BLVAR(NNVARS),BUVAR(NNVARS),BLCON(NFUN),BUCON(NFUN)
      DIMENSION XX(NNVARS),FCNS(NFUN),RMULTS(NFUN),IIBV(NFUN)
```

```
      DIMENSION RAMCON(NFUN),RAMVAR(NNVARS),INBIND(NFUN),IIUB(NFUN)
      DIMENSION NONBAS(NNVARS),REDGR(NNVARS),DEFAUL(41),Z(NCORE)
      CHARACTER*76 ATITLE
      DOUBLE PRECISION H(150),Ab1(75),Ab2(75),m0hno3(75)
      DOUBLE PRECISION m0nano2(75),m0h2o2(75),m0base(75),Na(75)
      INTEGER DATAPTS,SET
      DOUBLE PRECISION kw,kbase,t,rho,A,eps,conf1(75),conf2(75)
      CHARACTER*10 FILE

      DATA ATITLE/'NITRATE EQUILIBRIA FITTING PROCEDURE'/
      DATA RAMCON/NFUN*'        '/
      DATA RAMVAR/NNVARS*'        '/
      DATA BIG/1.D31/

      DATAPTS=DATA

      write (*,*) "Data Set > "
      read (*,*) SET

C     SET LOGICAL I/O UNITS

      IOIN =  1
      IOOUT = 2
      IOERR = 2
      IOTERM = 8

C ******************************************************************
C  SET INTIAL VALUES

      open (99,file='xinit.dat')
      open (98,file='data.dat')
      open (97,file='conf1.dat')
      open (96,file='conf2.dat')

      write (*,*) "Reading initialization file"
      do i=1,NNVARS
        read (99,20) XX(i)
 20       format(f21.16)
c         write (*,*) xx(i),i
      enddo

      do i=1,DATAPTS
c     set Na(i) = 1 for true at each data point
        Na(i)=1.0
      enddo

      k=0
c     find those data points that do not contain sodium
      do i=1,DATAPTS
        if(XX(1+k).lt.-45.0) then
          Na(i) = 0.0
```

```
c           write (*,*) "Na ",i,Na(i)
          endif
          k=k+16
        enddo

        write (*,*) "Reading data file"
        do i=1,DATAPTS
          read (98,35) m0hno3(i), m0base(i), m0h2o2(i), m0nano2(i),
     &        Ab1(i), Ab2(i)
c         read (97,36) conf1(i)
c         read (96,36) conf2(i)
          conf1(i)=1.0
          conf2(i)=1.0
 35       format (f9.6,f10.7,f8.5,f10.7,2f12.9)
 36       format (f3.1)
c         write (*,*) i,m0hno3(i),m0base(i),m0h2o2(i),m0nano2(i),
c    &        Ab1(i),Ab2(i)
c     this corrects for the fact that the data is in O2 and the model
c     accounts for H2O2
          m0h2o2(i)=2*m0h2o2(i)
        enddo

        close (99)
        close (98)

c     set temperature and density
        if (SET.eq.1) then
          t=380+273.15
          rho=0.506380
        endif
        if (SET.eq.2) then
          t=380+273.15
          rho=0.542991
        endif
        if (SET.eq.3) then
          t=380+273.15
          rho=0.567060
        endif
        if (SET.eq.4) then
          t=380+273.15
          rho=0.600454
        endif

        if (SET.eq.5) then
          t=400+273.15
          rho=0.242580
        endif
        if (SET.eq.6) then
          t=400+273.15
          rho=0.395498
        endif
```

```
      if (SET.eq.7) then
        t=400+273.15
        rho=0.467696
      endif
      if (SET.eq.8) then
        t=400+273.15
        rho=0.533327
      endif

      write (*,*) "Temp (K)",t
      write (*,*) "Density (g/cm^3)",rho
      write (*,*) "Determining Constants"
c     determine Kb and Kw
      call kwater(t,rho,kw)
      call epsilon(t,rho,eps)
      call kb(t,kbase)
      call Debye(t,rho,eps,A)

      write (*,*) "     Kw",kw
      write (*,*) "     Kb",kbase
      write (*,*) "     A",A

C *****************************************************************

CC  OTHER STUFF

      INPRNT = .TRUE.
      OTPRNT = .TRUE.
      DEBUG =  .FALSE.

      LVARS(1) = 0

      DO 10 I=1,41
10    DEFAUL(I) = 1.0D0

c      DEFAUL(9) = 0.0D0
c      IIPR = 1

c     tuned parameters

      DEFAUL(1) = 0.0
      FPNEWT=1d-8
      DEFAUL(2) = 0.0
      FPINIT=1d-4
      DEFAUL(3) = 0.0
      FPSTOP=1d-4
      DEFAUL(6) = 0.0
      NNSTOP=15
c      DEFAUL(8) = 0.0
c      LLMSER=200
c      DEFAUL(14) = 0.0
```

```
c     PPSTEP=1e-13
      DEFAUL(15) = 0.0
      IIQUAD=1
      DEFAUL(18) = 0.0
c     DEFAUL(28) = 0.0
c     IISCAL=1
c     DEFAUL(29) = 0.0
c     IISCLG=200
      DEFAUL(19) = 1.0D0
c     Hard bounds held
      DEFAUL(34) = 0.0
      DEFAUL(38) = 0.0

C
C   THIS NEXT STATEMENT IS CONVENIENT FOR PC'S.
C   YOU MAY WISH TO DELETE IT FOR MAINFRAMES,AND
C   LINK LOGICAL AND ACTUAL FILENAMES OUTSIDE THE LSGRG2
C   SYSTEM.
C

      OPEN(UNIT = IOOUT,FILE = 'results.out')

C*****************************************************************

      write (*,*) "Assigning Upper & Lower Bounds on Variables"
c     all concentrations
      do i=1,(16*DATA)
        BLVAR(i) = -50
        BUVAR(i) = -0.00000001
      enddo

c     reset values for ionic strength
      k=0
      do i=1,DATA
        BLVAR(15+k) = 0.0
        BUVAR(15+k) = 0.1
        k=k+16
      enddo

c     set tighter bounds on NO since it seems to be screwing up
      k=0
      do i=1,12
c         BLVAR(11+k) = -3.1
c         BLVAR(12+k) = -2.74
        k=k+16
      enddo
      do i=13,28
c         BLVAR(11+k) = -3.13
c         BLVAR(12+k) = -2.73
        k=k+16
      enddo
```

```
      do i=29,36
c         BLVAR(11+k) = -3.26
c         BLVAR(12+k) = -4.07
        k=k+16
      enddo
      do i=37,43
c         BLVAR(11+k) = -2.95
c         BLVAR(12+k) = -3.47
        k=k+16
      enddo


c      remove NO2- from model
      k=0
      do i=1,DATA
        BLVAR(4+k) = -50
        BUVAR(4+k) = -50
        k=k+16
      enddo

c      remove N2O3 from model
      k=0
      do i=1,DATA
        BLVAR(13+k) = -50
        BUVAR(13+k) = -50
        k=k+16
      enddo

      j=0
      do i=1,DATA
        if (Na(i).eq.0.0) then
          BUVAR(1+j) = -50
          BUVAR(8+j) = -50
          BUVAR(14+j) = -50
        endif
        j=j+16
      enddo

c      Ka1
      BLVAR(16*DATA + 1) = -4.0
      BUVAR(16*DATA + 1) = -2.0
c      Ka2
      BLVAR(16*DATA + 2) = -50.0
      BUVAR(16*DATA + 2) = -50.0
c      K1
      BLVAR(16*DATA + 3) = -2.0
      BUVAR(16*DATA + 3) = 2.0
c      K2
      BLVAR(16*DATA + 4) = -3.0
      BUVAR(16*DATA + 4) = -0.0
c      K3
```

```
      BLVAR(16*DATA + 5) = -3.0
      BUVAR(16*DATA + 5) = -0.0
c     K4
      BLVAR(16*DATA + 6) = -50.0
      BUVAR(16*DATA + 6) = -50.0
c     K5
      BLVAR(16*DATA + 7) = -3.0
      BUVAR(16*DATA + 7) = -0.0
c     K6
      BLVAR(16*DATA + 8) = -4.0
      BUVAR(16*DATA + 8) = -0.0
c     E1
      BLVAR(16*DATA + 9) = -1.5
      BUVAR(16*DATA + 9) = -1.0
C      E2
      BLVAR(16*DATA + 10) = -2.0
      BUVAR(16*DATA + 10) = -1.0


      j=0
      do i=1,DATA
        RAMVAR(1+j) = 'Na+ '
        RAMVAR(2+j) = 'H+ '
        RAMVAR(3+j) = 'NO3- '
        RAMVAR(4+j) = 'NO2- '
        RAMVAR(5+j) = 'OH- '
        RAMVAR(6+j) = 'HNO3 '
        RAMVAR(7+j) = 'HNO2 '
        RAMVAR(8+j) = 'NaOH '
        RAMVAR(9+j) = 'NO2 '
        RAMVAR(10+j) = 'O2 '
        RAMVAR(11+j) = 'NO '
        RAMVAR(12+j) = 'N2O '
        RAMVAR(13+j) = 'N2O3 '
        RAMVAR(14+j) = 'NaNO3'
        RAMVAR(15+j) = 'I '
        RAMVAR(16+j) = 'G+- '
        j=j+16
      enddo

      RAMVAR(16*DATA + 1) = 'Ka1 '
      RAMVAR(16*DATA + 2) = 'Ka2 '
      RAMVAR(16*DATA + 3) = 'K1 '
      RAMVAR(16*DATA + 4) = 'K2 '
      RAMVAR(16*DATA + 5) = 'K3 '
      RAMVAR(16*DATA + 6) = 'K4 '
      RAMVAR(16*DATA + 7) = 'K5 '
      RAMVAR(16*DATA + 8) = 'K6 '
      RAMVAR(16*DATA + 9) = 'E1 '
      RAMVAR(16*DATA + 10) = 'E2 '
```

```
C *****************************************************************
C *   SET FUNCTION LOWER AND UPPER BOUNDS AND NAMES FOR FUNCTIONS   *
C *   BLCON  -- Bound Lower CONstraints                         *
C *   BUCON  -- Bound Upper CONstraints                         *
C *   FUNNAME - UP TO EIGHT CHARACTERS                            *
C *

      write (*,*) "Assigning Upper & Lower Bounds on Constraints"
      do i=1,(16*DATA)
        BLCON(i) = 0.0
        BUCON(i) = 0.0
      enddo

c     reset the constraints on log Kb,and log kw
      j=0
      do i=1,DATA
        BLCON(5+j) = log10(kw)
        BUCON(5+j) = log10(kw)
c     need to account for Na(i)
        if (Na(i).eq.1) then
          BLCON(6+j) = log10(kbase)
          BUCON(6+j) = log10(kbase)
        endif
        j=j+16
      enddo

      BLCON(16*DATA + 1) = -BIG
      BUCON(16*DATA + 1) = BIG

      j=0
      do i=1,DATA
        RAMCON(1+j) = 'CHARGE BAL'
        RAMCON(2+j) = 'MB N'
        RAMCON(3+j) = 'STOICH BAL'
        RAMCON(4+j) = 'MB Na'
        RAMCON(5+j) = 'Kw CONSTR'
        RAMCON(6+j) = 'Kb CONSTR'
            RAMCON(7+j) = 'Ka1 CONSTR'
            RAMCON(8+j) = 'Ka2 CONSTR'
            RAMCON(9+j) = 'K1 CONSTR'
            RAMCON(10+j)= 'K2 CONSTR'
        RAMCON(11+j)= 'K3 CONSTR'
        RAMCON(12+j)= 'K4 CONSTR'
        RAMCON(13+j)= 'K5 CONSTR'
        RAMCON(14+j)= 'K6 CONSTR'
        RAMCON(15+j)= 'IONIC ST'
        RAMCON(16+j)= 'ACTIVITY'
        j=j+16
      enddo
```

```
      RAMCON(16*DATA + 1)= 'OBJECT'

C ******************************************************************

C     WRITE(6,*) 'CALLING GRGSUB'
      CALL GRGSUB(INPRNT,OTPRNT,NCORE,NNVARS,NFUN,MAXBAS,
     1
MAXHES,NNOBJ,ATITLE,LVARS,BLVAR,BUVAR,BLCON,BUCON,DEFAUL,FPNEWT,
     2 FPINIT,FPSTOP,FPSPIV,PPH1EP,NNSTOP,IITLIM,LLMSER,IIPR,IIPN4,
     3 IIPN5,IIPN6,IIPER,PPSTEP,IIQUAD,LDERIV,MMODCG,
     4 RAMCON,RAMVAR,AIJTOL,PIVPCT,MXTABU,FFUNPR,CONDTL,IDEGLM,
     5 FPBOUN,FPDEG,IISCAL,IISCLG,IMEMCG,IIBVBL,XX,IIBV,FCNS,
     6 INBIND,RMULTS,NONBAS,REDGR,IIUB,NBIND,NNONB,INFORM,Z)
C     WRITE(6,*) 'EXITING GRGSUB'
      STOP
      END




C ****************************************************************** *

      SUBROUTINE GCOMP(G,X)

c     x=DATA*mi + sum(ki,E)
c     G=DATA*CONSTRAINT EQUATIONS + OBJECTIVE
c     H=2*DATA

      COMMON /MYSTUF/H,Ab1,Ab2,m0hno3,m0base,m0nano2,m0h2o2,Na
      COMMON /MYSTUF2/DATAPTS
      COMMON /MYSTUF3/kw,kbase,t,rho,A,conf1,conf2

      INTEGER j,k,m,DATAPTS

      DOUBLE PRECISION G(*),x(*),H(150),t,rho,kw,kbase,eps,A,b
c     all arrays below are x(DATA)
      DOUBLE PRECISION m0base(75),m0hno3(75),m0nano2(75),m0h2o2(75)
      DOUBLE PRECISION Na(75),mtotal(75),Ab1(75),Ab2(75),conf1(75)
      DOUBLE PRECISION conf2(75),W(5)

      b=1.2

c      write (*,*) "In GCOMP()"
c      write (*,*) "m0hno3",m0hno3
c      write (*,*) "m0base",m0base
c      write (*,*) "m0h2o2",m0h2o2
c      write (*,*) "m0nano2",m0nano2
c      write (*,*) "Ab1",Ab1
c      write (*,*) "Ab2",Ab2

c      do i=1,684
```

```
c         write (*,*) x(i),i
c      enddo

c     determine total concentration
      do m=1,DATAPTS
        mtotal(m)=m0hno3(m)+m0base(m)+m0nano2(m)+m0h2o2(m)
      enddo

      j=0
      k=0
      do m=1,DATAPTS
c     charge bal
         G(1+j)=(10**x(1+k)+10**x(2+k)-10**x(3+k)-10**x(4+k)
     &        -10**x(5+k))/mtotal(m)
c     mass bal N
        G(2+j)=(m0hno3(m)+m0nano2(m)-10**x(3+k)-10**x(4+k)-10**x(6+k)
     &        -10**x(7+k)-10**x(9+k)-10**x(11+k)-2*10**x(12+k)
     &        -2*10**x(13+k)-10**x(14+k))/mtotal(m)
c     redox bal
         G(3+j)=(4.*(10**x(10+k)-10**x(13+k))-10**x(9+k)-3.*10**x(11+k)
     &        -2.*(m0h2o2(m)+10**x(7+k)+10**x(4+k)-m0nano2(m))
     &        -8.*10**x(12+k))/mtotal(m)
c     mass bal Na
        G(4+j)=(m0base(m)+m0nano2(m)-10**x(1+k)-10**x(8+k)-
     &        10**x(14+k))*Na(m)/mtotal(m)
c     kw rxn
        G(5+j)=(x(2+k)+x(5+k)+2.*x(16+k))
c     kb rxn
        G(6+j)=(-x(8+k)+x(1+k)+x(5+k)+2.*x(16+k))*Na(m)
c     ka1 rxn
         G(7+j)=x(16*DATAPTS+1)-x(2+k)-x(3+k)-2.*x(16+k)+x(6+k)
c     ka2 rxn
         G(8+j)=(x(16*DATAPTS+2)-x(2+k)-x(4+k)-2.*x(16+k)+x(7+k))*0.0
c     k1 rxn
         G(9+j)=x(16*DATAPTS+3)-2.*x(9+k)-0.5*x(10+k)+2.*x(6+k)
c     k2 rxn
        G(10+j)=x(16*DATAPTS+4)-x(6+k)-x(7+k)+2.*x(9+k)
c     k3 rxn
        G(11+j)=x(16*DATAPTS+5)-2.*x(11+k)-0.5*x(10+k)+2.*x(7+k)
c     k4 rxn
        G(12+j)=(x(16*DATAPTS+6)+2.*x(7+k)-x(13+k))*0.0
c     k5 rxn
        G(13+j)=x(16*DATAPTS+7)+2.*x(11+k)-x(12+k)-0.5*x(10+k)
c     k6 rxn
        G(14+j)=(x(16*DATAPTS+8)+x(14+k)-x(1+k)-x(3+k)-2.*x(16+k))*
     &        Na(m)*1.0
c     ionic strength
         G(15+j)=x(15+k)-0.5*(10**x(1+k)+10**x(2+k)+10**x(3+k)
     &        + 10**x(4+k)+10**x(5+k))
c     activity coef
        G(16+j)=x(16+k)+A/2.303*(sqrt(x(15+k))/(1.+b*sqrt(x(15+k)))
```

```
     &       + 2./b*log(1.+1.2*sqrt(x(15+k))))
        k=k+16
        j=j+16
      enddo

c      write (*,*) "out of eq"
c      do i=1,16*DATAPTS
c         write (*,*) "G(",i,")",G(i)
c      enddo
c      STOP

      k=0
      j=0

c     all the parts of the objective function
c     weights on specific parts of objective function
      W(1)=10000
      W(2)=100000

c     construct parts of objective function
      do m=1,DATAPTS
        H(1+j)=W(1)*abs((Ab1(m)-10**(x(16*DATAPTS+9)+x(9+k))))
        H(2+j)=W(2)*abs((Ab2(m)-10**(x(16*DATAPTS+10)+x(7+k))))
        j=j+2
        k=k+16
      enddo

      G(16*DATAPTS+1)=0
c     objective function
      do j=1,2*DATAPTS
        G(16*DATAPTS+1)=G(16*DATAPTS+1)+H(j)
      enddo

      return
      end

c     ************************************************************
      subroutine kb(t,k)
c     valid from 250 to 325 C
c     naoh
      double precision t,k

      k=10**(91651.5/t - 1646.989 - 0.251228*t + 597.461*log10(t) -
     &      5610500/t**2)

      return
      end

c     ************************************************************
      subroutine Debye(t,p,e,A)
c     this subroutine calculates the Debye-Huckel slope from the Pitzer Eq.
```

```
      double precision t,p,e,A

c     use scaling for Debye-Huckel slope
c     A=0.3910 at t=25 C // Pitzer Thermo of Electrolytes (1977)
      A=0.3910*sqrt(p/1)*(298.15/t)**1.5*(78.71351/e)**1.5
      return
      end

c     ***********************************************************
      subroutine epsilon(t,p,e)
c     this subroutine uses the Uematsu and Franck dielectric constant model

      double precision tr,t,p,e,A(10)

      A(1)=7.62571
      A(2)=244.003
      A(3)=-140.569
      A(4)=27.7841
      A(5)=-96.2805
      A(6)=41.7909
      A(7)=-10.2099
      A(8)=-45.2059
      A(9)=84.6395
      A(10)=-35.8644

      tr=t/298.15
      e=1. + A(1)*p/tr + p**2*(A(2)/tr + A(3) + A(4)*tr)
     &     + p**3*(A(5)/tr + A(6)*tr + A(7)*tr**2)
     &     + p**4*(A(8)/tr**2 + A(9)/tr + A(10))

      return
      end

c     ***********************************************************
      subroutine kwater(t,p,k)
c     this subroutine uses the Franck and Marshall Kw model

      double precision t,p,k

      k=10**(-4.098 - 3245.2/t + 2.2362e5/t**2 - 3.984e7/t**3 +
     &   log10(p)*(13.957 - 1262.3/t + 8.5641e5/t**2))
      return
      end

c     ***********************************************************
```

# Appendix B: Nitrate Bootstrap Optimization Program

This FORTRAN subroutine was an adaptation to the Nitrate Opimization Program described in Appendix A. It takes the data used to determine the equilibria constants and extinction coefficients and determines the error associated with the calculation of these values. This is only a measure of the error of the model in determining the correct parameter and not a measure of the experimental error associated in obtaining the data points. This program works by taking the data set to calculate the parameters at a given temperature and pressure, and removing one data point at a time to determine the effect it has on the optimization solution. Therefore, if 45 data points were do be used, the program in Appendix A was implemented 45 times using only 44 of the data points. The variance in the optimization solutions, therefore, gives statistical information on the reliability of the solution set.

```
c     last updated: 6/15/98

C   SET PROBLEM SIZE AND OBJECTIVE
      IMPLICIT  DOUBLE PRECISION(A-H,O-Z),INTEGER(I,J,L,M,N)
      INTEGER DATA
C   *DATA -- NUMBER OF DATA POINTS TO BE FITTED                    *
      PARAMETER (DATA = 45)
      PARAMETER (NCORE = 750000)
c     NCORE PREVIOSLY = 250000 small scale
      PARAMETER (NNVARS = 16*DATA + 10)
      PARAMETER (NFUN   = 16*DATA + 1)
      PARAMETER (NNOBJ = 16*DATA + 1)
```

```
      PARAMETER (MAXBAS = NFUN)
      PARAMETER (MAXHES = NNVARS)

      COMMON /DBUG/ DEBUG
      LOGICAL DEBUG
      COMMON /IOUNIT/ IOIN, IOOUT, IODUMP, IOERR, IOTERM
      COMMON /MYSTUF/H,Ab1,Ab2,m0hno3,m0base,m0nano2,m0h2o2,Na
      COMMON /MYSTUF2/DATAPTS
      COMMON /MYSTUF3/kw,kbase,t,rho,A,conf1,conf2

      INTEGER*4 LVARS(NNVARS)
      CHARACTER*8 RAMCON, RAMVAR
      LOGICAL INPRNT,OTPRNT
      DIMENSION BLVAR(NNVARS),BUVAR(NNVARS),BLCON(NFUN),BUCON(NFUN)
      DIMENSION XX(NNVARS),FCNS(NFUN),RMULTS(NFUN),IIBV(NFUN)
      DIMENSION RAMCON(NFUN),RAMVAR(NNVARS),INBIND(NFUN),IIUB(NFUN)
      DIMENSION NONBAS(NNVARS),REDGR(NNVARS),DEFAUL(41),Z(NCORE)
      CHARACTER*76 ATITLE
      DOUBLE PRECISION H(150),Ab1(75),Ab2(75),m0hno3(75)
      DOUBLE PRECISION m0nano2(75),m0h2o2(75),m0base(75),Na(75)
      INTEGER DATAPTS,SET
      DOUBLE PRECISION kw,kbase,t,rho,A,eps,conf1(75),conf2(75)
      CHARACTER*10 FILE

      DATA ATITLE/'NITRATE EQUILIBRIA FITTING PROCEDURE'/
      DATA RAMCON/NFUN*'        '/
      DATA RAMVAR/NNVARS*'        '/
      DATA BIG/1.D31/

      DATAPTS=DATA

      write (*,*) "Data Set > "
      read (*,*) SET

C     SET LOGICAL I/O UNITS

      IOIN =  1
      IOOUT = 2
      IOERR = 2
      IOTERM = 8

C ******************************************************************
C  SET INTIAL VALUES

      open (99,file='xinit.dat')
      open (98,file='data.dat')
      open (97,file='conf1.dat')
      open (96,file='conf2.dat')

      write (*,*) "Reading initialization file"
      do i=1,NNVARS
```

```
        read (99,20) XX(i)
 20       format(f21.16)
c         write (*,*) xx(i),i
      enddo

      do i=1,DATAPTS
c      set Na(i) = 1 for true at each data point
        Na(i)=1.0
      enddo

      k=0
c      find those data points that do not contain sodium
      do i=1,DATAPTS
        if(XX(1+k).lt.-45.0) then
          Na(i) = 0.0
c           write (*,*) "Na ",i,Na(i)
        endif
        k=k+16
      enddo

      write (*,*) "Reading data file"
      do i=1,DATAPTS
        read (98,35) m0hno3(i), m0base(i), m0h2o2(i), m0nano2(i),
     &        Ab1(i), Ab2(i)
c         read (97,36) conf1(i)
c         read (96,36) conf2(i)
        conf1(i)=1.0
        conf2(i)=1.0
 35       format (f9.6,f10.7,f8.5,f10.7,2f12.9)
 36       format (f3.1)
c         write (*,*) i,m0hno3(i),m0base(i),m0h2o2(i),m0nano2(i),
c      &        Ab1(i),Ab2(i)
c      this corrects for the fact that the data is in O2 and the model
c      accounts for H2O2
        m0h2o2(i)=2*m0h2o2(i)
      enddo

      close (99)
      close (98)

c      set temperature and density
      if (SET.eq.1) then
        t=380+273.15
        rho=0.506380
      endif
      if (SET.eq.2) then
        t=380+273.15
        rho=0.542991
      endif
      if (SET.eq.3) then
        t=380+273.15
```

```
        rho=0.567060
      endif
      if (SET.eq.4) then
        t=380+273.15
        rho=0.600454
      endif

      if (SET.eq.5) then
        t=400+273.15
        rho=0.242580
      endif
      if (SET.eq.6) then
        t=400+273.15
        rho=0.395498
      endif
      if (SET.eq.7) then
        t=400+273.15
        rho=0.467696
      endif
      if (SET.eq.8) then
        t=400+273.15
        rho=0.533327
      endif

      write (*,*) "Temp (K)",t
      write (*,*) "Density (g/cm^3)",rho
      write (*,*) "Determining Constants"
c     determine Kb and Kw
      call kwater(t,rho,kw)
      call epsilon(t,rho,eps)
      call kb(t,kbase)
      call Debye(t,rho,eps,A)

      write (*,*) "     Kw",kw
      write (*,*) "     Kb",kbase
      write (*,*) "     A",A

C *****************************************************************

CC  OTHER STUFF

      INPRNT = .TRUE.
      OTPRNT = .TRUE.
      DEBUG =  .FALSE.

      LVARS(1) = 0

      DO 10 I=1,41
10    DEFAUL(I) = 1.0D0

c     DEFAUL(9) = 0.0D0
```

```
c      IIPR = 1

c     tuned parameters

      DEFAUL(1) = 0.0
      FPNEWT=1d-8
      DEFAUL(2) = 0.0
      FPINIT=1d-4
      DEFAUL(3) = 0.0
      FPSTOP=1d-4
      DEFAUL(6) = 0.0
      NNSTOP=15
c      DEFAUL(8) = 0.0
c      LLMSER=200
c      DEFAUL(14) = 0.0
c      PPSTEP=1e-13
      DEFAUL(15) = 0.0
      IIQUAD=1
      DEFAUL(18) = 0.0
c      DEFAUL(28) = 0.0
c      IISCAL=1
c      DEFAUL(29) = 0.0
c      IISCLG=200
      DEFAUL(19) = 1.0D0
c     Hard bounds held
      DEFAUL(34) = 0.0
      DEFAUL(38) = 0.0

C
C   THIS NEXT STATEMENT IS CONVENIENT FOR PC'S.
C   YOU MAY WISH TO DELETE IT FOR MAINFRAMES,AND
C   LINK LOGICAL AND ACTUAL FILENAMES OUTSIDE THE LSGRG2
C   SYSTEM.
C

      OPEN(UNIT = IOOUT,FILE = 'results.out')

C*****************************************************************

      write (*,*) "Assigning Upper & Lower Bounds on Variables"
c     all concentrations
      do i=1,(16*DATA)
        BLVAR(i) = -50
        BUVAR(i) = -0.00000001
      enddo

c     reset values for ionic strength
      k=0
      do i=1,DATA
        BLVAR(15+k) = 0.0
        BUVAR(15+k) = 0.1
```

```
        k=k+16
      enddo

c     set tighter bounds on NO since it seems to be screwing up
      k=0
      do i=1,12
c         BLVAR(11+k) = -3.1
c         BLVAR(12+k) = -2.74
        k=k+16
      enddo
      do i=13,28
c         BLVAR(11+k) = -3.13
c         BLVAR(12+k) = -2.73
        k=k+16
      enddo
      do i=29,36
c         BLVAR(11+k) = -3.26
c         BLVAR(12+k) = -4.07
        k=k+16
      enddo
      do i=37,43
c         BLVAR(11+k) = -2.95
c         BLVAR(12+k) = -3.47
        k=k+16
      enddo


c     remove NO2- from model
      k=0
      do i=1,DATA
        BLVAR(4+k) = -50
        BUVAR(4+k) = -50
        k=k+16
      enddo

c     remove N2O3 from model
      k=0
      do i=1,DATA
        BLVAR(13+k) = -50
        BUVAR(13+k) = -50
        k=k+16
      enddo

      j=0
      do i=1,DATA
        if (Na(i).eq.0.0) then
          BUVAR(1+j) = -50
          BUVAR(8+j) = -50
          BUVAR(14+j) = -50
        endif
        j=j+16
```

```
      enddo

c      Ka1
      BLVAR(16*DATA + 1) = -4.0
      BUVAR(16*DATA + 1) = -2.0
c      Ka2
      BLVAR(16*DATA + 2) = -50.0
      BUVAR(16*DATA + 2) = -50.0
c      K1
      BLVAR(16*DATA + 3) = -2.0
      BUVAR(16*DATA + 3) = 2.0
c      K2
      BLVAR(16*DATA + 4) = -3.0
      BUVAR(16*DATA + 4) = -0.0
c      K3
      BLVAR(16*DATA + 5) = -3.0
      BUVAR(16*DATA + 5) = -0.0
c      K4
      BLVAR(16*DATA + 6) = -50.0
      BUVAR(16*DATA + 6) = -50.0
c      K5
      BLVAR(16*DATA + 7) = -3.0
      BUVAR(16*DATA + 7) = -0.0
c      K6
      BLVAR(16*DATA + 8) = -4.0
      BUVAR(16*DATA + 8) = -0.0
c      E1
      BLVAR(16*DATA + 9) = -1.5
      BUVAR(16*DATA + 9) = -1.0
C       E2
      BLVAR(16*DATA + 10) = -2.0
      BUVAR(16*DATA + 10) = -1.0


      j=0
      do i=1,DATA
        RAMVAR(1+j) = 'Na+ '
        RAMVAR(2+j) = 'H+ '
        RAMVAR(3+j) = 'NO3- '
        RAMVAR(4+j) = 'NO2- '
        RAMVAR(5+j) = 'OH- '
        RAMVAR(6+j) = 'HNO3 '
        RAMVAR(7+j) = 'HNO2 '
        RAMVAR(8+j) = 'NaOH '
        RAMVAR(9+j) = 'NO2 '
        RAMVAR(10+j) = 'O2 '
        RAMVAR(11+j) = 'NO '
        RAMVAR(12+j) = 'N2O '
        RAMVAR(13+j) = 'N2O3 '
        RAMVAR(14+j) = 'NaNO3'
        RAMVAR(15+j) = 'I '
```

```
      RAMVAR(16+j) = 'G+- '
      j=j+16
    enddo

    RAMVAR(16*DATA + 1) = 'Ka1 '
    RAMVAR(16*DATA + 2) = 'Ka2 '
    RAMVAR(16*DATA + 3) = 'K1 '
    RAMVAR(16*DATA + 4) = 'K2 '
    RAMVAR(16*DATA + 5) = 'K3 '
    RAMVAR(16*DATA + 6) = 'K4 '
    RAMVAR(16*DATA + 7) = 'K5 '
    RAMVAR(16*DATA + 8) = 'K6 '
    RAMVAR(16*DATA + 9) = 'E1 '
    RAMVAR(16*DATA + 10) = 'E2 '

C ******************************************************************

C *   SET FUNCTION LOWER AND UPPER BOUNDS AND NAMES FOR FUNCTIONS   *
C *   BLCON  -- Bound Lower CONstraints                          *
C *   BUCON  -- Bound Upper CONstraints                          *
C *   FUNNAME - UP TO EIGHT CHARACTERS                              *
C *

    write (*,*) "Assigning Upper & Lower Bounds on Constraints"
    do i=1,(16*DATA)
      BLCON(i) = 0.0
      BUCON(i) = 0.0
    enddo

c     reset the constraints on log Kb,and log kw
    j=0
    do i=1,DATA
      BLCON(5+j) = log10(kw)
      BUCON(5+j) = log10(kw)
c     need to account for Na(i)
      if (Na(i).eq.1) then
        BLCON(6+j) = log10(kbase)
        BUCON(6+j) = log10(kbase)
      endif
      j=j+16
    enddo

    BLCON(16*DATA + 1) = -BIG
    BUCON(16*DATA + 1) = BIG

    j=0
    do i=1,DATA
      RAMCON(1+j) = 'CHARGE BAL'
      RAMCON(2+j) = 'MB N'
      RAMCON(3+j) = 'STOICH BAL'
      RAMCON(4+j) = 'MB Na'
```

```
        RAMCON(5+j) = 'Kw CONSTR'
        RAMCON(6+j) = 'Kb CONSTR'
            RAMCON(7+j) = 'Ka1 CONSTR'
            RAMCON(8+j) = 'Ka2 CONSTR'
            RAMCON(9+j) = 'K1 CONSTR'
            RAMCON(10+j)= 'K2 CONSTR'
        RAMCON(11+j)= 'K3 CONSTR'
        RAMCON(12+j)= 'K4 CONSTR'
        RAMCON(13+j)= 'K5 CONSTR'
        RAMCON(14+j)= 'K6 CONSTR'
        RAMCON(15+j)= 'IONIC ST'
        RAMCON(16+j)= 'ACTIVITY'
        j=j+16
      enddo

      RAMCON(16*DATA + 1)= 'OBJECT'

C ******************************************************************

C     WRITE(6,*) 'CALLING GRGSUB'
      CALL GRGSUB(INPRNT,OTPRNT,NCORE,NNVARS,NFUN,MAXBAS,
     1
MAXHES,NNOBJ,ATITLE,LVARS,BLVAR,BUVAR,BLCON,BUCON,DEFAUL,FPNEWT,
     2 FPINIT,FPSTOP,FPSPIV,PPH1EP,NNSTOP,IITLIM,LLMSER,IIPR,IIPN4,
     3 IIPN5,IIPN6,IIPER,PPSTEP,IIQUAD,LDERIV,MMODCG,
     4 RAMCON,RAMVAR,AIJTOL,PIVPCT,MXTABU,FFUNPR,CONDTL,IDEGLM,
     5 FPBOUN,FPDEG,IISCAL,IISCLG,IMEMCG,IIBVBL,XX,IIBV,FCNS,
     6 INBIND,RMULTS,NONBAS,REDGR,IIUB,NBIND,NNONB,INFORM,Z)
C     WRITE(6,*) 'EXITING GRGSUB'
      STOP
      END




C ******************************************************************  *

      SUBROUTINE GCOMP(G,X)

c     x=DATA*mi + sum(ki,E)
c     G=DATA*CONSTRAINT EQUATIONS + OBJECTIVE
c     H=2*DATA

      COMMON /MYSTUF/H,Ab1,Ab2,m0hno3,m0base,m0nano2,m0h2o2,Na
      COMMON /MYSTUF2/DATAPTS
      COMMON /MYSTUF3/kw,kbase,t,rho,A,conf1,conf2

      INTEGER j,k,m,DATAPTS

      DOUBLE PRECISION G(*),x(*),H(150),t,rho,kw,kbase,eps,A,b
c     all arrays below are x(DATA)
```

```
      DOUBLE PRECISION m0base(75),m0hno3(75),m0nano2(75),m0h2o2(75)
      DOUBLE PRECISION Na(75),mtotal(75),Ab1(75),Ab2(75),conf1(75)
      DOUBLE PRECISION conf2(75),W(5)

      b=1.2

c      write (*,*) "In GCOMP()"
c      write (*,*) "m0hno3",m0hno3
c      write (*,*) "m0base",m0base
c      write (*,*) "m0h2o2",m0h2o2
c      write (*,*) "m0nano2",m0nano2
c      write (*,*) "Ab1",Ab1
c      write (*,*) "Ab2",Ab2

c      do i=1,684
c        write (*,*) x(i),i
c      enddo

c     determine total concentration
      do m=1,DATAPTS
        mtotal(m)=m0hno3(m)+m0base(m)+m0nano2(m)+m0h2o2(m)
      enddo

      j=0
      k=0
      do m=1,DATAPTS
c     charge bal
        G(1+j)=(10**x(1+k)+10**x(2+k)-10**x(3+k)-10**x(4+k)
     &        -10**x(5+k))/mtotal(m)
c     mass bal N
        G(2+j)=(m0hno3(m)+m0nano2(m)-10**x(3+k)-10**x(4+k)-10**x(6+k)
     &        -10**x(7+k)-10**x(9+k)-10**x(11+k)-2*10**x(12+k)
     &        -2*10**x(13+k)-10**x(14+k))/mtotal(m)
c     redox bal
        G(3+j)=(4.*(10**x(10+k)-10**x(13+k))-10**x(9+k)-3.*10**x(11+k)
     &        -2.*(m0h2o2(m)+10**x(7+k)+10**x(4+k)-m0nano2(m))
     &        -8.*10**x(12+k))/mtotal(m)
c     mass bal Na
        G(4+j)=(m0base(m)+m0nano2(m)-10**x(1+k)-10**x(8+k)-
     &        10**x(14+k))*Na(m)/mtotal(m)
c     kw rxn
        G(5+j)=(x(2+k)+x(5+k)+2.*x(16+k))
c     kb rxn
        G(6+j)=(-x(8+k)+x(1+k)+x(5+k)+2.*x(16+k))*Na(m)
c     ka1 rxn
        G(7+j)=x(16*DATAPTS+1)-x(2+k)-x(3+k)-2.*x(16+k)+x(6+k)
c     ka2 rxn
        G(8+j)=(x(16*DATAPTS+2)-x(2+k)-x(4+k)-2.*x(16+k)+x(7+k))*0.0
c     k1 rxn
        G(9+j)=x(16*DATAPTS+3)-2.*x(9+k)-0.5*x(10+k)+2.*x(6+k)
c     k2 rxn
```

```
        G(10+j)=x(16*DATAPTS+4)-x(6+k)-x(7+k)+2.*x(9+k)
c     k3 rxn
        G(11+j)=x(16*DATAPTS+5)-2.*x(11+k)-0.5*x(10+k)+2.*x(7+k)
c     k4 rxn
        G(12+j)=(x(16*DATAPTS+6)+2.*x(7+k)-x(13+k))*0.0
c     k5 rxn
        G(13+j)=x(16*DATAPTS+7)+2.*x(11+k)-x(12+k)-0.5*x(10+k)
c     k6 rxn
        G(14+j)=(x(16*DATAPTS+8)+x(14+k)-x(1+k)-x(3+k)-2.*x(16+k))*
     &        Na(m)*1.0
c     ionic strength
        G(15+j)=x(15+k)-0.5*(10**x(1+k)+10**x(2+k)+10**x(3+k)
     &        + 10**x(4+k)+10**x(5+k))
c     activity coef
        G(16+j)=x(16+k)+A/2.303*(sqrt(x(15+k))/(1.+b*sqrt(x(15+k)))
     &        + 2./b*log(1.+1.2*sqrt(x(15+k))))
        k=k+16
        j=j+16
      enddo

c      write (*,*) "out of eq"
c      do i=1,16*DATAPTS
c        write (*,*) "G(",i,")",G(i)
c      enddo
c      STOP

      k=0
      j=0

c     all the parts of the objective function
c     weights on specific parts of objective function
      W(1)=10000
      W(2)=100000

c     construct parts of objective function
      do m=1,DATAPTS
        H(1+j)=W(1)*abs((Ab1(m)-10**(x(16*DATAPTS+9)+x(9+k))))
        H(2+j)=W(2)*abs((Ab2(m)-10**(x(16*DATAPTS+10)+x(7+k))))
        j=j+2
        k=k+16
      enddo

      G(16*DATAPTS+1)=0
c     objective function
      do j=1,2*DATAPTS
        G(16*DATAPTS+1)=G(16*DATAPTS+1)+H(j)
      enddo

      return
      end
```

```
c     *************************************************************
      subroutine kb(t,k)
c     valid from 250 to 325 C
c     naoh
      double precision t,k

      k=10**(91651.5/t - 1646.989 - 0.251228*t + 597.461*log10(t) -
     &      5610500/t**2)

      return
      end

c     ************************************************************
      subroutine Debye(t,p,e,A)
c     this subroutine calculates the Debye-Huckel slope from the Pitzer Eq.

      double precision t,p,e,A

c     use scaling for Debye-Huckel slope
c     A=0.3910 at t=25 C // Pitzer Thermo of Electrolytes (1977)
      A=0.3910*sqrt(p/1)*(298.15/t)**1.5*(78.71351/e)**1.5
      return
      end

c     ***********************************************************
      subroutine epsilon(t,p,e)
c     this subroutine uses the Uematsu and Franck dielectric constant model

      double precision tr,t,p,e,A(10)

      A(1)=7.62571
      A(2)=244.003
      A(3)=-140.569
      A(4)=27.7841
      A(5)=-96.2805
      A(6)=41.7909
      A(7)=-10.2099
      A(8)=-45.2059
      A(9)=84.6395
      A(10)=-35.8644

      tr=t/298.15
      e=1. + A(1)*p/tr + p**2*(A(2)/tr + A(3) + A(4)*tr)
     &     + p**3*(A(5)/tr + A(6)*tr + A(7)*tr**2)
     &     + p**4*(A(8)/tr**2 + A(9)/tr + A(10))

      return
      end

c     *********************************************************
      subroutine kwater(t,p,k)
```

```
c     this subroutine uses the Franck and Marshall Kw model

      double precision t,p,k

      k=10**(-4.098 - 3245.2/t + 2.2362e5/t**2 - 3.984e7/t**3 +
     &    log10(p)*(13.957 - 1262.3/t + 8.5641e5/t**2))
      return
      end

c     ***********************************************************
```

# Appendix C: Jackknife Program

This FORTRAN subroutine was written to take the equilibrium constants and extinction coefficients determined from the Nitrate Bootstrap Optimization Program described in Appendix B and perform statistical manipulations to determine the error bars associated with the solution set obtained.

```
      double precision ka(75),k1(75),k2(75),k3(75),k5(75),k6(75)
      double precision E1(75),E2(75)
      double precision Kaavg,Kasd,SUMa
      double precision K1avg,K1sd,SUM1
      double precision K2avg,K2sd,SUM2
      double precision K3avg,K3sd,SUM3
      double precision K5avg,K5sd,SUM5
      double precision K6avg,K6sd,SUM6
      double precision E1avg,E1sd,SUME1
      double precision E2avg,E2sd,SUME2
      character*16 NAME
      double precision DATAPTS,temp
      double precision Za(75),Z1(75),Z2(75),Z3(75),Z4(75)
      double precision Z5(75),Z6(75),ZE1(75),ZE2(75)
      double precision Zatop,Zabot,Z1top,Z1bot,Z2top,Z2bot
      double precision Z3top,Z3bot,Z5top,Z5bot,Z6top,Z6bot
      double precision Ze1top,Ze1bot,Ze2top,Ze2bot
      double precision katop,kabot,k1top,k1bot,k2top,k2bot
      double precision k3top,k3bot,k5top,k5bot,k6top,k6bot
      double precision e1top,e1bot,e2top,e2bot
      integer top,bottom

      Kaavg=0.0
      K1avg=0.0
      K2avg=0.0
      K3avg=0.0
      K5avg=0.0
      K6avg=0.0
      E1avg=0.0
      E2avg=0.0

c     determine which file to use
      write (*,*) "Enter file name> "
      read (*,*) NAME
```

```
c     write (*,*) NAME

c    determine number of jackknifes
     write (*,*) "Number of data points> "
     read (*,*) DATAPTS

c    read in jackknifes
     open(15,file=NAME)
     read (15,*)
     do i=1,DATAPTS
        read (15,15) ka(i),k1(i),k2(i),k3(i),k5(i),k6(i),E1(i),E2(i)
c         write (*,15) ka(i),k1(i),k2(i),k3(i),k5(i),k6(i)
     enddo
 15   format (8f7.3)
     open(16,file='knife.dat')

c    determine average
     do i=1,DATAPTS
        Kaavg=Kaavg+ka(i)
        K1avg=K1avg+k1(i)
        K2avg=K2avg+k2(i)
        K3avg=K3avg+k3(i)
        K5avg=K5avg+k5(i)
        K6avg=K6avg+k6(i)
              E1avg=E1avg+E1(i)
              E2avg=E2avg+E2(i)
     enddo

     Kaavg=Kaavg/DATAPTS
     K1avg=K1avg/DATAPTS
     K2avg=K2avg/DATAPTS
     K3avg=K3avg/DATAPTS
     K5avg=K5avg/DATAPTS
     K6avg=K6avg/DATAPTS
     E1avg=E1avg/DATAPTS
     E2avg=E2avg/DATAPTS

c     write (*,*) "Kaavg",Kaavg
c     write (*,*) "K1avg",K1avg
c     write (*,*) "K2avg",K2avg
c     write (*,*) K3avg
c     write (*,*) K5avg
c     write (*,*) K6avg

c    determine standard deviation
     do i=1,DATAPTS
        SUMa=(ka(i)-Kaavg)**2
        SUM1=(k1(i)-K1avg)**2
        SUM2=(k2(i)-K2avg)**2
        SUM3=(k3(i)-K3avg)**2
        SUM5=(k5(i)-K5avg)**2
```

```
        SUM6=(k6(i)-K6avg)**2
            SUME1=(E1(i)-E1avg)**2
            SUME2=(E2(i)-E2avg)**2
      enddo

      Kasd=sqrt((DATAPTS-1)/DATAPTS*SUMa)
      K1sd=sqrt((DATAPTS-1)/DATAPTS*SUM1)
      K2sd=sqrt((DATAPTS-1)/DATAPTS*SUM2)
      K3sd=sqrt((DATAPTS-1)/DATAPTS*SUM3)
      K5sd=sqrt((DATAPTS-1)/DATAPTS*SUM5)
      K6sd=sqrt((DATAPTS-1)/DATAPTS*SUM6)
      E1sd=sqrt((DATAPTS-1)/DATAPTS*SUME1)
      E2sd=sqrt((DATAPTS-1)/DATAPTS*SUME2)

c      write (*,*) "sd",kasd
c      write (*,*) k1sd
c      write (*,*) k2sd
c      write (*,*) k3sd
c      write (*,*) k5sd
c      write (*,*) k6sd

      do i=1,DATAPTS
        Za(i)=(ka(i)-kaavg)/kasd
        Z1(i)=(k1(i)-k1avg)/k1sd
        Z2(i)=(k2(i)-k2avg)/k2sd
        Z3(i)=(k3(i)-k3avg)/k3sd
        Z5(i)=(k5(i)-k5avg)/k5sd
        Z6(i)=(k6(i)-k6avg)/k6sd
        ZE1(i)=(E1(i)-e1avg)/e1sd
        ZE2(i)=(E2(i)-e2avg)/e2sd
      enddo

      top=DATAPTS*0.05
      bottom=DATAPTS*0.95

c      sort out Z's
      i=1
      do while (i.lt.DATAPTS)
        j=DATAPTS
        do while (j.gt.i)
          if (Za(j-1).lt.Za(j)) then
            temp=Za(j-1)
            Za(j-1)=Za(j)
            Za(j)=temp
          endif
          if (Z1(j-1).lt.Z1(j)) then
            temp=Z1(j-1)
            Z1(j-1)=Z1(j)
            Z1(j)=temp
          endif
          if (Z2(j-1).lt.Z2(j)) then
```

```
            temp=Z2(j-1)
            Z2(j-1)=Z2(j)
            Z2(j)=temp
          endif
          if (Z3(j-1).lt.Z3(j)) then
            temp=Z3(j-1)
            Z3(j-1)=Z3(j)
            Z3(j)=temp
          endif
          if (Z5(j-1).lt.Z5(j)) then
            temp=Z5(j-1)
            Z5(j-1)=Z5(j)
            Z5(j)=temp
          endif
          if (Z6(j-1).lt.Z6(j)) then
            temp=Z6(j-1)
            Z6(j-1)=Z6(j)
            Z6(j)=temp
          endif
          if (ZE1(j-1).lt.ZE1(j)) then
            temp=ZE1(j-1)
            ZE1(j-1)=ZE1(j)
            ZE1(j)=temp
          endif
          if (ZE2(j-1).lt.ZE2(j)) then
            temp=ZE2(j-1)
            ZE2(j-1)=ZE2(j)
            ZE2(j)=temp
          endif
          j=j-1
        enddo
        i=i+1
      enddo

      i=1
c      do while (i.lt.DATAPTS+1)
c        write (16,*) Z1(i)
c        i=i+1
c      enddo

      Zatop=Za(top)
      Zabot=Za(bottom)
      katop=kaavg-Zatop*kasd
      kabot=kaavg-Zabot*kasd

      Z1top=Z1(top)
      Z1bot=Z1(bottom)
      k1top=k1avg-Z1top*k1sd
      k1bot=k1avg-Z1bot*k1sd

      Z2top=Z2(top)
```

```
      Z2bot=Z2(bottom)
      k2top=k2avg-Z2top*k2sd
      k2bot=k2avg-Z2bot*k2sd

      Z3top=Z3(top)
      Z3bot=Z3(bottom)
      k3top=k3avg-Z3top*k3sd
      k3bot=k3avg-Z3bot*k3sd

      Z5top=Z5(top)
      Z5bot=Z5(bottom)
      k5top=k5avg-Z5top*k5sd
      k5bot=k5avg-Z5bot*k5sd

      Z6top=Z6(top)
      Z6bot=Z6(bottom)
      k6top=k6avg-Z6top*k6sd
      k6bot=k6avg-Z6bot*k6sd

      Ze1top=ZE1(top)
      Ze1bot=ZE1(bottom)
      e1top=e1avg-Ze1top*e1sd
      e1bot=e1avg-Ze1bot*e1sd

      Ze2top=ZE2(top)
      Ze2bot=ZE2(bottom)
      e2top=e2avg-Ze2top*e2sd
      e2bot=e2avg-Ze2bot*e2sd

      write (16,*)

      write (16,*) "Averages"
      write (16,16) Kaavg,K1avg,K2avg,K3avg,K5avg,K6avg,E1avg,E2avg
      write (16,*) "Standard Errors"
      write (16,16) Kasd,K1sd,K2sd,K3sd,K5sd,K6sd,E1sd,E2sd
      write (16,*) " "
      write (16,16) katop,k1top,k2top,k3top,k5top,k6top,e1top,e2top
      write (16,16) kabot,k1bot,k2bot,k3bot,k5bot,k6bot,e1bot,e2bot
      write (16,*) " "
      write (16,16) Zatop,Z1top,Z2top,Z3top,Z5top,Z6top,Ze1top,Ze2top
      write (16,16) Zabot,Z1bot,Z2bot,Z3bot,Z5bot,Z6bot,ZE1bot,ZE2bot
16    format (8f9.4)

      close(15)
      close(16)
      end
```

# Appendix D: Reaction Cells and Equipment

The development of experimental apparatuses to handle the harsh conditions of high temperature supercritical fluids has been enhanced. The use of a piston delivery system allows highly corrosive solutions to be delivered with minimal contact to key components as shown in Chapter 2 or solutions that need to be maintained under pressure to eliminate exposure to the atmosphere as shown in Chapter 4. However, despite the added benefit of removing the contact with corrosive solutions or oxygen, the use of this system does make experimentation more difficult. The frequency of broken windows due to thermal shock is significantly increased. Therefore, great care should be taken to ensure that the flow rate is set to 2 mL/min or slower when operating at temperatures above 350°C.

The development of new reaction cells has aided in the development of nanocrystals synthesized within high temperature supercritical fluids. In the first study of nanocrystal synthesis of silicon, a titanium grade 2 reactor was used that had a volume of 200 μL. It quickly became apparent, that larger volumes were required to perform the analysis of these particles. Techniques such as X-ray diffraction (XRD), X-ray photoelectron spectroscopy (XPS), and size selective precipitation require substantial masses of crystalline material. Furthermore, these small reactors have increased sealing difficulties and failures due to the use of sapphire windows. Therefore, two new types of reactors were developed to allow quick exploratory reactions (1 mL volume) and obtain large quantities (10 mL volume). Both of these reactors are outlined in Chapter 6 and are based upon a similar design, which consists of a batch-type reactor sealed with a standard HIP (High Pressure Equipment, Erie, PA) connection. In addition, these cells are durable, easily machined, and use standard fittings.

# Appendix E: Quantum Yield Calculations

The determination of quantum yield is important in determining the intensity output of a luminescent species. It is defined as the number of photons emitted divided by the number of photons absorbed yielding an upper limit of $\varphi_f = 1$. The difficulty in determining the quantum yield is created by the difficulty in obtaining the correct fluorescence intensity, which is a function of the intensity of the lamp. Since the intensity of the lamp is typically a function of the wavelength, difficulties arise in comparing the fluorescence of one substance measured at a different excitation wavelength than another. For example, the intensity of a xenon lamp will give nearly 8 times more intense light at 475 nm compared to 250 nm. Therefore, any fluorescence spectra should be corrected for differences in the intensity of the excitation source. In addition, the emission spectra have to be corrected for the difference in the response that the photomultiplier tube has at different wavelengths. Therefore, the use of a corrected fluorometer is essential in the determination of quantum yields.

To determine the quantum yield of an unknown species, a standard of known efficiency is chosen. While there are several potential standards, care has to be taken that correct conditions are applied. Factors such as the amount of oxygen, concentration, excitation wavelength, etc. may all affect the emission spectra for the standard. Here, quinine bisulfate has been chosen to be the quantum yield standard with a known efficiency of $\varphi_f = 0.57$ in 0.1 N sulfuric acid. Using Equation A1, the quantum yield may be determined for an unknown by relating the yield of the standard to that of the unknown.

$$\varphi_{f,u} = \varphi_s \frac{F_S A_U \lambda_{Ex,S} d_S}{F_U A_S \lambda_{Ex,U} d_U} \tag{A1}$$

where, $F$ is the fluorescence emission area; $A$ is the absorbance at the excitation wavelength $\lambda_{Ex}$; and $d$ is the dilution of the sample (if any) between absorbance and fluorescence.

To ensure that the fluorometer used in determining the quantum yield of the germanium nanoparticles described in Chapter 6 was being corrected properly, the quantum yield was determined for β-naphthol. Because any error associated with the absorbance of the species is correlated directly into error associated with the quantum yield, a concentration was chosen such that the absorbance was at least 0.1 at the excitation wavelength. Likewise, the standard was chosen to have sufficient absorbance so that the error could be minimized. Because the concentration of the solutions was too high for accurate fluorescence measurements, each solution was diluted to 1/100 of the concentration. Using these solutions, the fluorescence was measured and the area of the emission spectra is determined shown in Figure A1. The area determined for the β-naphthol resulted in a quantum yield of 12 % compared to a literature value of 15 %.

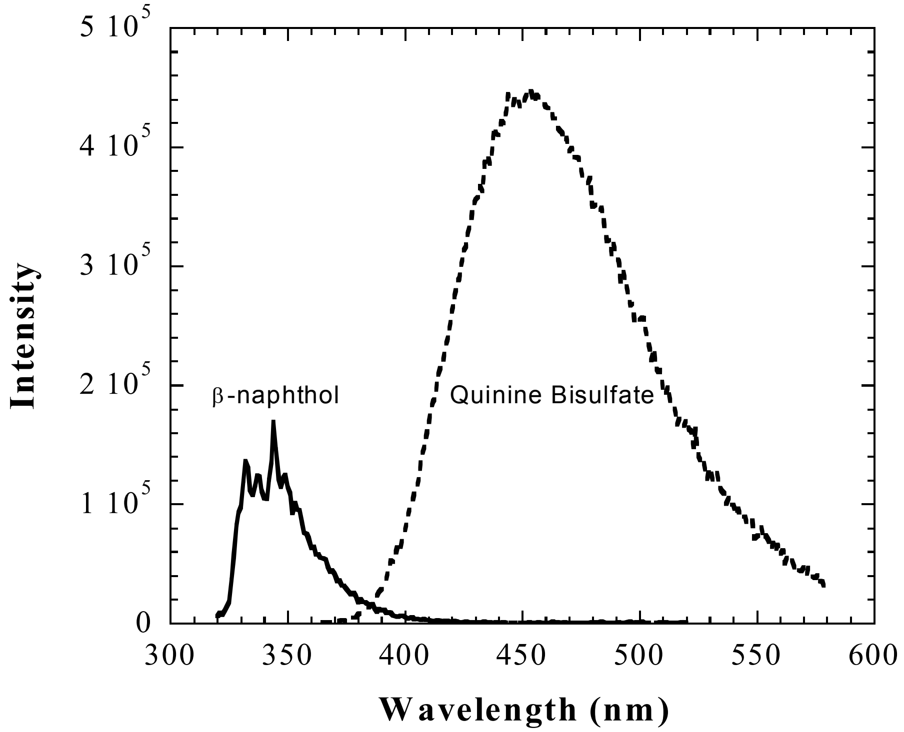

Fig. A1. PL spectra of quinine bisulfate and β-naphthol solutions for determination of quantum yields.

# Literature Cited

(1995). Official Methods of Analysis of AOAC International. Arlington, AOAC International.

(1997). CRC Handbook of Chemistry and Physics. Boca Raton, CRC Press.

Adschiri, T., Y. Hakuta and K. Arai (2000). "Hydrothermal Synthesis of Metal Oxide Fine Particles at Supercritical Conditions." Ind. Eng. Chem. Res. **29**: 4901-4907.

Adschiri, T., K. Kanazawa and K. Arai (1992). "Rapid and Continuous Hydrothermal Crystallization of Metal Oxide Particles in Supercritical Water." J.Am.Ceram.Soc. **75**(4): 1019.

Adschiri, T., K. Kanazawa and K. Arai (1992). "Rapid and Continuous Hydrothermal Synthesis of Boehmite Particles in Subcritical and Supercritical Water." J.Am.Ceram.Soc. **75**(9): 2615.

Adschiri, T., S. Yamane, S. Onai and K. Arai (1994). . Proc. 3rd Int. Symp. on Supercritical Fluids. Strasbourg, France. **T3:** 241.

Alivisatos, A. P. (1996). "Semiconductor Clusters, Nanocrystals, and Quantum Dots." Science **271**: 933.

Armerding, W., J. Walter, C. Ruger, M. Spiekermann and F. J. Comes (1993). "Local Monitoring of Absolute NO2 Concentrations in Ambient Air by Multipass Absorption Spectroscopy." Ber.Bunsenges.Phys.Chem. **97**(11): 1440.

Baes, C. F., Jr. and R. E. Mesmer (1976). The Hydrolysis of Cations. New York, Wiley.

Balbuena, P. B., K. P. Johnston and P. J. Rossky (1996). "Molecular Dynamics Simulation of Electrolyte Solutions in Ambient and Supercritical Water. 1. Ion Solvation." J. Phys. Chem. **100**: 2706.

Banin, U., C. J. Lee, G. A.A., A. V. Kadavanich, A. P. Alivisatos, W. Jaskolski, G. W. Bryant, A. L. Efros and M. Rosen (1998). "Size-dependent electronic level structure of InAs nanocrystal quantum dots: Test of multiband effective mass theory." J. Chem. Phys. **109**: 2306.

Barj, M., J. F. Bocquet, K. Chhor and C. Pommier (1992). "Submicron magnesium aluminum oxide ($MgAl_2O_4$) powder synthesis in supercritical ethanol." J. Mater. Sci. **27**: 2187.

Barton, C. J., G. M. Hebert and W. L. Marshall (1961). "Aqueous Systems at High temperature - II Liquid - liquid immiscibility in the system UO3-so3-N2O5-H2O above 300 $^oC$." J.inorg.nucl.Chem. **21**: 141.

Batson, P. E. and J. R. Heath (1993). "Electron energy loss spectroscopy of single silicon nanocrystals: The conduction band." Phys. Rev. Lett. **71**: 911.

Bayliss, N. S. and D. W. Watts (1956). "The spectra and equilibria of nitrosonium ion, nitroacidium ion, and nitrous acid in solutions of sulphuric, hydrochloric, and phosphoric acids." Aust.J.Chem. **9**: 319.

Beattie, I. R. and A. J. Vosper (1961). "Dinitrogen Trioxide. Part IV. Composition of the Vapour in Equilibrium with Liquid Mixtures of Nitrogen Dioxide and Nitric Oxide." J.Chem.Soc.: 2106.

Bennet, M. R., G. M. Brown, L. Maya and F. A. Posey (1982). "Oxidation of Hydroxylamine by Nitrous and Nitric Acids." Inorg.Chem. **21**: 2461.

Bennett, G. E. and K. P. Johnston (1994). "UV-visible Absorbance Spectroscopy of Organic Probes in Supercritical Water." J.Phys.Chem. **98**: 441.

Beverskog, B. and I. Puigdomenech (1997). "Revised Pourbaix Diagrams for Copper at 25 to 300 °C." J. Electrochem. Soc. **144**(10): 3476-3483.

Bley, R. A. and S. M. Kauzlarich (1996). "A low-temperature solution phase route for the synthesis of silicon nanoclusters." J. Am. Chem. Soc. **118**: 12461.

Borgohain, K., J. Singh, B., M. Rama Rao, V., T. Shripathi and S. Mahamuni (2000). "Quantum size effects in CuO nanoparticles." Phys. Rev. B: Condens. Matter Mater. Phys. **61**(16): 11093-11096.

Brenecke, J. F., D. L. Tomasko, J. Peshkin and C. A. Eckert (1990). "Fluorescence Spectroscopy Studies of Dilute Supercritical Solutions." J. Chem. Eng. **29**: 1682-1690.

Broll, D., C. Kaul, A. Kramer, P. Krammer, T. Richter, M. Jung, H. Vogel and P. Zehner (1999). "Chemistry in supercritical water." Angew. Chem. **Int. Ed.**(38): 2999- 3014.

Brooke, A., D. Kendrich and A. Meeraus (1992). GAMS: A User's Guide. Danvers, MA, Boyd and Fraser.

Brus, L. E. (1994). "Luminescence of silicon materials: chains, sheets, nanocrystals, nanowires, microcrystals, and porous silicon." J. Phys. Chem. **98**: 3575.

Brus, L. E., P. F. Szajowski, W. L. Wilson, T. D. Harris, S. Schuppeler and P. H. Citrin (1995). "Electronic spectroscopy and photophysics of Si nanocrystals: Relationship to bulk c-Si and porous Si." J. Am. Chem. Soc. **117**: 2915.

Brust, M., M. Walker, D. Bethell, D. J. Schiffrin and R. Whyman (1994). "Synthesis of Thiol-derivatised Gold Nanoparticles in a Two-phase Liquid-Liquid System." J. Chem. Soc. Chem. Comm.: 801-802.

Bundy, F. P. and J. S. Kasper (1963). "A new dense form of solid germanium." Science **139**: 340.

Bunton, C. A. and G. Stedman (1958). "The Absorption Spectra of Nitrous Acid in Aqueous Perchloric Acid." J.Chem.Soc.: 2440.

Cabanas, A., J. A. Darr, E. Lester and M. Poliakoff (2000). "A continuous and clean one-step synthesis of nano-particulate $Ce_{1-x}Zr_xO_2$ solid solutions in near-critical water." Chem. Commun.: 901-902.

Cabanas, A., J. A. Darr, E. Lester and M. Poliakoff (2001). "Continuous hydrothermal synthesis of inorganic materials in a near-critical water flow reactor; the one-step synthesis of nano-particulate $Ce_{1-x}Zr_xO_2$ (x=0-1) solid solutions." J. Mater. Chem. **11**: 561-568.

Calcott, P. D. J., K. J. Nash, L. T. Canham, M. J. Kane and D. Brumhead (1993). "Identification of radiative transitions in highly porous silicon." J. Phys.: Condens. Matter **5**: L91.

Canham, L. T. (1990). "Silicon quantum wire array fabrication by electrochemical and chemical dissolution of wafers." Appl. Phys. Lett. **57**: 1046.

Capewell, S., G. Hefter and P. M. May (1998). “Potentiometric Investigation of the Weak Association of Sodium and Carbonate Ions at 25°C.” J. Solution Chem. **27**(10): 865.

Carley, A. F., L. A. Dollard, P. R. Norman, C. Pottage and M. W. Roberts (1999). “The reactivity of copper clusters supported on carbon studied by XPS.” J. Electron Spectrosc. **98-99**: 223-233.

Caruana, C. M. (1995). “Supercritical Water Oxidation Aims for Wastewater Cleanup.” Chem. Eng. Progress **941**(4): 10-18.

Cason, J. and C. Roberts (2000). “Metallic Copper Nanoparticle Synthesis in AOT Reverse Micelles in Compressed Propane and Supercritical Ethane Solutions.” J. Phys. Chem. B **104**: 1217.

Cason, J. P., K. Khambaswadkar and C. B. Roberts (2000). “Supercritical Fluid and Compressed Solvent Effects on Metallic Nanoparticle Synthesis in Reverse Micelles.” Ind. Eng. Chem. Res. **39**: 4749-4755.

Chao, J., R. C. Wilhott and B. J. Zwolinski (1974). Thermochim.Acta **10**: 359.

Chase, M. W., Jr., C. A. Davies, J. R. Downey, Jr., D. J. Frurip, R. A. McDonald and A. N. Syverud (1985). JANAF Thermochemical Tables, American Chemical Society and the American Institute of Physics for the National Bureau of Standards.

Chen, X., R. M. Izatt and J. L. Oscarson (1994). “Thermodynamic Data for Ligand Interaction with Protons and Metal Ions in Aqueous Solutions at High Temperatures.” Chem.Rev. **94**: 467.

Chialvo, A. A. and P. T. Cummings (1994). “Hydrogen bonding in supercritical water.” J. Chem. Phys. **101**(5): 4466-4469.

Chlistunoff, J., K. J. Ziegler, L. Lasdon and K. P. Johnston (1999). “Nitric/Nitrous Acid Equilibria in Supercritical Water.” J. Physical Chem. **103**: 1678.

Chlistunoff, J. B. and K. P. Johnston (1998). “UV-Vis Spectroscopic Determination of the Dissociation Constant of Bichromate from 160 to 400°C.” J.Phys.Chem. B **102**(20): 3993.

Chusuei, C. C., M. A. Brookshier and D. W. Goodman (1999). “Correlation of Relative X-ray Photoelectron Spectroscopy Shake-up Intensity with CuO Particle Size.” Langmuir **15**: 2806-2808.

Clasen, R. J. (1984). “The Solution of the Chemical Equilibrium Programming Problem with Generalized Benders Decomposition.” Operations Research **32**(1): 70.

Connolly, J. F. (1966). “Solubility of hydrocarbons in water near the critical solution temperatures.” J. Chem. Eng. Data **11**: 13.

Corcoran, T. C., E. J. Beiting and M. O. Mitchell (1992). “High-Resolution Absolute Absorption Cross Sections of NO2 at 293,573, and 673 K at Visible Wavelengths.” J.Mol.Spectrosc. **154**: 119.

D'Angelo, J. C. and T. W. Collette (1997). “A Method for the Measurement of Site-Specific Tautomeric and Zwitterionic Microspecies Equilibrium Constants.” Anal. Chem. **69**: 1642.

Darr, J. A. and M. Poliakoff (1999). “New Directions in Inorganic and Metal-Organic Coordination Chemistry in Supercritical Fluids.” Chemical reviews **99**(2): 495.

Dell'Orco, P., B. Foy, E. Wilmanns, L. Le, J. Ely, K. Patterson and S. Buelow (1995). Hydrothermal Oxidation of Organic Compounds by Nitrate and Nitrite. Innovations in Supercritical Fluids. Science and Technology. K. W. Hutchenson, Foster, N.R. Washington, D.C., American Chemical Society**:** 179-196.

Dell'Orco, P. C. (1994). Reactions of Inorganic Nitrogen Species in Supercritical Water. University of Texas at Austin. Austin, University of Texas at Austin**:** 238.

Dell'Orco, P. C., B. F. Foy, J. M. Robinson and S. J. Buelow (1993). “Hydrothermal Treatment of Hanford Waste Constituents.” Haz.Waste Haz.Mat. **10**(2): 221.

Dixon, J. K. (1940). “The Absorption Coefficient of Nitrogen Dioxide in the Visible Spectrum.” J.Chem.Phys. **8**: 157.

Drud, A. (1992). “CONOPT - A Large-Scale GRG Code.” Journal on Computing **6**: 207.

Efron, B. and R. J. Tibshirani (1993). An Introduction to the Bootstrap. New York, Chapman & Hall.

England, C. and W. H. Corcoran (1974). "Kinetics and Mechanisms of the Gas-Phase Reaction of Water Vapor and Nitrogen Dioxide." Ind.Eng.Chem., Fundam. **13**(4): 373.

Flanagin, L. W., P. B. Balbuena, K. P. Johnston and P. J. Rossky (1997). "Ion Solvation in Supercritical Water Based on an Adsorption Analogy." J. Phys. Chem. B **101**(40): 7998.

Fourer, R., G. Gay and B. Kernighan (1993). AMPL: A Modeling Language for Mathematical Programming. Danvers, MA, Boyd and Fraser.

Franck, E. U. (1973). "Concentrated Electrolyte Solutions at High Temperatures and Pressures." J. Solution Chem. **2**(2/3): 339-356.

Frantz, J. D. (1998). "Raman spectra of potassium carbonate and bicarbonate aqueous fluids at elevated temperatures and pressures: comparison with theoretical simulations." Chemical Geology **152**: 211.

Frantz, J. D. and W. L. Marshall (1984). "Electrical conductances and ionization constants of salts, acids, and bases in supercritical aqueous fluids: I. Hydrochloric acid from 100° to 700°C and at pressures to 4000 bars." Amer. J. Sci. **284**: 651.

Friedlander, S. K. and C. S. Wang (1966). J. Colloid Interf. Sci. **22**: 126-132.

Friend, J. A. and L. E. Lyons (1959). "The Electronic Spectrum of the Nitrate Ion and Related Molecules." J.Chem.Soc.: 1572.

Fulton, J. L., M. M. Hoffman, J. G. Darab, B. J. Palmer and E. A. Stern (2000). "Copper (I) and Copper (II) Coordination Structure under Hydrothermal Conditions at 325°C: An X-ray Absorption Fine Structure and Molecular Dynamics Study." J. Phys. Chem. A **104**: 11651-11663.

Furukawa, S. and T. Miyasato (1988). "Quantum size effects on the optical band gap of microcrystalline Si:H." Phys. Rev. B **38**: 5726.

Galkin, A. A., B. G. Kostyuk, N. N. Kuznetsova, A. O. Turakulova, V. V. Lunin and M. s. Polyakov (2001). "Unusual Approaches to the Preparation of Heterogeneous Catalysts and Supports Using Water in Subcritical and Supercritical States." Kinetics and Catalysis **42**(2): 154-162.

Galkin, A. A., B. G. Kostyuk, V. V. Lunin and M. Poliakoff (2000). “Continuous Reactions in Supercritical Water: A New Route to $La_2CuO_4$ with a High Surface Area and Enhanced Oxygen Mobility.” Angew. Chem. Int. Ed. **39**(15): 2738-2740.

Gammons, C. H. and T. M. Seward (1996). “Stability of manganese (II) chloride complexes from 25 to 300°C.” Geochim.Cosmochim.Acta **60**: 4295.

Garcia, M. C., G. Ramis and C. Mongay (1982). “Spectrophotometric determination of protonation constants of mono-protic systems in strong acid and strong basic media.” Spectrochimica Acta **38A**(9): 1005.

Gazicki, M., R. Ledzion, R. Mazurczyk and S. Pawlowski (1998). “Deposition and properties of germanium/carbon films deposited from tetramethylgermanium in a parallel plate RF discharge.” Thin Solid Films **322**: 123-131.

Giannozzi, P., S. de Gironcoli, P. Pavone and S. Baroni (1991). “Ab initio calculation of phonon dispersions in semiconductors.” Phys. Rev. B **43**: 7231.

Gillet, M. (1977). “Structure of Small Metallic Particles.” Surf. Sci. **67**: 139-157.

Gloyna, E. F. and L. Li (1993). “Supercritical Water Oxidation: An Engineering Update.” Waste Management **13**: 379-394.

Gogotsi, Y. G. and M. Yoshimura (1994). “Formation of carbon films on carbides under hydrothermal conditions.” Nature **367**: 628.

Goia, D. V. and E. Matijevic (1998). “Preparation of monodispersed metal particles.” New J. Chem. **22**(11): 1203-1215.

Gorbaty, Y. E. and A. G. Kalinichev (1995). “Hydrogen bonding in supercritical water. I. Experimental results.” J. Phys. Chem. **99**(15): 5336-5340.

Gupta, R. B., J. R. Combes and K. P. Johnston (1993). “Solvent Effect on Hydrogen Bonding in Supercritical Fluids.” J. Phys. Chem. **97**(3): 707-715.

Gupta, R. B. and K. P. Johnston (1994). “Ion Hydration in Supercritical Water.” Ind. Eng. Chem. Res. **33**(11): 2819.

Gupta, R. B. and K. P. Johnston (1994). “Lattice fluid hydrogen bonding model with a local segment density.” Fluid Phase Equilibria **99**: 135.

Gupta, R. B., C. G. Panayoitou, I. C. Sanchez and K. P. Johnston (1992). “Theory of Hydrogen Bonding in Supercritical Fluids.” **38**(8): 1243-1253.

Hall, T. C. and F. E. Blacet (1952). “Separation of the Absorption Spectra of $NO_2$and $N_2O_4$ in the range of 2400-5000A.” J.Chem.Phys. **20**(11): 1745.

Heath, J. R. (1992). “A liquid-solution-phase synthesis of crystalline silicon.” Science **258**: 1131.

Heinrich, C. A. and T. M. Seward (1990). “A spectrophotometric study of aqueous iron (II) chloride complexing from 25 to 200°C.” Geochim.Cosmochim.Acta **54**(54): 2207.

Hill, N. A. and K. B. Whaley (1995). “Size dependence of excitons in silicon nanocrystals.” Phys. Rev. Lett. **75**: 1130.

Hill, N. A. and K. B. Whaley (1996). “A theoretical study of light emission from nanoscale silicon.” J. Electron. Mat. **25**: 269.

Hirano, M. and K. Etsuro (1996). “Hydrothermal Synthesis of Cerium (IV) Oxide.” J. Am. Ceram. Soc. **79**: 777-780.

Hirano, M. and K. Etsuro (1996). “The synthesis of ultrafine cerium (IV) oxide powders.” J. Mater. Sci. Lett. **15**: 1249-1250.

Hirth, T., R. Schweppe, S. Jahnke, G. Bunte, N. Eisenreich and H. Krause (1996). High Pressure Chem. Eng.(163-168).

Hisatsune, I. C. (1961). “Thermodynamic Properties of Some Oxides of Nitrogen.” J.Phys.Chem. **65**: 2249.

Hitch, B. F. and R. E. Mesmer (1976). “The Ionization of Aqueous Ammonia to 300°C in KCl Media.” J. Solution Chem. **5**(10): 667-680.

Ho, P. C. and D. A. Palmer (1996). “Ion association of dilute aqueous sodium hydroxide solutions to $600^oC$ and 300 MPa by conductance measurements.” J.Solution Chem. **25**(8): 711.

Ho, P. C. and D. A. Palmer (1997). “Ion association of dilute aqueous potassium chloride and potassium hydroxide solutions to 600°C and 300 MPa determined by electrical conductance measurements.” Geochim.Cosmochim. Acta **61**(15): 3027.

Ho, P. C., D. A. Palmer and R. E. Mesmer (1994). “Electrical Conductivity Measurements of Aqueous Sodium Chloride Solutions to 600°C and 300 MPa.” J. Solution Chem. **23**(9): 997.

Holmes, J. D., K. P. Johnston, R. C. Doty and B. A. Korgel (2000). “Orientation of Solution-Grown Silicon Nanowires.” Science **287**: 1471.

Holmes, J. D., K. J. Ziegler, R. C. Doty, L. E. Pell, K. P. Johnston and B. A. Korgel (2001). “Highly Luminescent Silicon Nanocrystals with Discrete Optical Transitions.” J. Am. Chem. Soc. **123**: 3743-3748.

Holmes, J. D. B., Prashant A.; Korgel, Brian A.; Johnston, Keith P. (1999). “Synthesis of Cadmium Sulfide Q Particles in Water-in-CO2 Microemulsions.” Langmuir **15**(20): 6613.

Huang, S., K. Daehling, T. E. Carlson, P. Taylor, C. Wai and A. Propp (1989). “Thermodynamic Analysis of Corrosion of Iron Alloys in Supercritical Water.” Am. Chem. Soc. Symp. Ser. **406**: 276.

Huh, Y., J.-G. Lee, D. C. McPhail and K. Kim (1993). “Measurement of pH at Elevated Temperatures Using the Optical Indicator Acridine.” J. Solution Chem. **22**(7): 651-661.

Inagaki, N. and M. Mitsuuichi (1983). “Glow Discharge Polymerization of Tetramethylgermanium.” J. Polym. Sci. **21**: 2887-2895.

Inczedy, J. (1976). Analytical Applications of Complex Equilibria. New York, John Wiley & Sons.

Ji, M., X. Chen, C. M. Wai and J. L. Fulton (1999). “Synthesizing and Dispersing Silver Nanoparticles in a Water-in-Supercritical Carbon Dioxide Microemulsion.” J. Am. Chem. Soc. **121**(11): 2631.

Ji, Q., E.M.E., R. van Eldik, K. P. Johnston, S. R. Goates and M. L. Lee (1995). J.Phys.Chem. **99**: 13461.

Jiang, Y., W. R. Smith and G. R. Chapman (1995). "Global Optimality Conditions and their Geometric Interpretation for the Chemical and Phase Equilibrium Problem." SIAM J. Optimization **5**(4): 813.

Johnston, K. P., G. E. Bennett, P. B. Balbuena and P. J. Rossky (1996). "Continuum electrostatic model for ion solvation and relative acidity of HCl in supercritical water." J. Am. Chem. Soc. **118**(28): 6746-6752.

Johnston, K. P. and J. B. Chlistunoff (1998). "Neutralization of acids and bases in subcritical and supercritical water: acetic acid and HCl." J. Supercritical Fluids **12**: 155.

Johnston, K. P., S. Kim and J. Combes (1989). "Spectroscopic determination of solvent strength and structure in supercritical fluid mixtures: A Review." **Chapter 5**: 53-69.

Kaiser, E. W. and C. H. Wu (1977). "A Kinetic Study of the Gas Phase Formation and Decomposition Reactions of Nitrous Acid." J.Phys.Chem. **81**(18): 1701.

Kaiser, E. W. and C. H. Wu (1977). "Measurement of the Rate of the Reaction of Nitrous Acid with Nitric Acid." J.Phys.Chem. **81**(3): 187.

Kanemitsu, Y., H. Uto, Y. Masumoto and Y. Maeda (1991). "On the origin of visible photoluminescence in nanometer-size Ge crystallites." Appl. Phys. Lett. **61**(18): 2187-2189.

Kato, A., S. Matsuda, T. Kamo, F. Nakajima, H. Kuroda and T. Narita (1981). "Reaction between NOx and NH3 on Iron Oxide-Titanium Oxide Catalyst." J.Phys.Chem. **85**: 4099.

Kettler, R. M., D. A. Palmer and D. J. Wesolowski (1995). "Dissociation Quotients of Succinic Acid in Aqueous Sodium Chloride Media to 225°C." J. Solution Chem. **24**: 65-87.

Kettler, R. M., D. J. Wesolowski and D. A. Palmer (1995). "Dissociation Quotient of Benzoic Acid in Aqueous Sodium Chloride Media to 250°C." J. Solution Chem. **24**: 385-407.

Kieke, M. L., J. W. Schooppelrei and T. B. Brill (1996). "Spectroscopy of Hydrothermal Reactions. 1. The $CO_2$-$H_2O$ System and Kinetics of Urea

Decomposition in an FTIR Spectroscopy Flow Reactor Cell Operable to 725 K and 335 bar." J. Phys. Chem. **100**(18): 7455.

Killilea, W. R., K. C. Swallow and G. T. Hong (1991). The Fate of Nitrogen in Supercritical Water Oxidation. 2nd International Symposium on Supercritical Fluids, Boston, MA, Department of Chemical Engineering, Johns Hopkins University.

Kim, M. H., C. S. Kim, H. W. Lee and K. Kim (1996). J. Chem. Soc., Faraday Trans. **92**: 4951.

Kim, S. and K. P. Johnston (1987). "Molecular Interactions in Dilute Supercritical Fluid Solutions." Ind. Eng. Chem. Res. **26**(6): 1206-1213.

Kiovsky, J. R., P. B. Koradia and C. T. Lim (1980). "Evaluation of a New Zeolitic Catalyst for NOx Reduction with NH3." Ind.Eng.Chem.Prod.Res.Dev. **19**: 218.

Klein, M. T., L. A. Torry, B. C. Wu and Y. G. Mentha (1990). "Hydrolysis in Supercritical Water: Solvent Effects as a Probe of the Reaction Mechanism." **Orlando, Florida**.

Kolthoff, I. M. and E. B. Sandell (1952). Textbook of Quantitative Inorganic Analysis. New York, The Macmillan Company.

Korzenski, M. B. and J. W. Kolis (1997). "Diels-Alder reactions using supercritical water as an aqueous solvent medium." Tetrahedron Lett. **38**(32): 5611-5614.

Kritzer, P., N. Boukis and E. Dinjus (1999). "Factors controlling corrosion in high-temperature aqueous solutions: a contribution to the dissociation and solubility data influencing corrosion processes." J. Supercritcal Fluids **15**: 205.

Lauerhaas, J. M. and M. J. Sailor (1993). "Chemical modification of the photoluminescence quenching of porous silicon." Science **261**: 1567.

Lee, C. T., Jr., P. Bhargava and K. P. Johnston (2000). "Percolation in Concentrated Water-in-Carbon Dioxide Microemulsions." J. Phys. Chem. B **104**(18): 4448-4456.

Lee, I. J., G. S. Jung and K. Kim (1994). “Spectrophotometric Determination of Dissociation Constants for Propionic Acid and 2,5-Dinitrphenol at Elevated Temperatures.” J. Solution Chem. **23**: 1283.

Lee, J. H. and N. R. Foster (1996). J. Supercrit. Fluids **9**: 99-105.

Leff, D. V., P. C. Ohara, J. R. Heath and W. M. Gelbart (1995). “Thermodynamic Control of Gold Nanocrystal Size: Experiment and Theory.” J. Phys. Chem. **99**: 7036-7041.

Liebman, J., L. Lasdon, L. Schrage and A. Warren (1986). Modeling and Optimization with GINO. Palo Alto, CA, Scientific Press.

Lingane, P. J. and Z. Z. Hugus (1970). “Normal Equations for the Gaussian Least-Squares Refinement of Formation Constants with Simultaneous Adjustment of the Spectra of the Absorbing Species.” Inorganic Chem. **9**(4): 757.

Lisiecki, I., F. Billoudet and M. Pileni, P. (1996). “Control of the shape and the size of copper metallic particles.” J. Phys. Chem. **100**(10): 4160-6.

Lisiecki, I., M. Bjorling, L. Motte, B. Ninham and M. P. Pileni (1995). “Synthesis of Copper Nanosize Particles in Anionic Reverse Micelles: Effect of the Addition of a Cationic Surfactant on the Size of the Crystallites.” Langmuir **11**(7): 2385-2392.

Lisiecki, I., A. Filankembo, H. Sack-Kongehl, K. Weiss, M. Pileni, P. and J. Urban (2000). “Structural investigations of copper nanorods by high-resolution TEM.” Phys. Rev. B: Condens. Matter Mater. Phys. **61**(7): 4968-4974.

Lisiecki, I. and M. Pileni, P. (1993). “Synthesis of copper metallic clusters using reverse micelles as microreactors.” J. Am. Chem. Soc. **115**(10): 3887-3896.

Lisiecki, I. and M. P. Pileni (1995). “Copper Metallic Particles Synthesized "in Situ" in Reverse Micelles: Influence of Various Parameters on the Size of the Particles.” J. Phys. Chem. **99**: 5077-5082.

Littau, K. A., P. J. Szajowski, A. J. Muller, A. R. Kortan and L. E. Brus (1993). “A luminescent silicon nanocrystal colloid via a high-termperature aerosol reaction.” J. Phys. Chem. **97**: 1224.

Longstaff, J. V. L. and K. Singer (1954). "The Kinetics of Oxidation by Nitrous Acid and Nitric Acid. Part II. Oxidation of Formic Acid in Aqueous Nitric Acid." J.Chem.Soc.: 2610.

Longstaff, J. V. L. and K. Singer (1954). "The Kinetics of Oxidation by Nitrous Acid and Nitric Acid. Part I. Oxidation of Formic Acid by Nitrous Acid." J.Chem.Soc.: 2604.

Lumme, P., P. Lahermo and J. Tummavuori (1965). "Thermodynamics of the Ionization of Hydroxylamine and Nitrous Acid in Water." Acta Chem. Scand. **19**: 2175.

Lumme, P. and J. Tummavuori (1965). "Potentiometric Determination of the Ionization Constant of Nitrous Acid in Aqueous Sodium Perchlorate Solutions at 25°C." Acta Chem.Scand. **19**: 617.

Luo, H. and S. C. Tucker (1995). "Compressible Continuum Solvation Model for Molecular Solutes." J. Am. Chem. Soc. **117**(45): 11359-11360.

Luo, H. and S. C. Tucker (1997). "A compressible continuum model study of the chloride plus methyl chloride reaction in supercritical water." J. Phys. Chem. **101**: 1063.

Macdonald, D. D., S. Hettiarachchi, H. Song, K. Makela, R. Emerson and M. Ben-Haim (1992). "Measurement of pH in subcritical and supercritical aqueous systems." J. Solution Chem. **21**(8): 849-881.

Maeda, Y. (1995). "Visible photoluminescence from nanocrystallite Ge embedded in a glassy $SiO_2$ matrix: Evidence in support of the quantum-confinement mechanism." Phys. Rev. B **51**(3): 1658-1670.

Maiella, P. G. and T. B. Brill (1996). "Spectroscopy of Hydrothermal Reactions. III. The Water- Gas Reaction, "Hot Spots", and Formation of Volatile Salts of $NCO^-$ from aqueous $[NH_3(CH_2)n\ NH_3]NO_3$ (n=2,3) at 720 K and 276 bar by T-jump/FT-IR Spectroscopy." Appl.Spectroscopy **50**(7): 829.

March, J. (1992). Advanced Organic Chemistry: Reactions, Mechanisms, and Structure. New York, Wiley.

Marshall, W. L. and E. U. Franck (1981). "Ion product of water substance, 0-1000°C, 1-10000 bars. New international formulation and its background." J.Phys.Chem.Ref.Data **10**(2): 1.

Marshall, W. L. and E. V. Jones (1974). "Liquid - Vapor Critical Temperatures of Aqueous Electrolyte Solutions." J.inorg.nucl.Chem. **36**: 2313.

Marshall, W. L. and R. Slusher (1975). "Experimental and calculated solubilities of magnesium sulfate monohydrate in aqueous nitric acid and related solubilities, 200-350°C; Ionization constants of nitric acid at 300-370°C." J.inorg.nucl.Chem. **37**: 2165.

Marshall, W. L. and R. Slusher (1975). "The ionization constant of nitric acid at high temperatures from solubilities of calcium sulfate in $HNO_3$-$H_2O$, 100-350°C; Activity coefficients and thermodynamic functions." J.inorg.nucl.Chem. **37**: 1191.

Martynova, O. I., Ed. (1976). Solubility of Inorganic Compounds in Subcritical and Supercritical Water. High Temperature, High Pressure Electrochemistry in Aqueous Solutions. Houston, National Association of Corrosion Engineers.

Mason (Banus), J. (1959). "Dinitrogen Trioxide: Some Observations on the Electronic Spectrum and Structure." J.Chem.Soc.: 1288.

Matijevic, E. (1987). "Uniform colloidal barium ferrite particles." J. Colloid Interface Sci. **117**: 593-595.

Matijevic, E. (1993). "Preparation and properties of uniform size colloids." Chem. Mater. **5**: 412-426.

McDonald, C. M. and C. A. Floudas (1995). "Global Optimization for the Phase and Chemical Equilibrium Problem: Application to the NRTL Equation." Computers chem. Engng **19**(11): 1111.

McFayden, P. and E. Matijevic (1973). J. Colloid Interface Sci. **44**: 95.

McHugh, M. A. and V. J. Krukonis (1993). Supercritical Fluids Extraction: Principles and Practice. MA, Butterworth-Heinman.

McLane, C. K. (1949). "Hydrogen Peroxide in the Thermal Hydrogen Oxide Reaction I. Thermal Decomposition of Hydrogen Peroxide." J.Chem.Phys. **17**(4): 379.

Mesmer, R. E., W. L. Marshall, D. A. Palmer, J. M. Simonson and H. F. Holmes (1988). "Thermodynamics of Aqueous Association and Ionization

Reactions at High Temperatures and Pressures." J.Solution Chem. **17**(8): 699.

Mihalcea, R. M., D. S. Baer and R. K. Hanson (1996). "Tunable diode-laser absorption measurements of $NO_2$ near 670 and 395 nm." Appl.Optics **35**(21): 4059.

Miller, J. A. and C. T. Bowman (1989). "Mechanism and modeling of nitrogen chemistry in combustion." Prog.Energy Combust.Sci. **15**: 287.

Murray, C. B., D. J. Norris and M. G. Bawendi (1993). "Synthesis and characterization of nearly monodisperse CdE (E=sulfur, selenium, tellurium) semiconductor nanocrystallites." J. Am. Chem. Soc. **115**: 8706.

Murtagh, B. A. and M. A. Saunders (1982). "A Projected Lagrangian Algorithm and Its Implementation for Sparse Nonlinear Constraints." Mathematical Programming Study **16**: 84.

Myers, A. K. and A. L. Myers (1986). "Numerical Solution of Chemical Equilibria with Simultaneous Reactions." J. Chem. Phys. **84**(10): 5787.

Nakayama, T., M. Y. Kitamura and K. Watanabe (1959). "Ionization Potential and Absorption Coefficients of Nitrogen Dioxide." J.Chem.Phys. **30**(5): 1180.

Niquet, Y. M., G. Allan, C. Delerue and M. Lannoo (2000). "Quantum confinement in germanium nanocrystals." Appl. Phys. Lett. **77**(8): 1182-1184.

Norris, M. S., S. A. Fleck and D. H. Lichtenfels (1955). "Ultraviolet Absorption Determination of Nitrogen Dioxide." Anal.Chem. **27**(10): 1565.

Odenbrand, C. U. I., L. A. H. Andersson, J. G. M. Brandin and S. T. Lundin (1986). "Catalytic Reduction of Nitrogen Oxides. 2. The Reduction of $NO_2$." Appl.Catalysis **27**: 363.

Okamoto, S. and Y. Kanemitsu (1996). "Photoluminescence properties of surface-oxidized Ge nanocrystals: Surface localization of excitons." Phys. Rev. B **54**(23): 16421-16424.

Oldenborg, R., J. M. Robinson, S. J. Buelow, R. B. Dyer, G. Anderson, P. C. Dell'Orco, K. Funk, E. Willmanns and K. Knutsen (1994). Hydrothermal

Processing of Inorganic Components of Hanford Tank Wastes. Los Alamos National Laboratories report LA-UR-94:3233. Los Alamos, Los Alamos National Laboratories.

Olynick, D. L., J. M. Gibson and R. S. Averback (1996). "Trace oxygen effects on copper nanoparticle size and morphology." Appl. Phys. Lett. **68**(3): 343-345.

Oscarson, J. L., S. E. Gillespie, R. M. Izatt, X. Chen and C. Pando (1992). "Thermodynamic Quantities for the Ionization of Nitric Acid in Aqueous Solution from 250 to 319°C." J.Solution Chem. **21**(8): 789-801.

Paine, D. C., C. Caragianis, T. Y. Kim, Y. Shigesato and T. Ishahara (2842). "Visible photoluminescence from nanocrystallite Ge formed by $H_2$ reduction of $Si_{0.6}Ge_{0.4}O_2$." Appl. Phys. Lett. **62**(22): 2842-2844.

Park, S., H. Kim, K. Kim, J. Lee and D.-S. Lho (1999). "Spectroscopic measurement of the acid dissociation constant of 2-naphthol and the second dissociation constant of carbonic acid at elevated temperatures." Pccp : physical chemistry, chemical physics, a **1**(8): 1893.

Park, S. N., C. S. Kim, M. H. Kim, I.-J. Lee and K. Kim (1998). "Spectrophotometric measurement of the first dissociation constants of carbonic acid at elevated temperatures." J.Chem.Soc., Faraday Trans. **94**(10): 1421.

Patterson, C. S., R. H. Busey and R. E. Mesmer (1984). "Second Ionization of Carbonic Acid in NaCl Media to 250°C." J. Solution Chem. **13**(9): 647-661.

Patterson, C. S., G. H. Slocum, R. H. Busey and R. E. Mesmer (1982). "Carbonate equilibria in hydrothermal systems: first ionization of carbonic acid in NaCl media to 300°C." Geochim. Cosmochim. Acta **46**: 1653-1663.

Peierls, R. E. (1935). Ann. Inst. Henri Poincare **5**: 177.

Peng, C. S., Q. Huang, W. Q. Cheng, J. M. Zhou, Y. H. Zhang, T. T. Sheng and C. H. Tung (1998). "Optical properties of Ge self-organized quantum dots in Si." Phys. Rev. B **57**(15): 8805-8808.

Pich, J., S. K. Friedlander and F. S. Lai (1970). Aerosol Science **1**: 115-126.

Pitzer, K. S. (1983). "Thermodynamics of Sodium Chloride Solution in Steam." J. Physical Chemistry **87**(7): 1120.

Pitzer, K. S. (1991). Ion Interaction Approach. Theory and Data Correlation. Activity Coefficients in Electrolyte Solutions**:** 75-153.

Pizzagalli, L., G. Galli, J. E. Klepeis and F. Gygi (2001). "Structure and stability off germanium nanoparticles." Phys. Rev. B **63**: 165324.

Pretsch, E., T. Clerc, J. Seibl and W. Simon (1942). Tables of Spectral Data for Structure Determination of Organic Compounds. Berlin, Springer-Verlag.

Proesmans, P. I., L. Luan and S. J. Buelow (1997). "Hydrothermal Oxidation of Organic Wastes Using Ammonium Nitrate." Ind.Eng.Chem.Res. **36**: 1559.

Ramakrishna, M. V. and R. A. Friesner (1992). "Prediction of the anomalous redshift in semiconductor clusters." J. Chem. Phys. **96**: 873.

Ratcliffe, C. I. and D. E. Irish (1985). "Vibrational spectral studies of solutions at elevated temperatures and pressures. VII. Raman spectra and dissociation of nitric acid." Can.J.Chem. **63**: 3521.

Rath, S., S. Sato, H. Ono, S. Nozaki and H. Morisaki (1998). "Evidence of a tetragonal structure of germanium nanocrystals prepared by the cluster-beam deposition technique." Mater. Chem. Phys. **54**: 244-246.

Rebert, C. J. and W. B. Kay (1959). "The Phase Behavior and Solubility Relations of the Benzene-Water System." AIChE J. **5**: 285.

Reboredo, F. A. and A. Zunger (2000). "L-to-X crossover in the conduction-band minimum of Ge quantum dots." Phys. Rev. B **62**(4): R2275-R2278.

Reboredo, F. A. and A. Zunger (2001). "Surface-passivation-induced optical changes in Ge quantum dots." Phys. Rev. B **63**: 235314.

Reiss, H. (1951). "The growth of uniform colloidal dispersions." J. Chem. Phys. **19**: 482.

Roman, E. S. and M. C. Gonzalez (1989). "Analysis of Spectrally Resolved Kinetic Data and Time-Resolved Spectra by Bilinear Regression." J. Phys. Chem. **93**: 3532.

Ron, H., H. Cohen, S. Matlis, M. Rappaport and I. Rubinstein (1998). "Self-Assembled Monolayers on Oxidized Metals. 4. Superior n-Alkanethiol Monolayers on Copper." J. Phys. Chem. **102**: 9861.

Ryan, E. T., T. Xiang, K. P. Johnston and M. A. Fox (1997). "Absorption and Fluorescence Studies of Acridine in Subcritical and Supercritical Water." J.Phys.Chem. A **101**: 1827.

Sanderson, R. T. (1976). Chemical Bonds and Bond Energy. New York, Academic Press.

Savage, P. E., S. Gopalan, T. I. Mizan, C. J. Martino and E. E. Brock (1995). "Reactions at Supercritical Conditions: Applications and Fundamentals." AIChE J. **41**(7): 1723-1778.

Savage, P. E., R. Li and J. T. Santini (1994). J. Supercrit. Fluids **7**: 135-144.

Schmid, G., M. Baumle, M. Geerkens, I. Heim, C. Osemann and T. Sawitowski (1999). "Current and future applications of nanoclusters." Chem. Soc. Rev. **28**: 179.

Schneider, W., G. K. Moortgat, G. S. Tyndall and J. P. Burrows (1987). "Absorption cross-sections of NO2 in the UV and Visible region (200-700 nm) at 298 K." J.Photochem.Photobiol. **40**: 195.

Scholten, A. J., A. V. Akimov and J. I. Dijkhuis (1993). "Nonequilibrium phonons in amorphous silicon studies by pulsed Raman spectroscopy." Phys. Rev. B **47**: 13910.

Schoppelrei, J. W., Kieke, M.L., Brill, T.B. (1996). "Spectroscopy of Hydrothermal Reactions. 2. Reactions and Kinetic Parameters of $[NH_3OH]NO_3$ and Equilibria of $(NH_4)_2CO_3$ Determined with a Flow Cell and FT Raman Spectroscopy." J.Phys.Chem. **100**: 7463.

Schoppelrei, J. W., Kieke, M.L., Wang, X., Klein, M.T., Brill, T.B. (1996). "Spectroscopy of Hydrothermal Reactions. 4. Kinetics of Urea and Guanidinium Nitrate at 200-300 °C in a Diamond Cell, Infrared Spectroscopy Flow Reactor." J.Phys.Chem. **100**: 14343.

Schoppelrei, J. W., Brill, T.B. (1997). "Spectroscopy of Hydrothermal Reactions. 7. Kinetics of Aqueous $[NH_3OH]NO_3$ at 463-523 K and 27.5 MPa by Infrared Spectroscopy." J.Phys.Chem. A. **101**: 8593.

Sealock, L. J., D. C. Elliott, E. G. Baker and R. S. Butner (1993). "Chemical Processing in High-Pressure Aqueous Environments. 1. Historical Perspective and Continuing Developments." Ind. Eng. Chem. Res. **32**: 1535.

Seward, T. M. (1984). "The formation of lead(II) chloride complexes to 300°C: A spectrophotometric study." Geochim.Cosmochim.Acta **48**: 121.

Shah, P. S., J. D. Holmes, R. C. Doty, K. P. Johnston and B. A. Korgel (2000). "Steric Stabilization of Nanocrystals in Supercritical $CO_2$ Using Fluorinated Ligands." J. Am. Chem. Soc. **122**: 4245.

Shah, P. S., J. D. Holmes, K. P. Johnston and B. A. Korgel (2001). in preparation.

Shah, P. S., S. Husain, K. P. Johnston and B. A. Korgel (2001). "Nanocrystal arrested precipitation in supercritical carbon dioxide." submitted.

Shapiro, N. Z. and L. S. Shapley (1965). "Mass Action Laws and the Gibbs Free Energy Function." J. Soc. Indust. Appl. Math. **13**(2): 353.

Shaw, R. W., T. B. Brill, A. A. Clifford, C. A. Eckert and E. U. Franck (1991). "Supercritical Water: A Medium for Chemistry." Chem. and Eng. News **69**(51): 26.

Shin, T. W., K. Kim and I.-J. Lee (1997). J.Solution.Chem. **26**: 379.

Singer, K. and P. A. Vamplew (1956). "Oxidation by Nitrous and Nitric Acid. Part IV. Spectroscopic Investigation of the Equilibrium between $NO^+$ and Nitrous Acid in Aqueous Perchloric Acid." J.Chem.Soc.: 3971.

Sitkoff, D., K. A. Sharp and B. Honig (1994). "Accurate Calculation of Hydration Free Energies Using Macroscopic Solvent Models." J.Phys.Chem. **98**: 1978.

Smith, S. and L. Lasdon (1992). "Solving Large Sparse Nonlinear Programs Using GRG." Journal on Computing **4**(1): 1.

Smith, W. R. and R. W. Missen (1982). Chemical Reaction Equilibrium Analysis: Theory and Algorithms. New York, John Wiley & Sons, Inc.

Socrates, G. (1994). Infrared Characteristic Group Frequencies Tables and Charts. New York, John Wiley & Sons.

Song, W. and M. Larson (1991). "Phase Equilibrium Calculation by using Large-Scale Optimization Technique." Chemical Engineering Science **46**(10): 2513.

Spohn, P. D. and T. B. Brill (1989). "Raman Spectroscopy of the Species in Concentrated Aqueous Solutions of $Zn(NO_3)_2$, $Ca(NO_3)_2$, $LiNO_3$, and $NaNO_3$ up to 450 oC and 30 MPa." J.Phys.Chem. **93**: 6224.

Sponer, H. and L. G. Bonner (1940). "Note on the Continuous Absorptions of $N_2O$." J.Chem.Phys. **8**: 33.

Strickler, S. J. and M. Kasha (1963). "Solvent Effects on the Electronic Absorption Spectrum of Nitrite Ion." J.Phys.Chem. or J.Am.Chem.Soc. **85**: 2899.

Sung, M. M., K. Sung, C. G. Kim, S. S. Lee and Y. Kim (2000). "Self-Assembled Monolayers of Alkanethiols on Oxidized Copper Surfaces." J. Phys. Chem. B **104**(10): 2273-2277.

Swift, D. L. and S. K. Friedlander (1964). J. Colloid Interf. Sci. **19**: 621-647.

Sze, S. M. (1981). Physics of Semiconductor Devices. New York, Wiley.

Takagahara, T. and K. Takeda (1992). "Theory of the quantum confinement effect on excitons in quantum dots of indirect-gap materials." Phys. Rev. B **46**(23): 15578-15581.

Takagai, H., H. Ogawa, Y. Yamzaki, A. Ishizaki and T. Nakagiri (1990). "Quantum size effects on photoluminescence in ultrafine Si particles." Appl. Phys. Lett. **56**: 2379.

Takagi, J. and K. Ishigure (1985). "Thermal Decomposition of Hydrogen Peroxide and Its Effect on Reactor Water Monitoring of Boiling Water Reactors." Nuc.Sci.Eng. **89**: 177.

Tamura, H. and E. Matijevic (1982). "Precipitation of cobalt ferrites." J.Colloid. Interface Sci. **90**: 100-109.

Taugbol, K., E. Augdahl and A. N. Sara (1967). "Germanium alkoxides. Attempt at synthesis by photochemical coupling." Acta Chem. Scand. **21**(3): 817-819.

Taylor, B. R., S. M. Kauzlarich, G. R. Delgado and H. W. H. Lee (1999). "Solution Synthesis and Characterization of Quantum Confined Ge Nanoparticles." Chem. Mater. **11**: 2493-2500.

Taylor, B. R., S. M. Kauzlarich, H. W. H. Lee and G. R. Delgado (1998). "Solution Synthesis of Germanium Nanocrystals Demonstrating Quantum Confinement." Chem. Mater. **10**: 22-24.

Tester, J. W., H. R. Holgate, F. J. Armellini, P. A. Webley, W. R. Killilea, G. T. Hong and H. E. Barner (1993). Supercritical Water Oxidation Technology: A Review of Process Development and Fundamental Research. Emerging Technologies in Hazardous Waste Management III. D. W. Tedder and F. G. Pohland. Washington, Am. Chem. Soc. **518:** 35-76.

Theobald, M., P. Baclet, O. Legaie and J. Durand (2001). "Doped CHx microshells prepared by radio frequency plasma enhanced chemical vapor deposition for intertial confinement fusion experiments." J. Vac. Sci. Technol. A **19**(1): 118-123.

Tummavuori, J. and P. Lumme (1968). "Protolysis of Nitrous Acid in Aqueous Sodium Nitrate and Sodium Nitrite Solutions at Different Temperatures." Acta Chem.Scand. **22**: 2003.

Urban, J., H. Sack-Kongehl and K. Weiss (1996). "HREM studies of the structure and the oxidation process of copper clusters created by inert gas aggregation." Z. Phys. D **36**: 73-83.

Urban, J., H. Sack-Kongehl and K. Weiss (1997). "Study of partial oxidation of Cu clusters by HRTEM." Catalysis Letters **49**: 101-108.

Van Buuren, T., L. N. Dinh, L. L. Chase, W. J. Siekhaus and L. J. Terminello (1998). "Changes in electronic properties of Si nanocrystals as a function of particle size." Phys. Rev. Lett. **80**: 3803.

Verhoek, F. H. and F. Daniels (1931). "The dissociation constants of nitrogen tetroxide and of nitrogen trioxide." J.Am.Chem.Soc. **53**: 1250.

Watkins, J. J., J. M. Blackburn and T. J. McCarthy (1999). "Chemical Fluid Deposition: Reactive Deposition of Platinum Metal from Carbon Dioxide Solution." Chem. Mater. **11**(2): 213-215.

Wendel, M. M. and R. L. Pigford (1958). "Kinetics of Nitrogen Tetroxide Absorption in Water." A.I.Ch.E. Journal **4**(3): 249.

Wikstrom, M. M. and K. Nobe (1965). "Catalytic Dissociation of Nitrogen Dioxide." I&EC Process Design and Development **4**(2): 191.

Wilcoxon, J. P. and G. A. Samara (1999). "Tailorable, visible light emission from silicon nanocrystals." Appl. Phys. Lett. **74**: 3164.

Wilcoxon, J. P., G. A. Samara and P. N. Provencio (1999). "Optical and electronic properties of Si nanoclusters synthesized in inverse micelles." Phys. Rev. B **60**: 2704.

Wilcoxon, J. P., P. P. Provencio and G. A. Samara (2001). "Synthesis and optical properties of colloidal germanium nanocrystals." Phys. Rev. B **64**: 035417.

Wilson, W. L., P. F. Szajowski and L. E. Brus (1993). "Quantum confinement in size-selected surface oxidized silicon nanocrystals." Science **262**: 1242.

Wofford, W. T., E. F. Gloyna and K. P. Johnston (1998). "Boric Acid Equilibria in Near-Critical and Supercritical Water." Ind. Eng. Chem. Res. **37**(5): 2045.

Wolkin, M. V., J. Jorne, P. M. Pauchet, G. Allan and C. Delerue (1999). "Electronic states and luminescence in porous silicon quantum dots: The role of oxygen." Phys. Rev. Lett. **82**: 197.

Wood, R. H., J. R. Quint and J.-P. E. Grolier (1981). "Thermodynamics of a charged hard sphere in a compressible dielectric fluid. A modification of the Born equation to include the compressibility of the solvent." J. Phys. Chem. **85**(25): 3944-3949.

Wu, Y. and P. Yong (2001). "Melting and Welding Semiconductor Nanowires in Nanotubes." Adv. Mater. **13**(7): 520-523.

Xiang, T. and K. P. Johnston (1994). "Acid-Base Behavior of Organic Compounds in Supercritical Water." J.Phys.Chem. **98**: 7915.

Xiang, T. and K. P. Johnston (1997). "Acid-base behavior in supercritical water: β-naphthoic acid ammonia equilibrium." J.Solution Chem. **26**: 13.

Xiang, T., K. P. Johnston, W. T. Wofford and E. F. Gloyna (1996). "Spectroscopic Measurement of pH in Aqueous Sulfuric Acid and

Ammonia from Sub- to Supercritical Conditions." Ind.Eng.Chem.Res. **35**: 4788.

Yang, C.-S., R. A. Bley, S. M. Kauzlarich, H. W. H. Lee and G. R. Delgado (1999). "Synthesis of Alkyl-Terminated Silicon Nanclusters by a Solution Route." Journal of the american chemical society **121**(22): 5191.

Yang, C.-S., S. M. Kauzlarich and Y. Wang, C. (1999). "Synthesis and Characterization of Germanium/Si-Alkyl and Germanium/Silica Core-Shell Quantum Dots." Chem. Mater. **11**(12): 3666-3670.

Zacharias, M. and P. M. Fauchet (1997). "Blue luminescence in films containing Ge and $GeO_2$ nanocrystals: The role of defects." Appl. Phys. Lett. **71**(3): 380-382.

Ziegler, K. J., J. Chlistunoff, L. Lasdon and K. P. Johnston (1999). "Optimization models for determining nitric acid equilibria in supercritical water." Computers and Chemistry **27**: 421.

Ziegler, K. J., R. C. Doty, K. P. Johnston and B. A. Korgel (2001). "Synthesis of Organic Monolayer-Stabilized Copper Nanocrystals in Supercritical Water." J. Am. Chem. Soc. **123**: 7797-7803.

# Vita

Kirk J. Ziegler, son of Mr. Gary Ziegler and Ms. Deanna Grime, was born in Wauseon, Ohio on June 4, 1973. After graduating from Findlay High School in June of 1991, he entered the University of Cincinnati in September of 1991. While at the University, he took part in the co-op program, and worked for Mead Paper in Chillicothe, Ohio for 6 months and for Siemens Energy & Automation in Norwood, Ohio for nearly 2 years. In the summer of 1996, he earned his B.S. degree in chemical engineering. From August of 1996 to August of 2001, he has pursued a Ph.D. degree in chemical engineering at The University of Texas at Austin under the supervision of Dr. Keith P. Johnston and Dr. Brian A. Korgel. He has received an Enterprise Ireland post-doctoral fellowship and has taken a position with Dr. Justin D. Holmes at the University College Cork in Cork, Ireland starting in October 2001.

Permanent Address: 3219 Ridgeview Drive
Findlay, Ohio 45840

This dissertation was typed by the author.